NUMERICAL METHOD FOR TSUNAMI CALCULATION USING FULL NAVIER-STOKES EQUATIONS AND THE VOLUME OF FLUID METHOD

A

DISSERTATION

Presented to the Faculty

of the University of Alaska Fairbanks

In Partial Fulfillment of the Requirements

for the Degree of

DOCTOR OF PHILOSOPHY

By

Juan J. Horrillo, MS.

Fairbanks, Alaska

May 2006

Reproduced with permission of the copyright owner. Further reproduction prohibited without permission.

UMI Number: 3229736

Copyright 2006 by
Horrillo, Juan J.

All rights reserved.

INFORMATION TO USERS

The quality of this reproduction is dependent upon the quality of the copy submitted. Broken or indistinct print, colored or poor quality illustrations and photographs, print bleed-through, substandard margins, and improper alignment can adversely affect reproduction.

In the unlikely event that the author did not send a complete manuscript and there are missing pages, these will be noted. Also, if unauthorized copyright material had to be removed, a note will indicate the deletion.

UMI®

UMI Microform 3229736
Copyright 2006 by ProQuest Information and Learning Company.
All rights reserved. This microform edition is protected against unauthorized copying under Title 17, United States Code.

ProQuest Information and Learning Company
300 North Zeeb Road
P.O. Box 1346
Ann Arbor, MI 48106-1346

Reproduced with permission of the copyright owner. Further reproduction prohibited without permission.

NUMERICAL METHOD FOR TSUNAMI CALCULATION USING FULL NAVIER-STOKES EQUATIONS AND THE VOLUME OF FLUID METHOD

By

Juan J. Horrillo

RECOMMENDED:

Advisory Committee Chair

Head, Program in Marine Science and Limnology

APPROVED:

Dean, School of Fisheries and Ocean Sciences

Dean of the Graduate School

July 20, 2006

Date

Reproduced with permission of the copyright owner. Further reproduction prohibited without permission.

Abstract

A two-dimensional numerical model was developed to study tsunami wave generation, propagation and runup. The model is based on solving the Navier-Stokes (NS) equations. The free-surface motion is tracked using the Volume of Fluid technique. The finite difference two-step projection method is used to solve NS equations and the forward time difference method to discretize the time derivative. A structured mesh is used to discretize the spatial domain. The model has been conceived as a versatile, efficient and practical numerical tool for tsunami computation, which could address a comprehensive understanding of tsunami physics with the ultimate aim of mitigating tsunami hazards. The prediction capability of tsunami generation, propagation and runup is improved by including more accurately the effects of vertical velocity/acceleration, dispersion and wave breaking. The model has the capability to represent complex curved boundaries within a Cartesian grid system and to deal with arbitrary transient-deformed moving boundaries. The numerical model was validated using laboratory experiments and analytical solutions. The model was used as a tool to determine the adequacy of the shallow water (SW) approximation in the application of tsunami simulations. Numerical results were compared with experimental data, analytical solutions and SW results in terms of the time-history free surface elevations and velocity. Reasonable agreements were observed based on the spatial and temporal distributions of the free surface and velocity.

Reproduced with permission of the copyright owner. Further reproduction prohibited without permission.

Table of Contents

Page

Reproduced with permission of the copyright owner. Further reproduction prohibited without permission.

Page

Reproduced with permission of the copyright owner. Further reproduction prohibited without permission.

Page

Reproduced with permission of the copyright owner. Further reproduction prohibited without permission.

Page

Reproduced with permission of the copyright owner. Further reproduction prohibited without permission.

List of Figures

Reproduced with permission of the copyright owner. Further reproduction prohibited without permission.

Figure **Page**

Reproduced with permission of the copyright owner. Further reproduction prohibited without permission.

Figure **Page**

Reproduced with permission of the copyright owner. Further reproduction prohibited without permission.

Figure **Page**

Reproduced with permission of the copyright owner. Further reproduction prohibited without permission.

List of Tables

Reproduced with permission of the copyright owner. Further reproduction prohibited without permission.

List of Appendices

Reproduced with permission of the copyright owner. Further reproduction prohibited without permission.

Notations

α	parameter to weight the upstream derivative
$\alpha_o, \beta_o, \gamma_o$	geometric coefficients resulting from coordinate transformation (Cartesian to natural)
β	landslide slope angle
δ	vertical landslide thickness
δt	time step
δ_{min}	minimum cell spacing
$\delta x, h_x$	cell size x-direction
$\delta y, h_y$	cell size y-direction
δy_{bot}	vertical averaged cell space at $v(i, j-1)$
δy_{top}	vertical averaged cell space at $v(i, j)$
δx_{left}	horizontal averaged cell space at $u(i-1, j)$
δx_{right}	horizontal averaged cell space at $u(i, j)$
δy_{bbot}	vertical averaged cell space at $v(i, j-2)$
δy_{ttop}	vertical averaged cell space at $v(i, j+1)$
δx_{lleft}	horizontal averaged cell space at $u(i-2, j)$
δx_{rright}	horizontal averaged cell space at $u(i+1, j)$
δx_α	horizontal weighted cell distance at $u(i, j)$
δy_α	vertical weighted cell distance at $v(i, j)$
$\delta x u_\alpha$	horizontal weighted cell distance at u_{avg}
$\delta y v_\alpha$	vertical weighted cell distance at v_{avg}
ΔF_{right}	volume of fluid F function advected through the right cell face
ΔF_{top}	volume of fluid F function advected through the top cell face
ΔV_{right}	volume of fluid advected through the right cell face per unit area

Reproduced with permission of the copyright owner. Further reproduction prohibited without permission.

ΔV_{top}	volume of fluid advected through the top cell face per unit area
η	free surface vertical displacement
$\eta_o(x,t)$	landslide thickness
Γ_b	stationary object boundary
Γ_o	moving object boundary
Γ_s	free surface boundary
κ	free surface curvature
μ	1) molecular viscosity
	2) landslide thickness-length ratio
μ_x	bottom friction in the x-direction
ν	kinematic viscosity
Ω	bounded computational domain
ϕ	internal volume function to account for volume taken or released by a moving object in a lapse of time δt
$\phi(\mathbf{x},t)$	time dependent internal moving-object function needed to force zero divergence in the control volume V
Φ	numerical internal moving-object function
ψ	potential function for pressure correction
ρ	fluid density
ρ_o	constant density in the fluid domain
ρ_{right}	averaged fluid density at the right cell face
ρ_{top}	averaged fluid density at the top cell face
σ	surface tension
τ	stress tensor
τ_{xx}	normal viscous stress in x-direction
τ_{yy}	normal viscous stress in y-direction

Reproduced with permission of the copyright owner. Further reproduction prohibited without permission.

$\tau_{xy} = \tau_{yx}$	off-diagonal viscous stress
Θ	element or cell aperture function
ϱ	smooth-level set function
(ξ, ζ)	natural coordinates of unit length
ζ	sea level
a	wave amplitude
A	matrix coefficients in the main diagonal
$Area$	polygon area
A_T	cell top-side fractional aperture area
A_R	cell right-side fractional aperture area
A_C	cell fractional aperture volume
A_{Cs}	cell fractional aperture volume without moving object
$A_{top_{i,j}}$	cell top-side aperture area
$A_{right_{i,j}}$	cell right-side aperture area
A_{Tbot}	weighted average aperture at the bottom of the control volume
A_{Ttop}	weighted average aperture at the top of the control volume
A_{Rleft}	weighted average aperture at the left of the control volume
A_{Rright}	weighted average aperture at the right of the control volume
$A_{Twest,east,south,north}$	horizontal cell aperture for the free surface boundary condition
$A_{Rwest,east,south,north}$	vertical cell aperture for the free surface boundary condition
$A_{Tcenter}$	averaged horizontal aperture for the free surface boundary condition
B_T	cell top-side fractional blocked area
B_R	cell right-side fractional blocked area

Reproduced with permission of the copyright owner. Further reproduction prohibited without permission.

B_C	cell fractional blocked volume
B_{Ts} and B_{Tm}	cell top-side fractional blocked area corresponding to stationary and moving object, respectively
B_{Rs} and B_{Rm}	cell right-side fractional blocked area corresponding to stationary and moving object, respectively
B_{Cs} and B_{Cm}	cell fractional blocked volume corresponding to stationary and moving object, respectively
B^{low}, B^{upp}	lower and upper matrix coefficients from the main diagonal
C^{low}, C^{upp}	lower and upper matrix coefficients offset $I_{max} - 2$ from the main diagonal
C	wave speed
C_f	wave speed over dry-bed
D	total depth
D_o	initial total depth
D_{long}	nondimensional distance from the cell center to the farther shifted velocity resulting from the application of the method of characteristic
D_{short}	nondimensional distance from the cell center to the closer shifted velocity resulting from the application of the method of characteristic
D_M	total depth at M (mass transport x-direction) points
D_r	total depth for runup condition
$F(\mathbf{x}, t)$	volume of fluid scalar field
F	fractional volume of fluid function
F_A	fractional volume of fluid function corresponding to acceptor cell
F_D	fractional volume of fluid function corresponding to donor cell

Reproduced with permission of the copyright owner. Further reproduction prohibited without permission.

F_r	Froude number
$\langle F \rangle$	fractional volume of fluid function corresponding to donor or acceptor cell according to velocity direction and fluid interface orientation
g	gravitational acceleration parameter
$\mathbf{g} = (g_x\ \hat{i} + g_y\ \hat{j})$	gravitational acceleration field (usually $g_x = 0$ and $g_y = -9.8\ \mathrm{ms}^{-2}$)
H, h	water depth
(i, j)	x-direction and y-direction indexes
I_{max}, J_{max}	total number of cells in the x-direction and y-direction
J	Jacobian determinant
k	wave number
L	1) domain or subdomain length 2) landslide length 3) wave length
m	old time level
$m+1$	new time level
M	1) operator matrix resulting from the finite difference scheme of the PPE 2) mass transport in the x-direction
n	polygon number of vertices
$n_{(i,j)}$	one-dimension index related to two-dimension indexes (i, j)
$\mathbf{n_F}$	fluid normal vector at the boundary of the control volume V
$\mathbf{n_O}$	normal vector at the object boundary
$\mathbf{n_{orm}}$	unit normal vector at the stationary solid boundary
N	number of cells along the domain length L

Reproduced with permission of the copyright owner. Further reproduction prohibited without permission.

N'	adjusted number of cells along the domain length L
N_{CFL}	Courant-Friedrichs-Lewy number
O	higher order terms
p	1) scalar pressure in momentum equation
	2) polygon index list
p_o	air pressure
S	column matrix from independent terms
S_O	object boundary surface area in the control volume V
S_F	fluid boundary surface area in the control volume V
S_{OF}	object-fluid interface boundary surface area in the control volume V
Su	sign of u velocity
Sv	sign of v velocity
Su_{avg}	sign of u_{avg} velocity
Sv_{avg}	sign of v_{avg} velocity
Su_r	sign of u_r velocity
Su_l	sign of u_l velocity
Sv_b	sign of v_b velocity
Sv_t	sign of v_t velocity
Su_{lt}	sign of u_{lt} velocity
Su_{rt}	sign of u_{rt} velocity
Sv_{rb}	sign of v_{rb} velocity
Sv_{rt}	sign of v_{rt} velocity
Sg_p	parameter for positive velocity whether the three neighboring velocities are monotonic or have an extreme velocity value
Sg_n	parameter for negative velocity whether the three neighboring

Reproduced with permission of the copyright owner. Further reproduction prohibited without permission.

	velocities are monotonic or have an extreme velocity value
t	time
t_*	dimensionless time
$\mathbf{t_{ang}}$	unit tangential vector at the stationary solid boundary
T	numerical time step
T_{half}	numerical time step for advection terms when the method of characteristic is used
u	horizontal velocity component
$\tilde{u}$	horizontal intermediate velocity
u_{norm}	normal velocity at the stationary solid boundary
u_{tang}	tangential velocity at the stationary solid boundary
u_{avg}	averaged horizontal velocity at v points
u_r	right-cell-center averaged horizontal-velocity
u_l	left-cell-center averaged horizontal-velocity
u_{lt}	averaged horizontal velocity at the left of the control volume for the y-momentum equation
u_{rt}	averaged horizontal velocity at the right of the control volume for the y-momentum equation
u_{west}	west horizontal-velocity for the free surface boundary condition
u_{east}	east horizontal-velocity for the free surface boundary condition
u_{south}	south horizontal-velocity for the free surface boundary condition
u_{north}	north horizontal-velocity for the free surface boundary condition
u_R	right flux-momentum horizontal velocity
u_L	left flux-momentum horizontal velocity
u_{RB}	right-bottom flux-momentum horizontal velocity
u_{RT}	right-top flux-momentum horizontal velocity

Reproduced with permission of the copyright owner. Further reproduction prohibited without permission.

$\mathbf{u} = (u\ \hat{i} + v\ \hat{j})$	velocity field vector
$\mathbf{u_o} = (u_o\ \hat{i} + v_o\ \hat{j})$	object velocity vector
$\tilde{\mathbf{u}} = (\tilde{u}\ \hat{i} + \tilde{v}\ \hat{j})$	intermediate velocity field
v	vertical velocity component
$\tilde{v}$	vertical intermediate velocity
v_{avg}	averaged vertical velocity at u points
v_b	bottom-cell-center averaged vertical-velocity
v_t	top-cell-center averaged vertical-velocity
v_{rb}	averaged vertical velocity at the bottom of the control volume for the x-momentum equation
v_{rt}	averaged vertical velocity at the top of the control volume for the x-momentum equation
v_{west}	west vertical-velocity for the free surface boundary condition
v_{east}	east vertical-velocity for the free surface boundary condition
v_{south}	south vertical-velocity for the free surface boundary condition
v_{north}	north vertical-velocity for the free surface boundary condition
v_{center}	averaged vertical velocity for the free surface boundary condition
v_B	bottom flux-momentum vertical velocity
v_T	top flux-momentum vertical velocity
v_{LT}	left-top flux-momentum vertical velocity
v_{RT}	right-top flux-momentum vertical velocity
V	arbitrary control volume or cell volume
V_O	object volume in the control volume V
V_F	fluid volume in the control volume V
V_{TSB}	triangular-solid-box velocity

Reproduced with permission of the copyright owner. Further reproduction prohibited without permission.

$V_{i,j}$	cell aperture volume
x	horizontal coordinate
$X(y)$	surface height-function with respect to X-axis
$\mathbf{x} = (x\ \hat{i} + y\ \hat{j})$	Cartesian coordinate
$\mathbf{X}(t)$	free surface position vector
y	vertical coordinate
$Y(x)$	surface height-function with respect to Y-axis
$Z(t)$	1) dam-gate motion in centimeter
	2) vertical displacement of the triangular solid box (TSB)
	in meters

Reproduced with permission of the copyright owner. Further reproduction prohibited without permission.

Acronyms

(B)	Boundary cell label
(E)	Empty cell label
(F)	Full cell label
(O)	Object cell label
(S)	Surface cell label
ADI	Alternating-Directional-Implicit
AMR	Adaptive Mesh Refinement
ARSC	Arctic Rigion Supercomputing Center
ASCE	American Society of Civil Engineering
CFD	Computational Fluid Dynamics
CFL	Courant-Friedrichs-Lewy
CMT	Centroid-Moment Tensor
CPU	Central Processing Unit
FAVOR	Fractional Area Volume Obstacle Representation
FDM	Finite Difference Method
FLAIR	Flux Line-segment model for Advection and Interface Reconstruction
NS	Navier-Stokes
NS-VOF	Navier-Stokes and Volume of Fluid
GMRES	General Minimum Residual
ICCG	Incomplete Cholesky Conjugate Gradient
IOT	Indian Ocean Tsunami
LES	Large Eddy Simulation
LSW	Linear Shallow Water
MAC	Marker and Cell

Reproduced with permission of the copyright owner. Further reproduction prohibited without permission.

MC	Micro Cell
NLB	Nonlinear Boussinesq
NLSW	Nonlinear Shallow Water
PPE	Pressure Poisson Equation
RIPPLE	Computer program for incompressible flows with free surfaces
SGS	Subgrid Scale
SLIC	Simple Line Interface Calculation
SM	Surface Marker
SMAC	Simplified MAC
SOLA	Solution Algorithm
SOR	Successive Over Relaxation
SW	Shallow Water
TSB	Triangular Solid Box
UAF	University of Alaska Fairbanks
VOF	Volume of Fluid

Reproduced with permission of the copyright owner. Further reproduction prohibited without permission.

Acknowledgments

To my mother, wife, son and daughters.

I have good reason to be grateful to a large number of people and would like to take this opportunity to express my sincere gratitude to all my friends and colleagues at the Institute of Marine Science, University of Alaska Fairbanks, for their help, suggestions and tolerance in what, at times, must have appeared to them to be almost interminable.

I would like to express my sincerest thanks to Professor Zygmunt Kowalik for his constant guidance, support and encouragement. It has been a privilege for me to do research under his supervision.

I am very grateful to Professors Sathy Naidu, Fumihiko Imamura, Mark Johnson and Tom Weingartner for serving on my committee.

Also, I would like to thank Edward Kornkven for the countless hours he spent helping me to improve the code's performance and Frank Williams for his unconditional support. This work would not have been possible without their collaborations.

I want to thank my wife. She has been my best and most critical reader, my greatest supporter and my constant encouragement.

I would like to express my profound gratitude to all my Professors, Edward Bueler, John Olson, Sathy Naidu, Fumihiko Imamura, Mark Johnson and Tom Weingartner for their time and guidance. Thanks are extended to Professor Stephan Grilli, who was my MS advisor and introduced me into this fascinating field.

Last, but by no means least, I would like to express my gratitude to Weislawa, 2×Laura, Christina, Beth, Robbie, Debbie, Carl, Ruth, Rose, 3×Jennifer, Yoshinori, Bill, Mark, Rob, Steve and Juan for their patience, kindness and unconditional help.

Reproduced with permission of the copyright owner. Further reproduction prohibited without permission.

Chapter 1

Introduction

1.1 Motivation

The coastal communities of Alaska are located in one of the most active seismic regions of the world; Alaska has the greatest tsunami potential in the entire United States. To ensure reliable tsunami hazard assessment capabilities, it is essential to create and refine tsunami calculation tools from different perspectives. Because the vertical acceleration associated with tsunami shallow-water waves is small compared with gravity acceleration, tsunami calculations are commonly resolved using two-dimensional hydrostatic models, named shallow water approximation. Shallow water models take into account only horizontal velocities and calculate vertical sea level change through the mass conservation equation. However, high vertical velocity/acceleration is often present within the wave runup and generation regions. Under these conditions, the hydrostatic assumption of the shallow water approximation is not valid. Application of shallow water approximation is not viable in situations where the wave regime is in deep or intermediate water depth, as they often occur in landslide and dispersive waves. A Navier-Stokes approach is most suitable for these situations, since: a) it is possible to include the vertical component of velocity/acceleration and b) it is nonhydrostatic so forces can be estimated more accurately.

A tsunami is a natural phenomenon consisting of a series of waves generated when water in an ocean basin or lake is rapidly displaced on a massive scale. Earthquakes, landslides, volcanic eruption or explosion and large meteorite impacts all have the potential to generate tsunamis. The effects of a tsunami along the coast can range from unnoticeable to devastating. However, a tsunami is much more likely to be produced by the vertical motion of a large submarine earthquake than by the impact of a

Reproduced with permission of the copyright owner. Further reproduction prohibited without permission.

large meteorite. The sudden vertical deformation of the seabed during an earthquake has the potential to displace massive volumes of water by several meters, resulting in a series of waves that can strike the surrounding coasts. The potential energy of tsunami waves could be in the order of 5×10^3 terajoules (5×10^{15} joules). This is a little more than the M_2 tidal potential energy of one tidal period in Cook Inlet bay, Alaska (Kowalik, 2004), but released in just a few minutes. This energy is still a couple of orders of magnitude less than the energy released by the earthquake that generated it. The length and orientation of submarine-earthquake faultlines are decisive factors determining energy spreading. Most of the energy spreads in a direction perpendicular to the faultline.

Tsunamis behave differently in deep water than in shallow water. In deep ocean, tsunami waves form only small swells, imperceptible and harmless, which generally travel at high speed of the order of 200 m/s (700 km/h or 450 miles/h); in shallow water near a coastline, a tsunami slows down to only tens of kilometers per hour but in doing so forms large destructive waves. Tsunami waves can reach a height of 24 m (80 feet) when moving ashore along large stretches of the coastline, rising up to 30 m (100 feet) in some areas when traveling inland. In some tsunami events the waves have reached as far as 2 km (1.25 miles) inland. However, coastal regions that have a wide and shallow continental shelf are usually safe. Tsunami waves can sometimes diffract around land mass hitting harder on the opposite side of the land or focusing energy on peninsulas. Distance alone is not a guarantee of safety; some places often do not have a natural barrier or wide continental shelf and could be hit harder despite being much farther away from the tsunami source.

Depending on the distance of generation and ocean bathymetry, tsunami waves can take anywhere from a few minutes to $\sim$ 16 hours to reach the various coastlines of a given ocean basin. For instance, in the tsunami event that took place in the

Reproduced with permission of the copyright owner. Further reproduction prohibited without permission.

Indian Ocean on December 26, 2004, the northern regions of the Indonesian island of Sumatra were hit earlier, while Sri Lanka and the east coast of India were hit roughly 90 minutes to two hours after the earthquake. Thailand was also struck about two hours later, despite being closer to the epicenter, because the tsunami traveled more slowly in the shallow Andaman Sea off its western coast. The tsunami was noticed as far as the southernmost point of Africa, some 8,500 km (5,300 miles) away, where 1.5 m (5 feet) high waves surged onshore about 16 hours after the quake.

Some of the tsunami energy can also escape into other ocean basins, where it produces small but measurable tsunami waves along the distant coastal regions, typically around 20 to 40 cm of wave height. This relatively large tsunami wave at such a great distance is caused by focusing effects of the local bathymetry and by submarine ridges that slow the wave and concentrate the energy as the wave propagates. Ocean passages or straits help reorganize waves as they propagate into the contiguous ocean basin; refraction causes wave energy to concentrate around headlands that form the strait, and the energy that gets through the gap is diffused or diffracted in an organized fashion into the contiguous ocean basin (Kowalik *et al.*, 2005).

To mitigate tsunami coastal hazards, the first step is to identify the tsunami-inundation zone, i.e., the coastal zone at higher tsunami risk. Such a task is achieved by using numerical models, consulting historical records or by conducting geologic and geomorphology studies to detect past tsunami events. In areas where the maximum potential tsunami source is known (i.e., areas with active subduction zones offshore), tsunami generation mechanisms, initial wave configuration, propagation and runup can be mathematically modeled and maximum tsunami wave heights and runup can be estimated. If the area has experienced tsunamis and earthquakes in the past, the historical records can constrain wave height expectations. In areas where the maximum potential source is unknown and no historic events have been recorded, the

Reproduced with permission of the copyright owner. Further reproduction prohibited without permission.

maximum expected wave height is difficult to determine. In this case, many potential sources must be considered in the numerical simulation to determine the possible maximum wave height.

One effective, practical, but costly way for tsunami mitigation is commonly used in Japan. To minimize the inundation area, tsunami seawalls (often more than 5 m high) have been constructed along the shoreline. In other places of the world, such walls are not considered a justifiable approach to hazard reduction. Tsunami research centers around the world, supported by government institutions, have been expending considerable effort into estimating potential inundation zones along the coasts. Once inundation zones are defined, government authorities can design evacuation routes, as well as routes for search and rescue, while urban planners can develop priorities for such measures as relocation of critical and high-occupancy facilities. One of the most important mitigation steps that researchers have been suggesting to government authorities is the development of comprehensive educational materials and workshops to improve tsunami awareness among the public.

To ensure a better and reliable prediction in tsunami generation and runup regions, it is essential to use tsunami calculation tools that consider the vertical component of velocity/acceleration. For that reason, the Navier-Stokes approach is adopted in this study, since it includes the vertical component of velocity/acceleration. Since this approach is nonhydrostatic, forces can be determined accurately. As tsunami waves run up beaches, waves often impact man-made or natural structures, picking up along their way debris and objects such as boats, cars and trees. These objects become projectiles that can impact and destroy other structures further inland. Perhaps many of these structures could withstand the tsunami load, but not the drifted-objects impacting them. Therefore, an important engineering problem is the determination of tsunami-induced forces or pressure on these objects and structures,

Reproduced with permission of the copyright owner. Further reproduction prohibited without permission.

which can be achieved using a Navier-Stokes approach. Obtaining dynamic pressure from the Navier-Stokes solver will enable better design of structures on the water-front and help guide the decision making process in issues of land use. Engineering analysis might suggest relocation of facilities that are generators of potentially deadly debris, e.g., marinas, parking lots, etc., close to vulnerable high-occupancy structures or located in the densely populated regions. Other tsunami sources, like subaerial landslide, volcanic explosion, snow avalanche, pyroclastic flow and glacier and rock fall can generate a devastating local impulsive wave affecting the surrounding region. A shallow water approximation is not often appropriate for modeling a landslide and the impulsive wave it may generate. It is therefore critical to advance further the capability of modeling tsunamis for the purposes of describing wave generation and interaction with moving objects. The numerical model which incorporates the vertical component in tsunami calculation must be extended to allow moving boundaries into the computational domain in order to properly simulate these sources. The advancement of this study should be seen as a next level of a mitigation strategy aiming to reduce loss of property and lives within the tsunami inundation zones by continuous improvement of existent tools for tsunami calculation.

1.2 Scope of present study

This study particularly emphasizes understanding tsunami physics that can lead to effective measures for damage mitigation. The work is based on the continued development of computational techniques in the Institute of Marine Sciences, University of Alaska Fairbanks (UAF), for the numerical simulation of tsunami waves and their behavior according with the generation sources, and interactions with coastal topology and structures. Coupled with the direct field experience of UAF researchers in the assessment of tsunami flooding and the identification of vulnerable regions,

Reproduced with permission of the copyright owner. Further reproduction prohibited without permission.

the collaborative computational and practical research efforts from the Arctic Region Supercomputing Center (ARSC) have enabled the development of this study, materialized in a tsunami computer code for understanding tsunami dynamics. The analysis of actual tsunami events and the study of a set of laboratory experiments will guide the numerical and practical efforts by focusing the proposed investigations on the most practical and relevant problems for tsunamis. The hope and intended impact in the near future of the proposed research is the mitigation of the devastating consequences of tsunami events, including loss of human life, destruction of property, damage to the environment and economic and social issues.

Numerical simulations of three recent tsunami events in Papua New Guinea (1998), Peru (2001) and the Indian Ocean (2004) have again uncovered the reality that prediction capabilities of tsunami phenomena have been inadequate in two major areas; a) in modeling the source mechanisms and b) in modeling accurately the wave generation processes and runup. While the initial tsunami condition at the source plays an essential role in determining the maximum runup heights along the coastline, the calculation of an accurate initial condition of a seismic event still remains a formidable task. The difficulty is mainly attributable to the lack of measurements of seafloor deformations and fault displacements. Whereas seismologists and geologists continue to develop better models to prescribe the initial condition, immediate needs for tsunami hazard mitigation can be more effectively addressed by improving the capability to calculate coastal inundation for any prescribed initial condition. Consequently, herein we propose to develop an efficient and practical numerical tool for tsunami computation which could address comprehensive study focusing on understanding tsunami physics, with the ultimate aim of mitigating tsunami hazards. This study has the following objectives:

Reproduced with permission of the copyright owner. Further reproduction prohibited without permission.

- To improve the prediction capability of the tsunami generation/runup model by including more accurately the effects of vertical velocity/acceleration, dispersion and wave breaking.
- To increase the current understanding of fundamental physics associated with tsunami generation, propagation, runup and effects by considering the vertical component of velocity/acceleration.
- To achieve a practical means of describing the complex runup flows within the context of their interactions with bottom topography or structures.
- To develop practical methods to prescribe complex wave generation mechanisms and wave propagation by means of curved boundaries and moving objects.
- To validate the proposed model using appropriate laboratory experiments selected from the existent literature.
- To determine the adequacy of the nonlinear shallow water approximation for application in tsunami simulation.
- The advancement of this study will contribute to other tsunami mitigation endeavors such as the tsunami database, hazard mapping, education, warning and planning.

Understanding the fluid-solid interactions requires that the fluid dynamics simulation technique be able to deal with the vertical component of velocity/acceleration, curvilinear boundaries and moving objects. At the initiation of this work, the Navier-Stokes solver, aided by the volume of fluid method technique previously developed at Los Alamos National Laboratory (Kothe *et al.*, 1991), could deal with stationary objects with their geometries represented only by conic functions, resulting in an impractical method for representation of complex topologies, like morphology of coasts,

Reproduced with permission of the copyright owner. Further reproduction prohibited without permission.

man-made structures and sea bottom profiles. Consequently, three parallel efforts were undertaken to develop:

1) a two-dimensional Navier-Stokes solver, aided by the volume of fluid method, to track the free surface to solve tsunami problems in a practical and efficient way;

2) a capability to represent complex curved boundaries within a Cartesian grid system;

3) a capability to deal with arbitrarily transient-deformed moving boundaries.

The first goal is achieved with the development and validation of a two-dimensional Navier-Stokes solver and the volume of fluid method. This method is capable of simulating incompressible fluid flow problems in Cartesian coordinates, where the free surface can undergo severe deformations, including impact with solid boundaries and impact between converging fluid fronts. The method is also capable of handling the breakup of a fluid front from the main body of fluid and their eventual reconnection.

In this study, significant progress has been made on the second and third goals by the development of a method to define and track arbitrary curvilinear surfaces by the use of Lagrangian boundary markers in a manner similar to the tracking of the free surface with surface markers. These latest advances have demonstrated their usefulness in tsunami simulation for landslide-generation of impulsive water waves.

1.3 Literature survey

This section is intended to review all existing methods which use Navier-Stokes (NS) approximation and free surface tracking technique. The advantages and limitation of each method, with respect to accuracy, numerical complexity and compu-

Reproduced with permission of the copyright owner. Further reproduction prohibited without permission.

tational efficiency are evaluated. Emphasis is placed on the Volume of Fluid (VOF) method, which is the technique adopted in this study.

Most of the incompressible-Newtonian fluid flow physics can be described by Navier-Stokes equations. Various numerical schemes have been developed in the past to solve these equations. When a free surface is present, tracking the movement of the free surface becomes a complicated task, especially when the free surface experiences severe deformation, i.e., during the wave breaking process. The Marker and Cell method (MAC) (Harlow & Welch, 1965), and the VOF method (Nichols, Hirt & Hotchkiss, 1980) are techniques that have been commonly used to track free surface motion. For some particular purposes, other methods have also been used. These methods are: the height function method, which is usually used in water wave studies; the shock capturing method, which is often used in the multi-phase fluid system; and the level set approach (Sussman, Smereka & Osher, 1994), which is a relatively recent interface tracking technique.

One of the earliest numerical models for solving the Navier-Stokes equations was developed by Harlow & Welch (1965). In their model, the NS equations were first discretized into a forward-time finite difference form. By enforcing zero divergence of velocity field at both the previous and current time steps, the pressure at the current time step was solved with an iterative method. With the use of updated pressure the velocity information at the new time step can be obtained. After the introduction of Harlow and Welch's model, researchers continued to develop more accurate, versatile and computationally efficient models to solve the NS equations. The projection method, developed by Chorin (1968, 1969), uncouples the pressure field from the velocity field when the momentum equations are solved. In the projection method, the calculation is split into two steps. During the first step, an intermediate velocity field is calculated without the pressure, so that the intermediate velocity field carries

Reproduced with permission of the copyright owner. Further reproduction prohibited without permission.

the right amount of vorticity. During the second step, the pressure is updated based on the Poisson pressure equation that not only preserves the vorticity but also forces zero divergence of the new velocity field; thus, the continuity equation is satisfied. Later, Amsden & Harlow (1970) proposed a simplified MAC method (SMAC), with a similar treatment for pressure as the projection method. Based on the original Harlow and Welch model, Hirt, Nichols & Romero (1975) and Nichols, Hirt & Hotchkiss (1980) developed a new code called solution-algorithm (SOLA) to facilitate its use by personnel with little experience in computational fluid dynamics. In this code, the VOF method replaced the MAC method to track the free surface. In the last fifteen years, as computer power has increased at an accelerated speed, the development of new numerical models to solve NS equations and the application of these models to theoretical and practical fluid dynamic problems have become much more active. Major efforts have been devoted to develop more accurate and faster numerical schemes, e.g., second-order accurate and more computationally-efficient models. Based on the projection method, Kim & Moi (1993) attempted to upgrade the nonlinear advective term to second order accuracy by using the Adams-Bashforth scheme. Employing the projection method, van Kan (1986) developed another second-order accurate scheme with the alternating-directional-implicit (ADI) method. Bell, Collela & Glaz (1989) approached this problem from a different direction. They proposed a new iterative method, which is equivalent to the second-order Crank-Nicolson method, to solve the momentum equation. On the other hand, Kothe, Mjolsness & Torrey (1991) developed a new model called RIPPLE which solved the Poisson pressure equation using the incomplete Cholesky Conjugate Gradient (ICCG) method (Kershaw, 1976), which is more efficient than conventional iterative methods such as the Gaussian elimination or Successive-Over-Relaxation (SOR) method. In their model, a new approach was also adopted to model the surface tension as a volume force.

Reproduced with permission of the copyright owner. Further reproduction prohibited without permission.

If the vertical displacement of the free surface, η, is a single-valued function of horizontal coordinates, i.e., $y = \eta(x,t)$, which is the assumption often adopted in the non-breaking water wave theory, an even simpler formulation of the kinematic free surface boundary can be derived (see Dean & Dalrymple, 1984) as:

$$v = \frac{\partial \eta}{\partial t} + u\frac{\partial \eta}{\partial x}$$

where u, and v are velocity components in the horizontal and vertical direction respectively. Free surface tracking using the above equation is referred to as the height function method in computational fluid dynamics (Hirt & Nichols, 1981). The employment of the height function method can greatly reduce the computational time. This method has been used for wave dynamics studies in conjuction with the NS solver for both two-dimensional (Sakakiyama & Kajima, 1992) and three-dimensional problems (Masamura & Fujima, 1995). However, its application is limited to circumstances where no free surface reconnection occurs. Because of this limitation, the method cannot be used to investigate wave breaking processes. Since this study is focused on the free surface tracking methods, which can be applied to general cases, it will not be discussed herein.

Mainly two approaches are used to track the free surface, the Lagrangian and Eulerian. Both approaches have advantages and weaknesses, and a brief discussion follows. The most representative of the Lagrangian technique is the MAC method introduced originally by Harlow & Welch (1965) which has been continously improved since. Harlow & Welch's method, in principle, is very simple; massless markers are initially distributed over the entire computational flow domain, so cells are flagged as either empty (cell without markers), fluid (with at least a marker and not adjacent to any empty cell) and surface (with at least a single marker and adjacent to at least one empty cell). Massless markers represent the body of the fluid itself; they move

Reproduced with permission of the copyright owner. Further reproduction prohibited without permission.

according to their local fluid velocity. In most numerical algorithms, velocities are determined only at the center of the computational cell faces. Therefore, for a given marker located at an arbitrary position, its velocity is estimated by interpolation. By re-flagging cell types at each time step, it is possible to trace the free surface deformation. The MAC method tracks individual markers independently, making the method robust and easy to apply to the three-dimensional domain. It can handle wave breaking problems or conditions where the free surface undergoes moderate deformation. However, this method is computationally expensive since it requires a large number of closely located markers to realistically represent the fluid motion. Furthermore, to maintain resolution, markers need to be dynamically added or removed as the free surface stretches or shrinks, thus adding burden to the computation. The free surface configuration is not clearly defined; it is possible to indicate more or less its location but not the exact shape. In addition, the interpolated marker velocity may result in large error near a highly deformed free surface.

Due to the disadvantages of the original MAC method, an improved version was developed by Chan & Street (1968) and Chan (1970) that comprises just a few markers. Instead of tracking markers in the entire flow domain, the method places markers on the free surface only. The continuous tracking of these markers provides the precise location of the free surface, reducing considerably the computational time. The method was applied to practical engineering problems concerning two-dimensional wave-structure interactions. Nichols & Hirt (1971) proposed a similar method to track the free surface but with a better approximation for the normal and tangential stress boundary conditions on the free surface. Nichols & Hirt (1975) further extended the model to three-dimensional cases. Miyata & Nishimura (1985) developed a similar three-dimensional model to study nonlinear ship waves. Hirt & Nichols (1981) observed that by connecting surface markers with line segments the free surface profile

Reproduced with permission of the copyright owner. Further reproduction prohibited without permission.

could be estimated. If there is no free surface reconnection involved, the line segment method is simple, accurate and efficient for the free surface tracking. However, when the free surface intersects the sequence of line segments, it needs to be re-ordered and some segments need to be added or removed. This numerical procedure becomes rather difficult when a complicated free surface geometry is present. If more than one air bubble is generated during the flow intersection, such as in the case of a broken wave, the task to discern which segment line to add or remove is extremely difficult. Miyata (1986) used the line segment method to simulate two-dimensional breaking waves. He presented a detailed treatment of re-ordering the sequence of segments during the wave overturning. Further approximations were employed to eliminate small air regions to avoid computational difficulties and numerical errors. Chen, Johnson & Raad (1993) proposed a Surface Marker (SM) method, which is essentially the same as the line segment method. Markers are added or removed dynamically during computations to maintain the proper number of markers to represent the free surface profile. Later, Raad (1995) introduced the Micro Cell (MC) treatment in conjuction with the SM method. In the MC method, the surface cell is divided into a number of sub-cells allowing a more accurate application of the dynamic boundary condition on the free surface. Although in principle the free surface intersection problem can be modeled by the line segment method and in fact has been attempted by dynamically re-ordering the line segment, the accuracy of various treatments has not been rigorously tested. The free surface intersection introduces difficulties not only in rearranging the surface markers, but also in interpolating the velocities needed to move the markers. In addition to this, the extension of the method to three dimensions with an intersecting free surface is nontrivial and so far few published works are available (e.g., Raad & Bidoae, 1998).

Reproduced with permission of the copyright owner. Further reproduction prohibited without permission.

As seen from the preceeding review, the original MAC method has no difficulty in treating the free surface intersection. Thus, it is easy to extend the method to three-dimensional cases. However, three-dimensional computations require substantially more computational resources due to the difficulty of identifying the free surface location. The line segment method, on the other hand, is computationally efficient and the free surface can be accurately located during computation. Nevertheless, the line segment method has great difficulties in treating the free surface overturning and reconnection, which makes the extension of this method to three-dimensional cases complicated. As a result, most of the MAC method models have been applied to two-dimensional situations.

Due to the limitation of the MAC method, other free surface tracking techniques have been explored. The most practical alternative is the tracking of the free surface using the Eulerian description. The basic governing equation is

$$\frac{\partial \rho}{\partial t} + \mathbf{u} \cdot \nabla \rho = 0, \tag{1}$$

which is referred to as the transport equation. The density $\rho(\mathbf{x}, t)$ can be continuous or a step function. By tracking the change of ρ it is possible to identify the location of the free surface. Using directly the numerical version of Eq. (1), one may end up with excessive numerical diffusion, so other approaches have been used for such a purpose. Nichols *et al.* (1980) developed the VOF method to track the free surface. The principle of the VOF method is simple. By using the transport equation and assuming that density is everywhere constant ($\rho = \rho_o$) in the flow domain and zero ($\rho = 0$) in the air domain, it is possible to normalize the transport equation by ρ_o. Defining $F = \rho/\rho_o$ as the fractional volume of fluid function (VOF function), the transport equation becomes:

$$\frac{\partial F}{\partial t} + \mathbf{u} \cdot \nabla F = 0. \tag{2}$$

Reproduced with permission of the copyright owner. Further reproduction prohibited without permission.

F is a step function, where $F = 1$ in elements containing fluid and $F = 0$ in elements containing air. In free surface elements, the value of F ranges between (0–1). Given the velocity field, one may update F using a special treatment of Eq. (2). Therefore, by tracking the VOF function F, one can identify the free surface elements at any time step. A special treatment has to be given to Eq. (2) to solve it numerically. The earliest special treatment is called the donor-acceptor method proposed by Hirt & Nichols (1981). The advection of F in a given element depends on the local free surface orientation. The free surface of the element is first reconstructed to be either horizontal or vertical based on the F values of the element and its neighboring elements. Such reconstruction method is often referred to as simple line interface calculation (SLIC), which was originally proposed by DeBar (1974) and refined by Noh & Woodward (1976). Next, according to the velocity direction at the elements common boundary, the donor or acceptor tags are given to the elements. Finally, based on the local free surface orientation, either a donor or acceptor treatment is applied. Since the donor treatment corresponds to the upwind scheme and will introduce excessive numerical diffusion and the acceptor treatment corresponds to the downwind scheme that will cause the sharpening of free surface, the combined use of the two methods will balance the numerical diffusion and instability and thus confine the free surface within a thin layer of a couple of elements. In addition, a special corrector is needed to prevent the occurrence of the unphysical situation, i.e, $(F > 1)$ / $(F < 0)$ or advecting more fluid than what an element may contain/give. By doing so, any possible numerical instability is eliminated. The donor-acceptor technique is the simplest treatment for controlling the numerical diffusion during the advection of the VOF function F. However, it is only first-order accurate. Major numerical errors are caused by the crude approximation of the free surface orientation and subsequent advection scheme by the donor acceptor treatment. The corrector

Reproduced with permission of the copyright owner. Further reproduction prohibited without permission.

introduces additional errors. Nevertheless, due to the simplicity of the donor-acceptor VOF method, most researchers still adapt this technique for free surface tracking purposes.

The inaccuracy in the donor-acceptor method is primarily caused by the over-simplification of the free surface geometry during the advection process. Youngs (1982) introduced a more accurate way to reconstruct the free surface. During the reconstruction, the free surface or interface line, which can be exactly defined inside the element by the slope and intercepts with element boundaries, is assigned to each surface element. The slope can be estimated by the gradient of VOF function F and the intercepts with the slope and the volume of fluid of the element. The resulting free surface is discontinuous at the element boundaries, since each element has its own free surface slope. The subsequent advection scheme is then based on the reconstructed sloping interface. Because the sloping interface is more accurate in representing the actual surface orientation, the advection could be improved significantly under certain circumstances. Ashgriz & Poo (1991) proposed a new sloping interface method called Flux Line-segment model for Advection and Interface Reconstruction (FLAIR) for two-dimensional problems. Instead of fitting the sloping interface inside the element as suggested by Youngs (1982), FLAIR method reconstructs the sloping interface at the element boundaries, avoiding in this way the free surface discontinuity. Because the free surface is reconstructed in a smoother fashion, Ashgriz & Poo showed that their interface reconstruction can generate more accurate results.

Although the sloping interface method is in general more accurate than the donor-acceptor method, it still suffers from a few limitations. First, the sloping interface reconstruction and consequent advection is much more computationally intensive than that of the donor-acceptor method and it is more difficult to code. Furthermore, the extension of the sloping interface method from two dimensions to three dimensions

Reproduced with permission of the copyright owner. Further reproduction prohibited without permission.

needs much more effort than that of the donor-acceptor method and it is subject to numerical uncertainties that have not been tested and discussed fully.

The difficulty in reconstructing the free surface accurately and efficiently prevents the practical application of the sloping interface method, especially in three-dimensional cases. To solve this problem, Welch, Trapp & Mortensen (1994) proposed a new method which employed a subgrid counting procedure to determine the accurate location of the interface and the correct advective flux. In their method, a free surface element is divided into a number of subgrid elements. First, the free surface orientation is estimated by evaluating the spatial gradients of F function similar to other sloping interface methods. Then, by sliding the free surface plane with its orientation along the normal direction, until the corresponding F value is obtained by counting the number of subgrid elements in the fluid side. The process is done through an iterative method which locates the free surface position precisely, based on the given F value in the element and the free surface plane. Welch *et al.* (1994) claimed that this method gives the same accurate results as the conventional sloping interface method but it is much easier to apply in three-dimensional cases. Because the detailed implementation of the sloping interface method has rarely appeared in the public domain, the use and the rigorous testing of this method have seldom been reported. The major research efforts at this stage are still focused on the numerical techniques rather than practical application.

The direct numerical solution to the transport equation (Eq. 1), referred to as the shock capturing method (Kothe & Rider, 1995) or the interface tracking method (Rider & Kothe, 1995), is usually used in multi-fluid flows or variable-density flows (Bell & Marcus, 1992). A high-order accurate upwind scheme was used by Bell & Marcus (1992) and the high-order Godunov method was tested by Rider & Kothe (1995). The above methods are similar to the shock capturing method employed

Reproduced with permission of the copyright owner. Further reproduction prohibited without permission.

in gas dynamics (Collela & Woodward, 1984). In principle, this method can also be applied to free surface flow problems. However, since large numerical diffusion may be induced because of the large density gradient near the interface (free surface) and the interface is generally more sensitive to the change of location, the application of the above methods to free surface tracking has not been used extensively. An example of this method is found in a study done by Watanabe & Saeki (1995). They investigated the wave-breaking problem by employing the cubic-polynomial interpolation method proposed by Yabe & Aoki (1991) and Yabe *et al.* (1991) to solve the density equation. However, based on the tests conducted by Kothe & Rider (1995), the shock capturing method, in general, provides a less accurate solution compared to other VOF methods.

Another technique for interface tracking is called the level set method (Sussman *et al.*, 1994). This method is an improved version of an early method developed by Unverdi & Tryggvason (1992) which used moving grids to track the interface motion. If the density is analyzed as a discontinuity function across the interface, it will induce an excessive numerical diffusion if the density transport Eq. (1) is solved directly with the conventional numerical method. Sussman *et al.* (1994) solved the problem by substituting ρ by the smooth-level set function ϱ. Thus, the new equation becomes

$$\frac{\partial \varrho}{\partial t} + \mathbf{u} \cdot \nabla \varrho = 0. \tag{3}$$

The function ϱ gives the normal distance from the interface, in which its original value is set to zero at the interface. By tracking the zero value of ϱ based on Eq. (3), one may identify the interface during the computation. Because the set level function ϱ is a smooth function, it is much easier to compute and it induces much less numerical diffusion. This method is capable of treating the originally multi-connected region problem, though it cannot solve the possible circumstance of free surface reconnection. It has also been shown (Rider & Kothe, 1995) that this method

Reproduced with permission of the copyright owner. Further reproduction prohibited without permission.

is subjected to significant mass loss under complicated situations since the scheme does not explicitly impose mass conservation. This method has not been widely used in practical applications of free surface flow computations. In Sussman & Fatemi (1999) the level set method was improved by using a re-distancing algorithm. Later, Sussman & Puckett (2000) combined their method with a VOF method in order to overcome problems with mass conservation.

Recently, several strategies to sharpen the interface using VOF methods have been developed. Ubbink & Issa (1999) proposed a high-order discretization scheme with bounding treatments. Gerrits (2001), used a piecewise constant interface reconstruction (donor-acceptor method) combined with a local height function. He concluded that an improvement in the interface definition is obtained if the local height function is used.

Based on the literature survey of different free surface tracking methods, it seems that the most widely used free surface tracking techniques for practical application are the line segment MAC method and the VOF method. These two methods are simple for coding, versatile and computationally efficient. The line segment method is limited by the difficulties in treating free surface reconnection. The VOF method has no difficulty in treating free surface reconnection. However, the VOF method has similar limitations in determining the precise location of the free surface because it only tracks the averaged quantity of F function in each computational element and thus it is unable to describe the exact geometry of the free surface. A special technique is needed for the reconstruction of the free surface and the advection of the fluid based on the F function. However, the VOF method possesses an exceptional advantage over the original MAC method in terms of the computational efficiency. The VOF method needs to store and calculate only one value per element per time step, while the original MAC method calculates tens or more of individual marker

Reproduced with permission of the copyright owner. Further reproduction prohibited without permission.

motions per element to achieve the same accurate information as the VOF method. Another advantage of the VOF method is that it avoids the interpolation of velocity in the calculation, which must be done in the MAC method (original and line segment) in all the markers, resulting in large numerical errors for highly nonlinear problems. Furthermore, the VOF method can explicity conserve the mass while the MAC method cannot. Because of these reasons, the VOF method is very robust and it has quickly become the most popular free surface tracking technique. The VOF method has low accuracy due to the simple free surface reconstruction scheme. However, in this study where tsunami waves undergo moderate deformation (i.e., waves generated by landslides or broken waves) the technique has proven to be satisfactory. More detailed information about the VOF technique is presented in Section 2.7.

1.4 Outline

This thesis is divided into three subsequent chapters. Chapter two deals with the mathematical basis of the proposed numerical method, starting with the continuity equation for incompressible flow, followed by the momentum equation and ending with the transport equation. The nonlinear Navier-Stokes momentum equations are presented in both conservative and nonconservative forms. Then, the entire set of equations is modified to account for stationary and moving objects. The equation of transport for advection of the free surface is described and the boundary conditions established. Discretization adopted to solve the set of equations in space and time using finite difference schemes and control volume techniques is described in detail. The Cartesian grid and location of variables are defined. Geometric quantity parameters resulting when stationary or moving objects cut a computational cell are defined. The tracking mechanism of a moving object on a two-dimensional Cartesian domain is explained. The volume of fluid function is introduced to assign the filling ratio of

Reproduced with permission of the copyright owner. Further reproduction prohibited without permission.

the cells with a labeling system to distinguish obstacle, moving object, fluid, surface and void cells. Boundary conditions for pressure and velocity at the free surface and objects are described. Derivation of the Poisson equation is explained and the technique to solve it is described. Difficulties regarding the curvilinear moving boundaries within a Cartesian grid system are discussed. Different sources of instabilities are discussed according to the proposed scheme, and some solutions are given to improve accuracy.

In Chapter three, numerical tests are conducted to evaluate model performance and accuracy. A total of five numerical experiments have been selected, presented and discussed. They are the numerical simulation of:

1) the initial stages of the dam-break wave problem

2) runup onto a plane beach

3) a deformable-subaerial landslide

4) a landslide triangular-sliding-box

5) wave propagation and dispersion. Indian Ocean tsunami, December 26, 2004.

The fundamental physics associated with the particular experiment are analyzed and reaffirmed. Effects related to the vertical component of velocity/acceleration are pointed out and comparisons with the analytical solution or other numerical approximations which do not include the vertical component of velocity/acceleration, are discussed. Brief descriptions are given for both nonlinear shallow water (Appendices A and B) and Boussinesq (Appendix C) numerical models used for comparison and analysis against the proposed model. Analytical solutions are presented for some specific experiments as well.

Reproduced with permission of the copyright owner. Further reproduction prohibited without permission.

In general, the accuracy of the free surface tracking technique and the conservation of mass and momentum of the proposed model are tested by means of laboratory experiment or analytical solution. The model results are compared with the laboratory measurements or analytical solution in terms of surface elevation, velocity profile, maximum sea level and maximum runup height. The detailed two-dimensional spatial distribution of the velocity field, as well as the inundation curve, are presented and discussed. The numerical model is employed to case studies of breaking-wave and wave-structure interaction. The turbulent characteristics of the fluid are validated by comparing them with the laboratory data.

Finally, in Chapter four, conclusions of this study are postulated and a list of future works and recommendations are given. A summary of conclusions related to the applicability of the nonlinear shallow water approach for the tsunami investigation of wave generation and runup is given.

Reproduced with permission of the copyright owner. Further reproduction prohibited without permission.

Chapter 2

Governing equations

Following Newton's second law, fluid motion of an incompressible Newtonian fluid can be described by the Navier-Stokes equations. The equations were derived independently by George-Gabriel Stokes, in England, and Claude-Louis Navier, in France, in the middle 1800's. The equations are extensions of the Euler equations and include the effects of viscosity on the flow. The Navier-Stokes equations and the conservation of mass equation are the foundation of fluid mechanics, which describe how velocity, pressure and density of a moving fluid are related. Although the Navier-Stokes equations correctly describe nearly all flows of practical interest, they are too complex for practical solution in many cases and a special reduced-form of the full equations is often used instead. However, nowadays computers have been used to solve approximations to the equations, using a variety of techniques, in an area of study called Computational Fluid Dynamics (CFD), like finite difference, finite volume, finite element and spectral methods.

As mentioned in Chapter one, for tsunami calculations, a Navier-Stokes approach is most suitable to study landslide generation of impulsive waves, runup and wave impact on structures, since it includes the vertical component of velocity/acceleration and it is nonhydrostatic so forces on structures can be estimated more accurately.

2.1 Equations of fluid dynamics

The governing equations and boundary conditions describing a flow field with fluid-air interfaces are described in this section. Governing equations are modified to take into account stationary and rigid moving objects.

Reproduced with permission of the copyright owner. Further reproduction prohibited without permission.

2.1.1 Continuity and Navier-Stokes equations

The flow of a Newtonian, incompressible fluid with free surface and density ρ in a bounded domain Ω is governed by the equation of conservation of mass

$$\nabla \cdot \mathbf{u} = 0 \tag{4}$$

and the equation for conservation of momentum

$$\frac{\partial \mathbf{u}}{\partial t} + (\mathbf{u} \cdot \nabla)\mathbf{u} = -\frac{1}{\rho}\nabla p + \nu \nabla^2 \mathbf{u} + \mathbf{g}. \tag{5}$$

Eq. (4) is referred to as the continuity equation, while Eq. (5) is known as the Navier-Stokes equation; where $\mathbf{u}(\mathbf{x}, t)$ is the velocity vector, p is the pressure, ν is the kinematic viscosity, $\mathbf{g}$ is the gravity acceleration vector and t is the time. The

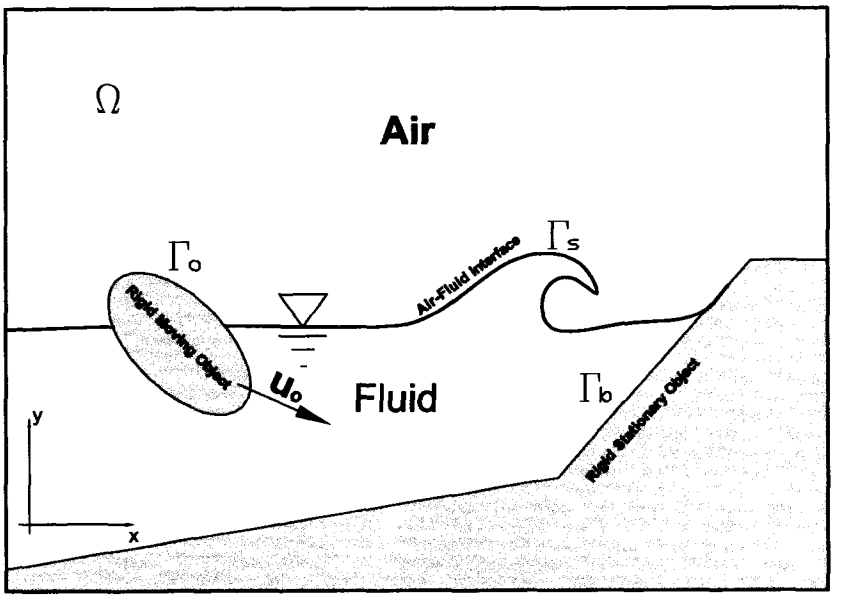

Figure 1: A typical computational domain with moving and stationary objects.

two-dimensional fluid flow is solved using an Eulerian frame in which fixed points

$$\mathbf{x} = x\hat{i} + y\hat{j}$$

Reproduced with permission of the copyright owner. Further reproduction prohibited without permission.

in the domain $\Omega(t)$ are described in a Cartesian system of coordinates (Fig. 1). The velocity field depends upon space and time, thus

$$\mathbf{u}(\mathbf{x},t) = u(x,y,t)\hat{i} + v(x,y,t)\hat{j}$$

where variables u and v represent the horizontal and vertical component of the velocity vector, respectively. Eq. (5) is written in nonconservative form, as inferred from the advective term form, $(\mathbf{u}\cdot\nabla)\mathbf{u}$. The nonconservative advective term can be expressed in conservative form as

$$(\mathbf{u}\cdot\nabla)\mathbf{u} = \nabla\cdot(\mathbf{uu}) - \mathbf{u}(\nabla\cdot\mathbf{u}) = \nabla\cdot(\mathbf{uu}), \tag{6}$$

where $\nabla\cdot\mathbf{u} = 0$ is assumed following the conservation of mass requirement. This is true under the premise that no external inflow or outflow exists in the control volume domain Ω, so conservation of mass holds. The resulting term $\nabla\cdot(\mathbf{uu})$, is a conservative expression of the former. In CFD an external inflow or outflow can be established by the incursion or retreat of a moving object into the domain. In such a case, to balance the mass conservation equation, $\nabla\cdot\mathbf{u} \neq 0 = \phi$, and Eq. (6) becomes

$$(\mathbf{u}\cdot\nabla)\mathbf{u} = \nabla\cdot(\mathbf{uu}) - \phi\mathbf{u}, \tag{7}$$

where ϕ is an internal function which accounts for the amount of volume taken or released by the object in a lapse of time in the control volume domain.

Since the fluid flow is assumed Newtonian, the frictional or viscous term can be better described as

$$\nu\nabla^2\mathbf{u} = \frac{1}{\rho}\nabla\cdot(\mu\nabla\mathbf{u}) = \frac{1}{\rho}\nabla\cdot\tau, \tag{8}$$

where the stress tensor τ is a function of the molecular viscosity μ and the rate of strain $\nabla\mathbf{u}$.

Reproduced with permission of the copyright owner. Further reproduction prohibited without permission.

2.1.2 Free surface equation

In most fluid flow problems, like water waves or tsunamis, the biggest part of the computational domain is filled with fluid, and a sharp interface or free surface separates the fluid from the air. The position of this interface is not known in advance and it needs to be located. The free surface can be described by a scalar field $F(\mathbf{x}, t)$ which satisfies the transport or conservation equation

$$\frac{dF}{dt} = \frac{\partial F}{\partial t} + (\mathbf{u} \cdot \nabla)F = 0, \tag{9}$$

stating that F propagates with the fluid velocity $\mathbf{u}$. $F(\mathbf{x}, t)$ at time $t = 0$ is given and the fluid density does not change in time. Eq. (9) is more consistent with the nonconservative expression of the advection term in Eq. (5) and it is solved only in the fluid domain.

In fluid flow calculation where the free surface interface may undergo large deformation, it is common to treat the fluid from an Eulerian point of view. Lagrangian representation may produce very poor results as the surface interface experiences breaking or intersection such as broken waves. The numerical solution of this advective equation requires an averaging of the flow properties. The simplest method is using an Eulerian approach to update the free surface location based on Eq. (9). In an Eulerian calculation, it is necessary to compute the flow of fluid through the mesh using a standard finite-difference approximation. The advection calculation requires an averaging of the flow properties in the fluid cell elements. This averaging process, inherent in the advective flux approximation, is the biggest drawback of the Eulerian method. The advection averaging results in a smoothing of fluid flow properties and, in particular, a spreading of the interface or discontinuity such as the free surface. The only way to overcome this numerical diffusion in the interface is to introduce some special treatment that recognizes a discontinuity and avoid averaging across

Reproduced with permission of the copyright owner. Further reproduction prohibited without permission.

it. Although there are several techniques developed to do this, they all have limitations. A comparison of the relative advantages and disadvantages of several methods for tracking the free surface was discussed in Chapter one. The discussion led to a technique that is simple and practical for fluid flow problems like water waves or tsunamis. The technique is the fractional volume of fluid (VOF) described by Nichols *et al.* (1980); Torrey *et al.* (1985); Kothe *et al.* (1991). The VOF technique is used in this study and explained in detail in Section 2.7. For a detailed compilation of different free surface tracking techniques, see Lin & Liu (1999).

2.1.3 Modification of governing equations due to internal objects

Seabottom, beach, land, submarine or aerial/subaerial structures, landslide, falling rocks, falling blocks, dam gates, wave makers and floating objects are examples of internal objects in a typical tsunami computational domain. In a computational domain Ω, computational elements that are completely immersed in an internal object are defined as object elements. Internal objects are usually approximated by blocking out entire object elements, which leads to boundaries having discrete steps. Geometric representation of curved object surfaces is possible if one defines an object cutting function through the fluid element interior. Such fluid cutting function within the element boundaries are the fractional face areas and the fractional volume through which the fluid can flow.

Internal objects can be considered as a special case of two-layer flow, in which the first layer is the fluid with fractional function Θ and the second layer is the object with quantity fraction $1.0 - \Theta$. An internal stationary object is characterized as a "fluid" of infinite density and zero velocity. Then, the spatial-dependent fractional

Reproduced with permission of the copyright owner. Further reproduction prohibited without permission.

function Θ is a scalar field and is defined as

$$\Theta(\mathbf{x}) = \begin{cases} 0.0, & \text{object element} \\ > 0.0 \text{ and } \leq 1, & \text{fluid element.} \end{cases}$$

The object geometry arbitrarily cuts computational elements causing Θ's values to range within $0.0 < \Theta \leq 1.0$. These elements are termed fluid elements because a portion of the cell is open for fluid to flow and the remaining portion $1.0 - \Theta$ is occupied by the object, which is closed for fluid to flow. The element faces and volume openings are termed apertures. In the presence of internal objects, Eqs. (4), (5) and (9) are modified to account for the element apertures, thus

$$\nabla \cdot (\Theta \mathbf{u}) = 0, \tag{10}$$

$$\Theta \frac{\partial \mathbf{u}}{\partial t} + (\Theta \mathbf{u} \cdot \nabla)\mathbf{u} = -\frac{\Theta}{\rho}\nabla p + \Theta \nu \nabla^2 \mathbf{u} + \Theta \mathbf{g}, \tag{11}$$

and

$$\frac{\partial(\Theta F)}{\partial t} + (\mathbf{u} \cdot \nabla)\Theta F = 0 \tag{12}$$

respectively.

The preceding set of equations can be modified to consider internal moving objects. Now, the fractional aperture function $\Theta(\mathbf{x}, t)$, is time dependent and it is explained in the following subsection.

2.1.4 Modification of governing equations due to moving objects

The continuity and momentum equations are modified to account for the incursion or retreat of rigid moving objects in Ω. Consider an arbitrary control volume V in Ω containing a moving object. Fig. 2 depicts the control volume V at a given time such that the object-fluid interface is passing through. The shaded region V_O represents the part of the moving object into the control volume, while the rest denoted by V_F, corresponds to the fluid region. $S = S_O + S_F$ and S_{OF} are boundary surface

Reproduced with permission of the copyright owner. Further reproduction prohibited without permission.

areas of the control volume and object-fluid interface area, respectively. If the object volume rate increases in a period of time δt, i.e. $dV_O(t)/dt > 0$, the fluid volume decreases. Conversely, if the object volume decreases, the fluid volume increases. The conservation of mass in the control volume V is therefore,

$$\oint_S (\mathbf{u} \cdot \mathbf{n}) dS = \int_{S_F} (\mathbf{u} \cdot \mathbf{n_F}) dS_F + \int_{S_O} (\mathbf{u_O} \cdot \mathbf{n_O}) dS_O = 0,$$

and

$$\int_{S_{OF}} (\mathbf{u_O} \cdot \mathbf{n_O}) dS_{OF} = \frac{dV_O}{dt}$$

is the rate of change of volume. Then, the new continuity equation in the control

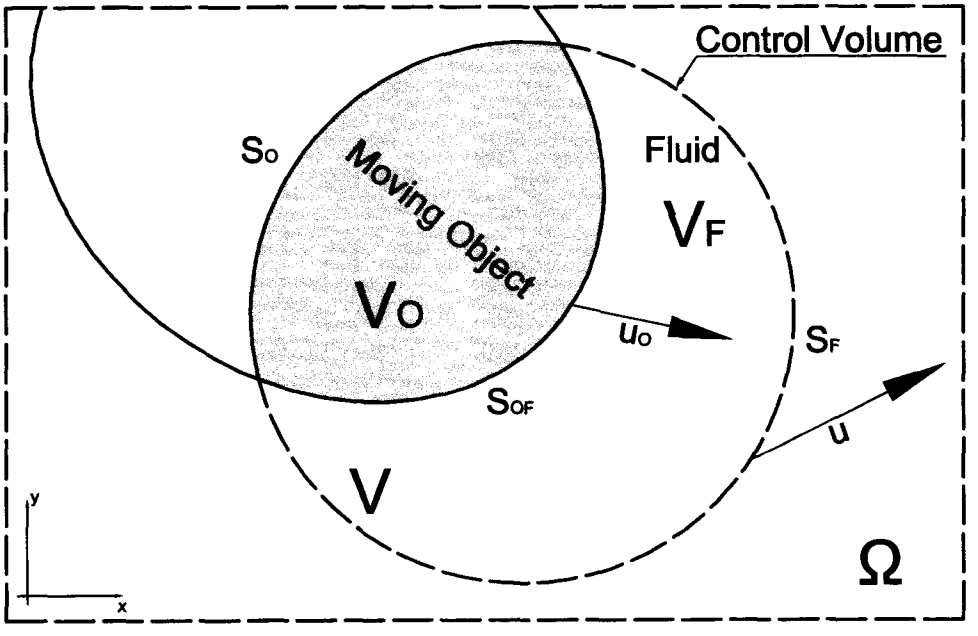

Figure 2: Sketch of an arbitrary two-dimensional control volume with a moving object.

volume V reads

$$\nabla \cdot \mathbf{u} = \frac{1}{V} \left(\frac{dV_O(t)}{dt} \right) = \phi(\mathbf{x}, t), \tag{13}$$

where $\phi(\mathbf{x}, t)$ is an internal moving object function needed to force zero divergence in the control volume V. Substituting Eq. (13) into Eq. (5), the momentum equation

Reproduced with permission of the copyright owner. Further reproduction prohibited without permission.

which includes moving objects is obtained, thus

$$\frac{\partial \mathbf{u}}{\partial t} + \nabla \cdot (\mathbf{uu}) - \phi \mathbf{u} = -\frac{1}{\rho}\nabla p + \nu \nabla^2 \mathbf{u} + \mathbf{g}. \tag{14}$$

This is the conservative form of the momentum equation. This form is particularly convenient for applications involving control volumes. Note that the resulting equation is just a rearrangement of the advective term and the continuity equation and holds for any material. Thus, control volumes containing non-Navier-Stokes fluids, e.g. rigid objects, can be handled in an accurate manner.

2.1.5 Boundary conditions

Tsunami sources are specified through the initial and boundary conditions. Boundary conditions are needed at the free surface and at the stationary or moving boundaries. The boundary conditions will introduce the dynamics and determine the nature of the solution. For instance, over a stationary boundary, Γ_b, the fluid normal velocity must vanish, Fig. 1. On the other hand, along a moving boundary Γ_o, the immediate fluid particle must have the same velocity as that of the moving boundary. In general, along any solid boundary (Γ_b, Γ_o) the fluid velocity must be the same as that of the boundary itself. The most important boundary condition will be at the free surface, Γ_s. In fact, this is where the dynamics of the fluid enters and it is often the most difficult to implement.

2.1.5.1 Stationary and moving boundary condition

At the solid boundary, Dirichlet and Neumann boundary conditions (Morse & Feshbach, 1953) are applied. For example, at the solid boundary of a stationary or moving object, the fluid velocity is equal to the boundary velocity $\mathbf{u_o} = (u_o\,\hat{i} + v_o\,\hat{j})$, thus

$$\mathbf{u} = \mathbf{u}_o, \qquad \text{on } \Gamma_b \text{ or } \Gamma_o, \tag{15}$$

Reproduced with permission of the copyright owner. Further reproduction prohibited without permission.

see Fig. 1. For stationary boundaries, $\mathbf{u} = \mathbf{u}_o = 0$ on Γ_b. This states that the boundary is impermeable and the fluid sticks to the wall due to the viscous effect, this is commonly known as no-slip boundary condition. However, in some situations a free-slip boundary condition as

$$u_{norm} = 0 \quad \text{and} \quad \frac{\partial u_{tang}}{\partial \mathbf{n_{orm}}} = 0, \qquad \text{on} \quad \Gamma_b \tag{16}$$

is prescribed to a stationary object, meaning that shear stresses are neglected at the solid boundary. Here, $u_{norm} = \mathbf{n_{orm}} \cdot \mathbf{u}$ and $u_{tang} = \mathbf{t_{ang}} \cdot \mathbf{u}$ denote the normal and tangential velocity at the stationary solid boundary, see Fig. 3. $\mathbf{t_{ang}}$ and $\mathbf{n_{orm}}$ are the unit tangential and unit normal vectors, respectively.

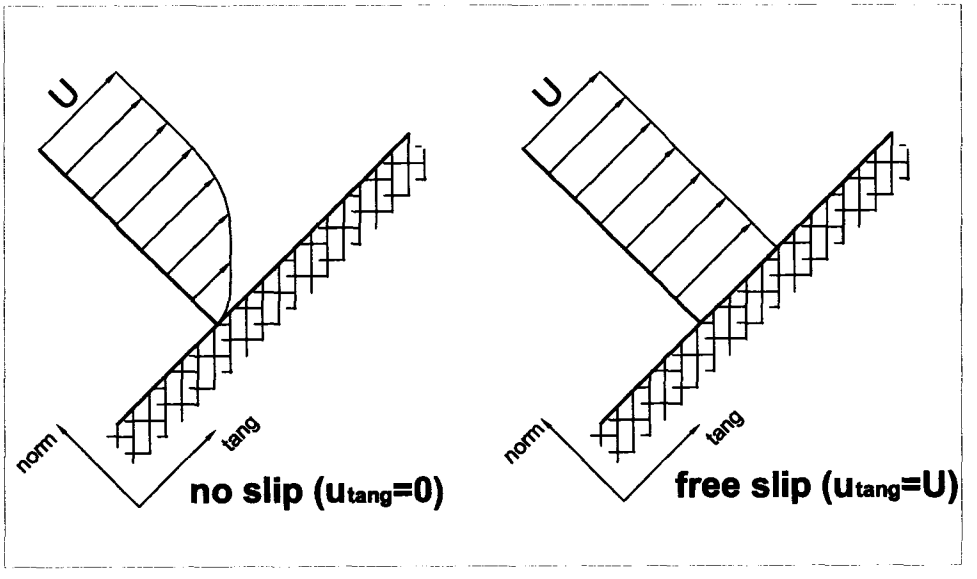

Figure 3: Velocity profile and boundary condition near a stationary object.

2.1.5.2 Free surface boundary condition

The distinctive behavior of water waves results from the physical boundary conditions at the interface between air and water. In numerical calculations the position

Reproduced with permission of the copyright owner. Further reproduction prohibited without permission.

of the water-air interface or sea surface is known only at the initial stage. Along the free surface, both dynamic and kinematic boundary conditions are needed. The dynamic boundary condition describes the stresses acting on the free surface, and the kinematic boundary condition describes the movement of the free surface. For the dynamic boundary condition, the normal and tangential stress components must be continuous and can be expressed as

$$-p + 2\mu \frac{\partial u_{norm}}{\partial \mathbf{n_{orm}}} = -p_o + \sigma\kappa, \tag{17}$$

and

$$\mu \left(\frac{\partial u_{norm}}{\partial \mathbf{t_{ang}}} + \frac{\partial u_{tang}}{\partial \mathbf{n_{orm}}} \right) = 0 \quad on \ \Gamma_s \tag{18}$$

(Kothe *et al.*, 1991), where *norm* and *tang* denote the outward normal and the tangential directions, respectively. p_o is the air pressure, σ is the surface tension and κ denotes the curvature of the free surface. The dynamic boundary condition usually includes the approximation that the air pressure is constant or zero. This approximation serves to decouple the motion of the air from that of the water. In tsunami or gravity wave calculations, the surface tension term can be neglected since gravitational and inertial forces dominate. Also, the viscous effects are neglected at the free surface (second term on the left-hand side of Eq. 17), since it is small compared with the other terms due to the small value of the molecular viscosity. In summary, the resultant equation for the dynamic of the water is solved without considering the motion of the air, surface tension and viscous effects. Doing so, Eq. (17) reduces to $p = p_o$.

Besides the dynamic condition, the kinematic boundary condition describing the free surface motion is also needed. Although the application of the kinematic boundary condition is standard following a Lagrangian or Eulerian approach, one may derive various forms of kinematic boundary conditions, which serve as the basis of different

Reproduced with permission of the copyright owner. Further reproduction prohibited without permission.

tracking techniques. Appropriate free surface boundary condition must be applied using any of those techniques on the air-water interface in conjuction with stationary and moving objects to satisfy the balancing forces. The position of the free surface boundary is known only at the initial stage, $t = 0$, thus the free surface position at later times has to be determined, and it is critical for the solution of the entire system and subsequent free surface locations.

From a Lagrangian system of coordinates, the transport equation (Eq. 9) describing the motion of a particle resting on the free surface can be written as

$$\mathbf{u} = \frac{d\mathbf{X}(t)}{dt}, \tag{19}$$

where $\mathbf{X}$ is the position vector of a fluid particle on the free surface at time t. The above equation implies that the fluid particle moves in accordance with the ambient flow field. If one tracks particles that are originally on the free surface based on Eq. (19), these particles will remain on the free surface unless the free surface breaks and reconnects. Note that this is a general equation which can be applied not only on the free surface but also to the entire fluid.

The Eulerian approach for tracking the free surface is to update the free surface location based on conservation or transport Eq. (9). F is a scalar function carrying the material information. The equation states that $F(\mathbf{x}, t)$ propagates with the fluid velocity without changing the material property. For instance, if $F(\mathbf{x}, t) = \rho$ then this density can be transported conserving its property (incompressible fluid).

Accurately tracking the free surface movement is important for accurately predicting wave evolution, therefore an appropriate boundary condition must be applied on the interface to satisfy the balancing forces. The Eulerian method is used in this study to update the free surface location based on Eq. (9) but using a geometric tracking technique which is described and discussed in Section 2.7.

Reproduced with permission of the copyright owner. Further reproduction prohibited without permission.

2.2 Geometric discretization

Numerical scheme construction starts by selecting an appropriate computational grid. Basically, a computational grid can be either structured or unstructured and boundary or non-boundary body fitted.

In unstructured grid, often with boundary body fitted, cell element sides follow object boundaries. The cells are not ordered and have different orientations and sizes, therefore cell elements can be joined in any manner, and a special list must be kept to identify neighboring elements. Although the generation of an unstructured grid is relatively easy, it is computationally expensive if moving objects are present since a new grid must be calculated to adjust to the new position of the moving object. In addition, the free surface needs to be located again throughout the new grid. When using unstructured grids, there is a potential problem with low-order numerical approximations, especially when it is used in conjunction with conservative formulations. The non-uniformity in the size of grid elements generally means a loss in numerical accuracy of one order. This arises from the fact that differences in fluxes on opposite sides of a control volume have errors that cancel in pairs when the grid is uniform, but do not cancel when the sizes of elements are different.

On the other hand, structured grids can be, depending on the shape of their elements, square, rectangular or circular sectors. The simplest grid is generated from a rectangular box by subdividing it into a set of rectangular elements whose faces are parallel to the faces of the box. A structured grid means that the volume elements are well ordered and a simple scheme, i.e., with i and j indices, can be used to label elements and identify neighbors. A grid composed of regular elements has the simplest structure since it is only necessary to define two or three one-dimensional arrays for the x, y and z values defining the element surfaces. The mesh is conformed with variable sizes in the x and y, horizontal and vertical direction respectively; i.e., δx_i

Reproduced with permission of the copyright owner. Further reproduction prohibited without permission.

for the i^{th} column and δy_j for the j^{th} row (Fig. 4). Although it is not as flexible as a mesh composed of arbitrary quadrilaterals, the variable mesh capability has considerable advantage for localized resolution over methods using equal-sized rectangles. To increase resolution in a specific region of interest and maintain numerical accuracy, slowly varying element sizes are used, Hirt & Nichols (1981). In any region or subdomain, arbitrary cell spacing is achieved in accordance with the desired number of cells and the minimum cell spacing to expand over the region of interest. In regions where maximum resolution is desired (convergence line), cell spacings are equal to the minimum value specified. From those convergence lines, cell spacings are then expanded quadratically. For instance, from a convergence line or point (convergence point is defined by two convergence lines), where maximum resolution is desired, cell locations along, i.e., x direction, are determined as follows

$$x_i = (L - \delta_{min}N)\left(\frac{N}{N-1}\right)\left(\frac{i-N}{N}\right)^2 - \left[L - (L - \delta_{min}N)\left(\frac{N}{N-1}\right)\right]\left(\frac{i-N}{N}\right). \tag{20}$$

L is the length of the domain or subdomain to be divided with slowly varying element sizes, δ_{min} is the minimum cell spacing, N is the number of cells in the span L and x_i is the cell location at $i = 1, 2, 3, ...N$, respectively. For the completeness of Eq. (20) an additional condition is needed: if $\delta_{min}N > L$ then $N' = int(L/\delta_{min})$; where N' is the adjusted number of cells such that $\delta_{min}N' = L$. The resulting mesh is uniformly spaced with cell spacings equal or slightly larger than δ_{min}. A rectangular grid with slowly varying element sizes assures a regularity that helps to maintain numerical accuracy (see Section 2.6.3). One disadvantage associated with this grid is that it cannot be distorted to increase resolution in a localized region. Grid lines can be constructed closer together in a particular region for better resolution, but these grid lines then extend across the entire domain. As a result, the number of elements may

Reproduced with permission of the copyright owner. Further reproduction prohibited without permission.

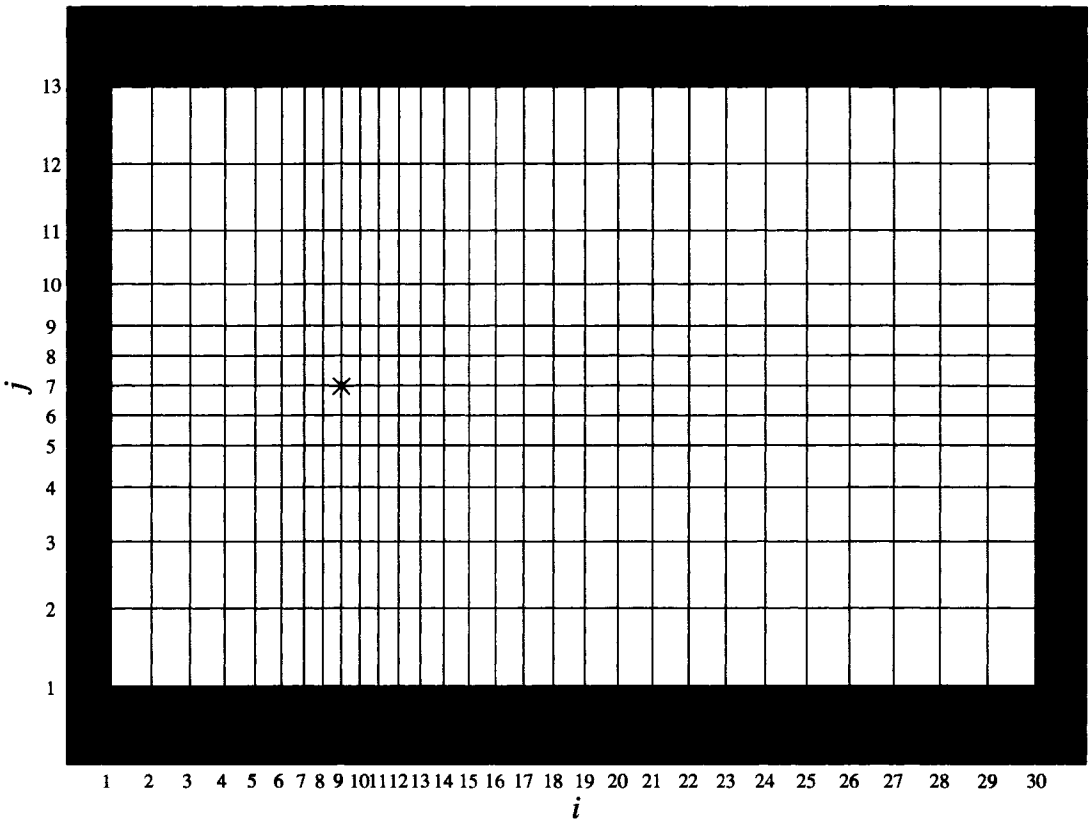

Figure 4: A finite-difference grid with variable rectangular cells showing maximum resolution around convergence point $(i, j) = (9, 7)$.

become large. However, this disadvantage is compensated for by the simplicity of grid generation and numerical accuracy.

One significant advance in grid generation, which could be implemented in the future to improve tsunami calculations, is the use of adaptive mesh refinement (AMR), (Archer *et al.*, 2004). AMR allows one to focus computations on regions of interest instead of computing over a region using a uniform or nonuniform fixed mesh. For example, AMR allows one to track sharp interfaces as a wave front or any other sharp-curved discontinuities with high resolution, while areas of lesser interest are kept at lower resolution. Adaptive-mesh techniques in some specific cases could be far more efficient than fixed grid, providing savings in both the computational time needed

Reproduced with permission of the copyright owner. Further reproduction prohibited without permission.

and data storage required. However, often there is overhead associated with AMR in terms of deciding when and how to adapt, and in keeping track of the evolving mesh. Adaptive cells are particularly suited to high-performance machines, both serial and parallel.

In summary, the best choice for a grid system depends on several factors: convenience in generation, memory requirements, numerical accuracy, flexibility to conform to complex geometries and flexibility for localized regions of high or low resolution.

2.3 Location of variables and apertures

Discrete values of the time dependent variables, including the fractional volume of fluid F used in the VOF technique, are located at cell positions shown in Fig. 5a. Velocity components u and v are located in the cell right face and top face respectively. Discrete values of pressure p and VOF function F are located at the cell center.

As seen from Fig. 5, cell variables are referenced with respect to the cell right-upper corner or indexes intersection, e.g., (i, j). This particular method for variable location differs from those commonly found in the literature, where half indexes are used instead. This system has been adopted in this study since it is more consistent with algorithm construction. Solution of the system is obtained using the central-variable configuration by means of the staggered grid scheme. Central configuration facilitates the calculation of momentum and fluxes amongst cells, and the resulting numerical algorithms are particularly simple and computationally efficient. Besides these obvious advantages of the central framework, there are also algorithmic difficulties caused by the use of staggered grids. One of these is the treatment of boundary condition when object or surface interfaces cut a computational cell.

One limitation of rectangular elements is that geometric object surfaces (stationary or moving objects) are usually approximated by blocking out entire elements,

Reproduced with permission of the copyright owner. Further reproduction prohibited without permission.

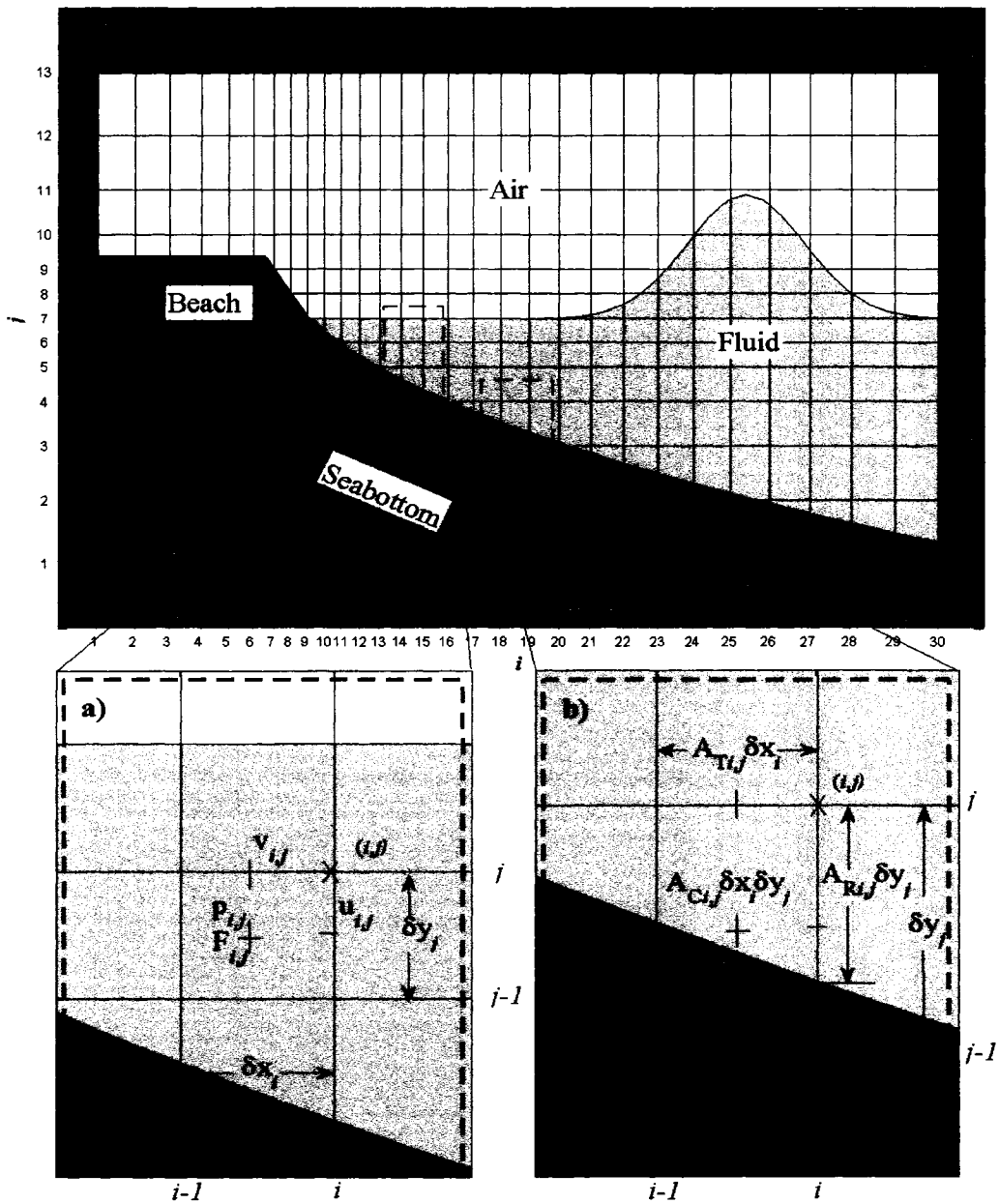

Figure 5: A typical tsunami computational domain. a) Location of variables in a computational cell. The horizontal ($u_{i,j}$) and vertical ($v_{i,j}$) velocity components are located at the right cell face and top cell faces, respectively. The pressure $p_{i,j}$ and VOF function $F_{i,j}$ are located at the cell center. b) Volume and side cell apertures.

Reproduced with permission of the copyright owner. Further reproduction prohibited without permission.

which leads to boundaries having discrete steps. These steps introduce flow losses and other undesirable effects. To eliminate the discrete steps and allow a better geometric representation of curved object surfaces, a technique is used. This technique keeps the rectangular elements, but supplements them with a function that defines the obstacle-cutting in the elements interior. Such a technique is called Fractional Area Volume Obstacle Representation (FAVOR), Nichols *et al.* (1980); Sicilian & Hirt (1984); Gentry *et al.* (1966). With the FAVOR technique, the geometry of a stationary or moving object can take any arbritrary shape. Object geometry is then defined within the grid by computing the fractional face areas and fractional volume of each element that is blocked by the object, see Fig. 5b. Open fractional cell face areas (right and top cell sides) and volume for the fluid to flow, $A_{T_{i,j}}$, $A_{R_{i,j}}$ and $A_{C_{i,j}}$, are referred to herein as apertures. They are calculated based on the complement of the fractional blocked face areas and volume, thus, $A_{T_{i,j}} = 1 - B_{T_{i,j}}$, $A_{R_{i,j}} = 1 - B_{R_{i,j}}$ and $A_{C_{i,j}} = 1 - B_{C_{i,j}}$, respectively. Here $B_{T_{i,j}}$, $B_{R_{i,j}}$ and $B_{C_{i,j}}$ represent the fraction of cell face areas and volume that are blocked for the object. The FAVOR method requires just two or three area fraction variables and one volume fraction variable for each element, which have relatively little information compared with the body-fitted grid technique. Another advantage is that the numerical algorithms are based on information consisting of only one pressure, one velocity, one density, etc. for each cell element, so it is consistent with the information to define the cell geometry. Thus, this technique retains the simplicity of rectangular elements, while representing complex geometric shapes at a level consistent with the use of averaged flow quantities within each volume element. Another powerful advantage is that the grid and object geometry are free to be defined independently of one another, so grid and object geometries can be generated and modified with very little time or effort. For these reasons, the FAVOR technique is implemented and used in this study.

Reproduced with permission of the copyright owner. Further reproduction prohibited without permission.

2.4 Cell labeling

Having the cell face areas and volume apertures calculated from the object geometry, the cells can be categorized as fluid flow cell ($A_C > 0$) and object cell ($A_C = 0$), see Fig. 6a. Fluid flow cells are open for fluid to fill them. They are filled by the initial condition or filled or emptied by the established fluid forcing. A fluid flow cell has to be distinguished from cells in air, immersed in the fluid or between the air and fluid. This is done by the volume of fluid function F that identifies cells that contain fluid with density ρ_{fluid}. Cells with zero F values are empty (E) or contain material of density $\rho_{air} = 0$. A cell with free surface or air-fluid interface (S) at, e.g., (i,j), is defined as a cell containing a nonzero value of F and having at least one neighboring cell $(i\pm1,j)$ or $(i,j\pm1)$ that contains a zero value of F (empty cell). Cells with nonzero F values and no empty neighbors are treated as full (F) cells with ρ_{fluid}, see Figs. 6b and c. In summary, fluid flow cells can be empty (E), full (F) or surface (S) cells. Object cells (O) have one distinction as boundary object cells (B), when the cell has at least one neighboring fluid flow cell, i.e., (E), (F) or (S), see Fig. 6c. In practical tsunami applications, often the influence of the air flow is assumed to be irrelevant to the wave propagation; thus, calculations are avoided in empty (E) cells. The cell labeling facilitates the application of boundary conditions and improves computational performance, since calculations are often excluded in empty and object cells. The cell labeling is needed in the application of boundary conditions as well for instance, the pressure boundary conditions are required in surface (S) cells, velocity boundary conditions are required in surface-empty (S)-(E) cell faces and (E)-(E) cell faces, e.g., for the tangential boundary condition for (S)-(S) velocities.

Reproduced with permission of the copyright owner. Further reproduction prohibited without permission.

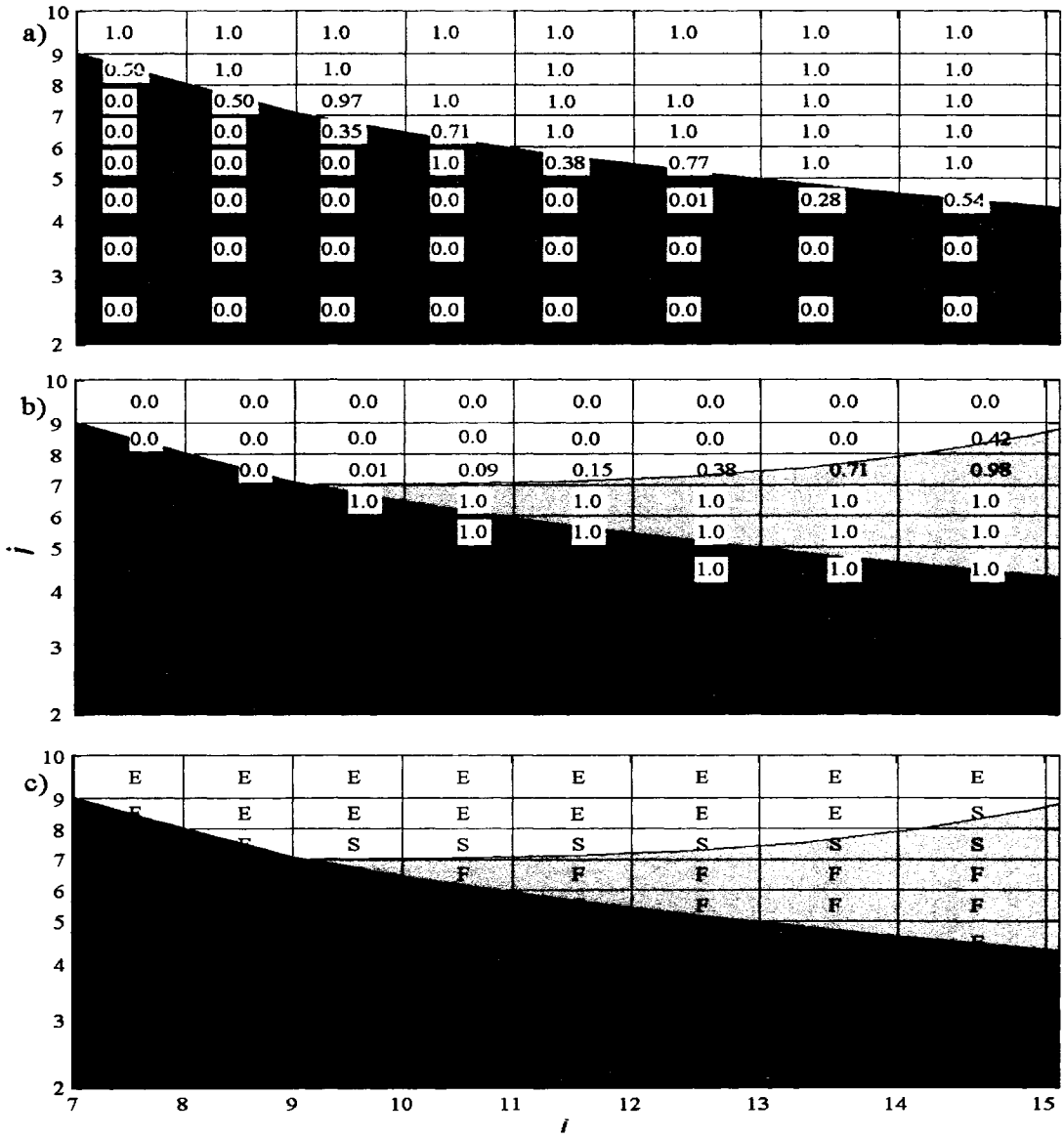

Figure 6: Fluid flow cells, volume of fluid function and cell labeling. a) Fluid flow cells (cell volume aperture $A_C > 0$) and object cells (cell volume aperture $A_C = 0$). b) Volume of fluid function values ($0 \leq F \leq 1$). c) Cell labeling: (E)mpty, fluid flow cell without fluid ($A_C > 0$, $F = 0$); (S)urface, fluid flow cell partially or completely filled by fluid and neighboring at least one empty cell; (F)ull, fluid flow cell completely or partially filled by fluid and no empty neighbors; (O)bject, cell completely occupied by the object; (B)oundary, object cell neighboring at least one fluid flow cell ((E), (F) or (S)).

Reproduced with permission of the copyright owner. Further reproduction prohibited without permission.

2.5 Aperture calculation

The aperture calculation in two-dimensional cells is not a difficult task but it must be done very carefully, especially if moving objects are present. Rigid moving objects travel through a cell making cell apertures A_T, A_R and A_C time dependent. In addition, if the fluid flow around the moving object is considered incompressible, the mass conservation constraint in surface cells makes the pressure very sensitive as unphysical velocities are originated when $A_T \rightarrow 0$ or $A_R \rightarrow 0$. Drastic changes in cell aperture cause numerical instability or pressure pulses that often do not compromise the integrity of numerical results but generate nonphysical pressure fluctuation (Fekken, 2004).

The exact computation of the apertures is based on Sutherland-Hodgman clipping algorithm (Foley *et al.*, 1995). The description of any curved-object geometry by a series of discrete points depends on the number of points used to track the exact geometry. The procedure is described in Fig. 7 where a non-curved polygon is clipped against a Cartesian grid cell (i,j) with cell-face coordinates x_{i-1}, x_i, y_{j-1} and y_j. First, the polygon is clipped against the line $x = x_{i-1}$. All points $p = [1, 2, ..., 5]$ which satisfy the condition $x_p > x_{i-1}$ are stored in a clip-list (all of them, in this case). In addition, all intersection points of the polygon with line x_{i-1}, which may be found following the sequence established, i.e. lines $1-2$, $2-3$ ... $4-5$ and $5-1$, are labeled and stored in the clip-list in order of appearance (none of them, in this case). Clipping against line $y = y_{j-1}$, all points satisfy the condition $y_p > y_{j-1}$ except point 2. As seen from the example, two interception points are found, labeled 6 and 7; the new clip-list becomes $p = [1, 6, 7, 3, 4, 5]$. Finally, doing the same for lines $x = x_i$ and $y = y_j$ the following clip-list is obtained, $p = [1, 6, 7, 8, 10, 11]$. The remainder of the polygon is the part of the object contained in the cell (i,j). The next step is to compute the faces and volume apertures blocked by the clipped polygon. Determining the areas

Reproduced with permission of the copyright owner. Further reproduction prohibited without permission.

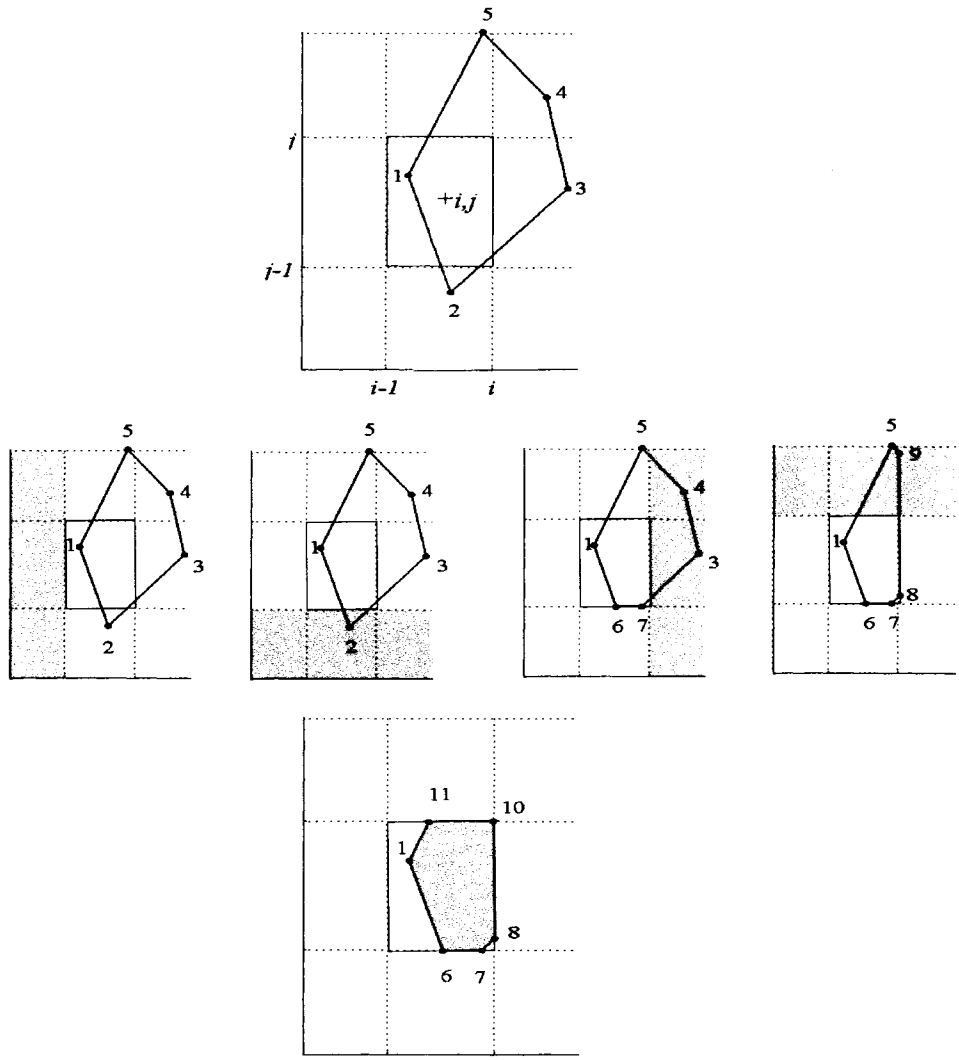

Figure 7: Clipping procedure for the determination of face and volume apertures in a computational cell (i,j).

of irregular objects is a common problem, perhaps the most basic examples come from surveying in determining the size of a parcel of land. The area of an arbitrary polygon can be found exactly by dividing it into trapezoids (see Fig. 8). The area of polygon $ABCDEF$ is the area between $ABCD$ and the x axis minus the area between $DEFA$ and the x axis. Note that the area between $ABCD$ and the x axis is

Reproduced with permission of the copyright owner. Further reproduction prohibited without permission.

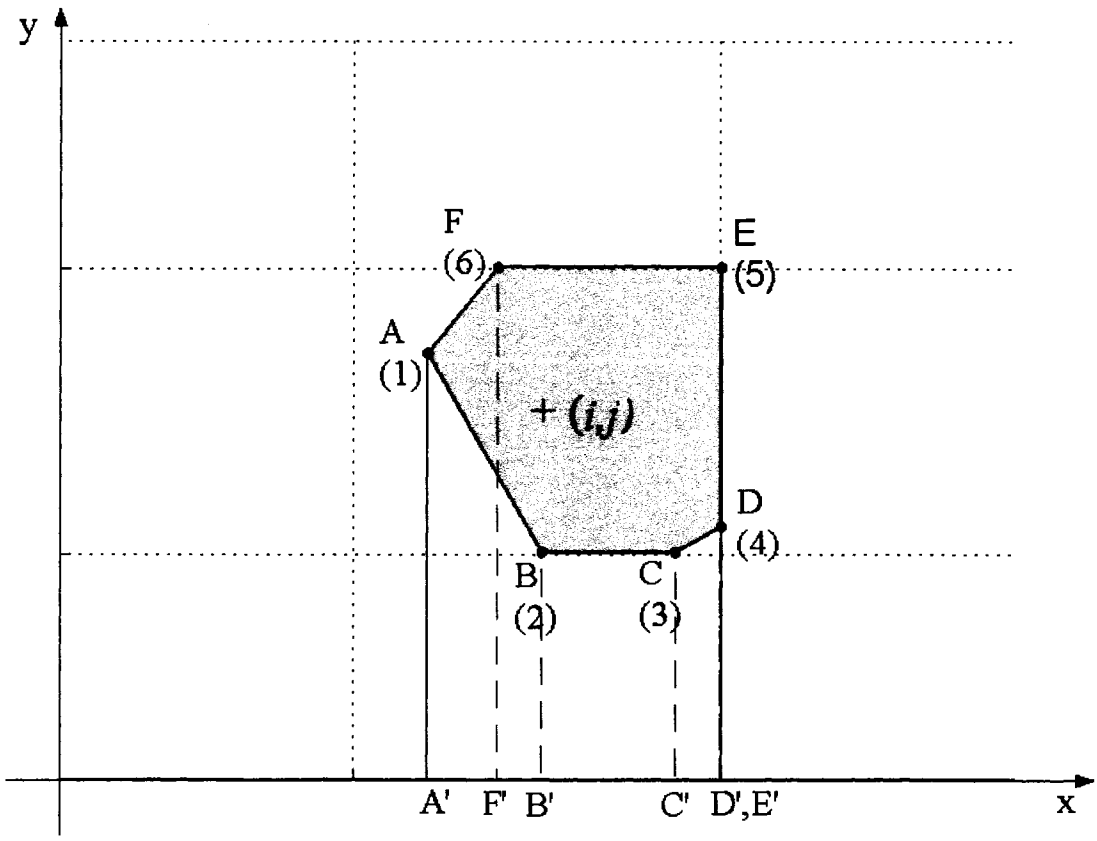

Figure 8: Sketch. Determination of the exact area of an arbitrary polygon using trapezoids.

the sum of the three trapezoids $ABB'A'$, $BCC'B'$, and $CDD'C'$. Similarly, the area between $DEFA$ and the x axis is the sum of three trapezoids (note that "trapezoid" $DEE'D'$ is just a vertical line with area equal to zero). Using subscript (1) for the x and y coordinates of point A, and subscript (2) for the coordinates of point B and so forth, then the area of this trapezoid in terms of its coordinates is positive. Starting and ending at the same point, say A, and going around the polygon in a counter-clockwise direction, the signed area of the polygons underneath the closed curve will automatically be negative. For example, the polygon $ABB'A'$ will have signed area determined by $\frac{(y_1+y_2)}{2}(x_1 - x_2)$ as negative, since $x_1 < x_2$. Hence, adding

Reproduced with permission of the copyright owner. Further reproduction prohibited without permission.

up the trapezoids all the way around and making the ending point the same as the starting point then determines the area of the enclosed polygon. In summary, the area of a polygon with n vertices can be found from

$$Area_{i,j} = \frac{1}{2}\sum_{p=1}^{n}(x(p)y(p+1) - x(p+1)y(p)). \tag{21}$$

Again, it is imperative to "close the path" by adding the starting coordinate point at the end of the coordinate list (when $p = n$ then $p+1 = n+1 = 1$). Also note the need of a simple closed polygon which is a polygon that doesn't intersect itself. Otherwise, parts of the polygon might not be traversed in a counter-clockwise direction, which would give the wrong signed area.

Finally, the following formulations define the fractional faces and volume apertures blocked by the clipped polygon in a computational cell (i,j).

$$\begin{aligned}
A_{C_{i,j}} &= 1 - B_{C_{i,j}} \qquad \text{where: } B_{C_{i,j}} = Area_{i,j}/(\delta x_i \delta y_j) \\
A_{R_{i,j}} &= 1 - B_{R_{i,j}}, \qquad B_{R_{i,j}} = |y_{p+1} - y_p|/\delta y_j \quad \text{at} \quad x_i \\
A_{T_{i,j}} &= 1 - B_{T_{i,j}}, \qquad B_{T_{i,j}} = |x_{p+1} - x_p|/\delta x_i \quad \text{at} \quad y_j
\end{aligned}$$

The volume and face areas of any cell open for the fluid to flow are then given by

$$\begin{aligned}
V_{i,j} &= A_{Ci,j}\delta x_i \delta y_j, \\
A_{top_{i,j}} &= A_{Ti,j}\delta x_i, \\
A_{right_{i,j}} &= A_{Ri,j}\delta y_j.
\end{aligned}$$

2.6 Discretization of the governing equations

Numerical solutions require the domain to be discretized and the governing equations to be reduced to their finite difference equivalents. Fig. 5a shows the grid employed for the discretization. In a variable staggered grid, quantities such as p and VOF function F are defined at the center of the cell, while the horizontal component of velocity is displaced half a grid to the right from the center and the vertical

Reproduced with permission of the copyright owner. Further reproduction prohibited without permission.

component displaced half a grid up from the center, see Section 2.3. For application to shallow coastal waters and wave generation areas, high spatial resolution is rather imperative so that the shorter spatial-time scale typical of the process in these regions can be resolved. A staggered slowly variable grid is better suited to these applications. The objective is to solve for the unknown variables u, v, p and F as a function of time, starting from a specified set of initial static-conditions (tsunami source waves) or dynamic-conditions (landslide, seabottom uplift, rock impact, etc.) with an appropriate boundary condition treated according to the model requirements.

The governing equations are solved using a finite difference method (FDM) following basically the same principles used in the marker and cell (MAC) method by Harlow & Welch (1965). They introduced a finite difference solution scheme for solution of the velocity field in which the staggering of pressures, densities (VOF function) and velocities results in second order central difference. This configuration also implies offset of the momentum control volume centered at the cell side, and cell volume centered at the cell center.

2.6.1 Temporal discretization

The continuity equation (Eq. 4) and momentum equation (Eq. 5) are discretized in time using an explicit forward Euler method, which reads

$$\nabla \cdot \mathbf{u} = 0, \tag{22}$$

and

$$\frac{\mathbf{u}^{m+1} - \mathbf{u}^m}{T} \approx -(\mathbf{u} \cdot \nabla)\mathbf{u}^m - \frac{1}{\rho^m}\nabla p^{m+1} + \nu \nabla^2 \mathbf{u}^m + \mathbf{g}. \tag{23}$$

The superscript m indicates the time level, i.e., m for old time level, and $m+1$ for new time level; T is the time stepping. The continuity equation is discretized at the new time level $m+1$ to preserve a divergence free velocity field. In the momentum equation, all terms are discretized at the old time level m, except the pressure term.

Reproduced with permission of the copyright owner. Further reproduction prohibited without permission.

In other words, the advective and frictional terms are computed explicitly and the pressure term is computed implicitly. The purpose of this procedure is to develop a single equation for the computation of pressure based on Eqs. (4) and (5).

Solution of Eqs. (22) and (23) uses the first-order two-fractional-steps projection method (Chorin (1968) and Harlow & Welch (1965)). The two fractional steps are given by

$$\frac{\tilde{\mathbf{u}} - \mathbf{u}^m}{T} \approx -(\mathbf{u} \cdot \nabla)\mathbf{u}^m + \nu \nabla^2 \mathbf{u}^m + \mathbf{g} \tag{24}$$

and

$$\frac{\mathbf{u}^{m+1} - \tilde{\mathbf{u}}}{T} \approx -\frac{1}{\rho^m} \nabla p^{m+1}, \tag{25}$$

where Eq. (24) is an explicit expression for the intermediate velocity field $\tilde{\mathbf{u}} = (\tilde{u}\,\hat{i} + \tilde{v}\,\hat{j})$, referred to as the predictor step and Eq. (25) is an implicit expression for the new velocity field $\mathbf{u}^{m+1}$ termed as the projection step. In Eq. (24), all terms are explicit and known from the previous time level or initial condition, so the intermediate velocity field $\tilde{\mathbf{u}}$ can be easily determined. If the pressure gradient term is discretized at the old time level, then both the continuity equation and the momentum equation could predict a velocity field at the new time level ($\mathbf{u}^{m+1}$), which may not necessarily be equal. Basically, the attempt here is to apply a correction to the intermediate velocity field $\tilde{\mathbf{u}}$ by discretizing the pressure at the new time level, so that the new velocity field is divergent free (Gerrits, 2001).

Eq. (25) and the continuity equation (Eq. 22) can be combined into a single equation for the solution of the pressure as

$$\nabla \cdot \left[\frac{1}{\rho^m} \nabla p^{m+1}\right] \approx \frac{\nabla \cdot \tilde{\mathbf{u}}}{T}. \tag{26}$$

Eq. (26) is named the Pressure Poisson Equation (PPE). Although the fluid is assumed incompressible, the density in Eq. (26) is retained inside the divergence operator. This results in an extra term in the PPE proportional to $\nabla \rho$, which contributes

Reproduced with permission of the copyright owner. Further reproduction prohibited without permission.

to the pressure solution within the free surface transition region where $\nabla\rho \neq 0$ (Kothe *et al.*, 1991). As in the majority of incompressible models, the PPE is formulated with the pressure p and densityρ as separate terms instead of using the kinematic pressure, p/ρ. Formulation of the PPE in this fashion follows that of an implicit pressure solution technique in the MAC method by Brackbill & Ruppel (1986), where the PPE was found to be ideally suited for obtaining a pressure field when "voids" (air) are present in the domain because the density and pressure go to zero near the void at the same rate.

The system of linear equations generated by the finite difference of the PPE can be solved iteratively through a successive over relaxation (SOR) method, i.e., a Gauss-Seidel method with over relaxation, or by an incomplete Cholesky conjugate gradient (ICCG) technique. Once the pressure field is determined by solving the system of linear equations, the new velocity field, $\mathbf{u}^{m+1}$, is obtained from the projection step (Eq. 25), thus

$$\mathbf{u}^{m+1} = \tilde{\mathbf{u}} - \frac{T}{\rho^m}\nabla p^{m+1}. \tag{27}$$

2.6.2 Temporal discretization including moving objects

Eqs. (22–26) can be modified to account for the transit of moving objects through the computational domain. From Eq. (13) recall from Section 2.5 that the fractional blocked volume and open volume for fluid to flow are given by $B_C\delta x\delta y$ and $A_C\delta x\delta y$, respectively. The temporal discretization of the continuity equation including moving objects (calculated a new time level) reads

$$\nabla \cdot \mathbf{u}^{m+1} = \Phi,^{m+1} \tag{28}$$

where

$$\Phi^{m+1} = \frac{1}{V}\left(\frac{({B_C}^{m+1} - {B_C}^{m})\delta x\delta y}{T}\right) = \frac{{A_C}^{m} - {A_C}^{m+1}}{A_{C_s}T}, \tag{29}$$

Reproduced with permission of the copyright owner. Further reproduction prohibited without permission.

and $V = A_{Cs}\delta x \delta y$ is the control volume. Φ^{m+1} represents the new fraction of volume cell taken or released by the moving object in the lapse T to force zero divergence in the control volume cell. A_{Cs} is the fractional volume open for the fluid to flow with no moving objects. In other words, it is the fractional volume open for the fluid to flow due to stationary objects only.

The predictor step for temporal discretization of the momentum equation, including moving objects, is obtained from Eq. (14), and reads

$$\frac{\tilde{\mathbf{u}} - \mathbf{u}^m}{T} \approx -\nabla \cdot (\mathbf{uu})^m + (\Phi \mathbf{u})^m + \nu \nabla^2 \mathbf{u}^m + \mathbf{g}. \tag{30}$$

For the projection step the same Eq. (25) described for the temporal discretization without moving objects holds.

Notice that term Φ in the predictor step is at the old time level meaning that

$$\Phi^m = ({A_C}^{m-1} - {A_C}^m)/(A_{Cs}T).$$

Again, Eq. (25) and the continuity equation (Eq. 28) can be combined into a single equation for the solution of the pressure including moving objects. The new PPE, which takes into consideration the moving object becomes

$$\nabla \cdot \left[\frac{1}{\rho^m} \nabla p^{m+1}\right] = \frac{\nabla \cdot \tilde{\mathbf{u}} - \Phi^{m+1}}{T}. \tag{31}$$

As before, once the pressure field is determined by solving the PPE, the new velocity field $\mathbf{u}^{m+1}$ is obtained from Eq. (27).

2.6.3 Spatial discretization

The governing differential equations are treated in flux-conservative form so mass and momentum are conserved when the equations are discretized. Using control volume at cell center and cell sides, the spatial finite difference equations are derived. For the discretization of the continuity equation and the momentum equation, the

Reproduced with permission of the copyright owner. Further reproduction prohibited without permission.

FDM is applied in such a way that the discrete difference operators of the advective and diffusion terms preserve the symmetry properties of the corresponding continuous differential operators. Thus, advection is discretized with a skew-symmetric difference operator and diffusion is discretized by a symmetric difference operator.

2.6.3.1 Continuity equation discretization

Eq. (4) accounts for the mass conservation of an incompressible fluid flow. To ensure global mass conservation, i.e., the total amount of fluid in the entire computational domain, and local conservation, i.e., the amount of fluid in the computational cell, the change in the surface level must be consistent with the mass fluxes. Consider a computational cell (i, j) in the domain Ω. The control volume at cell center, $V = \delta x_i \delta y_j$, is bounded by lines $x = x_{i-1}$, $x = x_i$, $y = y_{j-1}$ and $y = y_j$ as shown in Fig. 9.

The shaded region represents a stationary rigid object, i.e., seabottom topography, which partially obstructs cell face areas and volume. The horizontal velocities (u) and vertical velocities (v) are assumed to be constant along the cell apertures. The continuity equation is then discretized using mass fluxes through the apertures, thus

$$u_{i,j} A_{Ri,j} \delta y_j + v_{i,j} A_{Ti,j} \delta x_i - u_{i-1,j} A_{Ri-1,j} \delta y_j - v_{i,j-1} A_{Ti,j-1} \delta x_i = 0. \qquad (32)$$

The conservation of mass for an incompressible fluid assures that the sum of all mass fluxes cancels out. The resulting numerical equation corresponds to a second order central discretization of Eq. (4). Mass fluxes are restricted along object boundaries by the fractional value of the apertures, i.e., in Fig. 9, $A_{Ri,j} < 1$ and $A_{Ti,j-1} < 1$. Values of cell aperture equal to one, i.e., $A_{Ri-1,j} = 1$ and $A_{Ti,j} = 1$, indicate that these cell face areas are not cut by the object boundary. Then, Eq. (32) is independent of the object boundary geometry within the control volume and the

Reproduced with permission of the copyright owner. Further reproduction prohibited without permission.

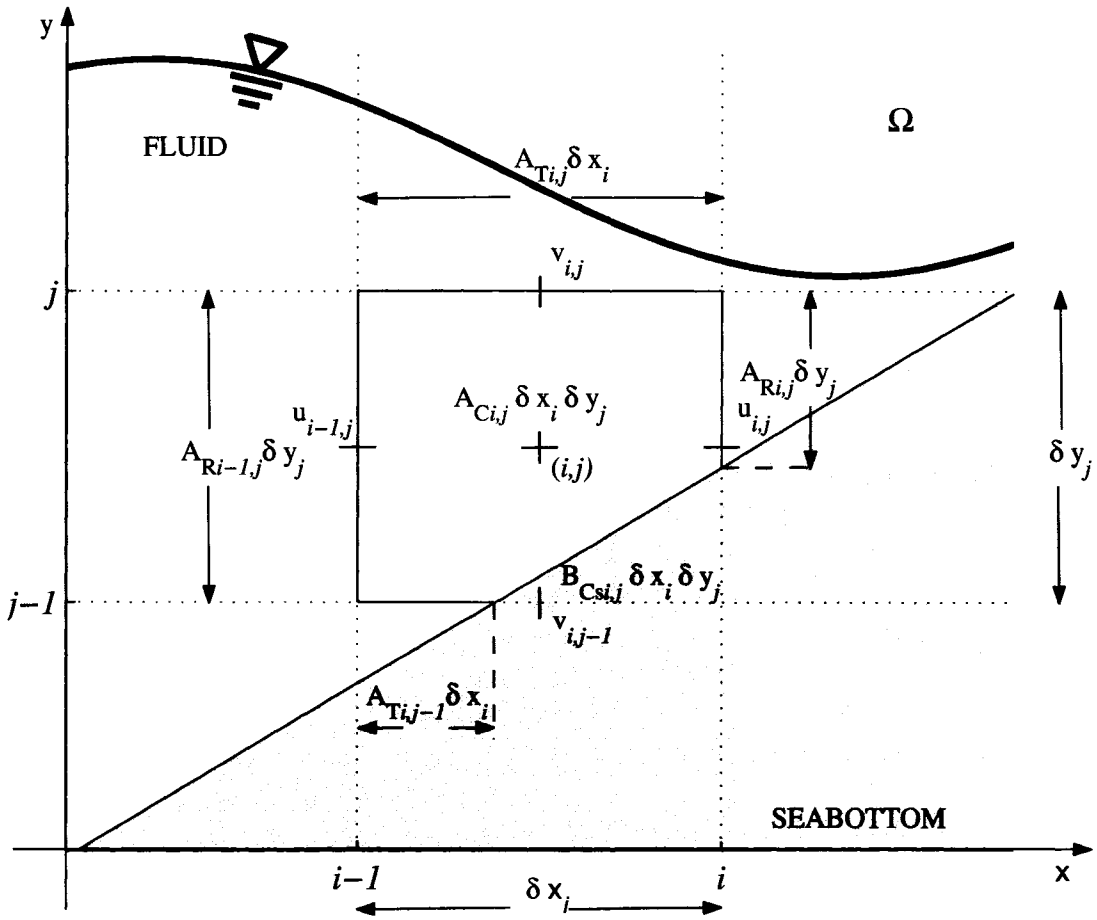

Figure 9: Grid cell for discretization of the continuity equations.

only geometrical information needed to fulfill the mass conservation in an obstructed cell is cell apertures.

To account for the incursion or retreat of moving objects in the cell control volume Eq. (13) is used. The corresponding spatial discretization of Eq. (13) is tailored with the help of Fig. 10 and reads

$$u_{i,j}A_{Ri,j}\delta y_j + v_{i,j}A_{Ti,j}\delta x_i - u_{i-1,j}A_{Ri-1,j}\delta y_j - v_{i,j-1}A_{Ti,j-1}\delta x_i = \Phi, \qquad (33)$$

where

$$\Phi = \frac{(A_{Ci,j}(t-T) - A_{Ci,j}(t))\delta x_i \delta y_j}{T}.$$

Reproduced with permission of the copyright owner. Further reproduction prohibited without permission.

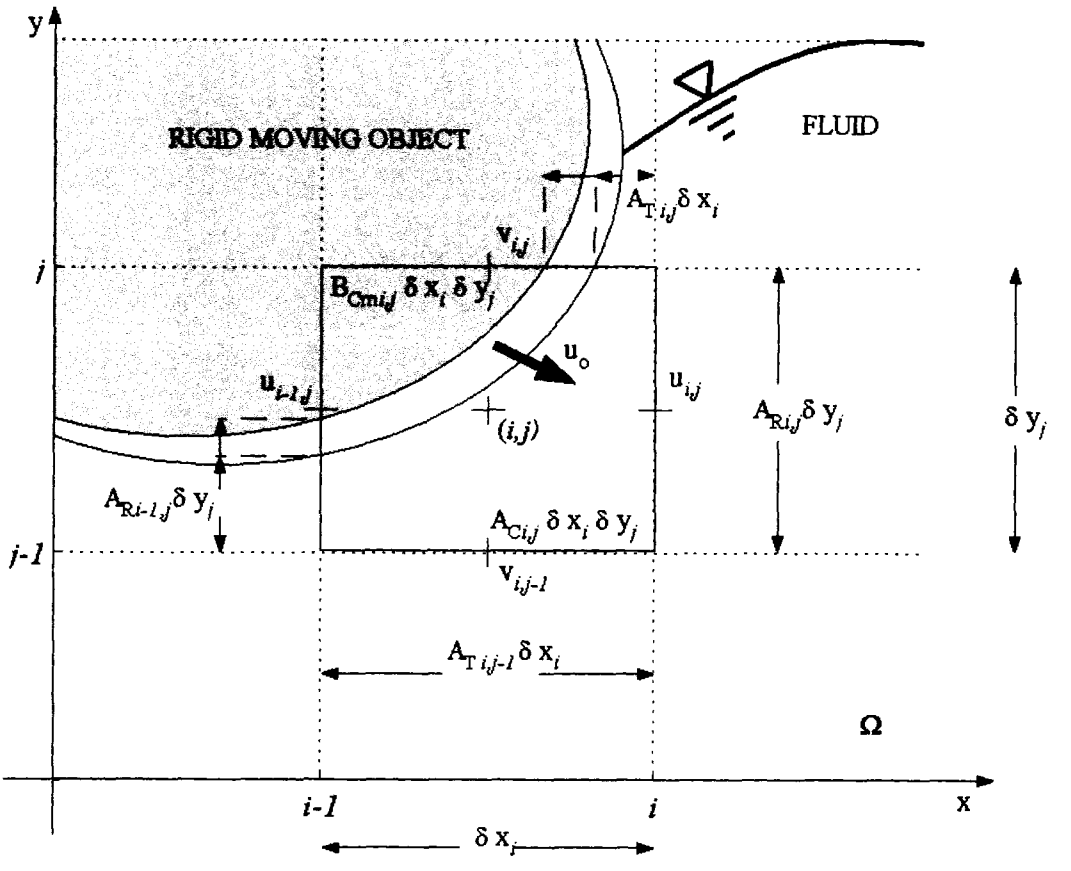

Figure 10: Grid cell for discretization of the continuity equations with rigid moving object.

Note that A_C, A_R, and A_T are time dependent and represent the fractional cell volume and face areas apertures for the fluid to flow. They are calculated based on the stationary and moving object fractional-blocked volume and areas in the control volume, i.e., $A_C = 1-(B_{Cs}+B_{Cm})$, $A_R = 1-(B_{Rs}+B_{Rm})$ and $A_T = 1-(B_{Ts}+B_{Tm})$. Here, subscript s and m stand for stationary and moving objects respectively. Eq. (33) is independent of the moving object boundary geometry within the control volume. The velocity direction of the moving object is given indirectly as the object blocks cell face apertures. Only the time dependent cell aperture information is needed to account for mass conservation and velocity direction.

Reproduced with permission of the copyright owner. Further reproduction prohibited without permission.

2.6.3.2 Momentum equation discretization

The law of the conservation of momentum states that the rate of change of momentum in the control volume must equal the net momentum flux into the control volume, plus any external forces acting on the control volume. The momentum flux in the control volume is determined by the inertial and advective momentum of the flow and they must be rigorously consistent with the external or body forces. In water gravity waves or tsunami, common external forces are the pressure, viscosity and gravity.

To facilitate and better visualize the spatial numerical derivation, the two-dimensional momentum equation is split in its vertical and horizontal components. From Eq. (23), the x-momentum and y-momentum read

$$\frac{u^{m+1}-u^m}{T} \approx -\left(u\frac{\partial u}{\partial x}+v\frac{\partial u}{\partial y}\right)^m - \frac{1}{\rho^m}\frac{\partial p}{\partial x}^{m+1} + \frac{1}{\rho^m}\left(\frac{\partial \tau_{xx}}{\partial x}+\frac{\partial \tau_{xy}}{\partial y}\right)^m + g_x \quad (34)$$

and

$$\frac{v^{m+1}-v^m}{T} \approx -\left(u\frac{\partial v}{\partial x}+v\frac{\partial v}{\partial y}\right)^m - \frac{1}{\rho^m}\frac{\partial p}{\partial y}^{m+1} + \frac{1}{\rho^m}\left(\frac{\partial \tau_{xy}}{\partial x}+\frac{\partial \tau_{yy}}{\partial y}\right)^m + g_y, \quad (35)$$

respectively. In the above equations, advective terms are in nonconservative form and are evaluated using the old time level velocity field values.

The equivalent conservative expressions of Eqs. (34 and 35) are

$$\frac{u^{m+1}-u^m}{T} \approx -\left(\frac{\partial uu}{\partial x}+\frac{\partial uv}{\partial y}-\phi u\right)^m - \frac{1}{\rho^m}\frac{\partial p}{\partial x}^{m+1} + \frac{1}{\rho^m}\left(\frac{\partial \tau_{xx}}{\partial x}+\frac{\partial \tau_{xy}}{\partial y}\right)^m + g_x \quad (36)$$

and

$$\frac{v^{m+1}-v^m}{T} \approx -\left(\frac{\partial uv}{\partial x}+\frac{\partial vv}{\partial y}-\phi v\right)^m - \frac{1}{\rho^m}\frac{\partial p}{\partial y}^{m+1} + \frac{1}{\rho^m}\left(\frac{\partial \tau_{xy}}{\partial x}+\frac{\partial \tau_{yy}}{\partial y}\right)^m + g_y \quad (37)$$

where the respective momentum contribution for moving objects is included (ϕu for the x-momentum and ϕv for the y-momentum).

Reproduced with permission of the copyright owner. Further reproduction prohibited without permission.

2.6.3.2.1 Advective terms discretization. In this study, three different numerical approximations are used to treat the momentum advection terms either conservatively or nonconservatively. They are: a) the backward/forward/central difference method (first up to second order accurate); b) the method of characteristics with van Leer's limiter (second order accurate) and c) third order accurate method. Advective terms are incorporated into the predictor estimate of the two-fractional-steps projection method using old time (t^m) velocity field values (see Eq. (24)).

Discretization of the advective terms in Eqs. (34) and (35) require the approximation of the first partial derivative, e.g., $\partial u/\partial x$ (see Fig. 11). Assume that $u(x)$

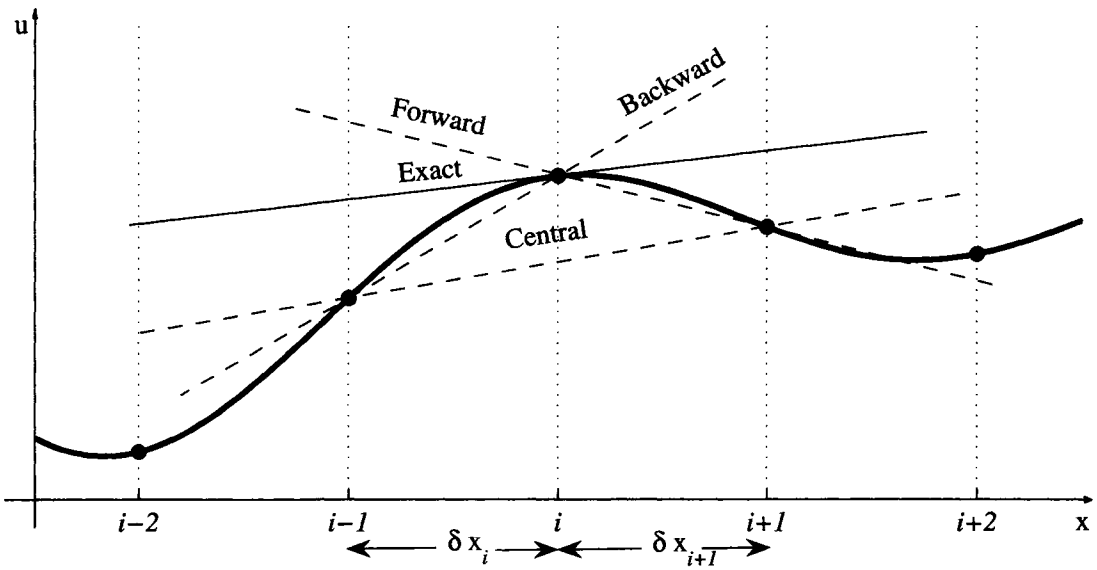

Figure 11: Definition of a derivative and its approximation.

is a continuous differentiable function in a one-dimensional domain which can be expressed in the vicinity of x_i, as a Taylor series, thus

$$u(x) = u(x_i) + (x - x_i)\left(\frac{\partial u}{\partial x}\right)_i + \frac{(x-x_i)^2}{2!}\left(\frac{\partial^2 u}{\partial x^2}\right)_i + \frac{(x-x_i)^3}{3!}\left(\frac{\partial^3 u}{\partial x^3}\right)_i + \ldots\ldots + \frac{(x-x_i)^n}{n!}\left(\frac{\partial^n u}{\partial x^n}\right)_i + O,$$

Reproduced with permission of the copyright owner. Further reproduction prohibited without permission.

where O means "higher order terms". By replacing x in Taylor expansion equation by x_{i-1} or x_{i+1}, one obtains expressions for the variable values at these points in terms of the variable and its derivatives at x_i. Using the Taylor expansion for u at point x_{i-1} it is easy to show that:

$$\left(\frac{\partial u}{\partial x}\right)_i = \frac{u_i - u_{i-1}}{\delta x_i} + \frac{\delta x_i}{2}\left(\frac{\partial^2 u}{\partial x^2}\right)_i - \frac{\delta x_i^2}{6}\left(\frac{\partial^3 u}{\partial x^3}\right)_i + O, \tag{38}$$

at point x_{i+1},

$$\left(\frac{\partial u}{\partial x}\right)_i = \frac{u_{i+1} - u_i}{\delta x_{i+1}} - \frac{\delta x_{i+1}}{2}\left(\frac{\partial^2 u}{\partial x^2}\right)_i - \frac{\delta x_{i+1}^2}{6}\left(\frac{\partial^3 u}{\partial x^3}\right)_i + O, \tag{39}$$

and at both points x_{i-1} and x_{i+1},

$$\left(\frac{\partial u}{\partial x}\right)_i = \frac{u_{i+1} - u_{i-1}}{\delta x_i + \delta x_{i+1}} - \frac{\delta x_{i+1}^2 - \delta x_i^2}{2(\delta x_i + \delta x_{i+1})}\left(\frac{\partial^2 u}{\partial x^2}\right)_i - \frac{\delta x_{i+1}^3 + \delta x_i^3}{6(\delta x_i + \delta x_{i+1})}\left(\frac{\partial^3 u}{\partial x^3}\right)_i + O. \tag{40}$$

This can be extended to any other point near x_i, e.g., x_{i+2} or x_{i-2} to look for higher order approximations of the first derivative. These three expressions are calculated exactly if all terms on the right hand side are retained. Because the higher order derivatives are unknown (since no more grid points are included in the derivations), one can assume that the higher order derivatives do not make a significant contribution if the element sizes, e.g. δx_i and δx_{i+1}, are small. Indeed, the higher order terms will be small except in the unusual situation in which higher derivatives are locally very large, e.g. as the case of shock waves. Ignoring the latter possibility, approximations of the first derivative result from truncating each of the series terms after the first term on the right hand sides, thus

$$\left(\frac{\partial u}{\partial x}\right)_i \approx \frac{u_i - u_{i-1}}{\delta x_i}, \tag{41}$$

$$\left(\frac{\partial u}{\partial x}\right)_i \approx \frac{u_{i+1} - u_i}{\delta x_{i+1}}, \tag{42}$$

$$\left(\frac{\partial u}{\partial x}\right)_i \approx \frac{u_{i+1} - u_{i-1}}{\delta x_i + \delta x_{i+1}}. \tag{43}$$

Reproduced with permission of the copyright owner. Further reproduction prohibited without permission.

These are the backward, forward and central differences of $(\partial u/\partial x)_i$, respectively. The terms dropped from the right hand sides of the equations are the truncation errors, which measure the accuracy of the approximation and determine the rate at which the error decreases as the element size is reduced. In particular, the first truncated term is usually the principal source of error (smallest exponent). Often the element sizes are uniform, i.e. $\delta x_i = \delta x_{i+1}$, and in such a case, the truncation error due to the second derivative in a central difference scheme becomes zero (see first term of the truncation error in Eq. (40)). When the element sizes are not uniform, truncation errors become generally large. However, this error is reduced to a minimum if a slowly varying element size is used, as it was mentioned in Section 2.2.

2.6.3.2.1.1 Backward/forward/central difference method (first up to second order). The discretization of the momentum Eqs. (34) and (35) follows the algorithm outlined by Nichols *et al.* (1980) and Kothe *et al.* (1991). The finite difference forms of advective terms are derived first using the backward, forward and central difference method with the help of the momentum control volumes shown in Figs. 12 and 13. Note the location of cell variables are referenced with respect to the right-upper corner (see Section 2.3 for details).

The advective term in the nonconservative form of the x-momentum equation (Eq. 34) reads

$$\left(u\frac{\partial u}{\partial x} + v\frac{\partial u}{\partial y}\right)^m .$$

Using an upstream/downstream scheme for the treatment of the advective term, the first term is discretized as follows: if $u_{i,j} \geq 0$ (backward derivative), meaning flow is coming from the left, then

$$u\frac{\partial u}{\partial x} \approx u_{i,j}\frac{u_{i,j} - u_{i-1,j}}{\delta x_i}; \tag{44}$$

Reproduced with permission of the copyright owner. Further reproduction prohibited without permission.

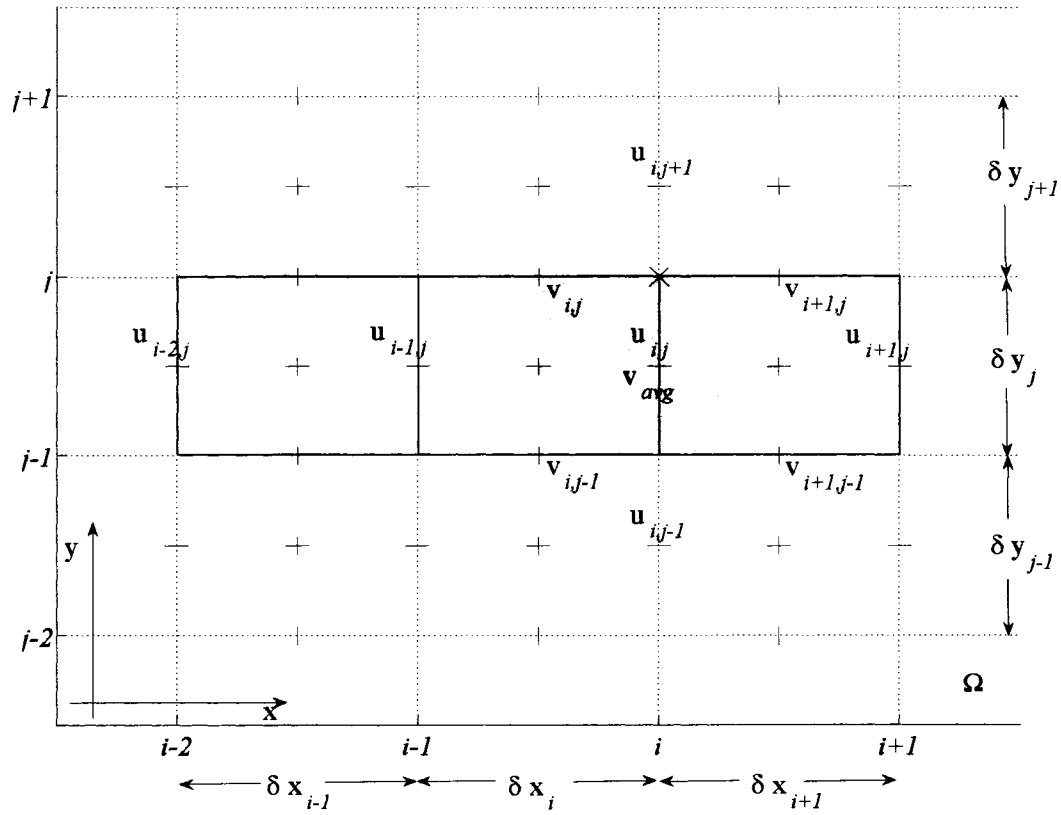

Figure 12: Momentum control volume is centered right cell face for the $x-$momentum. Flux velocities at the momentum control volume boundaries are obtained from interpolation of neighboring fluid velocities.

now, in case that $u_{i,j} < 0$ (forward derivative), meaning that the flow is approaching from the right, then

$$u\frac{\partial u}{\partial x} \approx u_{i,j}\frac{u_{i+1,j} - u_{i,j}}{\delta x_{i+1}}. \tag{45}$$

Eqs. (44) and (45) are combined in a single equation to account for both horizontal velocity directions. The "two-in-one" equation is tailored by the use of two numerical switches that turn on/off or off/on the numerical derivative terms according to the velocity sign $Su = sign(u_{i,j})$, $\langle \frac{1+Su}{2} / \frac{1-Su}{2} \rangle$. If $u_{i,j} \geq 0$, then $Su = 1$ and $\langle \frac{1+Su}{2} / \frac{1-Su}{2} \rangle = \langle 1/0 \rangle$. Conversely, if $u_{i,j} < 0$, then $Su = -1$ and $\langle \frac{1+Su}{2} / \frac{1-Su}{2} \rangle = \langle 0/1 \rangle$.

Reproduced with permission of the copyright owner. Further reproduction prohibited without permission.

The finite difference forms of the first advective term of the x-momentum equation becomes

$$u\frac{\partial u}{\partial x} \approx u_{i,j}\left(\left\langle\frac{1+Su}{2}\right\rangle\frac{u_{i,j}-u_{i-1,j}}{\delta x_i}+\left\langle\frac{1-Su}{2}\right\rangle\frac{u_{i+1,j}-u_{i,j}}{\delta x_{i+1}}\right). \tag{46}$$

The second term of the advective expression is obtained in a similar manner and it is given by

$$v\frac{\partial u}{\partial y} \approx v_{avg}\left(\left\langle\frac{1+Sv_{avg}}{2}\right\rangle\frac{u_{i,j}-u_{i,j-1}}{\delta y_{bot}}+\left\langle\frac{1-Sv_{avg}}{2}\right\rangle\frac{u_{i,j+1}-u_{i,j}}{\delta y_{top}}\right), \tag{47}$$

where variable v_{avg} is the vertical velocity average at $u_{i,j}$ location, based on the weighted vertical velocity averages at the cell corners, and defined by

$$v_{avg}=0.5\left(\frac{v_{i,j}\delta x_{i+1}+v_{i+1,j}\delta x_i}{\delta x_i+\delta x_{i+1}}+\frac{v_{i,j-1}\delta x_{i+1}+v_{i+1,j-1}\delta x_i}{\delta x_i+\delta x_{i+1}}\right).$$

Here, $Sv_{avg}=sign(v_{avg})$, $\delta y_{bot}=0.5(\delta y_j+\delta y_{j-1})$ and $\delta y_{top}=0.5(\delta y_{j+1}+\delta y_j)$. This vertically averaged velocity adds some filtering, improving the numerical stability.

For the y-momentum equation (Eq. 35), the advective term in nonconservative form,

$$\left(u\frac{\partial v}{\partial x}+v\frac{\partial v}{\partial y}\right)^m,$$

can be discretized following the same derivation made for the x-momentum advective terms. With the help of Fig. 13, the finite difference form of the y-momentum is

$$u\frac{\partial v}{\partial x} \approx u_{avg}\left(\left\langle\frac{1+Su_{avg}}{2}\right\rangle\frac{v_{i,j}-v_{i-1,j}}{\delta x_{left}}+\left\langle\frac{1-Su_{avg}}{2}\right\rangle\frac{v_{i+1,j}-v_{i,j}}{\delta x_{right}}\right) \tag{48}$$

and

$$v\frac{\partial v}{\partial y} \approx v_{i,j}\left(\left\langle\frac{1+Sv}{2}\right\rangle\frac{v_{i,j}-v_{i,j-1}}{\delta y_j}+\left\langle\frac{1-Sv}{2}\right\rangle\frac{v_{i,j+1}-v_{i,j}}{\delta y_{j+1}}\right). \tag{49}$$

Again, u_{avg} is the horizontal velocity average at $v_{i,j}$ location which reads

$$u_{avg}=0.5\left(\frac{u_{i,j}\delta y_{j+1}+u_{i,j+1}\delta y_j}{\delta y_j+\delta y_{j+1}}+\frac{u_{i-1,j}\delta y_{j+1}+u_{i-1,j+1}\delta y_j}{\delta y_j+\delta y_{j+1}}\right).$$

Reproduced with permission of the copyright owner. Further reproduction prohibited without permission.

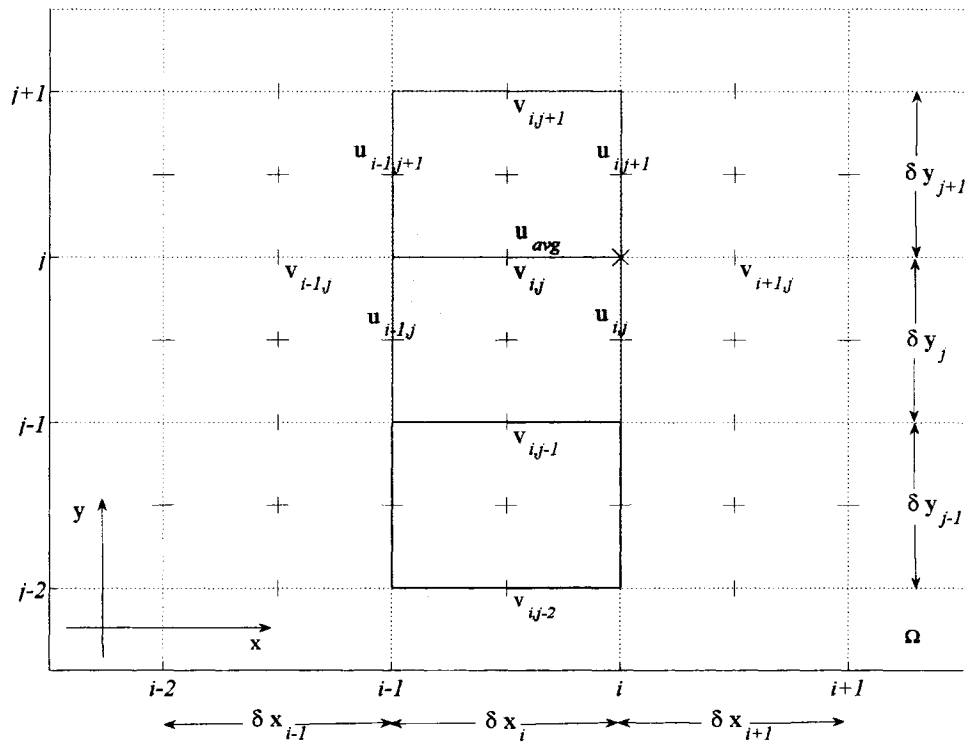

Figure 13: Momentum control volume is centered top cell face for the $y-$momentum. Flux velocities at the momentum control volume boundaries are obtained from interpolation of neighboring fluid velocities.

The remaining parameters are given by $Sv = sign(v_{i,j})$, $Su_{avg} = sign(u_{avg})$, $\delta x_{left} = 0.5(\delta x_{i-1} + \delta x_i)$ and $\delta x_{right} = 0.5(\delta x_i + \delta x_{i+1})$, respectively.

Eqs. (46 to 49) are very useful at the boundaries, i.e., air-water interface or in the immediate computational element to a stationary or moving object boundary where no more than two grid points are available. These equations are often used in the fluid interior as well, due to the stability advantages of the backward/forward difference method, which can be retained even in a variable element size with no reduction in formal accuracy.

Reproduced with permission of the copyright owner. Further reproduction prohibited without permission.

Higher order approximation of the first derivative can be obtained by using more grid points to eliminate more of the truncation error terms in the Taylor expression. For instance, using u_{i-1} to obtain an expression for the second derivative at x_i and substituting this expression in Eq. (40), the following second order approximation is obtained, which can be applied to any variable cell spacing,

$$\left(\frac{\partial u}{\partial x}\right)_i = \frac{u_{i+1}\delta x_i^2 - u_{i-1}\delta x_{i+1}^2 + u_i(\delta x_{i+1}^2 - \delta x_i^2)}{\delta x_i \delta x_{i+1}(\delta x_i + \delta x_{i+1})} - \frac{\delta x_i \delta x_{i+1}}{6}\left(\frac{\partial^3 u}{\partial x^3}\right)_i + O. \quad (50)$$

Note that for uniform cell spacing ($\delta x_i = \delta x_{i+1}$), the above expression reduces to the central difference scheme approximation given in Eq. (43).

The second order approximation in the advective terms is achieved by introducing a parameter, α, and two numerical switches that control the linear combination of the backward/forward and the centered differences into a single expression. Then, the preceding set of advective term equations becomes

$$u\frac{\partial u}{\partial x} \approx u_{i,j}\left(\left\langle\frac{\delta x_{i+1}(1+\alpha Su)}{\delta x_\alpha}\right\rangle\frac{u_{i,j}-u_{i-1,j}}{\delta x_i} + \left\langle\frac{\delta x_i(1-\alpha Su)}{\delta x_\alpha}\right\rangle\frac{u_{i+1,j}-u_{i,j}}{\delta x_{i+1}}\right), \quad (51)$$

$$v\frac{\partial u}{\partial y} \approx v_{avg}\left(\left\langle\frac{\delta y_{top}(1+\alpha Sv_{avg})}{\delta y v_\alpha}\right\rangle\frac{u_{i,j}-u_{i,j-1}}{\delta y_{bot}} + \left\langle\frac{\delta y_{bot}(1-\alpha Sv_{avg})}{\delta y v_\alpha}\right\rangle\frac{u_{i,j}-u_{i,j-1}}{\delta y_{bot}}\right), \quad (52)$$

$$u\frac{\partial v}{\partial x} \approx u_{avg}\left(\left\langle\frac{\delta x_{right}(1+\alpha Su_{avg})}{\delta x u_\alpha}\right\rangle\frac{u_{i,j+1}-u_{i,j}}{\delta y_{top}} + \left\langle\frac{\delta x_{left}(1-\alpha Su_{avg})}{\delta x u_\alpha}\right\rangle\frac{v_{i+1,j}-v_{i,j}}{\delta x_{right}}\right) \quad (53)$$

and

$$v\frac{\partial v}{\partial y} \approx v_{i,j}\left(\left\langle\frac{\delta y_{j+1}(1+\alpha Sv)}{\delta y_\alpha}\right\rangle\frac{v_{i,j}-v_{i,j-1}}{\delta y_j} + \left\langle\frac{\delta y_j(1-\alpha Sv)}{\delta y_\alpha}\right\rangle\frac{v_{i,j+1}-v_{i,j}}{\delta y_{j+1}}\right); \quad (54)$$

Reproduced with permission of the copyright owner. Further reproduction prohibited without permission.

where

$$\begin{aligned}
\delta x_\alpha &= \langle 1-\alpha Su\rangle \delta x_i + \langle 1+\alpha Su\rangle \delta x_{i+1},\\
\delta y v_\alpha &= \langle 1-\alpha Sv_{avg}\rangle \delta y_{bot} + \langle 1+\alpha Sv_{avg}\rangle \delta y_{top},\\
\delta x u_\alpha &= \langle 1-\alpha Su_{avg}\rangle \delta x_{left} + \langle 1+\alpha Su_{avg}\rangle \delta x_{right},\\
\delta y_\alpha &= \langle 1-\alpha Sv\rangle \delta y_j + \langle 1+\alpha Sv\rangle \delta y_{j+1}.
\end{aligned}$$

For instance, in Eq. (51), if $\alpha = 0$ the finite difference of $\partial u/\partial x$ reduces to

$$\frac{\partial u}{\partial x} \approx \frac{\delta x_{i+1}\frac{u_{i,j}-u_{i-1,j}}{\delta x_i} + \delta x_i \frac{u_{i+1,j}-u_{i,j}}{\delta x_{i+1}}}{\delta x_i + \delta x_{i+1}} \approx \frac{u_{i+1,j}-u_{i-1,j}}{\delta x_i + \delta x_{i+1}},$$

which is a weighted central difference scheme at $u_{i,j}$ point. Note as well, if $\delta x_i = \delta x_{i+1}$ (uniform element sizes), a central difference scheme is obtained as Eq. (43). Now, in the case that $\alpha = 1$ and $u_{i,j} > 0$, the backward difference is obtained, see Eq. (41).

The basic idea used above is to weight the upstream derivative of the quantity being fluxed more than the downstream derivative. The weighted factors are $1+\alpha$ and $1-\alpha$ for the upstream and downstream derivatives, respectively. The parameter α could be set within $[0-1]$ to control the linear combination of the backward/forward and the central difference. Above expressions reduce to first order when $\alpha = 1$ (backward/forward difference) and second order (central difference) when $\alpha = 0$. Values of α greater than $\sim \frac{1}{2}$ are useful to offset the unstable negative diffusion brought about by the first order forward time differencing of Eq. (23).

Note, that neither the x-momentum nor the y-momentum finite difference equations have considered cell apertures due to the presence of a stationary or moving object. To account for cell face apertures, Eqs. (51-54) are modified as follows:
for the x-momentum

$$\begin{aligned}
u\frac{\partial u}{\partial x} \approx u_{i,j}\Bigg(&\left\langle \frac{\delta x_{i+1}(1+\alpha Su)}{\delta x_\alpha}\right\rangle \left[\frac{A_{Ci,j}}{A_{Ri,j}}\right]\frac{u_{i,j}-u_{i-1,j}}{\delta x_i}\\
&+\left\langle \frac{\delta x_i(1-\alpha Su)}{\delta x_\alpha}\right\rangle \left[\frac{A_{Ci+1,j}}{A_{Ri,j}}\right]\frac{u_{i+1,j}-u_{i,j}}{\delta x_{i+1}}\Bigg),
\end{aligned} \tag{55}$$

Reproduced with permission of the copyright owner. Further reproduction prohibited without permission.

$$v\frac{\partial u}{\partial y} \approx v_{avg}\left(\left\langle\frac{\delta y_{top}(1+\alpha S v_{avg})}{\delta y v_\alpha}\right\rangle\left[\frac{A_{Tbot}}{A_{Ri,j}}\right]\frac{u_{i,j}-u_{i,j-1}}{\delta y_{bot}} + \left\langle\frac{\delta y_{bot}(1-\alpha S v_{avg})}{\delta y v_\alpha}\right\rangle\left[\frac{A_{Ttop}}{A_{Ri,j}}\right]\frac{u_{i,j+1}-u_{i,j}}{\delta y_{top}}\right), \tag{56}$$

and for the y-momentum,

$$u\frac{\partial v}{\partial x} \approx u_{avg}\left(\left\langle\frac{\delta x_{right}(1+\alpha S u_{avg})}{\delta x u_\alpha}\right\rangle\left[\frac{A_{Rleft}}{A_{Ti,j}}\right]\frac{v_{i,j}-v_{i-1,j}}{\delta x_{left}} + \left\langle\frac{\delta x_{left}(1-\alpha S u_{avg})}{\delta x u_\alpha}\right\rangle\left[\frac{A_{Rright}}{A_{Ti,j}}\right]\frac{v_{i+1,j}-v_{i,j}}{\delta x_{right}}\right) \tag{57}$$

and

$$v\frac{\partial v}{\partial y} \approx v_{i,j}\left(\left\langle\frac{\delta y_{j+1}(1+\alpha S v)}{\delta y_\alpha}\right\rangle\left[\frac{A_{Ci,j}}{A_{Ti,j}}\right]\frac{v_{i,j}-v_{i,j-1}}{\delta y_j} + \left\langle\frac{\delta y_j(1-\alpha S v)}{\delta y_\alpha}\right\rangle\left[\frac{A_{Ci,j+1}}{A_{Ti,j}}\right]\frac{v_{i,j+1}-v_{i,j}}{\delta y_{j+1}}\right); \tag{58}$$

where

$$\begin{aligned} A_{Tbot} &= \frac{\delta x_i A_{Ti+1,j-1} + \delta x_{i+1} A_{Ti,j-1}}{\delta x_i + \delta x_{i+1}}, \\ A_{Ttop} &= \frac{\delta x_i A_{Ti+1,j} + \delta x_{i+1} A_{Ti,j}}{\delta x_i + \delta x_{i+1}}, \\ A_{Rleft} &= \frac{\delta y_j A_{Ri-1,j+1} + \delta y_{j+1} A_{Ri-1,j}}{\delta y_j + \delta y_{j+1}}, \\ A_{Rright} &= \frac{\delta y_j A_{Ri,j+1} + \delta y_{j+1} A_{Ri,j}}{\delta y_j + \delta y_{j+1}}, \end{aligned}$$

are the weighted average apertures at the bottom, top, left and right of the control volume, respectively. Terms in brackets account for the cell apertures, adjusting the mass fluxes proportional to the magnitude of the control volume and cell apertures.

Higher order approximations always involve more nodes, yielding more complex equations to solve and more complicated treatment of boundary conditions, so a trade-off has to be made. Second order approximation usually offers a good combination of ease of use, accuracy and cost-effectiveness in tsunami application.

Reproduced with permission of the copyright owner. Further reproduction prohibited without permission.

2.6.3.2.1.2 The method of characteristics and van Leer limiter (second order accurate). The method of characteristics improves the accuracy of the upstream approximation by retaining second order terms in the Taylor series expansion of the advective term (Kowalik *et al.*, 2005). Using the conservative form of Eq. (34), the advective term of the x-momentum equation reads

$$\left(\frac{\partial uu}{\partial x}+\frac{\partial uv}{\partial y}\right)^{m}.$$

The equivalent finite difference equation for each term is

$$\frac{\partial uu}{\partial x}\approx\frac{u_R u_r-u_L u_l}{\delta x_{right}}$$

and

$$\frac{\partial uv}{\partial y}\approx\frac{u_{RT}v_{rt}-u_{RB}v_{rb}}{\delta y_j},$$

respectively. Upper and lower case letter subscripts on velocities indicate flux-momentum velocity and cell-center velocity, respectively.

For instance, using the control volume depicted in Fig. 14, the right flux-momentum velocity u_R is obtained as follows

$$\begin{aligned}u_R=&\left\langle\frac{1+Su_r}{2}\right\rangle\left[u_{i,j}\left(\frac{1}{2}+\frac{|u_r|T}{\delta x_{i+1}}\right)+u_{i+1,j}\left(\frac{1}{2}-\frac{|u_r|T}{\delta x_{i+1}}\right)\right]\\&+\left\langle\frac{1-Su_r}{2}\right\rangle\left[u_{i+1,j}\left(\frac{1}{2}+\frac{|u_r|T}{\delta x_{i+1}}\right)+u_{i,j}\left(\frac{1}{2}-\frac{|u_r|T}{\delta x_{i+1}}\right)\right],\end{aligned}\tag{59}$$

where $u_r=0.5(u_{i,j}+u_{i+1,j})$ is the averaged cell center-velocity, $Su_r=sign(u_r)$, meaning $Su_r=1$ if $u_r\geq 0$ or $Su_r=-1$ if $u_r<0$. T is the advection time step. Note that Eq. (59) weights the upstream velocity according to the control volume cell center-velocity (u_r) direction or sign. The actual cell boundary velocities are transported $2|u_r|T_{half}/\delta x_{i+1}$ nondimensional units during a lapse of time $T_{half}=T/2$. The shifted velocities, $u_{i,j}$ and $u_{i+1,j}$, are located at $\frac{1}{2}-\frac{|u_r|T}{\delta x_{i+1}}$ and $\frac{1}{2}+\frac{|u_r|T}{\delta x_{i+1}}$ nondimensional units from the cell center, respectively. The numerical switches $\langle\frac{1+Su_r}{2}/\frac{1-Su_r}{2}\rangle$ select the upstream term by turning off the downstream term.

Reproduced with permission of the copyright owner. Further reproduction prohibited without permission.

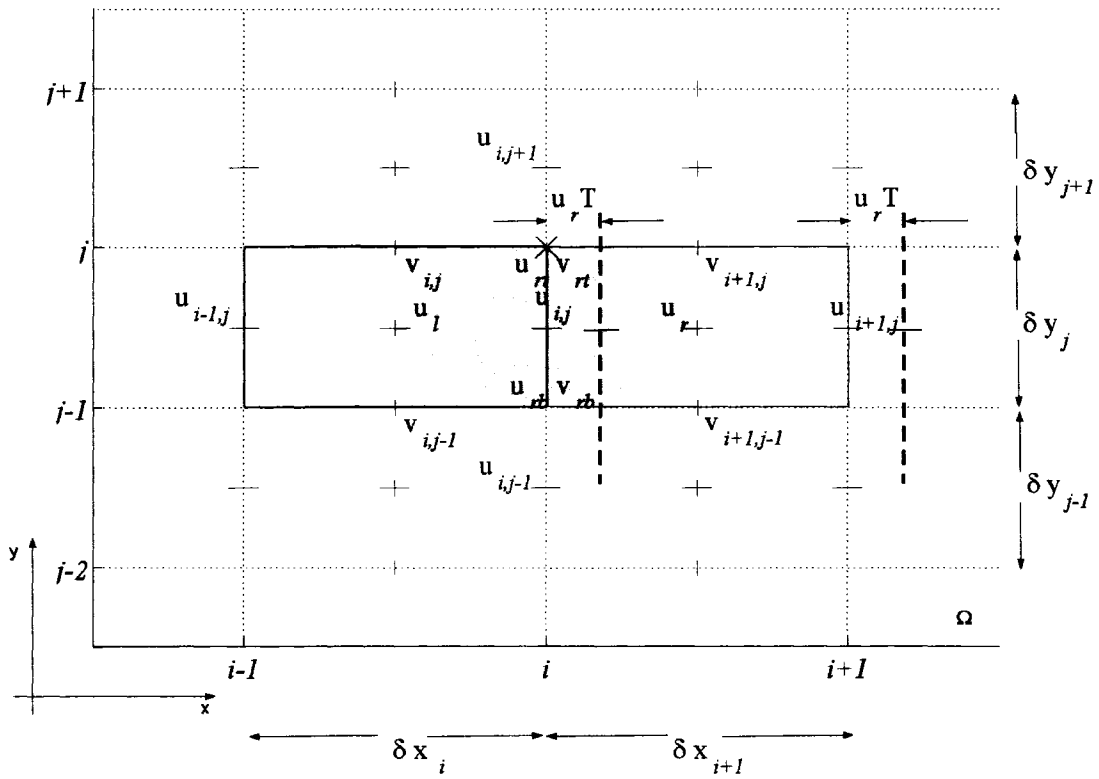

Figure 14: Momentum control volume for the $x-$momentum using the method of characteristics, assuming $u_r > 0$ and advection time step equal to $T/2$. Flux velocities at the momentum control volume boundaries are obtained from interpolation of neighboring fluid velocities.

Since $T_{half} = T/2$ is used for the advection terms, then determination of the advective term in Eq. (30) is broken down into two separate calculations, each with an advection time $T/2$.

The higher order of the momentum velocity u_R can be easily explained by re-arranging Eq. (59) as follows

$$u_R = \begin{cases} u_{i,j} & +\delta x_{i+1} \left(\frac{\partial u}{\partial x}\right)_{i+1,j} \left[\frac{1}{2} - \frac{|u_r|T}{\delta x_{i+1}}\right] \quad \text{if } u_r \geq 0 \\ u_{i+1,j} & -\delta x_{i+1} \left(\frac{\partial u}{\partial x}\right)_{i+1,j} \left[\frac{1}{2} - \frac{|u_r|T}{\delta x_{i+1}}\right] \quad \text{if } u_r < 0, \end{cases} \tag{60}$$

where $\frac{u_{i+1,j} - u_{i,j}}{\delta x_{i+1}}$ has been replaced by its equivalent partial derivative $\left(\frac{\partial u}{\partial x}\right)_{i+1,j}$.

Reproduced with permission of the copyright owner. Further reproduction prohibited without permission.

The upstream velocity is represented by the right-hand-side first term in the Taylor series expansion for u_R flux-velocity ($u_{i,j}$ or $u_{i+1,j}$, depending on the cell u_r center-velocity direction). The method of characteristics improves the accuracy of the upstream approximation by retaining the second order term in the Taylor expansion. In this example, the quantities within the square brackets in Eq. (60) bring the Taylor expansion to the right boundary of the control volume or to the cell center.

By limiting values of the first order derivative in the expansion, weak monotonicity in the advected quantity (van Leer, 1979) is enforced. This insures that no new velocity extrema at time t^{m+1} (after advection) are introduced relative to those at time t^m (before advection). As an example of van Leer's implementation method, consider

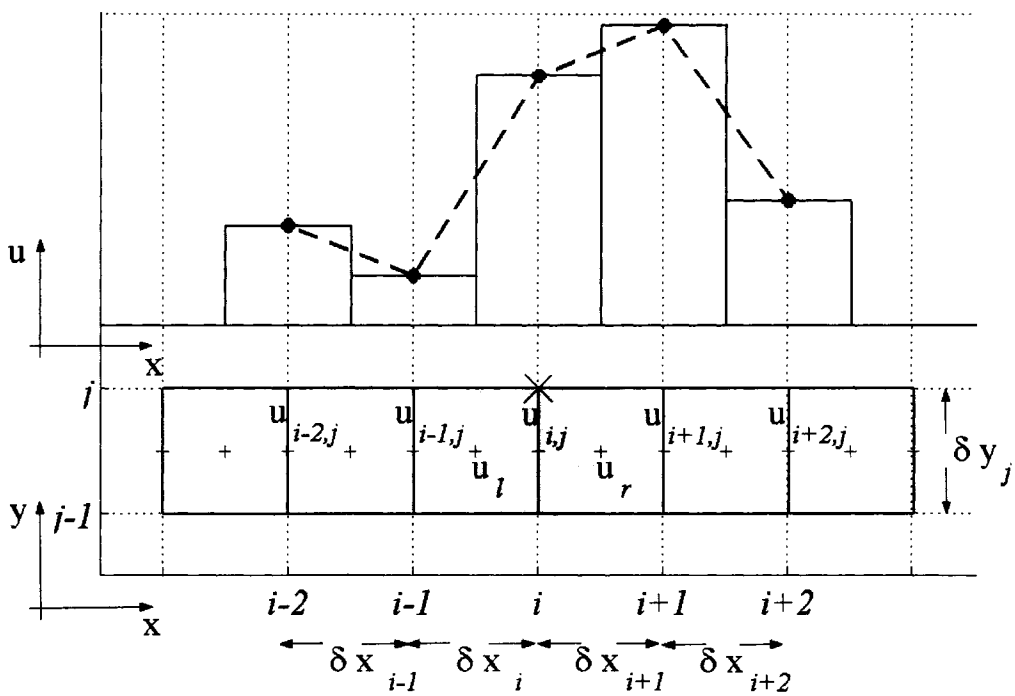

Figure 15: van Leer limiter.

the discrete x-velocity data prior to advection depicted in Fig. 15. For $u_r > 0$, if the

Reproduced with permission of the copyright owner. Further reproduction prohibited without permission.

velocity satisfies $u^m_{i-1,j} \leq u^m_{i,j} \leq u^m_{i+1,j}$ prior to advection, then $u^m_{i-1,j} \leq u^{m+1}_{i,j} \leq u^m_{i+1,j}$ must hold after advection. The monotonicity constraints enforced by the van Leer limiter require that velocities in any three neighboring cells be monotonic. If they are not, e.g., in Fig. 15 when $u_r < 0$, the middle cell velocity is a local extreme value, then its velocity gradient is set to zero and the resulting flux momentum velocity is estimated with the upstream cell expression, meaning $u_R = u_{i+1,j}$.

Eq. (59) is tailored with limiting gradient switches to force the gradient to zero as explained above. It follows then, that Eq. (59) becomes

$$\begin{aligned} u_R = &\left\langle \frac{1+Su_r}{2} \right\rangle \left[\langle Sg_p \rangle \left(u_{i,j} D_{long} + u_{i+1,j} D_{short} \right) + \langle 1 - Sg_p \rangle \, u_{i,j} \right] \\ &+ \left\langle \frac{1-Su_r}{2} \right\rangle \left[\langle Sg_n \rangle \left(u_{i+1,j} D_{long} + u_{i,j} D_{short} \right) + \langle 1 - Sg_n \rangle \, u_{i+1,j} \right], \end{aligned} \tag{61}$$

where

$$\langle Sg_p \rangle = 0.5 | sign(u_{i,j} - u_{i-1,j}) + sign(u_{i+1,j} - u_{i,j}) |$$

and

$$\langle Sg_n \rangle = 0.5 | sign(u_{i+1,j} - u_{i,j}) + sign(u_{i+2,j} - u_{i+1,j}) |$$

are numerical switches ($\langle Sg/(1-Sg) \rangle$) which toggle the equation terms $\langle on/off \rangle$ or $\langle off/on \rangle$ whether the three neighboring velocities are monotonic or have an inflection or extreme velocity value. If they are monotonic, $\langle Sg_p \rangle$ or $\langle Sg_n \rangle$ equals one, otherwise they equal zero. D_{long} and D_{short} are the nondimensional distances from the cell center to the shifted velocities $u_{i,j}$ and $u_{i+1,j}$, respectively, resulting from the application of the method of characteristics. They are given by

$$D_{long} = \frac{1}{2} + \frac{|u_r| T}{\delta x_{i+1}},$$

and

$$D_{short} = \frac{1}{2} - \frac{|u_r| T}{\delta x_{i+1}}.$$

Reproduced with permission of the copyright owner. Further reproduction prohibited without permission.

Note, using the example depicted in (Fig. 15), if $u_r < 0$, then $\langle Su_r \rangle = -1$ and $\langle Sg_n \rangle = 0$, so $u_R = u_{i+1,j}$. Likewise, the gradient is limited at position $i-1$ when $u_l = 0.5(u_{i-1,j} + u_{i,j}) > 0$ to prevent a new maximum from being introduced by the Taylor expansion.

The momentum flux velocity to the left side of the control volume reads

$$\begin{aligned} u_L = &\left\langle \frac{1+Su_l}{2} \right\rangle \left[\langle Sg_p \rangle \left(u_{i-1,j} D_{long} + u_{i,j} D_{short} \right) + \langle 1 - Sg_p \rangle u_{i-1,j} \right] \\ &+ \left\langle \frac{1-Su_l}{2} \right\rangle \left[\langle Sg_n \rangle \left(u_{i,j} D_{long} + u_{i-1,j} D_{short} \right) + \langle 1 - Sg_n \rangle u_{i,j} \right], \end{aligned} \tag{62}$$

where

$$\begin{aligned} Su_l &= sign(u_l), \\ Sg_p &= 0.5 | sign(u_{i-1,j} - u_{i-2,j}) + sign(u_{i,j} - u_{i-1,j}) |, \\ Sg_n &= 0.5 | sign(u_{i,j} - u_{i-1,j}) + sign(u_{i+1,j} - u_{i,j}) |, \end{aligned}$$

$$\begin{aligned} D_{long} &= \frac{1}{2} + \frac{|u_l| T}{\delta x_i}, \\ D_{short} &= \frac{1}{2} - \frac{|u_l| T}{\delta x_i}. \end{aligned}$$

A similar procedure is employed to determine u_{RT} and u_{RB}. With the help of Fig. 14, then

$$\begin{aligned} u_{RT} = &\left\langle \frac{1+Sv_{rt}}{2} \right\rangle \left[\langle Sg_p \rangle \left(u_{i,j} D_{long} + u_{i,j+1} D_{short} \right) + \langle 1 - Sg_p \rangle u_{i,j} \right] \\ &+ \left\langle \frac{1-Sv_{rt}}{2} \right\rangle \left[\langle Sg_n \rangle \left(u_{i,j+1} D_{long} + u_{i,j} D_{short} \right) + \langle 1 - Sg_n \rangle u_{i,j+1} \right], \end{aligned} \tag{63}$$

where

$$\begin{aligned} v_{rt} &= (v_{i+1,j} \delta x_i + v_{i,j} \delta x_{i+1}) / (\delta x_i + \delta x_{i+1}), \\ Sv_{rt} &= sign(v_{rt}), \end{aligned}$$

$$\begin{aligned} Sg_p &= 0.5 | sign(u_{i,j} - u_{i,j-1}) + sign(u_{i,j+1} - u_{i,j}) |, \\ Sg_n &= 0.5 | sign(u_{i,j+1} - u_{i,j}) + sign(u_{i,j+2} - u_{i,j+1}) |, \end{aligned}$$

Reproduced with permission of the copyright owner. Further reproduction prohibited without permission.

$$
\begin{aligned}
D_{long} &= \frac{1}{2} + \frac{|v_{rt}|T}{\delta y_{top}}, \\
D_{short} &= \frac{1}{2} - \frac{|v_{rt}|T}{\delta y_{top}}
\end{aligned}
$$

and

$$
\begin{aligned}
u_{RB} = &\left\langle \frac{1+Sv_{rb}}{2} \right\rangle \left[\langle Sg_p \rangle \left(u_{i,j-1} D_{long} + u_{i,j} D_{short} \right) + \langle 1 - Sg_p \rangle u_{i,j-1} \right] \\
&+ \left\langle \frac{1-Sv_{rb}}{2} \right\rangle \left[\langle Sg_n \rangle \left(u_{i,j} D_{long} + u_{i,j-1} D_{short} \right) + \langle 1 - Sg_n \rangle u_{i,j} \right],
\end{aligned}
\tag{64}
$$

where

$$
\begin{aligned}
v_{rb} &= (v_{i+1,j-1}\delta x_i + v_{i,j-1}\delta x_{i+1})/(\delta x_i + \delta x_{i+1}), \\
Sv_{rb} &= sign(v_{rb}),
\end{aligned}
$$

$$
\begin{aligned}
Sg_p &= 0.5|sign(u_{i,j-1} - u_{i,j-2}) + sign(u_{i,j} - u_{i,j-1})|, \\
Sg_n &= 0.5|sign(u_{i,j} - u_{i,j-1}) + sign(u_{i,j+1} - u_{i,j})|,
\end{aligned}
$$

$$
\begin{aligned}
D_{long} &= \frac{1}{2} + \frac{|v_{rb}|T}{\delta y_{bot}}, \\
D_{short} &= \frac{1}{2} - \frac{|v_{rb}|T}{\delta y_{bot}}.
\end{aligned}
$$

Now, using the conservative form of Eq. (35) the advective term in the y-momentum equation is

$$
\left(\frac{\partial uv}{\partial x} + \frac{\partial vv}{\partial y} \right)^m.
$$

The equivalent finite difference equation for each term is

$$
\frac{\partial uv}{\partial x} \approx \frac{v_{RT}u_{rt} - v_{LT}u_{lt}}{\delta x_i}
$$

and

$$
\frac{\partial vv}{\partial y} \approx \frac{v_T v_t - v_B v_b}{\delta y_{top}},
$$

Reproduced with permission of the copyright owner. Further reproduction prohibited without permission.

respectively.

Using the control volume depicted in Fig. 16, the flux momentum velocity v_T is obtained as follows

$$v_T = \left\langle \frac{1+Sv_t}{2} \right\rangle \left[\langle Sg_p \rangle \left(v_{i,j}(\frac{1}{2} + \frac{|v_t|T}{\delta y_{j+1}}) + v_{i,j+1}(\frac{1}{2} - \frac{|v_t|T}{\delta y_{j+1}}) \right) + \langle 1 - Sg_p \rangle v_{i,j} \right] + \left\langle \frac{1-Sv_t}{2} \right\rangle \left[\langle Sg_n \rangle \left(v_{i,j+1}(\frac{1}{2} + \frac{|v_t|T}{\delta y_{j+1}}) + v_{i,j}(\frac{1}{2} - \frac{|v_t|T}{\delta y_{j+1}}) \right) + \langle 1 - Sg_n \rangle v_{i,j+1} \right], \tag{65}$$

where

$$\begin{aligned} v_t &= 0.5(v_{i,j} + v_{i,j+1}), \\ Sv_t &= sign(v_t), \end{aligned}$$

$$\begin{aligned} Sg_p &= 0.5|sign(v_{i,j} - v_{i,j-1}) + sign(v_{i,j+1} - v_{i,j})|, \\ Sg_n &= 0.5|sign(v_{i,j+1} - v_{i,j}) + sign(v_{i,j+2} - v_{i,j+1})|. \end{aligned}$$

Terms v_B, v_{RT} and v_{LT} are determined in the same manner as the previous one, then

$$v_B = \left\langle \frac{1+Sv_b}{2} \right\rangle \left[\langle Sg_p \rangle \left(v_{i,j-1} D_{long} + v_{i,j} D_{short} \right) + \langle 1 - Sg_p \rangle v_{i,j-1} \right] + \left\langle \frac{1-Sv_b}{2} \right\rangle \left[\langle Sg_n \rangle \left(v_{i,j} D_{long} + v_{i,j-1} D_{short} \right) + \langle 1 - Sg_n \rangle v_{i,j} \right], \tag{66}$$

where

$$\begin{aligned} v_b &= 0.5(v_{i,j-1} + v_{i,j}), \\ Sv_b &= sign(v_b), \end{aligned}$$

$$\begin{aligned} Sg_p &= 0.5|sign(v_{i,j-1} - v_{i,j-2}) + sign(v_{i,j} - v_{i,j-1})|, \\ Sg_n &= 0.5|sign(v_{i,j} - v_{i,j-1}) + sign(v_{i,j+1} - v_{i,j})|, \end{aligned}$$

Reproduced with permission of the copyright owner. Further reproduction prohibited without permission.

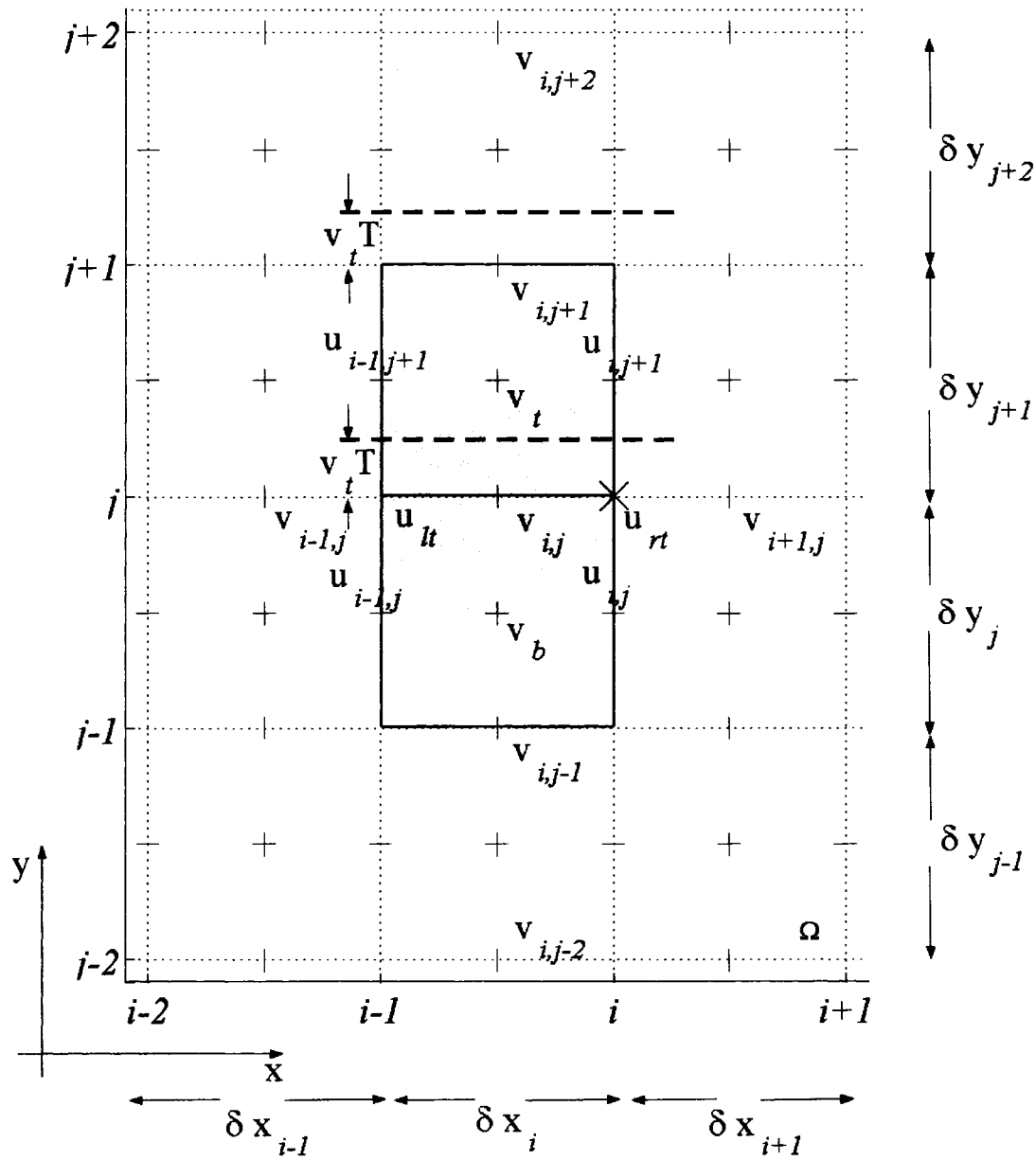

Figure 16: Momentum control volume for the $y-$momentum using the method of characteristics, assuming $v_t > 0$ and advection time step equal to $T/2$. Flux velocities at the momentum control volume boundaries are obtained from interpolation of neighboring fluid velocities.

Reproduced with permission of the copyright owner. Further reproduction prohibited without permission.

$$D_{long} = \frac{1}{2} + \frac{|v_b|T}{\delta y_j},$$
$$D_{short} = \frac{1}{2} - \frac{|v_b|T}{\delta y_j};$$

$$\begin{aligned} v_{RT} = &\left\langle \frac{1+Su_{rt}}{2} \right\rangle \left[\langle Sg_p \rangle \left(v_{i,j} D_{long} + v_{i+1,j} D_{short} \right) + \langle 1 - Sg_p \rangle v_{i,j} \right] \\ &+ \left\langle \frac{1-Su_{rt}}{2} \right\rangle \left[\langle Sg_n \rangle \left(v_{i+1,j} D_{long} + v_{i,j} D_{short} \right) + \langle 1 - Sg_n \rangle v_{i+1,j} \right], \end{aligned} \tag{67}$$

where

$$\begin{aligned} u_{rt} &= (u_{i,j+1}\delta y_j + u_{i,j}\delta y_{j+1})/(\delta y_j + \delta y_{j+1}), \\ Su_{rt} &= sign(u_{rt}), \end{aligned}$$

$$\begin{aligned} Sg_p &= 0.5|sign(v_{i,j} - v_{i-1,j}) + sign(v_{i+1,j} - v_{i,j})|, \\ Sg_n &= 0.5|sign(v_{i+1,j} - v_{i,j}) + sign(v_{i+2,j} - v_{i+1,j})|, \end{aligned}$$

$$\begin{aligned} D_{long} &= \frac{1}{2} + \frac{|u_{rt}|T}{\delta x_{right}}, \\ D_{short} &= \frac{1}{2} - \frac{|u_{rt}|T}{\delta x_{right}} \end{aligned}$$

and

$$\begin{aligned} v_{LT} = &\left\langle \frac{1+Su_{lt}}{2} \right\rangle \left[\langle Sg_p \rangle \left(v_{i-1,j} D_{long} + v_{i,j} D_{short} \right) + \langle 1 - Sg_p \rangle v_{i-1,j} \right] \\ &+ \left\langle \frac{1-Su_{lt}}{2} \right\rangle \left[\langle Sg_n \rangle \left(v_{i,j} D_{long} + v_{i-1,j} D_{short} \right) + \langle 1 - Sg_n \rangle v_{i,j} \right], \end{aligned} \tag{68}$$

where

$$\begin{aligned} u_{lt} &= (u_{i-1,j+1}\delta y_j + u_{i-1,j}\delta y_{j+1})/(\delta y_j + \delta y_{j+1}), \\ Su_{lt} &= sign(u_{lt}), \end{aligned}$$

$$\begin{aligned} Sg_p &= 0.5|sign(v_{i-1,j} - v_{i-2,j}) + sign(v_{i,j} - v_{i-1,j})|, \\ Sg_n &= 0.5|sign(v_{i,j} - v_{i-1,j}) + sign(v_{i+1,j} - v_{i,j})|, \end{aligned}$$

Reproduced with permission of the copyright owner. Further reproduction prohibited without permission.

$$D_{long} = \frac{1}{2} + \frac{|u_{lt}|T}{\delta x_{left}},$$
$$D_{short} = \frac{1}{2} - \frac{|u_{lt}|T}{\delta x_{left}}.$$

Similar methods of limiting gradient have been implemented in the CAVEAT fluid dynamic code (Addessio *et al.*, 1986) and RIPPLE (Kothe *et al.*, 1991), which are slightly different from van Leer's original prescription. Stronger monotonicity constraints on the first order derivative in the Taylor expansion have been devised in Amsden, O'Rourke & Butler (1989) as well.

In summary, with van Leer's limiter the velocity gradient is forced to zero at the position where the velocity is a local maximum or minimum. The velocity gradient is limited at that position to prevent a new maximum from being introduced by the Taylor expansion. The method of characteristics together with van Leer's limiter is second order accurate in those cells where gradients are not limited, but prevents unstable oscillations by forcing monotonicity in the expansion about upstream points. On the other hand, the backward/forward approximation is diffusive since the momentum flux velocity is overestimated. The centered difference approximation is second order accurate, but leads to unstable zone-to-zone oscillations.

2.6.3.2.1.3 Third order accurate method. The finite difference form of the nonconservative advective terms of Eqs. (34) and (35) are derived using the third order accurate upstream/downstream scheme (Lemos, 1996). The solution is based on four points, including the point (i,j), two upstream points and one downstream point. The advective term in nonconservative form of the x-momentum equation (Eq. 34) reads

$$\left(u\frac{\partial u}{\partial x} + v\frac{\partial u}{\partial y}\right)^m,$$

Reproduced with permission of the copyright owner. Further reproduction prohibited without permission.

and it is discretized in space with the help of Fig. 12. The first term of the previous equation is discretized as follows:

if $u_{i,j} \geq 0$ then

$$\begin{aligned} u\frac{\partial u}{\partial x} \approx u_{i,j} \Bigg[& \left(\frac{\delta x_i(\delta x_{i-1} + \delta x_i)}{\delta x_{i+1}(\delta x_i + \delta x_{i+1})(\delta x_{i-1} + \delta x_i + \delta x_{i+1})} \right) u_{i+1,j} \\ & + \left(\frac{(\delta x_{i+1} - \delta x_i)(\delta x_{i-1} + \delta x_i) + \delta x_i \delta x_{i+1}}{\delta x_i \delta x_{i+1}(\delta x_{i-1} + \delta x_i)} \right) u_{i,j} \\ & - \left(\frac{\delta x_{i+1}(\delta x_{i-1} + \delta x_i)}{\delta x_{i-1}\delta x_i(\delta x_i + \delta x_{i+1})} \right) u_{i-1,j} \\ & + \left(\frac{\delta x_i \delta x_{i+1}}{\delta x_{i-1}(\delta x_{i-1} + \delta x_i)(\delta x_{i-1} + \delta x_i + \delta x_{i+1})} \right) u_{i-2,j} \Bigg] ; \end{aligned} \tag{69}$$

if $u_{i,j} < 0$ then

$$\begin{aligned} u\frac{\partial u}{\partial x} \approx u_{i,j} \Bigg[& - \left(\frac{\delta x_{i+1}(\delta x_{i+1} + \delta x_{i+2})}{\delta x_i(\delta x_i + \delta x_{i+1})(\delta x_i + \delta x_{i+1} + \delta x_{i+2})} \right) u_{i-1,j} \\ & - \left(\frac{(\delta x_i - \delta x_{i+1})(\delta x_{i+1} + \delta x_{i+2}) + \delta x_i \delta x_{i+1}}{\delta x_i \delta x_{i+1}(\delta x_{i+1} + \delta x_{i+2})} \right) u_{i,j} \\ & + \left(\frac{\delta x_i(\delta x_{i+1} + \delta x_{i+2})}{\delta x_{i+1}\delta x_{i+2}(\delta x_i + \delta x_{i+1})} \right) u_{i+1,j} \\ & - \left(\frac{\delta x_i \delta x_{i+1}}{\delta x_{i+2}(\delta x_{i+1} + \delta x_{i+2})(\delta x_i + \delta x_{i+1} + \delta x_{i+2})} \right) u_{i+2,j} \Bigg] . \end{aligned} \tag{70}$$

The finite difference of the second term of the advective term reads:

if $v_{avg} \geq 0$ then

$$\begin{aligned} v\frac{\partial u}{\partial y} \approx v_{avg} \Bigg[& \left(\frac{\delta y_{bot}(\delta y_{bbot} + \delta y_{bot})}{\delta y_{top}(\delta y_{bot} + \delta y_{top})(\delta y_{bbot} + \delta y_{bot} + \delta y_{top})} \right) u_{i,j+1} \\ & + \left(\frac{(\delta y_{top} - \delta y_{bot})(\delta y_{bbot} + \delta y_{bot}) + \delta y_{bot}\delta y_{top}}{\delta y_{bot}\delta y_{top}(\delta y_{bbot} + \delta y_{bot})} \right) u_{i,j} \\ & - \left(\frac{\delta y_{top}(\delta y_{bbot} + \delta y_{bot})}{\delta y_{bbot}\delta y_{bot}(\delta y_{bot} + \delta y_{top})} \right) u_{i,j-1} \\ & + \left(\frac{\delta y_{bot}\delta y_{top}}{\delta y_{bbot}(\delta y_{bbot} + \delta y_{bot})(\delta y_{bbot} + \delta y_{bot} + \delta y_{top})} \right) u_{i,j-2} \Bigg] , \end{aligned} \tag{71}$$

where $\delta y_{bbot} = 0.5(\delta y_{j-2} + \delta y_{j-1})$;

Reproduced with permission of the copyright owner. Further reproduction prohibited without permission.

if $v_{avg} < 0$ then

$$
\begin{aligned}
v\frac{\partial u}{\partial y} \approx v_{avg}\Bigg[& -\left(\frac{\delta y_{top}(\delta y_{top}+\delta y_{ttop})}{\delta y_{bot}(\delta y_{bot}+\delta y_{top})(\delta y_{bot}+\delta y_{top}+\delta y_{ttop})}\right) u_{i,j-1} \\
& -\left(\frac{(\delta y_{bot}-\delta y_{top})(\delta y_{top}+\delta y_{ttop})+\delta y_{bot}\delta y_{top}}{\delta y_{bot}\delta y_{top}(\delta y_{top}+\delta y_{ttop})}\right) u_{i,j} \\
& +\left(\frac{\delta y_{bot}(\delta y_{top}+\delta y_{ttop})}{\delta y_{top}\delta y_{ttop}(\delta y_{bot}+\delta y_{top})}\right) u_{i,j+1} \\
& -\left(\frac{\delta y_{bot}\delta y_{top}}{\delta y_{ttop}(\delta y_{top}+\delta y_{ttop})(\delta y_{bot}+\delta y_{top}+\delta y_{ttop})}\right) u_{i,j+2}\Bigg],
\end{aligned}
\tag{72}
$$

where $\delta y_{ttop} = 0.5(\delta y_{j+1} + \delta y_{j+2})$.

The advective term in nonconservative from for the y-momentum equation (Eq. 34) reads

$$
\left(u\frac{\partial v}{\partial x} + v\frac{\partial v}{\partial y}\right)^m.
$$

The first term is discretized as:

if $u_{avg} \geq 0$ then

$$
\begin{aligned}
u\frac{\partial v}{\partial x} \approx u_{avg}\Bigg[& \left(\frac{\delta x_{left}(\delta x_{lleft}+\delta x_{left})}{\delta x_{right}(\delta x_{left}+\delta x_{right})(\delta x_{lleft}+\delta x_{left}+\delta x_{right})}\right) v_{i+1,j} \\
& +\left(\frac{(\delta x_{right}-\delta x_{left})(\delta x_{lleft}+\delta x_{left})+\delta x_{left}\delta x_{right}}{\delta x_{left}\delta x_{right}(\delta x_{lleft}+\delta x_{left})}\right) v_{i,j} \\
& -\left(\frac{\delta x_{right}(\delta x_{lleft}+\delta x_{left})}{\delta x_{lleft}\delta x_{left}(\delta x_{left}+\delta x_{right})}\right) v_{i-1,j} \\
& +\left(\frac{\delta x_{left}\delta x_{right}}{\delta x_{lleft}(\delta x_{lleft}+\delta x_{left})(\delta x_{lleft}+\delta x_{left}+\delta x_{right})}\right) v_{i-2,j}\Bigg],
\end{aligned}
\tag{73}
$$

where $\delta x_{lleft} = 0.5(\delta x_{j-2} + \delta x_{j-1})$;

if $u_{avg} < 0$ then

$$
\begin{aligned}
u\frac{\partial v}{\partial x} \approx u_{avg}\Bigg[& -\left(\frac{\delta x_{right}(\delta x_{right}+\delta x_{rright})}{\delta x_{left}(\delta x_{left}+\delta x_{right})(\delta x_{left}+\delta x_{right}+\delta x_{rright})}\right) v_{i-1,j} \\
& -\left(\frac{(\delta x_{left}-\delta x_{right})(\delta x_{right}+\delta x_{rright})+\delta x_{left}\delta x_{right}}{\delta x_{left}\delta x_{right}(\delta x_{right}+\delta x_{rright})}\right) v_{i,j} \\
& +\left(\frac{\delta x_{left}(\delta x_{right}+\delta x_{rright})}{\delta x_{right}\delta x_{rright}(\delta x_{left}+\delta x_{right})}\right) v_{i+1,j} \\
& -\left(\frac{\delta x_{left}\delta x_{right}}{\delta x_{rright}(\delta x_{right}+\delta x_{rright})(\delta x_{left}+\delta x_{right}+\delta x_{rright})}\right) v_{i+2,j}\Bigg],
\end{aligned}
\tag{74}
$$

Reproduced with permission of the copyright owner. Further reproduction prohibited without permission.

where $\delta x_{rright} = 0.5(\delta x_{j+1} + \delta x_{j+2})$.

The finite difference of the second term of y-momentum of the advective term reads:

if $v_{i,j} \geq 0$ then

$$
\begin{aligned}
v\frac{\partial v}{\partial y} \approx v_{i,j} \Bigg[& \left(\frac{\delta y_j(\delta y_{j-1} + \delta y_j)}{\delta y_{j+1}(\delta y_j + \delta y_{j+1})(\delta y_{j-1} + \delta y_j + \delta y_{j+1})} \right) v_{i,j+1} \\
& + \left(\frac{(\delta y_{j+1} - \delta y_j)(\delta y_{j-1} + \delta y_j) + \delta y_j \delta y_{j+1}}{\delta y_j \delta y_{j+1}(\delta y_{j-1} + \delta y_j)} \right) v_{i,j} \\
& - \left(\frac{\delta y_{j+1}(\delta y_{j-1} + \delta y_j)}{\delta y_{j-1}\delta y_j(\delta y_j + \delta y_{j+1})} \right) v_{i,j-1} \\
& + \left(\frac{\delta y_j \delta y_{j+1}}{\delta y_{j-1}(\delta y_{j-1} + \delta y_j)(\delta y_{j-1} + \delta y_j + \delta y_{j+1})} \right) v_{i,j-2} \Bigg] ;
\end{aligned}
\tag{75}
$$

if $v_{i,j} < 0$ then

$$
\begin{aligned}
v\frac{\partial v}{\partial y} \approx v_{i,j} \Bigg[& - \left(\frac{\delta y_{j+1}(\delta y_{j+1} + \delta y_{j+2})}{\delta y_j(\delta y_j + \delta y_{j+1})(\delta y_j + \delta y_{j+1} + \delta y_{j+2})} \right) v_{i,j-1} \\
& - \left(\frac{(\delta y_j - \delta y_{j+1})(\delta y_{j+1} + \delta y_{j+2}) + \delta y_j \delta y_{j+1}}{\delta y_j \delta y_{j+1}(\delta y_{j+1} + \delta y_{j+2})} \right) v_{i,j} \\
& + \left(\frac{\delta y_j(\delta y_{j+1} + \delta y_{j+2})}{\delta y_{j+1}\delta y_{j+2}(\delta y_j + \delta y_{j+1})} \right) v_{j,j+1} \\
& - \left(\frac{\delta y_j \delta y_{j+1}}{\delta y_{j+2}(\delta y_{j+1} + \delta y_{j+2})(\delta y_j + \delta y_{j+1} + \delta y_{j+2})} \right) v_{i,j+2} \Bigg] .
\end{aligned}
\tag{76}
$$

Application of third order accurate approximation is restricted close to the water-air interface and internal obstacle boundaries. Velocity values are not available beyond the fluid domain. Therefore, when computing the approximation for the advective term at a given point, i.e, (i,j), it is necessary to verify whether the required velocities stated in the numerical formulation belong to a void region or an internal obstacle. If one of these conditions holds, then a lower-order differencing is used instead. The third order accurate approximation is much less diffusive than the backward/forward approximation and much more stable than the centered difference approximation. However, the method requires higher spacial and temporal resolution than its coun-

Reproduced with permission of the copyright owner. Further reproduction prohibited without permission.

terparts. Third order schemes offer higher accuracy when spacing is sufficiently fine, but they are more difficult to use.

2.6.3.2.2 Turbulence. Real turbulent flows are inherently three-dimensional, even when the propagation is in one direction. When turbulence cascades occur, there is always energy fed in the cross-stream direction. In numerical modeling, the dissipation mechanisms inherent to the numerical method may alone be sufficient to produce reasonable results on turbulent processes. Since it is expected turbulence will be transient (short duration) in all model setups used in this study, the turbulence model has not been incorporated. In other cases it may be necessary to supply additional dissipation with a simple turbulent model, such as a constant eddy viscosity or a mixing length assumption. Therefore, the model presented in this study should be advanced to consider this phenomena. Unfortunately, there is no simple mechanism to answer this question and the modeler must exercise some engineering judgment. For instance, a large eddy simulation (LES) with an appropriate classical Smagorinsky model or subgrid scale (SGS) model could be an option (Wu, 2004). Most models of turbulence are designed to approximate a smoothed out or time averaged effect of turbulence. An exception is the LES model. The idea behind this model is that computations should be directly capable of modeling all the fluctuating details of a turbulent flow except for those too small to be resolved by the grid. The unresolved eddies are then treated by approximating their effect using a local eddy viscosity. Generally, this eddy viscosity is made proportional to the local grid size and some measure of the local flow velocity, such as the magnitude of the rate of strain.

In this study the laminar dissipation is included through the molecular viscosity. Nevertheless, in all model setups, viscous effect and bed friction have been neglected. This assumption mostly aims to identify model inherent numerical dissipation.

Reproduced with permission of the copyright owner. Further reproduction prohibited without permission.

2.6.3.2.3 Frictional terms discretization. The fluid is assumed to be Newtonian. Viscous forces are incorporated into the predictor estimate using old time (t^m) velocity field values, see Eq. (24). Recalling Eq. (8) and using Eqs. (34) and (35) the viscous term is expressed in its horizontal and vertical components as follows

$$\frac{1}{\rho}\nabla\cdot\tau=\frac{1}{\rho^m}\left[\left(\frac{\partial\tau_{xx}}{\partial x}+\frac{\partial\tau_{xy}}{\partial y}\right)^m\hat{\mathbf{i}}+\left(\frac{\partial\tau_{xy}}{\partial x}+\frac{\partial\tau_{yy}}{\partial y}\right)^m\hat{\mathbf{j}}\right]. \tag{77}$$

The finite difference expression of Eq. (77) is simplified when diagonal components τ_{xx} and τ_{yy} of the viscous stress are located in the cell centers, and the off-diagonal component $\tau_{xy}(=\tau_{yx})$ is located at vertices as shown in Fig. 17. Using this configuration for the location of viscous variables, the viscous forces are centered appropriately in the momentum control volume. The x-component of Eq. (77) is evaluated at the horizontal velocity location $u_{i,j}$ as

$$\frac{1}{\rho}\left(\frac{\partial\tau_{xx}}{\partial x}+\frac{\partial\tau_{xy}}{\partial y}\right)\approx\frac{1}{\rho}\left(\frac{\tau_{xxi+1,j}-\tau_{xxi,j}}{0.5(\delta x_i+\delta x_{i+1})}+\frac{\tau_{xy_{i,j}}-\tau_{xy_{i,j-1}}}{\delta y_j}\right) \tag{78}$$

where

$$\tau_{xxi,j}\approx 2\mu\left(\frac{u_{i,j}-u_{i-1,j}}{\delta x_i}\right),$$

$$\tau_{xxi+1,j}\approx 2\mu\left(\frac{u_{i+1,j}-u_{i,j}}{\delta x_{i+1}}\right),$$

$$\tau_{xy_{i,j}}\approx\mu\left(\frac{u_{i,j+1}-u_{i,j}}{0.5(\delta y_j+\delta y_{j+1})}+\frac{v_{i+1,j}-v_{i,j}}{0.5(\delta x_i+\delta x_{i+1})}\right),$$

and

$$\tau_{xy_{i,j-1}}\approx\mu\left(\frac{u_{i,j}-u_{i,j-1}}{0.5(\delta y_{j-1}+\delta y_j)}+\frac{v_{i+1,j-1}-v_{i,j-1}}{0.5(\delta x_i+\delta x_{i+1})}\right).$$

The y-component, second term of Eq. (77), is evaluated at the vertical velocity location $v_{i,j}$ as

$$\frac{1}{\rho}\left(\frac{\partial\tau_{xy}}{\partial x}+\frac{\partial\tau_{yy}}{\partial y}\right)\approx\frac{1}{\rho}\left(\frac{\tau_{xy_{i,j}}-\tau_{xy_{i-1,j}}}{\delta x_i}+\frac{\tau_{yy_{i,j+1}}-\tau_{yy_{i,j}}}{0.5(\delta y_j+\delta y_{j+1})}\right) \tag{79}$$

Reproduced with permission of the copyright owner. Further reproduction prohibited without permission.

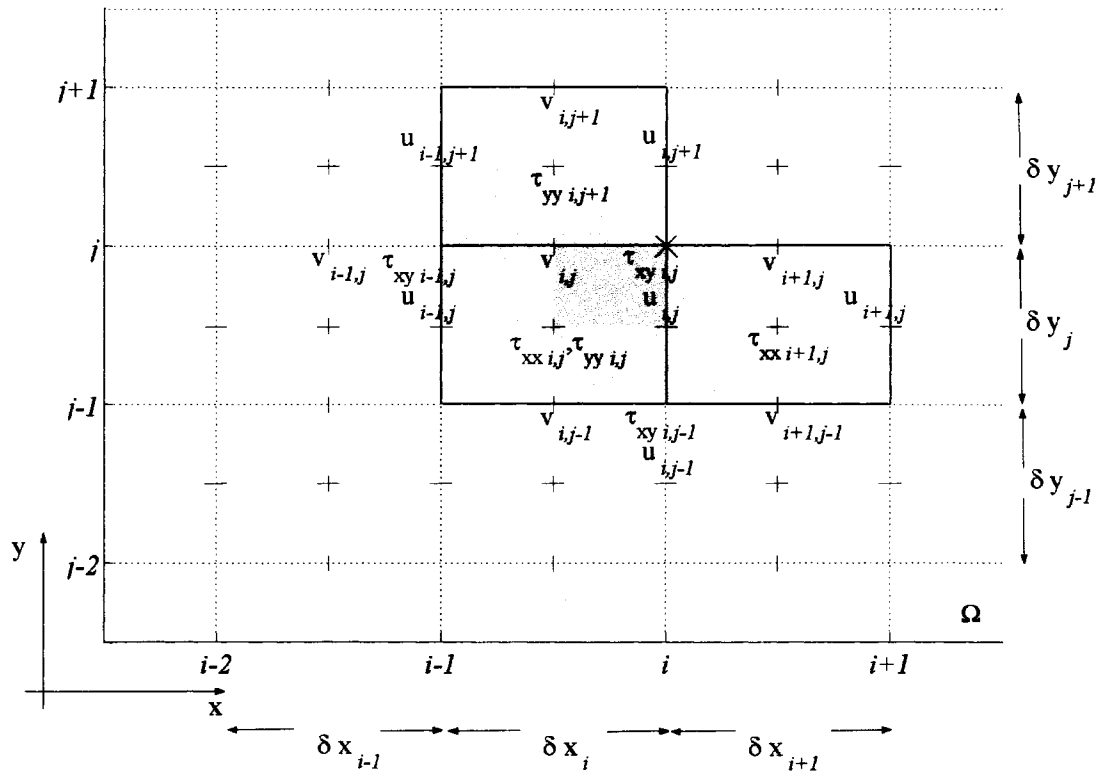

Figure 17: Location of viscous stresses in the momentum control volume.

where

$$\tau_{yy_{i,j}} \approx 2\mu \left(\frac{v_{i,j} - v_{i,j-1}}{\delta y_j} \right),$$

$$\tau_{yy_{i,j+1}} \approx 2\mu \left(\frac{v_{i,j+1} - v_{i,j}}{\delta y_{j+1}} \right)$$

and

$$\tau_{xy_{i-1,j}} \approx \mu \left(\frac{u_{i-1,j+1} - u_{i-1,j}}{0.5(\delta y_j + \delta y_{j+1})} + \frac{v_{i,j} - v_{i-1,j}}{0.5(\delta x_{i-1} + \delta x_i)} \right).$$

This explicit treatment of the frictional term is therefore subject to a linear stability time step constraint which is discussed in Section 2.9.

Reproduced with permission of the copyright owner. Further reproduction prohibited without permission.

2.6.4 Calculation of intermediate velocities

Once advective and frictional terms are available, the intermediate velocities $\tilde{u}_{i,j}$ and $\tilde{v}_{i,j}$ can be determined using the predictor estimate of the two-fractional-steps projection method which is based on the old time (t^m) velocity field values. From Eq. (24) the intermediate velocities are given by:

$$\tilde{u}_{i,j} = u^m_{i,j} + T\left[g_x - \left(u\frac{\partial u}{\partial x}\right)^m_{i,j} - \left(v\frac{\partial u}{\partial y}\right)^m_{i,j} + \frac{1}{\rho}\left(\frac{\partial \tau_{xx}}{\partial x} + \frac{\partial \tau_{xy}}{\partial y}\right)^m_{i,j}\right] \tag{80}$$

for the x-direction, and

$$\tilde{v}_{i,j} = v^m_{i,j} + T\left[g_y - \left(u\frac{\partial v}{\partial x}\right)^m_{i,j} - \left(v\frac{\partial v}{\partial y}\right)^m_{i,j} + \frac{1}{\rho}\left(\frac{\partial \tau_{xy}}{\partial x} + \frac{\partial \tau_{yy}}{\partial y}\right)^m_{i,j}\right] \tag{81}$$

for the y-direction. In tsunami calculations usually $g_x = 0$, and $g_y = -9.80$ m s^{-2}. Note that advective terms in previous equations are in nonconservative form. Eqs. (80) and (81) are modified to account for the moving object according to Eq. (30) thus

$$\begin{aligned}\tilde{u}_{i,j} = {} & u^m_{i,j}\left(1 - \frac{A_{C^m_{i,j}} - A_{C^{m-1}_{i,j}}}{A_{Cs\ i,j}}\right) \\ & + T\left[g_x - \left(\frac{\partial uu}{\partial x}\right)^m_{i,j} - \left(\frac{\partial uv}{\partial y}\right)^m_{i,j} + \frac{1}{\rho}\left(\frac{\partial \tau_{xx}}{\partial x} + \frac{\partial \tau_{xy}}{\partial y}\right)^m_{i,j}\right]\end{aligned} \tag{82}$$

and

$$\begin{aligned}\tilde{v}_{i,j} = {} & v^m_{i,j}\left(1 - \frac{A_{C^m_{i,j}} - A_{C^{m-1}_{i,j}}}{A_{Cs\ i,j}}\right) \\ & + T\left[g_y - \left(\frac{\partial uv}{\partial x}\right)^m_{i,j} - \left(\frac{\partial vv}{\partial y}\right)^m_{i,j} + \frac{1}{\rho}\left(\frac{\partial \tau_{xy}}{\partial x} + \frac{\partial \tau_{yy}}{\partial y}\right)^m_{i,j}\right],\end{aligned} \tag{83}$$

respectively. If the method of characteristcs is used to solve advective terms, then determination of the advective terms in Eqs. (82 and 83) are broken down into two separate calculations, each with an advection time $T/2$, see Section 2.6.3.

Reproduced with permission of the copyright owner. Further reproduction prohibited without permission.

2.6.5 The pressure Poisson equation (PPE)

The divergence operator in Eq. (26) or Eq. (31) is simplified by mapping physical coordinates (x,y) into natural coordinates (ξ, ζ), which are linear quadrilaterals of unit length. In (ξ, ζ) space, the operator becomes (see Brackbill & Saltzman, 1982)

$$\begin{aligned}\nabla \cdot \left[\frac{1}{\rho^m}\nabla p^{m+1}\right] =& \frac{1}{J}\left[\left(\frac{\alpha_o}{\rho}\right)\frac{\partial p^{m+1}}{\partial \xi} - \left(\frac{\beta_o}{\rho}\right)\frac{\partial p^{m+1}}{\partial \zeta}\right]_\xi \\ &+\frac{1}{J}\left[\left(\frac{\gamma_o}{\rho}\right)\frac{\partial p^{m+1}}{\partial \zeta} - \left(\frac{\beta_o}{\rho}\right)\frac{\partial p^{m+1}}{\partial \xi}\right]_\zeta\end{aligned} \tag{84}$$

where J is the Jacobian determinant of the transformation

$$J = \left|\frac{\partial(x,y)}{\partial(\xi,\zeta)}\right| = \begin{vmatrix} \frac{\partial x}{\partial \xi} & \frac{\partial x}{\partial \zeta} \\ \frac{\partial y}{\partial \xi} & \frac{\partial y}{\partial \zeta} \end{vmatrix} = \frac{\partial x}{\partial \xi}\frac{\partial y}{\partial \zeta} - \frac{\partial x}{\partial \zeta}\frac{\partial y}{\partial \xi}, \tag{85}$$

and the geometric coefficients α_o, β_o and γ_o are defined by

$$\begin{aligned}\alpha_o =& \frac{1}{J}\left[\left(\frac{\partial x}{\partial \zeta}\right)^2 + \left(\frac{\partial y}{\partial \zeta}\right)^2\right], \\ \beta_o =& \frac{1}{J}\left[\frac{\partial x}{\partial \xi}\frac{\partial x}{\partial \zeta} + \frac{\partial y}{\partial \xi}\frac{\partial y}{\partial \zeta}\right], \\ \gamma_o =& \frac{1}{J}\left[\left(\frac{\partial x}{\partial \xi}\right)^2 + \left(\frac{\partial y}{\partial \xi}\right)^2\right].\end{aligned} \tag{86}$$

The partial derivatives of $\mathbf{x}$ are given by

$$\left.\frac{\partial \mathbf{x}}{\partial \xi}\right|_{i,j} = \left.\frac{\partial x}{\partial \xi}\hat{\mathbf{i}} + \frac{\partial y}{\partial \xi}\hat{\mathbf{j}}\right|_{i,j}, \qquad \left.\frac{\partial \mathbf{x}}{\partial \zeta}\right|_{i,j} = \left.\frac{\partial x}{\partial \zeta}\hat{\mathbf{i}} + \frac{\partial y}{\partial \zeta}\hat{\mathbf{j}}\right|_{i,j},$$

where

$$\left.\frac{\partial x}{\partial \xi}\right|_{i,j} = x_i - x_{i-1} = \delta x_i, \qquad \left.\frac{\partial x}{\partial \zeta}\right|_{i,j} = 0 \tag{87}$$

and

$$\left.\frac{\partial y}{\partial \zeta}\right|_{i,j} = y_j - y_{j-1} = \delta y_j, \qquad \left.\frac{\partial y}{\partial \xi}\right|_{i,j} = 0. \tag{88}$$

The partial derivative $\partial x/\partial \zeta$ and $\partial y/\partial \xi$ are zero because the mesh is orthogonal. Substitution of Eqs. (87) and (88) into Eqs. (85) and (86) gives

$$\alpha_{oi,j} = \left.\frac{(\partial y/\partial \zeta)^2}{J}\right|_{i,j} = \frac{\delta y_j}{\delta x_i}, \quad \beta_{oi,j} = 0, \quad \gamma_{oi,j} = \left.\frac{(\partial x/\partial \xi)^2}{J}\right|_{i,j} = \frac{\delta x_i}{\delta y_j},$$

Reproduced with permission of the copyright owner. Further reproduction prohibited without permission.

for the geometric coefficients, and

$$J_{i,j} = \left.\frac{\partial x}{\partial \xi}\frac{\partial y}{\partial \zeta}\right|_{i,j} = \delta x_i \delta y_j$$

for the Jacobian. Pressure and density are located at the cell center (Fig. 18), therefore geometric coefficients and Jacobian are located at the cell center as well. Note, the

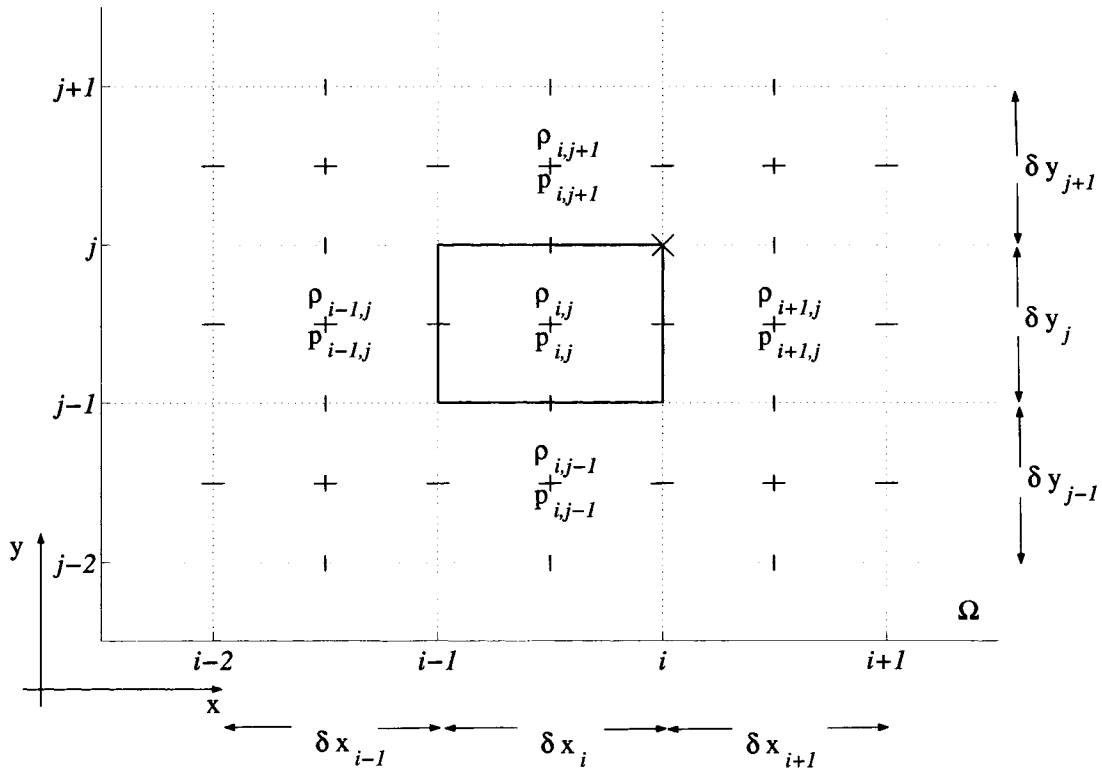

Figure 18: Location of pressure and density in a computational cell.

Jacobian equals the total cell volume. The net flux in cell (i,j) is found from Eq. (84) by differencing cell face quantities, giving

$$\begin{aligned}\frac{1}{J}\left[\frac{\alpha_o}{\rho}\frac{\partial p^{m+1}}{\partial \xi} - \frac{\beta_o}{\rho}\frac{\partial p^{m+1}}{\partial \zeta}\right]_{\xi i,j} = &\frac{1}{J}\left[\frac{\alpha_o}{\rho}\frac{\partial p^{m+1}}{\partial \xi} - \frac{\beta_o}{\rho}\frac{\partial p^{m+1}}{\partial \zeta}\right]_{right} \\ &-\frac{1}{J}\left[\frac{\alpha_o}{\rho}\frac{\partial p^{m+1}}{\partial \xi} - \frac{\beta_o}{\rho}\frac{\partial p^{m+1}}{\partial \zeta}\right]_{left}\end{aligned} \tag{89}$$

Reproduced with permission of the copyright owner. Further reproduction prohibited without permission.

for the ξ-derivative, and

$$\frac{1}{J}\left[\frac{\gamma_o}{\rho}\frac{\partial p^{m+1}}{\partial \zeta} - \frac{\beta_o}{\rho}\frac{\partial p^{m+1}}{\partial \xi}\right]_{\zeta i,j} = \frac{1}{J}\left[\frac{\gamma_o}{\rho}\frac{\partial p^{m+1}}{\partial \zeta} - \frac{\beta_o}{\rho}\frac{\partial p^{m+1}}{\partial \xi}\right]_{top} - \frac{1}{J}\left[\frac{\gamma_o}{\rho}\frac{\partial p^{m+1}}{\partial \zeta} - \frac{\beta_o}{\rho}\frac{\partial p^{m+1}}{\partial \xi}\right]_{bot} \tag{90}$$

for the ζ-derivative.

Although ρ is constant everywhere in the fluid, it is retained inside the divergence operator because a pressure solution is needed within the free surface transition region where $\nabla\rho \neq 0$. This ratio is expressed within the free surface as a quotient of two averages rather than an average of two quotients, thereby keeping the principal contribution within the free surface region rather than at the edge near the void. This form of averaging gives better results in practice, introducing very small errors only when the mesh is nonuniform. The α_o/ρ and γ_o/ρ ratios at the cell faces are estimated by

$$\begin{aligned}
[\alpha_o/\rho]_{right} &= 0.5(\alpha_{oi+1,j} + \alpha_{oi,j})/\left(\frac{\delta x_i \rho_{i+1,j} + \delta x_{i+1,j}\rho_{i,j}}{\delta x_i + \delta x_{i+1}}\right), \\
[\alpha_o/\rho]_{left} &= 0.5(\alpha_{oi-1,j} + \alpha_{oi,j})/\left(\frac{\delta x_{i-1} \rho_{i,j} + \delta x_{i,j}\rho_{i-1,j}}{\delta x_{i-1} + \delta x_i}\right), \\
[\gamma_o/\rho]_{top} &= 0.5(\gamma_{oi,j+1} + \gamma_{oi,j})/\left(\frac{\delta y_j \rho_{i,j+1} + \delta y_{i,j+1}\rho_{i,j}}{\delta y_j + \delta y_{j+1}}\right), \\
[\gamma_o/\rho]_{bot} &= 0.5(\gamma_{oi,j-1} + \gamma_{oi,j})/\left(\frac{\delta y_{j-1} \rho_{i,j} + \delta y_{i,j}\rho_{i,j-1}}{\delta y_{j-1} + \delta y_j}\right).
\end{aligned} \tag{91}$$

Therefore, special attention must be paid to the cell face values of the ratio of a geometric coefficient to the fluid density, i.e. α_o/ρ, in cell within an obstacle, a void or the free surface. In the fluid, ρ is of course a constant, so α_o/ρ becomes an average of α_o only. Singularities are avoided in void and obstacle cells (where ρ is zero and undefined) by setting this ratio equal to a very large number. Void and obstacle cells are internal Dirichlet and Neumann boundaries, that are easily enforced by manipulating coefficients in the assembled matrix used for the determination of the pressure field.

Reproduced with permission of the copyright owner. Further reproduction prohibited without permission.

Cell face derivatives are trivial in a direction perpendicular to the cell edge, i.e. right face of cell (i,j), a derivative with respect to ξ becomes

$$\left.\frac{\partial p^{m+1}}{\partial \xi}\right|_{right} \approx p^{m+1}_{i+1,j} - p^{m+1}_{i,j},$$

whereas derivatives in a direction parallel to the cell face result from a box scheme, i.e., at the right face of the cell (i,j), a derivative with respect to ζ becomes

$$\left.\frac{\partial p^{m+1}}{\partial \zeta}\right|_{right} \approx 0.25(p^{m+1}_{i,j+1} + p^{m+1}_{i+1,j+1} - p^{m+1}_{i,j-1} - p^{m+1}_{i+1,j-1}).$$

With th above definitions, the PPE can be written in finite difference form as a matrix equation

$$Mp^{m+1} = S, \tag{92}$$

where the p^{m+1} and S are column vectors and M is the operator matrix resulting from the finite difference scheme of the PPE. The column vectors p^{m+1} and S have the following structures

$$p^{m+1} = \begin{pmatrix} p^{m+1}_1 \\ \vdots \\ p^{m+1}_n \end{pmatrix}, \qquad S = \begin{pmatrix} S_1 \\ \vdots \\ S_n \end{pmatrix}, \tag{93}$$

with elements $p^{m+1}_{n(i,j)} = p^{m+1}_{i,j}$ and

$$S_{n(i,j)} = -J_{i,j}\nabla \cdot \tilde{\mathbf{u}}/T,$$

or

$$S_{n(i,j)} = -J_{i,j}(\nabla \cdot \tilde{\mathbf{u}} - \Phi^{m+1})/T$$

if moving objects are considered (see Eq. (31)). Note that the term $J_{i,j}$ is brought to the right hand side of Eq. (92). For construction of column vectors $p^{m+1}_{n(i,j)}$ and $S_{n(i,j)}$, index $n_{(i,j)}$ is related to indices i and j by

$$n_{(i,j)} = (j-2)(I_{max} - 2) - 1 + i$$

Reproduced with permission of the copyright owner. Further reproduction prohibited without permission.

where I_{max} is the total number of cells in the x-direction. A typical computational domain has ghost cells around the entire domain (see Fig. 4). The ghost cells are necessary for the application of boundary and initial conditions but they are excluded in the assembling of the pressure coefficients. The number of effective cells in the x-direction is $I_{max} - 2$, $(i = 2 \ \ldots \ I_{max} - 1)$. The same consideration is applied to the y-direction, where the number of effective cells equals $J_{max} - 2$, $(j = 2 \ \ldots \ J_{max} - 1)$. The first element $(n_{(2,2)} = 1)$ in the column vector represents the cell at the lower-left-corner of the grid, or cell $(i, j) = (2, 2)$.

Then, the column vector $S_{n(i,j)}$ is given by

$$S_{n(i,j)} \approx -\frac{J_{i,j}}{T}\left[\frac{A_{Ri,j}\tilde{u}_{i,j} - A_{Ri-1,j}\tilde{u}_{i-1,j}}{\delta x_i} + \frac{A_{Ti,j}\tilde{v}_{i,j} - A_{Ti,j-1}\tilde{v}_{i,j-1}}{\delta y_j}\right] \tag{94}$$

for cases with stationary objects, and

$$S_{n(i,j)} \approx -\frac{J_{i,j}}{T}\left[\frac{A_{Ri,j}^{m+1}\tilde{u}_{i,j} - A_{Ri-1,j}^{m+1}\tilde{u}_{i-1,j}}{\delta x_i} + \frac{A_{Ti,j}^{m+1}\tilde{v}_{i,j} - A_{Ti,j-1}^{m+1}\tilde{v}_{i,j-1}}{\delta y_j} + \frac{(A_{Ci,j}^{m+1} - A_{Ci,j}^{m})/A_{Cs\ i,j}}{T}\right] \tag{95}$$

for cases with moving objects. The intermediate velocity $\tilde{u}$ and $\tilde{v}$ are calculated from Eqs. (80 - 83).

Multiplying square matrix M by column-vector p^{m+1}, each resulting equation has the following structure:

$$Mp^{m+1}\big|_{n(i,j)} = C_{i,j}^{low}p_{i,j-1}^{m+1} + B_{i,j}^{low}p_{i-1,j}^{m+1} + A_{i,j}p_{i,j}^{m+1} + B_{i,j}^{upp}p_{i+1,j}^{m+1} + C_{i,j}^{upp}p_{i,j+1}^{m+1} = S_{n(i,j)}. \tag{96}$$

Thus, the pressure coefficients fill five diagonals in matrix M. The superscripts *low* and *upp* refer to lower and upper diagonals, respectively. The coefficient A lays on the main diagonal, B^{low} and C^{low} are diagonals located at the lower triangular matrix. Conversely, B^{upp} and C^{upp} are located at the upper triangular matrix. B^{low} and B^{upp}

Reproduced with permission of the copyright owner. Further reproduction prohibited without permission.

are located just next to the main diagonal A, while C^{low} and C^{upp} are diagonals offset $I_{max} - 2$.

Matrix coefficients in cell(i, j) are constructed as

$$A_{i,j} = \left.\frac{\alpha_o}{\rho}\right|_{right} + \left.\frac{\alpha_o}{\rho}\right|_{left} + \left.\frac{\gamma_o}{\rho}\right|_{top} + \left.\frac{\gamma_o}{\rho}\right|_{bot}, \tag{97}$$

$$B^{upp}_{i,j} = -\left.\frac{\alpha_o}{\rho}\right|_{right}, \qquad B^{low}_{i,j} = -\left.\frac{\alpha_o}{\rho}\right|_{left}, \tag{98}$$

$$C^{upp}_{i,j} = -\left.\frac{\gamma_o}{\rho}\right|_{top} \text{ and } C^{low}_{i,j} = -\left.\frac{\gamma_o}{\rho}\right|_{bot}. \tag{99}$$

where α_o/ρ and γ_o/ρ ratios are defined in Eq. (91).

The system of linear equations formulated above must apply everywhere in the domain because the resulting matrix equation is solved in every cell, regardless of whether that cell represents fluid, surface, void or obstacle. The resulting matrix M is sparce-symmetric, positive and banded. Matrices of this form are inverted easily and quickly using the ICCG method (Kershaw, 1976). The ICCG method uses a hybrid matrix scheme that combines an incomplete Cholesky decomposition preconditioning of M with a conjugate gradient iteration. The decomposition transforms M into $LDL^T + E$, where L is a lower triangular matrix, D is a diagonal matrix (an approximated identity matrix), and E is a small error matrix. A conjugate gradient then accelerates an equivalent problem, neglecting E, toward the solution x of $L^{-1}M(L^T)^{-1}(L^Tx) = L^{-1}y$, where $(LL^T)_{-1}$ is used as an approximate inverse for M. Further details can be found in Kershaw (1976).

The disadvantage of the ICCG matrix solution technique is its memory requirements. However, the memory requirements are counterbalanced by the advantages of the ICCG method due to its robustness and speed. With well conditioned matrices, the ICCG method would generally converge faster than any of the other standard methods.

Reproduced with permission of the copyright owner. Further reproduction prohibited without permission.

2.6.6 Calculation of field velocity

Calculation of the new estimates for the velocities at cell faces is possible once the pressure field is determined. The new velocity field $\mathbf{u}^{m+1}$ is obtained from Eq. (27), thus

$$u_{i,j}^{m+1} = \tilde{u}_{i,j} - \frac{T}{\rho_{right}^{m}} \frac{p_{i+1,j}^{m+1} - p_{i,j}^{m+1}}{\delta x_{right}}, \tag{100}$$

for the x-direction, and

$$v_{i,j}^{m+1} = \tilde{v}_{i,j} - \frac{T}{\rho_{top}^{m}} \frac{p_{i,j+1}^{m+1} - p_{i,j}^{m+1}}{\delta y_{top}}, \tag{101}$$

for the y-direction. The densities ρ_{right}^{m} and ρ_{top}^{m} are averaged fluid concentration located at the right and top cell faces, respectively. They are calculated by

$$\rho_{right}^{m} = \frac{\delta x_{i+1}\rho_{i,j}^{m} + \delta x_i \rho_{i+1,j}^{m}}{\delta x_i + \delta x_{i+1}}$$

and

$$\rho_{top}^{m} = \frac{\delta y_{j+1}\rho_{i,j}^{m} + \delta y_j \rho_{i,j+1}^{m}}{\delta y_j + \delta y_{j+1}},$$

where cell fluid concentration $\rho_{i,j}$ is determined based on the fractional volume of fluid function F and the fluid density ρ_o, thus

$$\rho_{i,j}^{m} = \rho_o F_{i,j}^{m}.$$

A new estimate of velocity field is then obtained. The last procedure completes the solution of the NS equations. For more discussion on the numerical solution to the NS equations, readers can refer to Gresho (1990, 1991) and Glowinski (1992).

2.7 Free surface discretization

Parcels of fluids having a free surface are advected once the velocity field is determined. The fluid advection is done following the principle of the VOF method (Section 1.3). By using the transport equation and assuming that density is everywhere constant ($\rho = \rho_o$) in the flow domain and zero ($\rho = 0$) in the air domain,

Reproduced with permission of the copyright owner. Further reproduction prohibited without permission.

it is possible to normalize the transport equation by ρ_o. Defining $F = \rho/\rho_o$ as the fractional volume of fluid function (VOF function), the transport equation (Eq. 2) is written in conservative form as

$$\frac{\partial \phi F}{\partial t} + \frac{\partial \phi F u}{\partial x} + \frac{\partial \phi F v}{\partial y} = 0, \tag{102}$$

where F is a step function discussed earlier ($F = 1$ in elements containing fluid and $F = 0$ in elements containing air). Values of F range between $(0 - 1)$ in free surface elements. The function ϕ accounts for the cell aperture as seen in Section 2.3. The temporal discretization of Eq. 102 which serves as the basis for the advection of F is given by

$$\begin{aligned} F_{i,j}^{m+1} = F_{i,j}^{m} - \frac{T}{A_{Ci,j}} \Bigg[& \frac{1}{\delta x_i} \left(A_{Ri,j} u_{i,j}^{m+1} \langle F \rangle_{right} - A_{Ri-1,j} u_{i-1,j}^{m+1} \langle F \rangle_{left} \right) \\ & + \frac{1}{\delta y_j} \left(A_{Ti,j} v_{i,j}^{m+1} \langle F \rangle_{top} - A_{Ti,j-1} v_{i,j-1}^{m+1} \langle F \rangle_{bot} \right) \Bigg], \end{aligned} \tag{103}$$

where bracketed quantities $\langle F \rangle$ are fractional fluid volume crossing each of the four cell faces, left, right, top and bottom, respectively. Because F is discontinuous, transferring fluid through cell faces must be computed in a special way that preserves the sharp interface configuration, conserves the total volume and leads to a numerically stable computation. Given the velocity field, one may update F by a special treatment to the $\langle F \rangle$ quantities, using the donor-acceptor method proposed by Hirt & Nichols (1981). The advection of F in a given element depends on the local free surface orientation and the velocity direction. The free surface of the element is first reconstructed using the SLIC method (Section 1.3) to be either horizontal or vertical, based on the cell value F and its eight neighboring elements. Determination of whether the fluid is mostly horizontal or vertical in a surface element relies on estimating the local slope of the fluid/air interface. It is assumed that the fluid/air interface is a straight line segment partitioning the cell. Then, the slope is estimated by introducing two

Reproduced with permission of the copyright owner. Further reproduction prohibited without permission.

surface-height functions $X(y)$ and $Y(x)$ which encompass the amount of fluid in the cell being considered and the fluid of its eight neighbor cells, packing the fluid in a columnwise fashion according to the axis of reference. For instance, using Fig. 19a an approximation to $Y(x_i)$ is

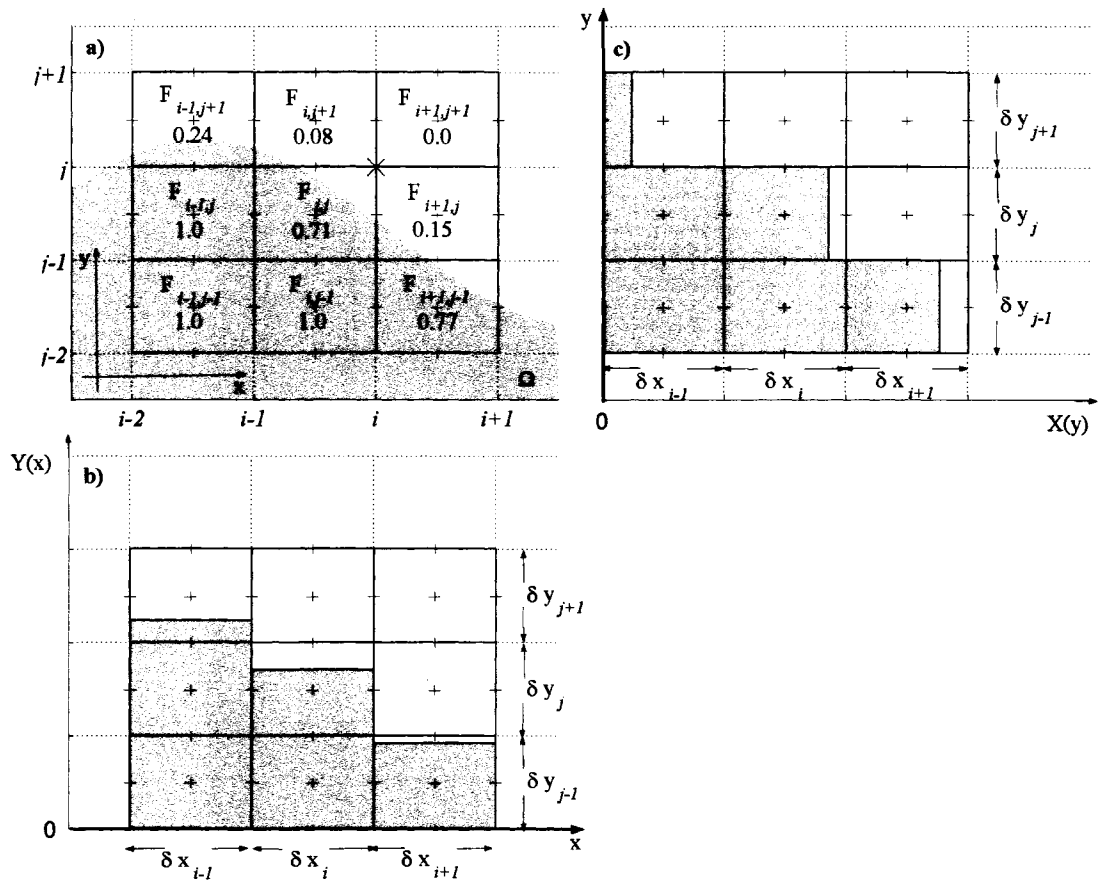

Figure 19: Sketches for fluid slope estimation at cell (i, j) based on the F values. a) A typical computational domain for fluid slope calculation. b) Height-function $Y(x_j)$ results according to local F values. c) Height-function $X(y_j)$ results.

$$Y(x_i) = Y_i = F_{i,j-1}\delta y_{j-1} + F_{i,j}\delta y_j + F_{i,j+1}\delta y_{j+1}, \tag{104}$$

Reproduced with permission of the copyright owner. Further reproduction prohibited without permission.

where axis $Y = 0$ has been taken at $(j-2)$. Packing the fluid toward the axis, the fluid slope at cell (i,j) is given by

$$\left.\frac{dY}{dx}\right|_i = \left(\delta x_{left}\frac{Y_{i+1}-Y_i}{\delta x_{right}} + \delta x_{right}\frac{Y_i - Y_{i-1}}{\delta x_{left}}\right)/(\delta x_{left} + \delta x_{right}), \qquad (105)$$

see Fig. 19b, in which the fluid slope at cell (i,j) is obtained by weighting the fluid slopes corresponding to the cell faces. In the same manner, a similar expression can be constructed for the surface-height function $X(y)$, see Fig. 19c,

$$\left.\frac{dX}{dy}\right|_j = \left(\delta y_{bot}\frac{X_{j+1}-X_j}{\delta y_{top}} + \delta y_{top}\frac{X_j - X_{j-1}}{\delta y_{bot}}\right)/(\delta y_{bot} + \delta y_{top}), \qquad (106)$$

where, for instance, the surface-height function at X_j can be defined by

$$X(y_j) = X_j = F_{i-1,j}\delta x_{i-1} + F_{i,j}\delta x_i + F_{i+1,j}\delta x_{i+1}. \qquad (107)$$

When evaluating the X or Y surface-height functions, it is necessary to include the corresponding height of the obstacle volume. This is easily carried out by introducing the obstacle contribution to the total surface height function in Eqs. (104) and (107).

If $|dY/dx|$ is smaller than $|dX/dy|$ the local slope interface is more horizontal than vertical. Otherwise, it is more vertical. The side where the fluid lies is chosen depending on the sign of the larger derivative. For example, assuming that $|dY/dx|$ is the smaller (fluid-air interface mostly horizontal), and dX/dy is negative, then the fluid lies below the interface. If dX/dy is positive, the fluid lies at the top of the fluid-air interface. Using this formulation it is very easy to identify whether a fluid-air interface is nearly horizontal or vertical and in which side of the interface the fluid lies.

Next, according to the velocity direction at the elements common face, the two cells immediately adjacent are distinguished. A donor or acceptor identifier are given to the cells, (D)onor/(A)cceptor. The labeling is accomplished by means of the fluid

Reproduced with permission of the copyright owner. Further reproduction prohibited without permission.

velocity normal to the cell face, where the donor cell is always upstream and the acceptor cell downstream from the common face. A problem arises when choosing which F to use (F_D or F_A) for $\langle F \rangle$ which appears at the four boundaries, see Eq. (103). The D and A labels are assigned separately for each cell face. Thus, each computational cell has four separate assignments of D or A corresponding to each of its cell faces (left, right, bottom and top). Fig. 20 shows a set of possible cases in which $\langle F \rangle_{right}$ in cell (i, j) has to be determined according to the velocity x-direction and fluid-air interface orientation.

The flux or volume crossing the cell face is $\langle F \rangle |uT| \delta y_j$, where u is the normal velocity at the cell right face. For instance, in Fig. 20a where the free surface orientation is nearly horizontal, $\langle F \rangle$ is taken as F_D. Then, the amount of fluid that is actually fluxed across the cell face per unit area is

$$\Delta V_{right} = \langle F \rangle |uT| = F_D |uT|.$$

Fig. 20b depicts a case where the free surface on cell (i, j) is reconstructed vertically. Here, $|dY/dx|$ is larger than $|dX/dy|$, so $\langle F \rangle$ has been taken as F_A. The previous equation can be easily modified to account for this consideration. The amount of fluid advected through the right cell face per unit area is determined by

$$\Delta V_{right} = \langle F \rangle |uT| + [(1.0 - \langle F \rangle)|uT| - (1.0 - F_D)\delta x_D].$$

Note, the first terms between brackets defines the amount of fluid in the donor cell that could be advected to the acceptor cell, assuming that the vertical fluid-air interface lies exactly on the right cell face; the second term indicates the amount of air or void the donor cell has. Since the fluid-air interface is vertical and moving toward the right cell face, the air/void must go through the common boundary first; the remainder of the advection corresponds to the fluid. If the expression between brackets becomes negative, then it indicates that the vertical fluid-air interface has not reached the right

Reproduced with permission of the copyright owner. Further reproduction prohibited without permission.

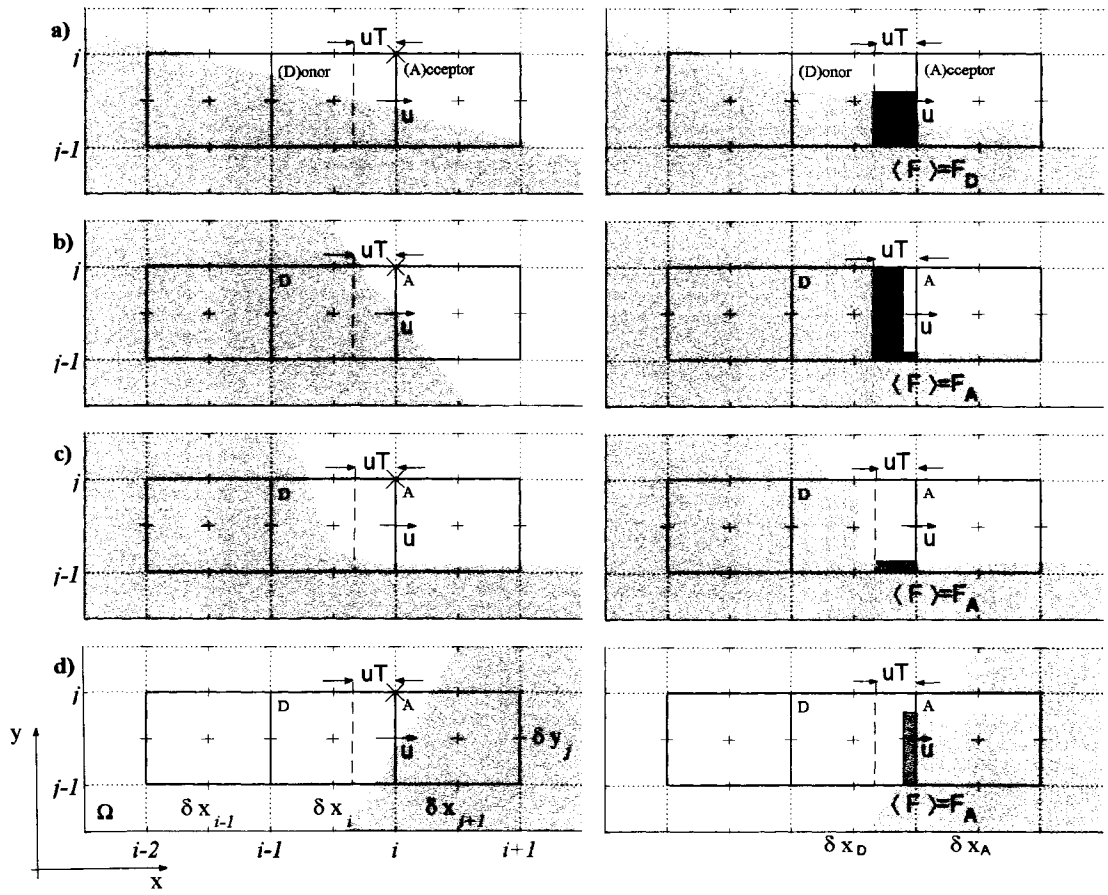

Figure 20: Examples of free surface reconstruction used in the x-advection of F through the right cell face. The free surface in cell (i, j) is reconstructed horizontally in a) and vertically in b), c) and d). The darker regions in cell (i, j) are the actual amount of $\langle F \rangle_{right}$ fluxed in each case.

cell face yet. To consider this possibility, the equation is then modified one more time as

$$\Delta V_{right} = \langle F \rangle |uT| + \max[(1.0 - \langle F \rangle)|uT| - (1.0 - F_D)\delta x_D, 0.0],$$

see Fig. 20c. However, this expression is not limited when the fluid/void volume advected through the cell face is larger than the volume contained in the donor cell. So, an additional modification is needed to account for this possibility. With the help

Reproduced with permission of the copyright owner. Further reproduction prohibited without permission.

of Fig. 20d, finally, the equation becomes

$$\Delta V_{right} = \min \begin{bmatrix} \langle F \rangle |uT| + \max[(1.0 - \langle F \rangle)|uT| - (1.0 - F_D)\delta x_D, 0.0], \\ F_D \delta x_D \end{bmatrix}. \quad (108)$$

The value ΔV computed by Eq. (108) is subtracted from the donor cell volume and added to the acceptor cell. For instance, the cell volume calculation for the right flux is given by

$$F_{i,j}^{m+1} A_{Ci,j} \delta x_i \delta y_j \big|_A^D = F_{i,j}^m A_{Ci,j} \delta x_i \delta y_j \mp \Delta V_{right} A_{Ri,j} \delta y_j \quad (109)$$

and

$$F_{i+1,j}^{m+1} A_{Ci+1,j} \delta x_{i+1} \delta y_j \big|_D^A = F_{i+1,j}^m A_{Ci+1,j} \delta x_{i+1} \delta y_j \pm \Delta V_{right} A_{Ri,j} \delta y_j, \quad (110)$$

$$F_{i+1,j}^{m+1} A_{Ci+1,j} \delta x_{i+1} \delta y_j \big|_D^A = F_{i+1,j}^m A_{Ci+1,j} \delta x_{i+1} \delta y_j \pm \Delta V_{right} A_{Ri,j} \delta y_j, \quad (110)$$

respectively. Note, for the calculation of acceptor/donor cell volume, the (A)cceptor/(D)onor script must match the sign of the last term.

The amount of ΔV fluxed through the right face will modify the cell fluid concentration or F function. The increment or reduction of F values can be determined using Eqs. (109) and (110), thus

$$\begin{aligned} \Delta F_{right\ i,j} \big|_A^D &= \mp \Delta V_{right} A_{Ri,j} / (A_{Ci,j} \delta x_i) \\ \Delta F_{right\ i+1,j} \big|_D^A &= \pm \Delta V_{right} A_{Ri,j} / (A_{Ci+1,j} \delta x_{i+1}). \end{aligned} \quad (111)$$

The same process is repeated to obtain ΔF_{top} values according to the velocity y-direction and fluid-air interface orientation for the cell top boundary. They are give by

$$\begin{aligned} \Delta F_{top\ i,j} \big|_A^D &= \mp \Delta V_{top} A_{Ti,j} / (A_{Ci,j} \delta y_j) \\ \Delta F_{top\ i,j+1} \big|_D^A &= \pm \Delta V_{top} A_{Ti,j} / (A_{Ci,j+1} \delta y_{j+1}). \end{aligned} \quad (112)$$

Finally, the F^{m+1} values are determined by

$$F_{i,j}^{m+1} = F_{i,j}^m \pm \Delta F_{right\ i-1,j} \pm \Delta F_{right\ i,j} \pm \Delta F_{top\ i,j-1} \pm \Delta F_{top\ i,j}. \quad (113)$$

Reproduced with permission of the copyright owner. Further reproduction prohibited without permission.

The resulting new F^{m+1} values will define the new fluid configuration. Occasionally, the time-advanced F^{m+1} values may have values slightly less than zero or greater than one. Hence, after the F advection calculation has been completed, the computational domain is swept to reset values of F^{m+1} less than zero back to zero, and values of F^{m+1} greater than one back to one. Since the donor treatment corresponds to the upwind scheme and will introduce numerical diffusion and the acceptor treatment corresponds to the downwind scheme that will cause the sharpening of free surface, the combined use of the two methods will balance the numerical diffusion and instability. The special corrector needed to prevent the occurrence of nonphysical situations, i.e, $F > 1$ and $F < 0$, eliminates any possible numerical instability. The donor-acceptor technique is the simplest treatment for controlling the numerical diffusion during the advection of the VOF function F, however, it is only first-order accurate. Major numerical errors are caused by the crude approximation of the free surface orientation and subsequent advection by the donor/acceptor treatment. The corrector introduces additional errors. Nevertheless, due to the simplicity of the donor-acceptor VOF method, most researchers still use this technique for free surface tracking purposes.

2.8 Boundary condition formulations

In tsunami calculations, boundary conditions are needed at the free surface and at the stationary or moving boundaries. The fundamental governing equations and mechanisms have been explained in Section 2.1.5. Free surface boundary conditions are imposed in several ways. For instance, the kinematic free surface boundary condition is automatically generated in the advection of VOF function F after the velocity boundary condition has been defined on surface cell by means of the fluid cell orientation and mass conservation equation. The dynamic free surface boundary condition is imposed during the implicit pressure calculation, see Section 2.6.1. At the station-

Reproduced with permission of the copyright owner. Further reproduction prohibited without permission.

ary or moving boundaries the free-slip or no-slip boundary condition is applied. For instance, the initial conditions for a tsunami wave are obtained by boundary deformations, e.g., seabottom uplift, or by the displacement of a rigid object, e.g., an object falling into the fluid, or by using a combination of deformation and displacement, i.e, a submarine landslide. For any generation mechanism the free-slip or no-slip boundary condition is applied to the immediate boundary object cell. In general, the boundary conditions for stationary objects, moving objects and free surface fall into three categories: no-slip (Dirichlet), free-slip (Neumann) and mass conservation boundary conditions.

2.8.1 No-slip and free-slip boundary conditions.

In the no-slip boundary mechanism it is assumed that the object boundary is impermeable and there is a tangential shear stress generated on the object boundary by the relative motion of the object-fluid. Therefore, in a stationary object, the viscous fluid is stuck on the object boundary, so both normal and tangential velocity components at the boundary are set to zero. On the other hand, for stationary objects with the free-slip condition, only the normal velocity component at the object boundary is zero, but the tangential velocity gradient at the boundary interface is equal to zero (Eq. 16). This can be referred to as a tangential continuative boundary condition. The tangential zero-derivative condition is intended to represent a slippery flow parallel to the boundary. It must be mentioned that the tangential continuative boundary condition has no physical basis, rather it is a numerical statement that may or may not provide the desired flow behavior.

In applying boundary conditions, the velocity at the boundary cells is manipulated to obtain the desired derivative. It is important to establish whether the object interface is nearly horizontal or vertical, since velocities are discretized at cell faces,

Reproduced with permission of the copyright owner. Further reproduction prohibited without permission.

the interface orientation helps to identify those tangential discrete velocities from normal discrete velocities. A simplified method is adopted for velocity assignment at boundary cell (B)-(S) or (B)-(F) faces. The boundary condition is carried out as follows. First, consider a stationary object with a vertical boundary interface coinciding with cell faces, as illustrated in Fig. 21a. In such a case, if a no-slip

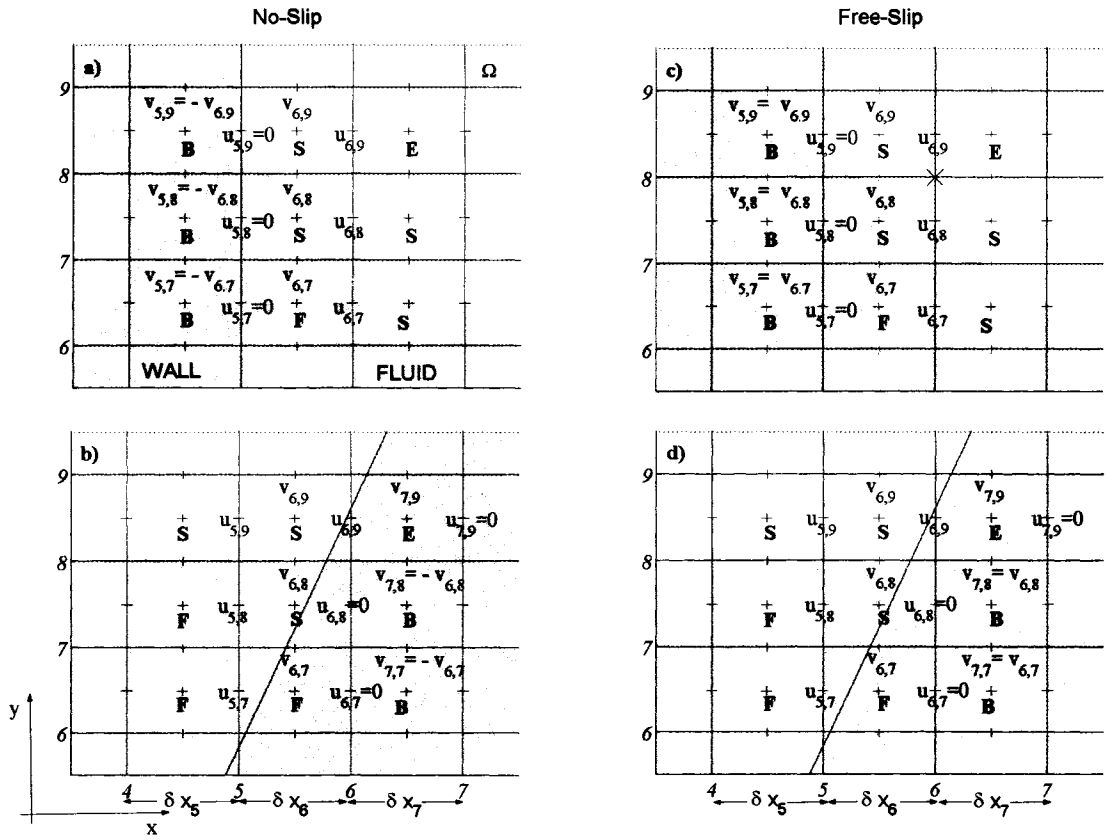

Figure 21: Example of velocity boundary condition for stationary or moving objects. Cell size has been assumed constant ($\delta x_5 = \delta x_6 = \delta x_7$). a) and b) no-slip boundary condition for a vertical and inclined (nearly vertical) wall; c)and d) free-slip boundary condition for a vertical and inclined wall.

boundary condition is established, both normal and tangential velocity components are set to zero by means of setting the cell face velocities at the immediate boundary cell (B) as indicated in Fig. 21a. A general formulation can be easily determined for

Reproduced with permission of the copyright owner. Further reproduction prohibited without permission.

a no-slip condition at a given boundary cell i, j (B) located at the left side of the fluid domain as follows

$$u_{i,j}|_{left} = 0 \quad \text{and} \quad v_{i,j}|_{left} = -\left(\frac{\delta x_i}{\delta x_{i+1}}\right) v_{i+1,j},$$

where cell sizes have been taken into consideration. A similar expression for no-slip condition can be deduced for other boundary interface orientations in which boundary cells are located at the right (with nearly vertical interface), bottom and top (both with nearly horizontal interface) of the fluid domain, thus

$$u_{i,j}|_{right} = 0, \qquad v_{i+1,j}|_{right} = -\left(\frac{\delta x_{i+1}}{\delta x_i}\right) v_{i,j},$$

$$v_{i,j}|_{bot} = 0, \qquad u_{i,j}|_{bot} = -\left(\frac{\delta y_j}{\delta y_{j+1}}\right) u_{i,j+1}$$

and

$$v_{i,j}|_{top} = 0, \qquad u_{i,j+1}|_{top} = -\left(\frac{\delta y_{j+1}}{\delta y_j}\right) u_{i,j},$$

respectively. This setting for the boundary condition forces the tangential velocity to be zero at the cell boundary or cell corners.

It is very common that object boundaries cut cells demanding a more rigorous boundary treatment to locate the normal and tangential velocity components at the object interface. This boundary treatment becomes more computationally demanding if moving objects are considered. The benefit obtained in numerical accuracy using a more rigorous boundary treatment is not appreciably greater. Nevertheless, as shown in Fig. 21b, the determination of boundary velocities when cut cells are presented is carried out in the same manner as uncut cells. This assumption, while not exact, had proven to be satisfactory in water wave and tsunami calculations.

The most common boundary mechanism used in water wave and tsunami application is the free-slip condition. This mechanism is very easy to apply in a structured grid. Along the boundary interface of a stationary object the normal velocity and

Reproduced with permission of the copyright owner. Further reproduction prohibited without permission.

the gradient of the tangential velocity are both set to zero. Fig.21c and d show the mechanism used to set the boundary cell velocities for vertical and nearly vertical walls. The formulation can be easily determined for a free-slip condition at a given boundary cell i, j (B) located at the left, right, bottom and top sides of the fluid domain as follows

$$u_{i,j}|_{left} = 0, \qquad v_{i,j}|_{left} = v_{i+1,j}.$$

$$u_{i,j}|_{right} = 0, \qquad v_{i+1,j}|_{right} = v_{i,j},$$

$$v_{i,j}|_{bot} = 0, \qquad u_{i,j}|_{bot} = u_{i,j+1}$$

and

$$v_{i,j}|_{top} = 0, \qquad u_{i,j+1}|_{top} = u_{i,j},$$

respectively.

In most tsunami simulations, if moving objects are present, boundary velocities (on (B) cells) are given according to the prescribed trajectory in time of the object, i.e, $\mathbf{u}_o(x, y, t) = u_o\hat{i} + v_o\hat{j}$. This means that the fluid itself does not have any effect on the motion of the object. The object motion is determined using linear or angular momentum equations or a combination of both. The object boundary velocities are imposed by the kinematics of the object at each boundary cell location according to the object linear/angular velocity/acceleration and trajectory. In practice, for instance, in a submarine landslide, the motion of the object (landslide) is affected by the fluid response. Driving forces describing the object motion are coupled with the fluid responses by means of forces and torques that the fluid, via pressure (normal stress) and viscosity (tangential effect), exerts on the boundary of the object. Unfortunately, this specific topic of driving forces coupled with fluid responses has not been explored herein and it has been left for future work. Detailed discussion on the topic is given by Gerrits (2001) and Fekken (2004).

Reproduced with permission of the copyright owner. Further reproduction prohibited without permission.

In applying boundary conditions, extreme care has to be taken when the no-slip condition is used, since the chosen spatial and temporal resolutions may be decisive for the validity of the model result. Often, higher spatial discretizations are required close to the object boundary interfaces, since small scale processes might play an important role.

2.8.2 Velocity boundary condition for the free surface

Velocity at cell faces are only computed by the numerical momentum equations at surface (S) and full (F) cells. In empty (E) cells, i.e., in the air, the momentum equations are not solved. The air resistance is considered to be insignificant in affecting tsunami or wave propagation, so the (E) cells are considered as voids. Discrete velocities are known at (F)-(F), (F)-(S), (F)-(E) and (S)-(S) cell faces. They are given either by the initial condition or by the previous velocity field (old estimate), see Fig 22. In (S) cells, velocities at cell sides facing (E) cells must be provided because they are not defined and they are required in the numerical equations. Also, velocities are needed in (E)-(E) cell faces, facing (S)-(E), (S)-(S) or (F)-(E) cells. These unknown velocities are used in the normal and tangential derivative of the advection and frictional momentum terms, and in the advection of the fluid itself (F function). The velocities must be provided in such a way that normal and tangential derivatives are continuative (zero-derivative) and conserve mass.

Fig 23 shows three possible cases, amongst others, which a (S) cell could encounter in a numerical simulation. A velocity convention is introduced to discern between defined-velocity and required-velocity using the geographic four cardinal directions, north, east, south and west. For instance, Fig 23a presents a (S) cell facing three (E) cells. Here, there is just one defined-velocity, v_{south} on the (S) cell. Applying continuative boundary condition and forcing mass conservation, then the required-

Reproduced with permission of the copyright owner. Further reproduction prohibited without permission.

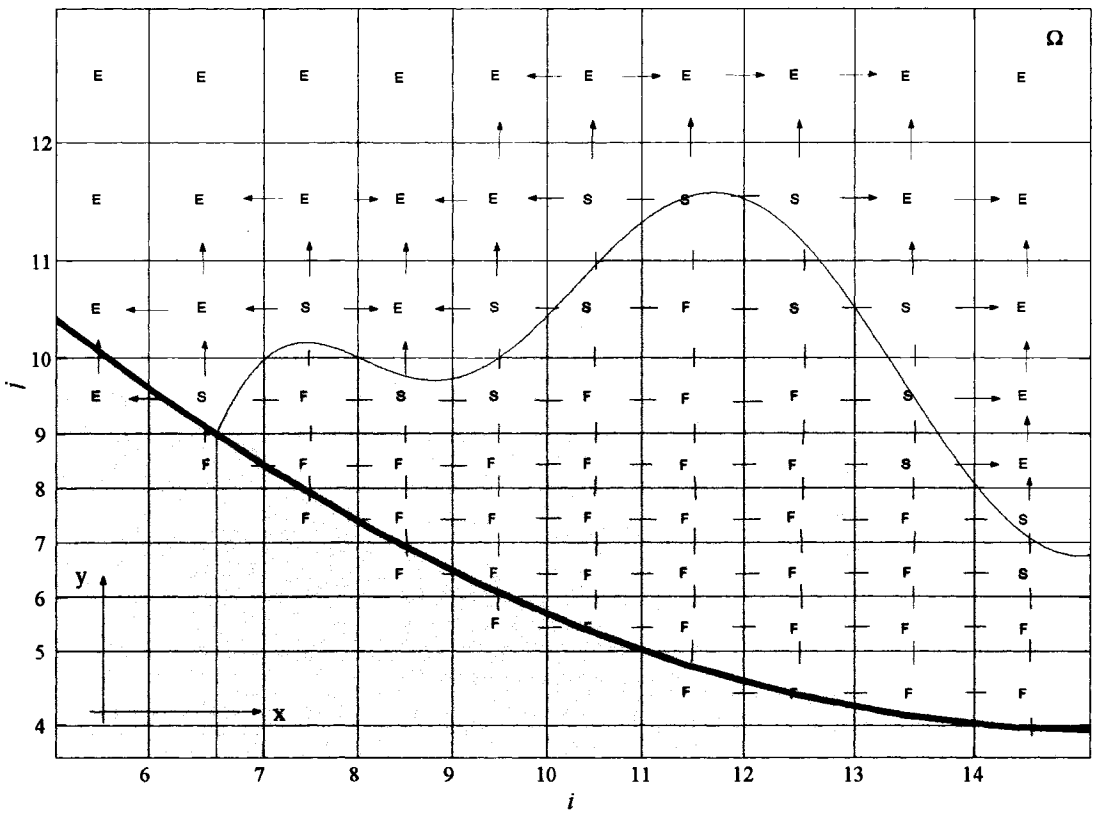

Figure 22: Example of velocity boundary condition at the free surface. Dashes at cell faces represent the fluid defined-velocities. Arrows indicate required-velocities needed for computation of new estimate of velocity field and VOF function F advection. The required-velocities are determined based on the surrounding defined-velocities.

velocities are calculated by

$$v_{north} = (A_{T\,south}/A_{T\,north})v_{south} \quad \text{and} \quad u_{west} = u_{east} = 0.$$

In the event that a (S) cell neighbored two (E) cells, as shown in Fig 23b, the required-velocities are easily calculated by corresponding each one with the opposite defined-velocities, thus

$$u_{west} = (A_{Reast}/A_{Rwest})u_{east} \quad \text{and} \quad v_{north} = (A_{T\,south}/A_{T\,north})v_{south}.$$

Reproduced with permission of the copyright owner. Further reproduction prohibited without permission.

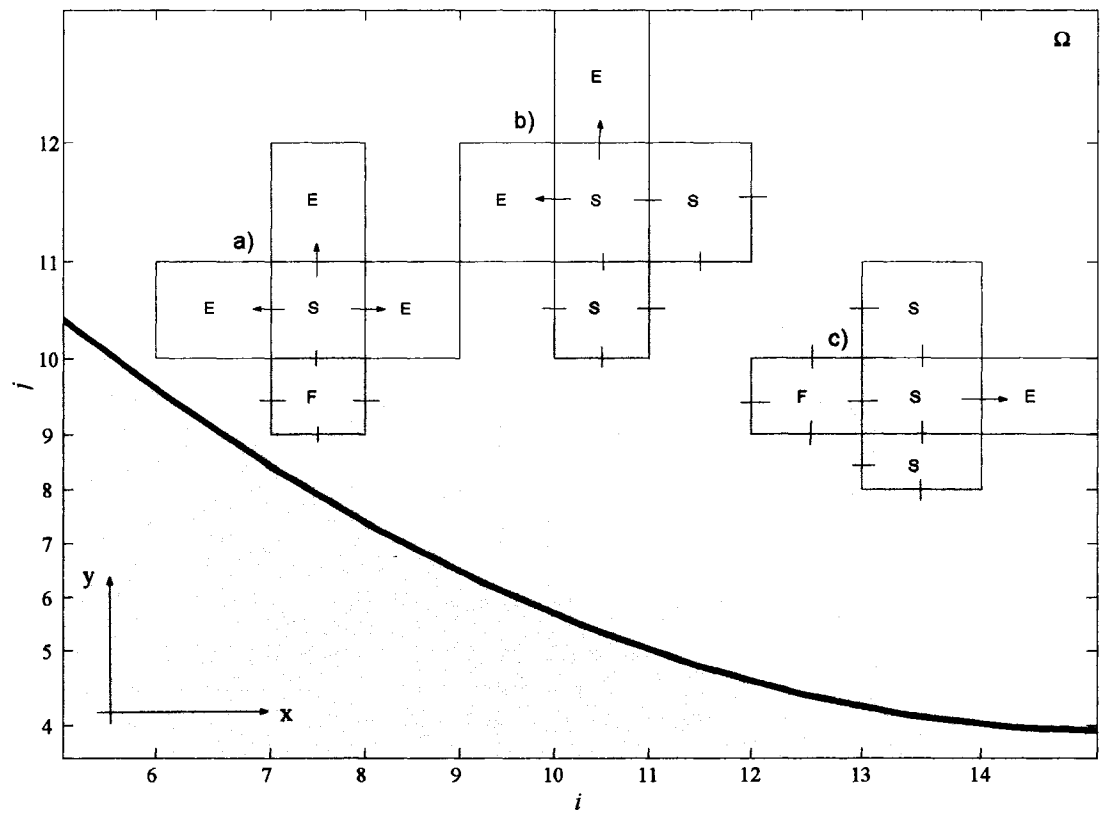

Figure 23: Three possible cases for surface velocity boundary condition at (S)urface-(E)mpty cells. Dashes at cell faces represent the fluid defined-velocities. Arrows indicate required-velocities at (S)-(E) cells needed for numerical computation of a new estimate of velocity field and advection of the VOF function F.

Finally, Fig 23c depicts a case where just one required-velocity is needed to be defined. In this case, mass conservation (Eq. 32) is applied. Then, the required-velocity u_{east} is determined from

$$\frac{u_{east}A_{Reast} - A_{Rwest}u_{west}}{\delta x} + \frac{A_{Tnorth}v_{north} - A_{Tsouth}v_{south}}{\delta y} = 0.$$

After all velocities are defined at (S)-(E) cell faces, then it is possible to determine the velocities at (E)-(E) cell faces, which are needed in the discrete numerical equations. Since (E)-(E) velocities are approximately tangential to the free surface, they are often in front of (S)-(S) velocities. For example, Fig. 24a presents a case where only a

Reproduced with permission of the copyright owner. Further reproduction prohibited without permission.

required-velocity is needed. Using the discrete form of Eq. (18), the required-velocity u_{north} can be obtained from

$$\mu\left(\frac{u_{north}-u_{south}}{0.5(\delta y_{south}+\delta y_{north})}+\frac{v_{east}-v_{west}}{0.5(\delta x_{west}+\delta x_{east})}\right)=0.$$

However, there are situations where (E)-(E) velocities are in front of (S)-(E) veloc-

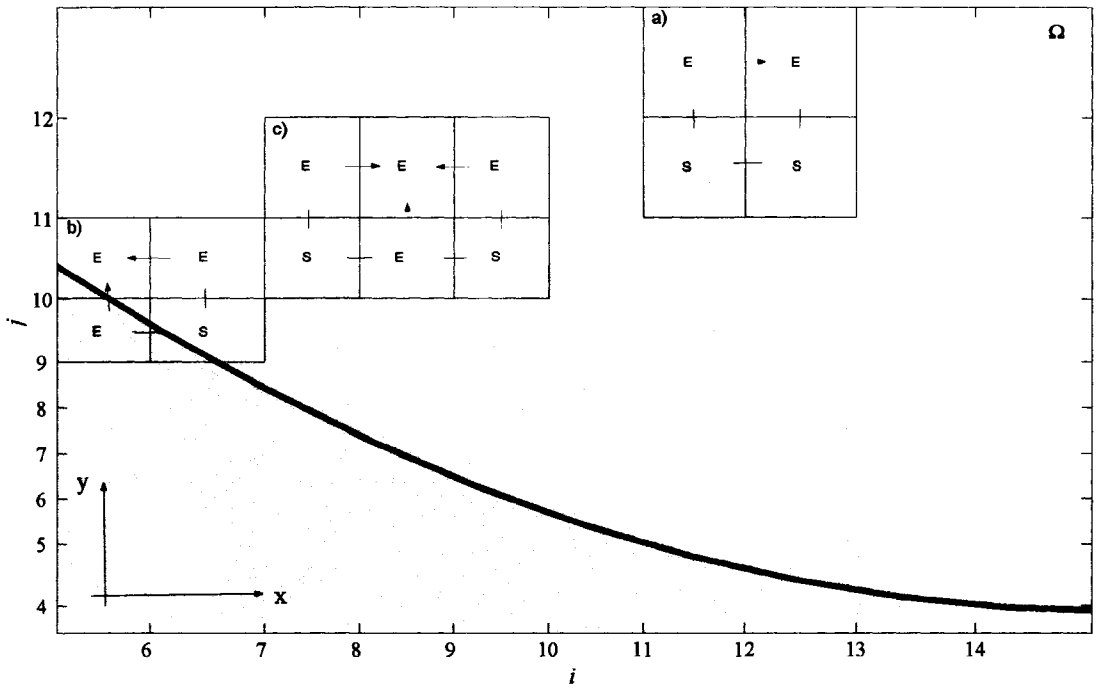

Figure 24: Three possible cases for surface velocity boundary condition at (E)mpty-(E)mpty cells. Dashes at cell faces represent the fluid defined-velocities. Arrows indicate required-velocities at (E)-(E) cells needed for numerical computation of a new estimate of velocity field and advection of the VOF function F.

ities, like the situation depicted in Fig 24b. The continuative tangential derivatives are calculated by corresponding each (E)-(E) velocities with the opposite (S)-(E) velocities, so (E)-(E) velocities, v_{west} and u_{north}, can be easily determined by

$$u_{north}=\frac{A_{Tsouth}}{A_{Tnorth}}u_{south}\quad\text{and}\quad v_{west}=\frac{A_{Reast}}{A_{Rwest}}v_{east}.$$

Reproduced with permission of the copyright owner. Further reproduction prohibited without permission.

Often there are cases in which an (E)-(E) velocity is influenced by two (S)-(S) or (S)-(E) velocities, as depicted in Fig 24c. In this particular case, the vertical (E)-(E) velocity is compromised by the right and left contributions of the boundary condition. Individual calculations are done as it was explained in the previous case, but an averaged value is used for the fusion of both boundary conditions, thus

$$v_{center} = \frac{1}{2}\left(\frac{v_{west}A_{Twest} + v_{east}A_{Teast}}{A_{Tcenter}}\right).$$

2.9 Error analysis and numerical stability

One of the main goals in fluid dynamic computation is to achieve an acceptable numerical reproduction of a physical phenomena. Therefore, there are differences between the approximated solution and the true physical solution. The differences, or errors, have several sources which can be identified as: model-scheme errors, discretization errors and machine-iteration errors. Model-scheme errors depend on the approximation adopted (governing equations chosen) to solve the physical phenomena and the numerical scheme given to the governing equations. These errors can be negligible or large according to the approximation used to solve a specific case, e.g., NS or SW approach, or the type of fluid flow regime the case has, i.e., laminar or turbulent. Other sources of model-scheme errors could also be introduced by the treatment given to the boundary condition. Model-scheme errors can only be evaluated by comparing the numerical solution with accurate experimental data or analytical solution. Obviously, identification of the other errors is required as well, to discern and quantify model-scheme errors.

Discretization errors are introduced by the spatial and temporal discretization used in the computational domain. They can be easily reduced by refining the computational grid and reducing the time step. Successive refinement of grid size and time step is commonly practiced in numerical simulation to find efficient grid-independent

Reproduced with permission of the copyright owner. Further reproduction prohibited without permission.

domains and stable solutions. Numerical modelers search for grid independence and efficiency, by testing several grid sizes and time steps and comparing the model performance and accuracy. As the grid size and time stepping approach to zero, the finite difference equations should approximate the partial differential equations and solution of the finite difference equations should converge to the solution of the partial differential equations. Unfortunately, the numerical approximation does not provide convergence by itself. Errors introduced by the numerical scheme and machine round off errors may grow in time in an unbounded manner. A stability analysis based on the finite difference scheme adopted is required. For the linear partial differential equations, the most widely used method to analyze the numerical stability of a numerical scheme is the von Neumann stability analysis method, Kowalik & Murty (1993*a*). In this method, the error described by a series of Fourier modes is substituted into the finite difference equations and tested for amplification during one time step. For a stable scheme, the amplification factor of each Fourier modes has to be smaller than 1.0. However, the momentum equation has nonlinear and frictional terms, for which the von Neumann's method is not applicable directly.

Machine-iteration errors are those that occur in large iterative processes due to the round off error of the computer. They are defined as the differences between successive iterates. They are predictable, easy to estimate and can be controlled by setting the variable precision in the code algorithm.

Discretization errors are the most flexible to control by model users. The discretization errors are mostly related to the advection terms, so the analysis is focused on the advection terms numerical stability. Since the advection terms are evaluated explicitly, the time step T adopted must be smaller than a certain critical value to prevent instability. Once the computational grid has been defined, several restrictions are considered for T to insure that it is below the critical value. First, a parcel of

Reproduced with permission of the copyright owner. Further reproduction prohibited without permission.

fluid or moving object cannot travel more than one cell width per time step. The advection of the F function (Section 2.7), as well as the momentum advection discussed previously in Section 2.6.3, is approximated explicitly in time. Typically, T is chosen to be some fairly small fraction of the minimum value, so the constraint is imposed by means of the Courant-Friedrichs-Lewy (CFL) number, N_{CFL}. This constraint must be enforced along both coordinate directions, so the transport time step limit T, is taken as the minimum of the transport time step limits of the x-direction and y-direction, thus

$$T < N_{CFL} \min \left[\frac{(\delta x_i)}{|u_{i,j}|}, \frac{(\delta y_j)}{|v_{i,j}|} \right]. \tag{114}$$

The multiplier N_{CFL} should be less than 1.0 in theory, or more conservatively, less than 1/2 in practice. A value of $N_{CFL} = 0.33$ is recommended for tsunami calculations. Second, the frictional term is evaluated using old time t^m velocity field, see Eq. (77). This explicit treatment is therefore subjected to a linear stability time step constraint, which is evaluated conservatively under the premise that the momentum must not diffuse more than one cell in one time step, thus

$$T < \frac{1}{2\nu} \min \left[\frac{(\delta x_i)^2 (\delta y_j)^2}{(\delta x_i)^2 + (\delta y_j)^2} \right]. \tag{115}$$

These stability conditions are only approximate, since they are based on the linear von Neumann analysis, which does not include the simultaneous effect of the pressure gradient in the momentum equation. Finally, with T chosen to satisfy above inequalities (Eqs. 114 and 115) the advection flux is reevaluated. If the advection flux exceeds more than 1/3 of the cell volume, the time step T is reduced automatically and all calculations are restarted with the reduced T.

Reproduced with permission of the copyright owner. Further reproduction prohibited without permission.

Chapter 3

Model Testing

3.1 Numerical modeling of the initial stages of the dam-break wave problem

3.1.1 Introduction

In this case study, results of the nonlinear shallow water (NLSW) equations to study wave generation, propagation and runup of long waves are compared against the analytical solution and the proposed Navier-Stokes and volume of fluid (NS-VOF) model. Here, it is intended to juxtapose the hydrostatic behavior expressed by NLSW approach against the nonhydrostatic given by NS model. The dam-break problem can be seen as a simplified case study to investigate the initial stage of wave front propagation or runup over a flat beach.

The NLSW equations have been used widely in tsunami investigations to determine wave generation, propagation, runup and forecast/hindcast inundation areas, see Appendix A for a brief description of the NLSW numerical model. In general, analytical and numerical results using the NLSW approach appear to be in agreement with measurements when the flow condition is mostly hydrostatic and vertical acceleration is small compared to gravity. However, when water flow presents high vertical velocity/acceleration, the hydrostatic assumption is no longer valid. From previous investigations on the topic, it is well established that the NLSW approach is not valid during the initial stage of the dam-break problem, where pressure distribution is nonhydrostatic immediately after the dam breaks (Phole, 1952). In addition, wave breaking and turbulence are dominating features in the fluid layer immediate to the bed. However, Stanby *et al.* (1998) showed that this initial nonhydrostatic and turbulent stage does not substantially affect the long-term results of the NLSW

Reproduced with permission of the copyright owner. Further reproduction prohibited without permission.

approach. The NS model is suitable for this type of flow condition since it includes the vertical velocity/acceleration component.

In this case study, the NS model is used as a tool to validate the NLSW solution through a simple model setup taken from the literature. The dam-break case starts from a hydrostatic condition where the velocity field is zero at $t = 0$. The case is solved numerically using the NLSW approach and compared with NLSW analytical and NS numerical solution.

To validate the dam-break NS numerical model a laboratory experiment performed at Cornell University (Shigematsu *et al.*, 2004) has been chosen. The experiment takes into account the effect of the pull-up motion of the dam-gate. They concluded that the agreement between the experimental data and their numerical solution is much better when the actual dam-gate movement is taken into account.

Several studies have been devoted to the topic for both the dry-bed condition (i.e., no water in front of dam) and the wet-bed condition. Ritter (1892) studied the problem of the dry-bed case with an infinite reservoir length. He presented an analytical solution using NLSW equations. Later, Dressler (1952) and Whitham (1955), included the effect of bed resistance in the analysis, and derived analytical expressions for the velocity and height of the wave front. Phole (1952) demonstrated that the pressure distribution is nonhydrostatic immediately after the dam breaks. Stoker (1957) investigated the case of the dam-break wave propagating into and over a wetted bed in a reservoir of infinite length, and he derived an analytical expression for the surface profile in terms of the initial upstream and downstream depths. Hunt (1982, 1987) presented an analytical solution considering a reservoir with finite length and the wave kinematic. Kosorin (1983) demonstrated that nonhydrostatic pressure distribution reduces the wave speed (over dry-bed) by about 30% and it could have an effect on the long-term results.

Reproduced with permission of the copyright owner. Further reproduction prohibited without permission.

Laboratory experiments for the dam-break problem have been conducted by several researchers and empirical solutions have been proposed to account for breaking, friction and turbulent conditions of the wave front. Martin & Moyce (1952) carried out a series of dam-break experiments determining the time histories of the wave front location and the changes of the water level at the back wall of the water tank. Later, Dressler (1954) experimentally showed that the water depth at the dam site does not attain a constant value instantaneously after the dam-gate breaks as predicted by Ritter using the hydrostatic assumption. He showed that it takes approximately 9 nondimensional time units to reach the constant value given by Ritter.

Stanby *et al.* (1998) carried out a set of experiments using a digital video camera and recorded a series of snapshots of surface profiles of the dam-break wave during the initial stage. Analysis of the snapshots showed that the difference of wave profile at the initial stage is substantial if it is compared with the NLSW analytical solution. However, the wave profile eventually becomes quite similar to the NLSW results after the wave front has developed downstream. Recently, Shigematsu *et al.* (2004) performed a laboratory experiment at Cornell University to investigate the effect of the pull-up motion of the dam-gate. They observed that the agreement between the experimental data and their numerical solution is much better when the actual dam-gate movement is taken into account.

Numerical simulation of the dam-break problem using NS equations has been reported by various researchers as well. For the dry-bed condition: Harlow & Welch (1965), Amsden & Harlow (1970), Hirt & Nichols (1981), Strelkoff (1986), Chen *et al.* (1993) and Nakayama & Mori (1996). For the wet-bed condition: Mohapatra *et al.* (1999) and Shigematsu *et al.* (2004).

From the above, it is well established that the NLSW approach is not valid during the initial stage of the dam-break problem, where the wave breaking and turbulence

Reproduced with permission of the copyright owner. Further reproduction prohibited without permission.

are dominating features. Although the pressure distribution is nonhydrostatic immediately after the dam collapses, this initial nonhydrostatic state does not affect the long-term NLSW results. In summary, the major objective in this investigation is to validate the nonhydrostatic NS model and juxtapose the hydrostatic behavior expressed by NLSW.

3.1.2 Analytical solution for the dam-break problem

An analytical solution for the dam-break problem using the NLSW equations is derived based on the method of characteristics Hederson (1966) and Méhauté (1976). The free surface profile of the water surging over a dry bed for an infinite reservoir is defined as:

$$\frac{x}{t} = 2\sqrt{gD_0} - 3\sqrt{gD} \tag{116}$$

Here x is the coordinate along the channel as shown in Fig. 25, t is the time, $D = H+\zeta$ is the total depth and g the gravity acceleration. The dam breaks instantaneously at

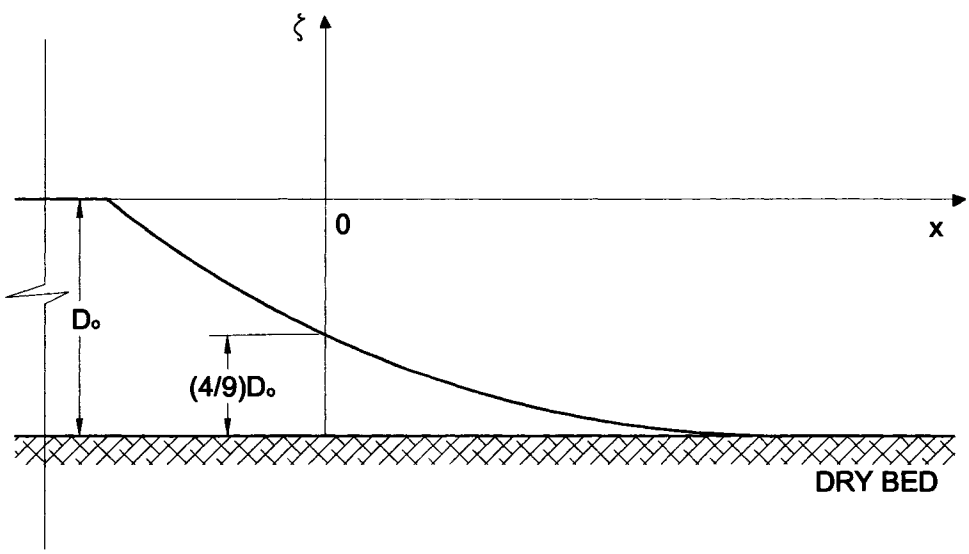

Figure 25: Definition sketch for the dam-break problem.

Reproduced with permission of the copyright owner. Further reproduction prohibited without permission.

$t = 0$. Since undisturbed depth is taken as $H = 0$, the total depth is equal to the sea level $D = \zeta$. The wave front of the nonviscous fluid propagates over the dry-bed with a speed

$$C_f = 2\sqrt{gD_0}, \tag{117}$$

which is two times greater than the wave front speed moving in the negative direction. At the dam site, the water depth drops instantaneously to a constant value of $\frac{4}{9}D_o$ and constant horizontal velocity of $\frac{2}{3}\sqrt{gD_o}$ (Ritter, 1892).

3.1.3 Results and discussion

As a first step, the NS model is tested with a dam-break laboratory experiment. The experiment described in Shigematsu *et al.* (2004) is used for the test. They investigated the effect of the pull-up motion of the dam-gate, concluding that the agreement between the experimental data and the NS numerical solution is much better when the actual dam-gate movement is taken into account. The tank is 90 cm long, 29.5 cm wide, and 42.5 cm high. The dam-gate, a plate of 5 mm thickness, is located at 29 cm from one end of the tank. The reservoir is filled with water up to $D_o = 20$ cm. The dam-gate is gradually pulled up by hand, taking approximately 0.1 s. In terms of the dimensionless time $t_* = t\sqrt{\frac{g}{D_o}} \simeq 0.7$. The dam-gate motion is described by

$$Z(t) = 2.36 \times 10^3 t^2 + 1.34 \times 10t - 20, \tag{118}$$

where t is time in seconds and $Z(t)$ is given in centimeters. The dam-gate is removed gradually in the numerical computation according to Eq. (118). Parameters for the numerical computation are: model domain [90 cm×21 cm], $\delta x = \delta y$ =0.25 cm and $T = 2 \times 10^{-4}$s. The time step T ensures that water particles or moving objects traverse a cell in at least three time steps. Viscous effects and bed friction have

Reproduced with permission of the copyright owner. Further reproduction prohibited without permission.

been neglected. The slip condition is used at the bottom bed since the given spatial resolution cannot resolve the near-bed layer turbulence.

Fig. 26 shows NS results compared with experiment data for $t_* = [0.28, 0.63, 0.98, 1.33, 1.68, 2.03]$. Overall agreement with the experiment is good and very similar to the NS results reported by Shigematsu *et al.* (2004). There are some small differences in the wave front at early stages, i.e., $t_* = 0.28$ and $t_* = 0.63$. The experiment shows small-scale turbulence that the two-dimensional NS model cannot reproduce by the numerical laminar dissipation or by unresolved near-bed layer dissipation. This small turbulence is generated through either bottom friction or wave breaking and it is confined in a thin layer near the bed. It is noticeable that most of the turbulence concentrates near the wave front at very early stages. However, this case study has proved that the proposed NS solver can be used for describing flows with similar characteristics and as a validation tool for the NLSW approach.

To study the hydrostatic-nonhydrostatic models behavior some modifications to the latter setup are done. Now, the numerical tank has an infinite reservoir and the dam-gate brakes instantaneously (no gate) at $t = 0$ releasing the water immediately upstream. Under these conditions, the NLSW result for the free surface profile is depicted in Figs. 27–29 and compared with its analytical solution and NS model's results. As seen from Figs. 27–29, the NLSW numerical model reproduces both shapes of the free surface and the motion of the positive and negative waves of its analytical solution well. Small differences are noticeable at the location of the wave front tip, which can be minimized if a finer space-time resolution is used. It is worth mentioning that, in a finer resolution, the NLSW numerical model reproduces exactly the analytical solution. However, NS results are quite different in the early stages, i.e., $0 < t^* \leq 2.03$. The wave front speed on the dry bed is smaller than the speed obtained by the NLSW solutions. Strong vertical velocities develop during the wave

Reproduced with permission of the copyright owner. Further reproduction prohibited without permission.

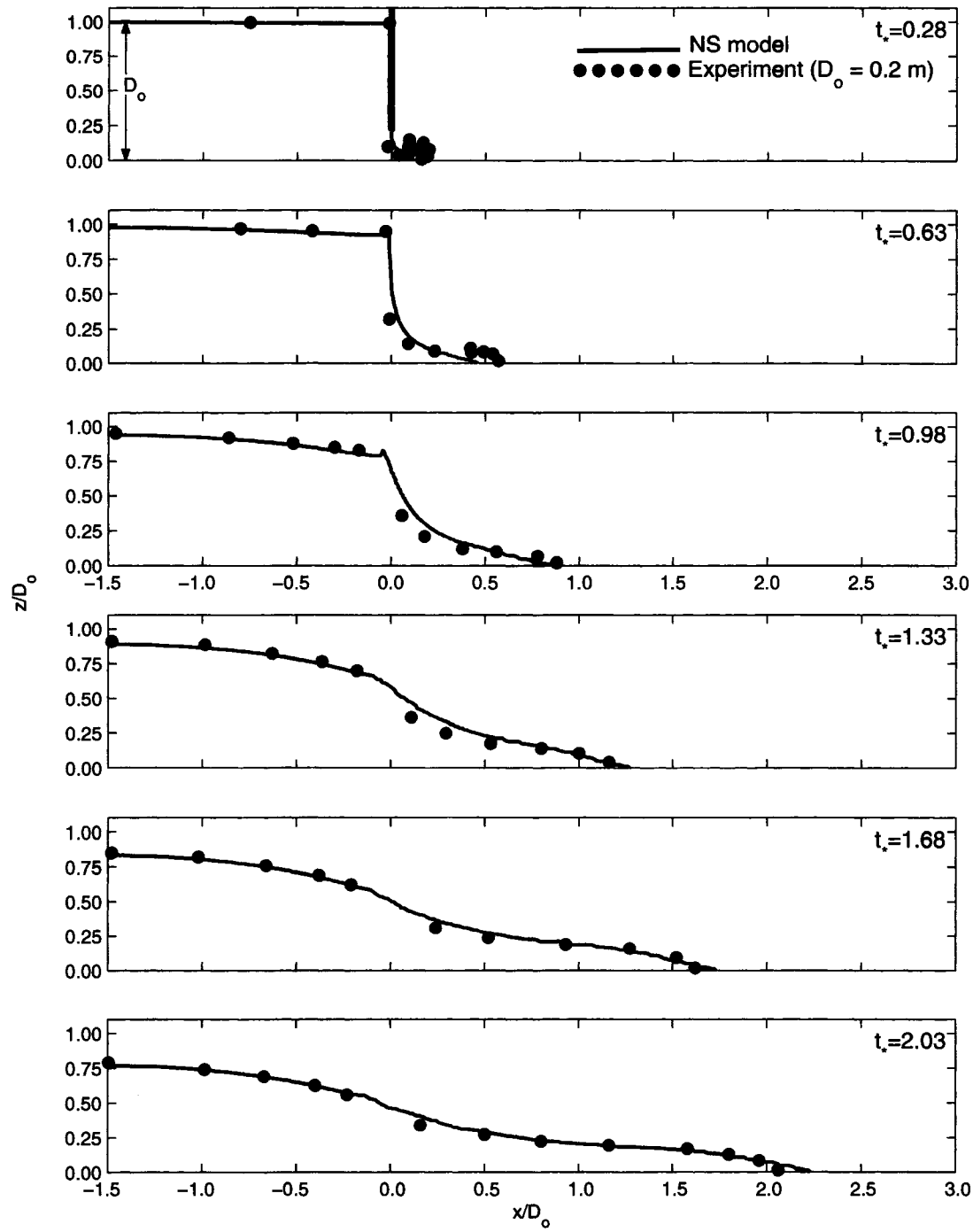

Figure 26: Gradual dam-break free surface profiles by NS model and laboratory experiment.

Reproduced with permission of the copyright owner. Further reproduction prohibited without permission.

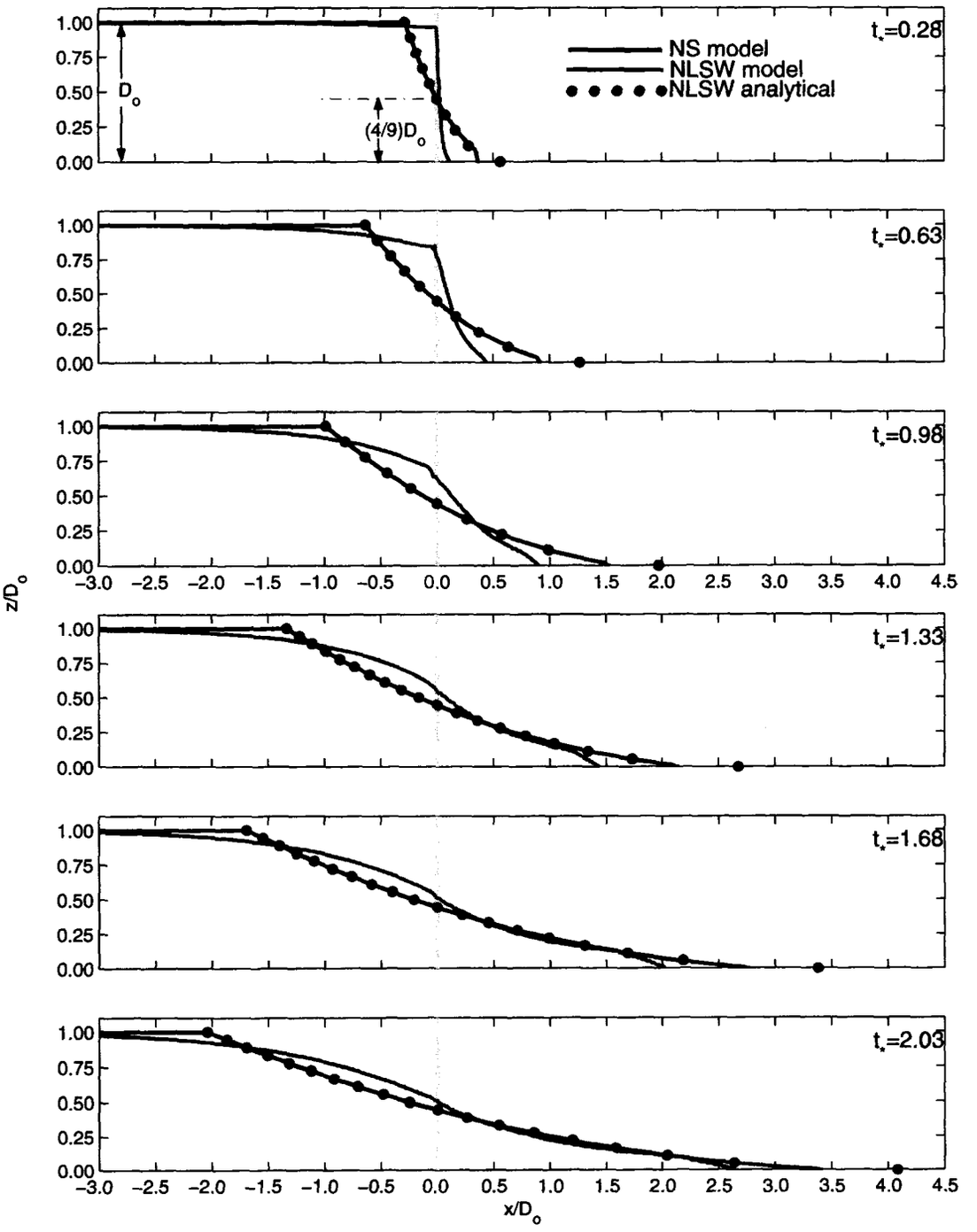

Figure 27: Instantaneous dam-break free surface profiles ($t_* = [0.28\ 0.63\ 0.98\ 1.33\ 1.68\ 2.03]$) by NS, NLSW results and analytical solution.

Reproduced with permission of the copyright owner. Further reproduction prohibited without permission.

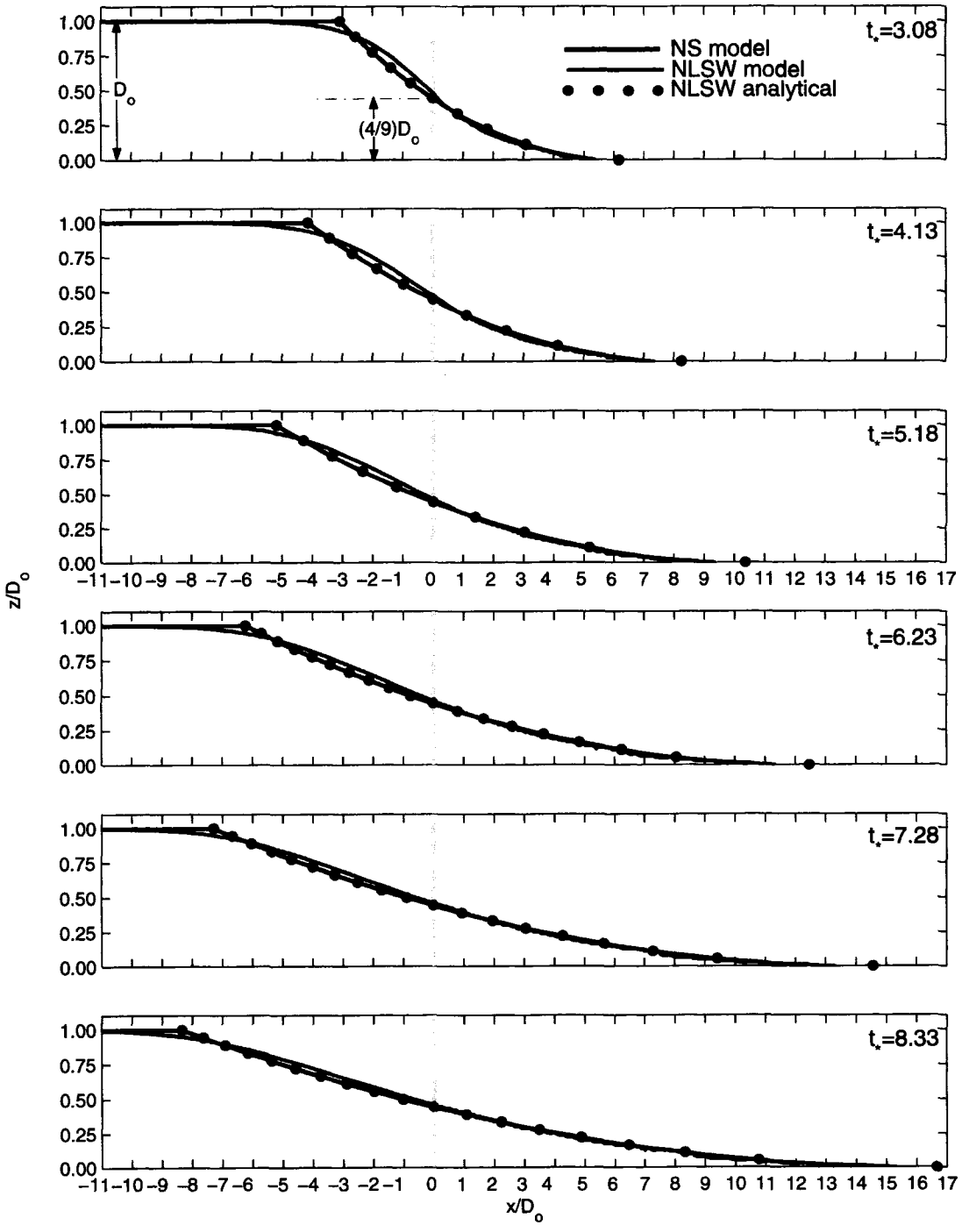

Figure 28: Instantaneous dam-break free surface profiles (t_* = [3.08 4.13 5.18 6.23 7.28 8.33]) by NS, NLSW results and analytical solution.

Reproduced with permission of the copyright owner. Further reproduction prohibited without permission.

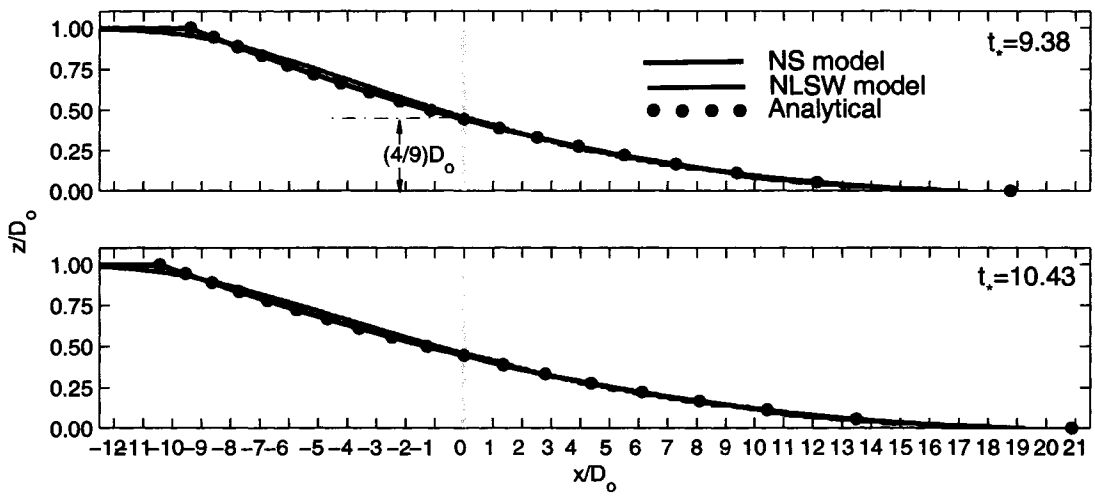

Figure 29: Instantaneous dam-break free surface profiles ($t_* = [9.38\ 10.43]$) by NS, NLSW results and analytical solution.

gravitational collapse, therefore, in this initial stage, the negative wave front is much faster than the positive wave front. This phenomenon significantly increases the leading edge thickness of the fluid propagating onto the dry bed. At later times ($t_* > 2.03$), the NS and NLSW solutions agree better.

Kosorin (1983) demonstrated that the nonhydrostatic pressure distribution reduces the wave tip speed by about 30%. Fig.30 shows a comparison of the NS wave tip location and velocity against the NLSW solution. The solution based on the hydrostatic assumption (NLSW) overpredicts the location of the wave tip, which is more pronounced during the initial stage ($0 < t^* \leq 2.03$). On the average, the NS wave tip speed is ≈ 1.3 nondimensional velocity units rather than a value of 2 as predicted by the hydrostatic solution. In this initial stage the hydrostatic approach overpredicts by about 54% the wave tip speed.

For a longer period of averaging, i.e., $0 < t^* \leq 10.43$, the averaged NS wave tip speed is 1.6. In this range, hydrostatic solution overpredicts the wave tip speed by

Reproduced with permission of the copyright owner. Further reproduction prohibited without permission.

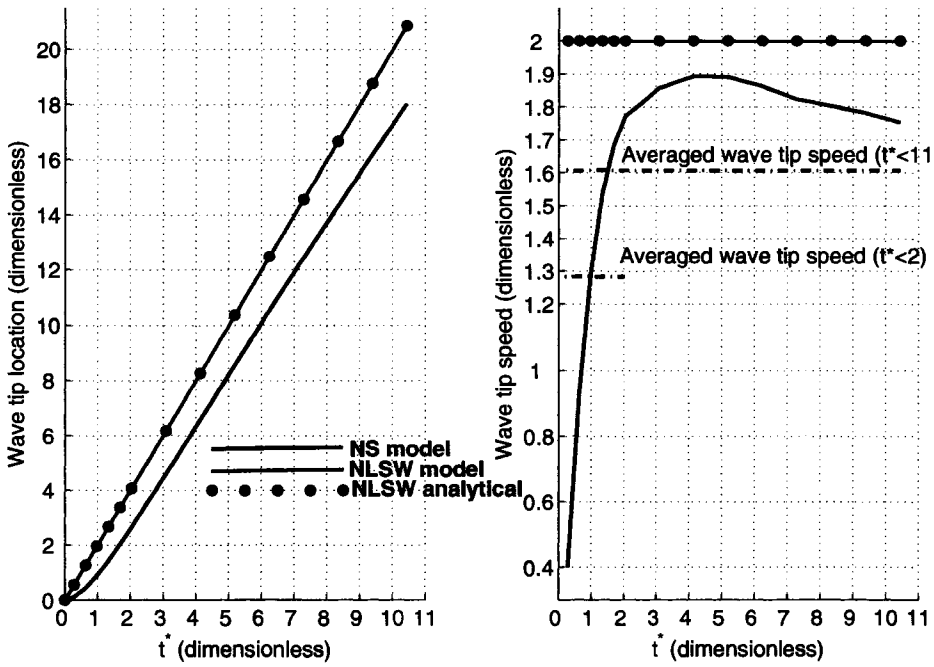

Figure 30: Comparison of wave tip location and wave speed by NLSW solutions and NS model.

about 25%. This value is close to the value of 30% suggested by Kosorin (1983). Similar results have been reported by Mohapatra *et al.* (1999).

Another interesting observation is the evolution of the water depth at the dam site. Dressler (1954) experimentally showed that the water depth at the dam site does not reach a constant value instantaneously after the dam-gate breaks, as predicted by Ritter (1892) and Stoker (1957) who used the hydrostatic assumption. It takes approximately 9 nondimensional time units to reach the constant value of $(4/9)D_o$. This is observed in the nonhydrostatic solution, i.e., at $t_* > 9.38$, where the water depth at the dam site practically matches the constant value of $(4/9)D_o$.

Reproduced with permission of the copyright owner. Further reproduction prohibited without permission.

3.1.4 Conclusions

The dam-break wave front during the initial stage cannot be modeled adequately by NLSW approach. The vertical velocity component is significant and can not be neglected, furthermore, turbulence plays an important role in the early stage of the wave front evolution. However, at a later time this initial nonhydrostatic state does not appreciably affect the long-term NLSW results. The solutions based on the hydrostatic assumption overpredict the location of the wave tip, being more pronounced during the initial stage, i.e., $0 < t^* \leq 2$; in this range, the averaged tip speed is overpredicted by about 54%. In the long-term, i.e., $0 < t^* \leq 11$, the averaged tip speed is overpredicted by 25%. The water depth at the dam site does not reach a constant value instantaneously after the dam-gate breaks as predicted by the hydrostatic assumption. It takes approximately 9 nondimensional time units to reach the constant value of $(4/9)D_o$. The free surfaces computed by the NS approach agree fairly well with experiment. Some differences are noticeable where turbulence near the free surface occurs. An advance in time of the wave profile is visible shortly after the wave generation, which might be attributed to initial turbulence phenomena and compressibility that the NS model does not consider.

3.2 Numerical simulation of runup onto a plane beach

3.2.1 Introduction

This is a simple setup for tsunami runup models validation, where the analytical solution of the problem is compared with results of three numerical models, namely nonlinear shallow water (NLSW) first and second order accurate in time, and the Navier-Stokes aided by the volume of fluid method (NS-VOF). A uniformly sloping beach and no variation in the lateral direction is used (one-dimension for NLSW models and two-dimension for the NS-VOF). The initial-value-problem technique introduced by Carrier, Wu & Yeh (2003) is used to produce the benchmark data. The

Reproduced with permission of the copyright owner. Further reproduction prohibited without permission.

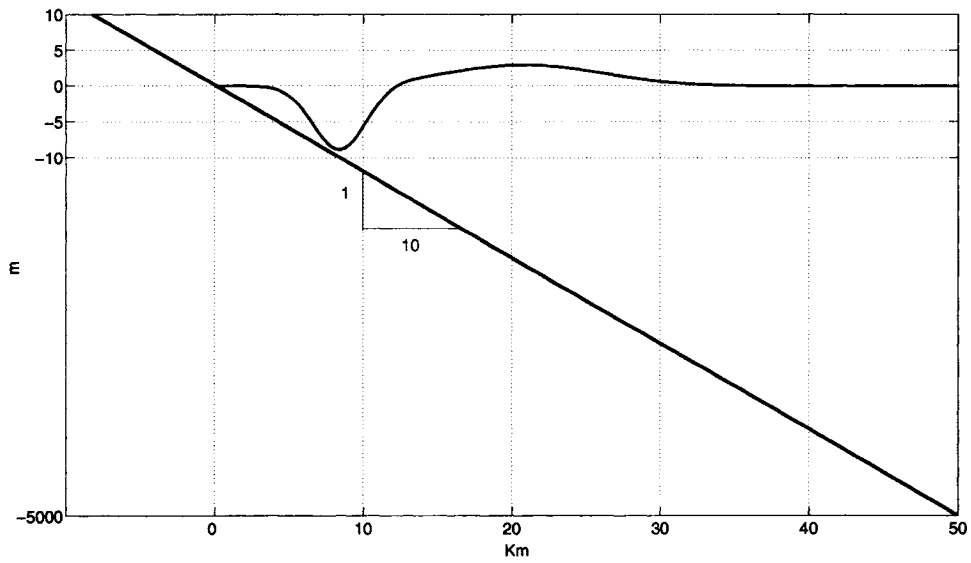

Figure 31: Model setup for numerical simulation of runup onto a plane beach.

beach slope is 1/10 and the initial free surface elevation is given as described in Fig. 31.

The objective is to compute and present the snapshots of the free surface and velocity profiles at nondimensional time t^* =2.2411 (160 s), 2.45512 (175 s) and 3.0815 (220 s) using the three models, and compare them with the analytical result. The detailed shoreline trajectory is the primary theme. The motion of the shoreline from $t^* = 1.5$ (107 s) to 3.5 (250 s) is presented using the three models. The analytical solution of the problem is given by Carrier *et al.* (2003).

To solve the model problem three approaches have been carried out:

1) NLSW (first order approximation in time).

2) NLSW (second order approximation in time (leap-frog)).

Reproduced with permission of the copyright owner. Further reproduction prohibited without permission.

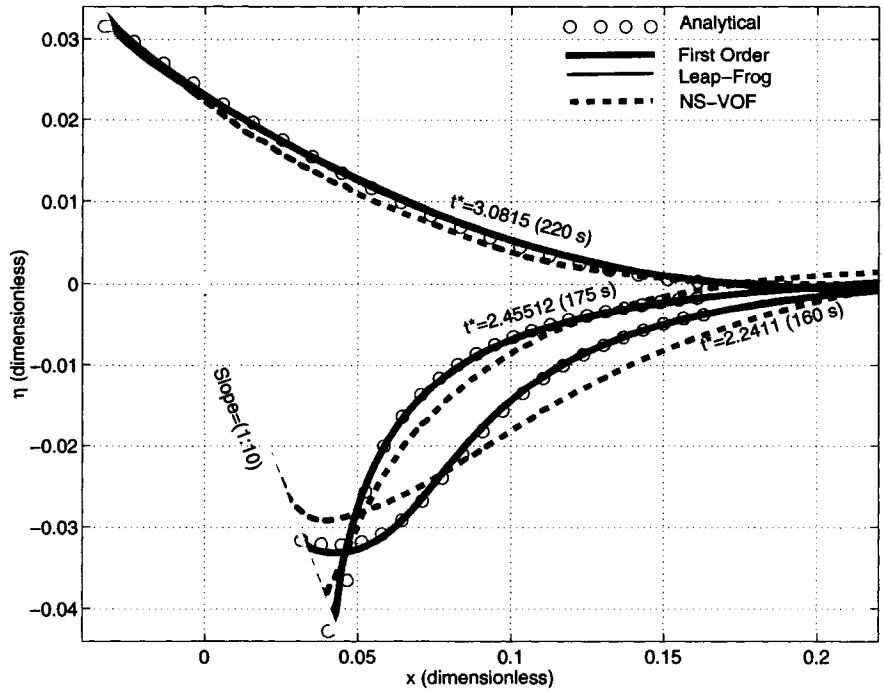

Figure 32: Snapshots of free surface profile at time $t = [160, 175, 220]s$.

3) The proposed NS approximation aided by the VOF method to track the free surface.

Approach 1) and 2) use one-dimensional NLSW wave theory. The finite difference solution of the equations of motion and continuity are solved on a staggered grid where both methods have second order approximation in space, see Appendices A and B for model information. The NS-VOF approach is used to visualize differences against the NLSW approaches and analytical solution. The NS equation includes the vertical component of velocity/acceleration so a more accurate solution is expected.

3.2.2 Discussion and conclusions

Figs. 32, 33 and 34 summarize results for the validation and comparison between models. The simple velocity extrapolation used in the first order method for runup (see Appendix A) seems to follow the shoreline evolution as prescribed by the NLSW

Reproduced with permission of the copyright owner. Further reproduction prohibited without permission.

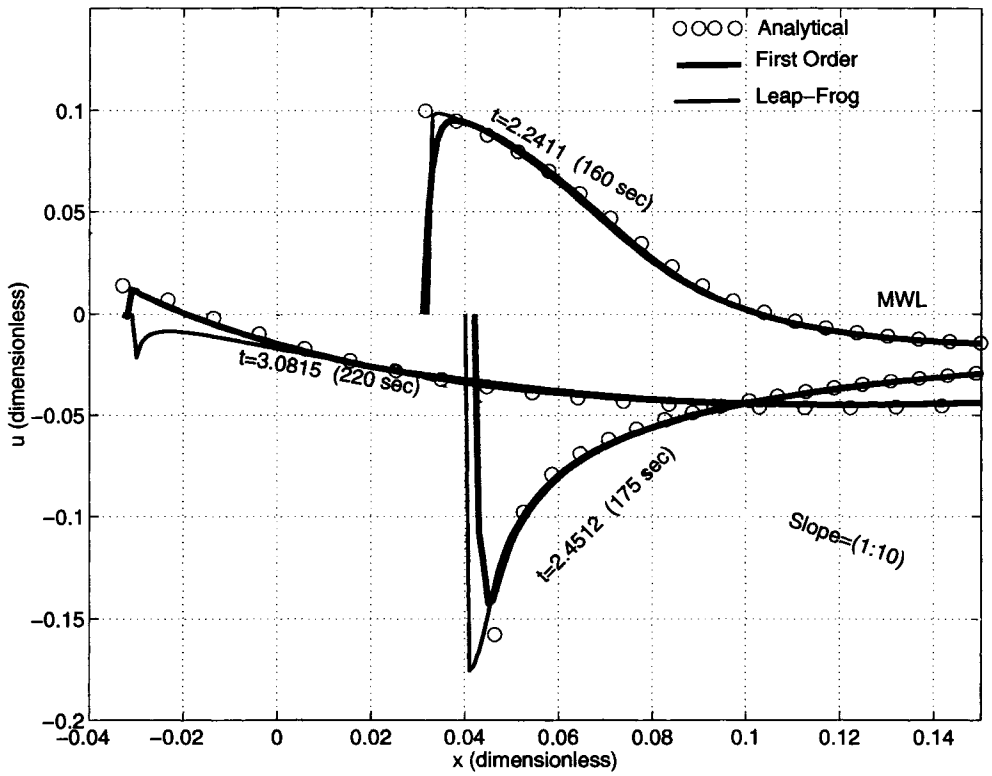

Figure 33: Snapshots of velocity profiles.

analytical solution. Sea level (Fig. 32) and velocity profile (Fig. 33) match very well with the analytical solution. The extrapolation of the velocity from the immediate wet cell to the dry cell used in the first order method facilitates runup, improving the timing. On the other hand, the leap frog method does well in predicting the analytical solution of the shoreline evolution, sea level and velocity profile, as well. However, due to the small difference in timing, some discrepancy in the velocity profile can be seen, i.e., at time t^* =3.0815 (220 s) in Fig. 33. The NS-VOF method gives a frame of reference to validate the NLSW solutions. Some differences in wave profile, shore line evolution and timing are quite plausible, since the NS approximation allows vertical fluid velocity/acceleration while the NLSW theory does not. Note, that NS's velocity profiles are not presented in Fig. 33, since NS's velocity distribution in the

Reproduced with permission of the copyright owner. Further reproduction prohibited without permission.

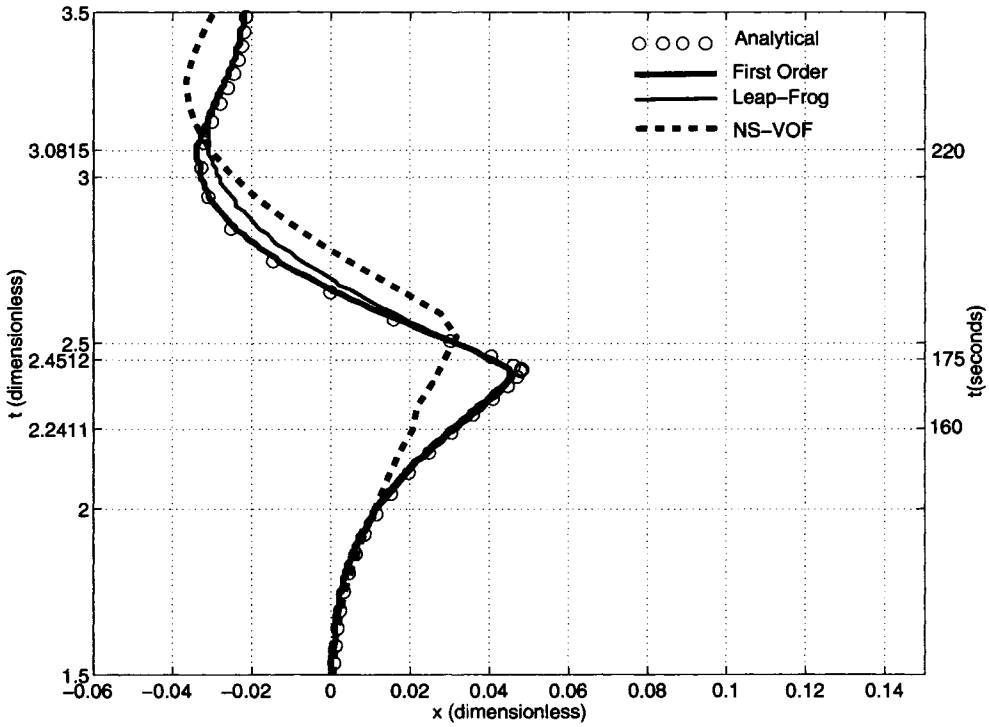

Figure 34: Temporal and spatial variations of the shoreline.

vertical direction is not constant. From Figs. 32 and 34, it is clear that dispersion effects are important. NLSW models and NLSW analytical solution underestimate the runup and overestimate the rundown. Timing of maximum runup and rundown occur slightly earlier in the NLSW solutions.

3.3 Numerical simulation of a deformable-subaerial landslide

3.3.1 Introduction

The objective of this case study is to predict the free surface elevation and runup associated with translating a Gaussian shaped mass which is initially at the shoreline. The mass moves down slope and deforms according to a given prescription. Fig. 35 depicts model setup and shows sequences of the Gaussian shaped mass translating down slope.

Reproduced with permission of the copyright owner. Further reproduction prohibited without permission.

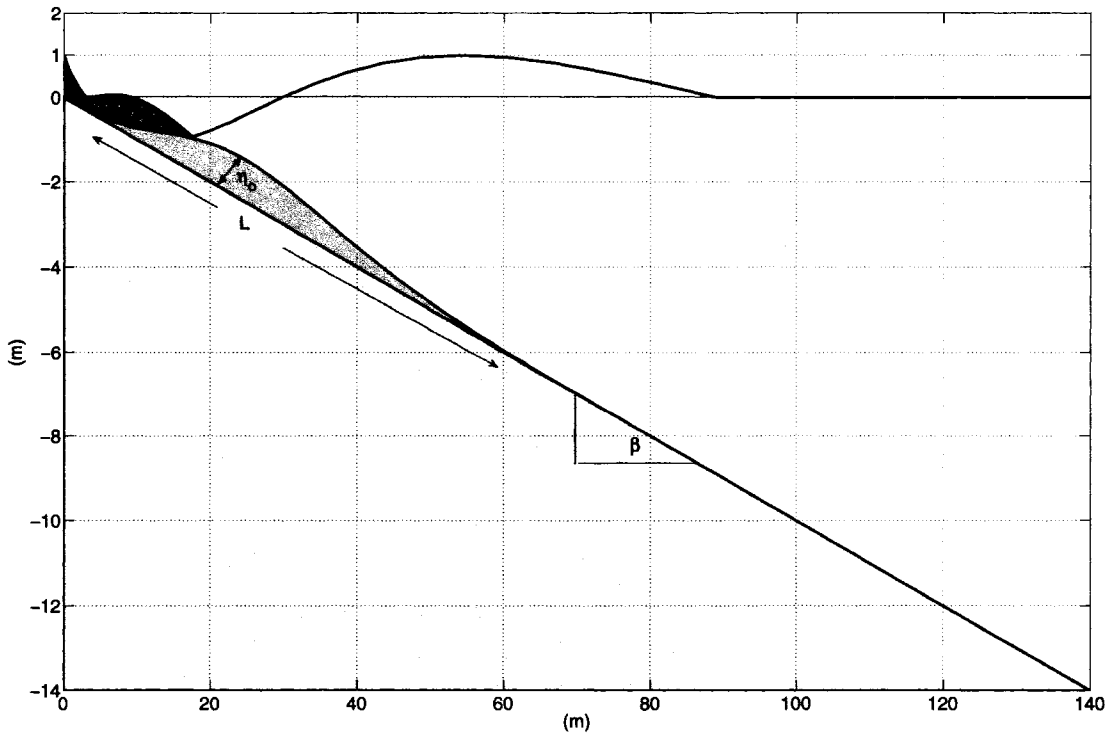

Figure 35: Definition sketch for the deformable-subaerial landslide. Sequences of a Gaussian shaped mass translating down slope.

In dimensional form, the seafloor can be described by

$$\eta(x,t) = H(x) + \eta_o(x,t) \tag{119}$$

where

$$H(x) = x\tan(\beta), \tag{120}$$

and

$$\eta_o(x,t) = \delta \exp\left[-\left(2\sqrt{\frac{x\mu^2}{\delta\tan(\beta)}} - \sqrt{\frac{g}{\delta}}\mu t\right)^2\right]. \tag{121}$$

η_o is the slide thickness, δ is the maximum vertical slide thickness, $\mu = \delta/L$ is the slide thickness-length ratio, and β is the slope angle. Once in motion, the mass moves at constant acceleration. For the prediction of the free surface, two numerical models

Reproduced with permission of the copyright owner. Further reproduction prohibited without permission.

are used, namely the linear and nonlinear shallow water (NLSW and LSW) and the Navier-Stokes aided by the volume of fluid method (NS-VOF).

Two experiment setups are used to test the numerical models. The experimental setups are:

A. $\tan\beta/\mu = 10$. Where: $\beta = 5.7°$, δ =1 m and $\mu = 0.01$

B. $\tan\beta/\mu = 1$. Where: $\beta = 5.7°$, δ =1 m and $\mu = 0.1$.

The free surface locations are determined at selected times as follows:

A. $\sqrt{\frac{g}{\delta}}\mu t = 0.1, 0.5, 1.0, 1.5$ (non-dimensional times)

B. $\sqrt{\frac{g}{\delta}}\mu t = 0.5, 1.0, 2.5, 4.5$.

In addition, a LSW analytical solution is used for validation of the models and to compare results when nonlinear terms are not taken into account. The analytical solution of the problem is described by Liu, Lynett & Synolakis (2003).

3.3.2 Numerical results and comparison with analytical solution

LSW and NLSW approaches use one-dimensional linear and nonlinear shallow water wave theories, respectively. The finite difference solution of equations of motion and continuity is obtained using a staggered grid (Kowalik & Murty, 1993*a*). This method has second order approximation in space and first order in time. More detailed information is given in Appendix A.

The two-dimensional NS-VOF solution has been included to visualize differences against the shallow water solutions and its linear analytical solution. The NS's finite difference solution is obtained on a rectilinear mesh using the algorithm extension for moving objects. Since NS's equation includes the vertical component of velocity/acceleration and dispersion effects, more accurate results are expected. Some differences could be enhanced if nonhydrostatic effects are strong.

Reproduced with permission of the copyright owner. Further reproduction prohibited without permission.

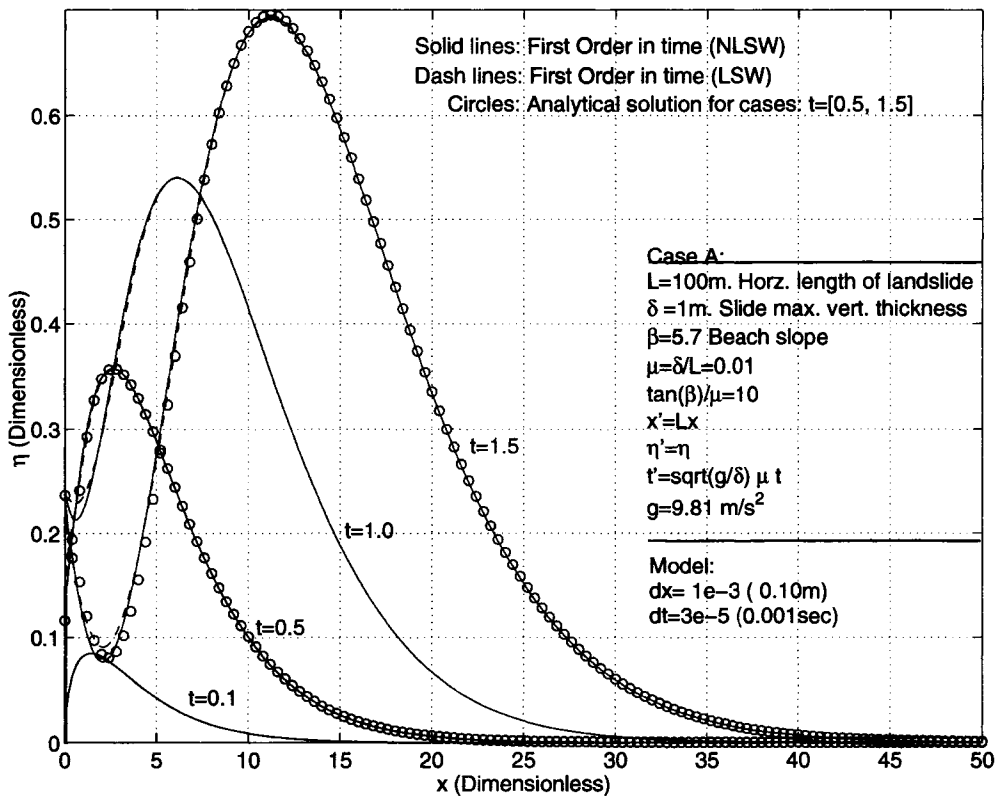

Figure 36: CASE A: ($\tan\beta/\mu = 10$). Free surface comparison. Numerical model parameters and information.

3.3.3 Discussion

For Case A, model setup information and results obtained using NLSW, LSW models and LSW analytical solution are depicted in Fig. 36. Agreement of the numerical model results, NLSW and LSW, with the analytical solution are quite good. For thin slide, i.e., $\tan\beta/\mu = 10$, the shallow water numerical models do an excellent job in reproducing analytical solution. i.e., wave runup and free surface. As is seen, no major differences exist between the NLSW and LSW results when slide thickness is small, i.e., $\mu = 0.01$.

A NS-VOF solution is presented just for Case B to compare with the NLSW model solution. NS-VOF model was chosen to solve Case B, since it offers a more interesting

Reproduced with permission of the copyright owner. Further reproduction prohibited without permission.

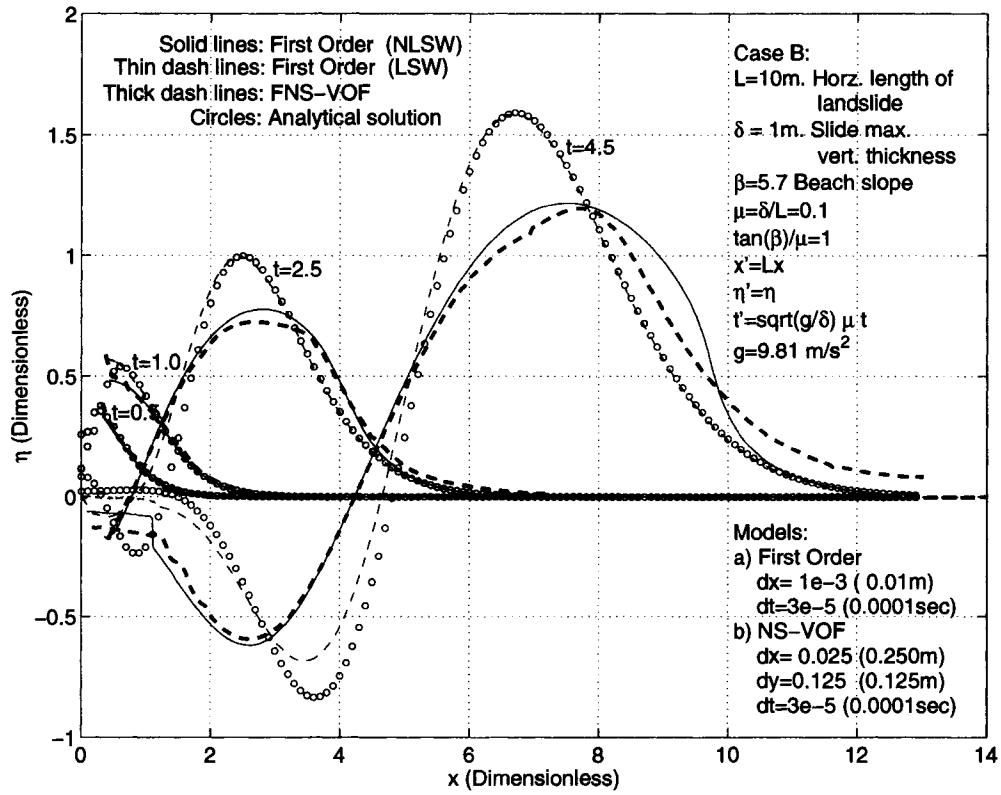

Figure 37: CASE B: $(\tan\beta/\mu) = 1)$. Free surface comparison. Numerical model parameters and information.

vertical acceleration than Case A. The NS-VOF solution is ideally suited for cases where relatively high vertical velocity occurs. In Fig. 37, all numerical models and analytical solution agree very well at earlier stages, i.e., $t = 0.5$ and $t = 1$. However, due to dispersion effects, NS-VOF model predicts a wave profile a bit more elongated, skewed but slightly shorter than the NLSW model, i.e., at $t = 2.5$ and $t = 4.5$.

For the thicker slide (Case B), the omission of nonlinearity leads to disagreements in later stages of wave propagation and runup, i.e., $t > 1.0$ (see Figs. 37 and the zoomed shoreline region in Fig. 38). Note that the LSW numerical result follows its analytical solution in all stages of wave propagation very well and fairly well the runup location. However, LSW solutions when compared with NLSW and NS-VOF

Reproduced with permission of the copyright owner. Further reproduction prohibited without permission.

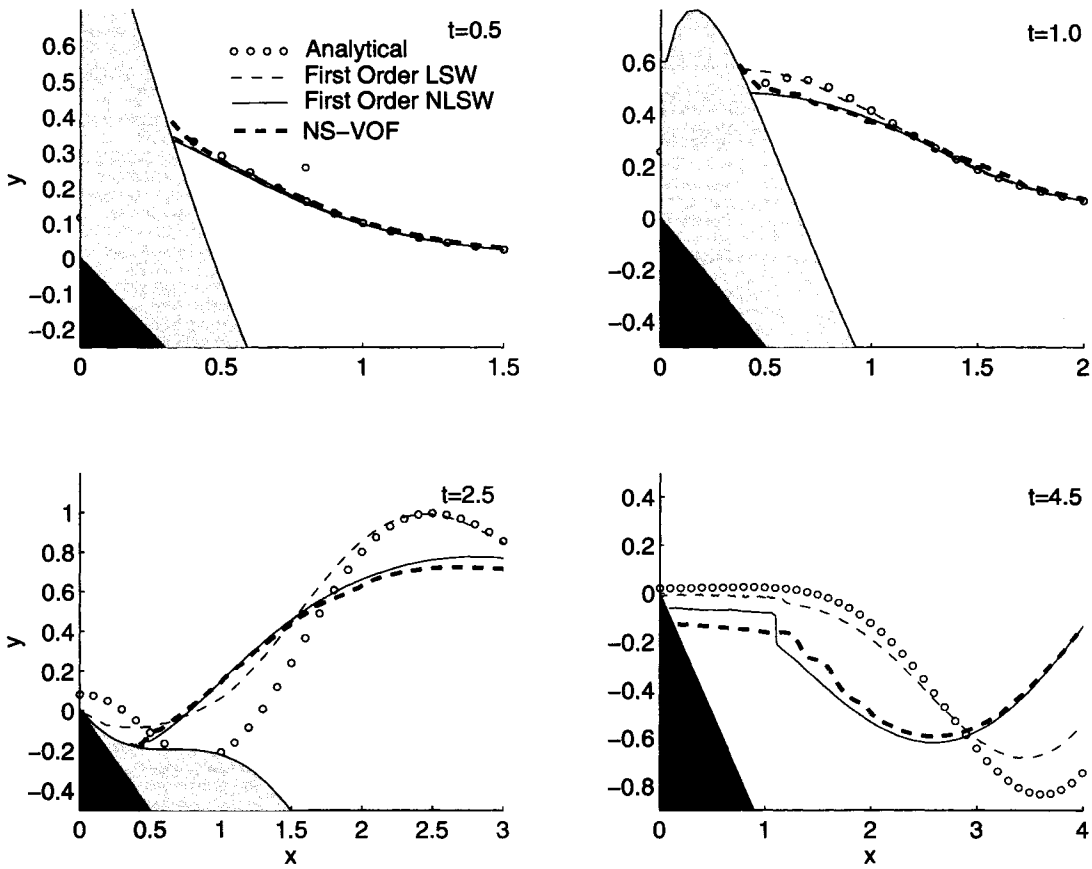

Figure 38: Case B: ($\tan\beta/\mu = 1$). Shoreline location comparison (shoreline zoom from Fig. 37).

model solutions disagree completely at later stages of wave propagation (i.e., $t > 1.0$). This is due to omission of the nonlinear terms.

3.3.4 Conclusion

Agreements of LSW and NLSW models versus analytical solution are quite good when slide thickness is small, i.e $\tan\beta/\mu = 10$, and no major differences exist between the LSW and NLSW results. For thick slides, omission of the nonlinear term leads to differences in solutions, which becomes stronger in time.

A NS-VOF solution is presented for Case B to compare with the NLSW solution. The comparison shows some reasonable differences since this method solves the two-

Reproduced with permission of the copyright owner. Further reproduction prohibited without permission.

dimensional NS equations with the vertical velocity being variable along the water column, while the shallow water approach assumes constant horizontal velocity. Results obtained by this method describe a more realistic wave evolution and shoreline location.

3.4 Numerical simulation of a landslide triangular-sliding-box (TSB)

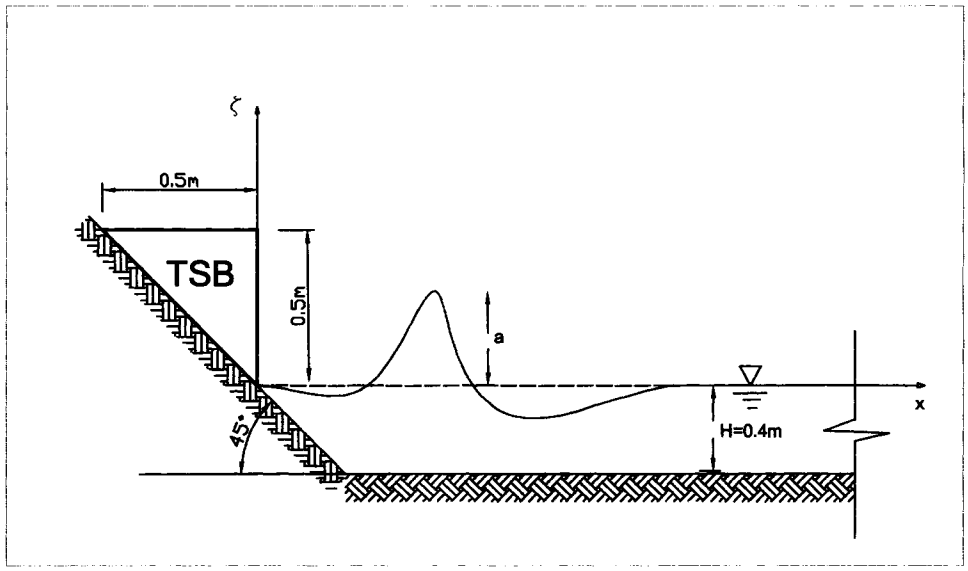

Figure 39: Definition sketch for wave generation by a triangular sliding box (TSB).

3.4.1 Introduction

The experimental case of waves generated by a TSB performed by Heinrich (1992), the aerial landslide case on a 45° plane has been chosen to test NS numerical model and its extension for moving object. This particular experiment is of interest due to the presence of high nonlinear and breaking waves. Fig. 39 depicts Heinrich's experiment.

Reproduced with permission of the copyright owner. Further reproduction prohibited without permission.

The experimental objective is to generate an impulsive wave by sliding the TSB (0.5×0.5 m section and 105 kg weight) on a 45° inclined plane. The TSB is initially just above the still water level and slides freely down slope into a water tank with water depth of 0.4 m. The vertical displacement of the TSB bottom-tip , $Z(t)$, can be approximated by

$$Z(t) = 0.4916 \times t^3 - 1.3178 \times t^2 - 0.1266 \times t,$$

where t is time in seconds and $Z(t)$ is given in meters. The TSB stops abruptly when it reaches an impact absorber just above the tank bottom at $t \approx 0.55$ s.

Fig. 40 shows NS and experiment results. In the experiment, shortly after wave generation ($0 < t < 0.55$ s), the resulting impulsive wave breaks featuring nonlinearity. The first wave, due to gravitational collapse, produces a visible second wave after reflection from the TSB vertical wall. The averaged TSB's Froude number ($F_r = V_{TSB}/\sqrt{gH}$) is roughly 0.6.

The NS numerical model information is: computational domain=[8.0 cm×0.92 m], $\delta x = \delta y = 0.01$ m and $T \simeq 10^{-3}$ s (variable). The given time step T ensures that water particles or moving object's edges traverse a cell in at least three time steps. Space resolutions have been tested for convergence. Viscous effects and bed friction have been neglected. This calculation required 800 s of CPU time on a Cray X1 for 2 s of model simulation. The generated impulsive waves are located in the intermediate water depth regime. Here, the nonlinear shallow water (NLSW) numerical model is not used, since the generated waves are under the intermediate water depth regime (no shallow water wave). Furthermore, the NLSW approach is often inaccurate for wave generation over steep slopes, since the vertical acceleration/velocity is neglected.

Reproduced with permission of the copyright owner. Further reproduction prohibited without permission.

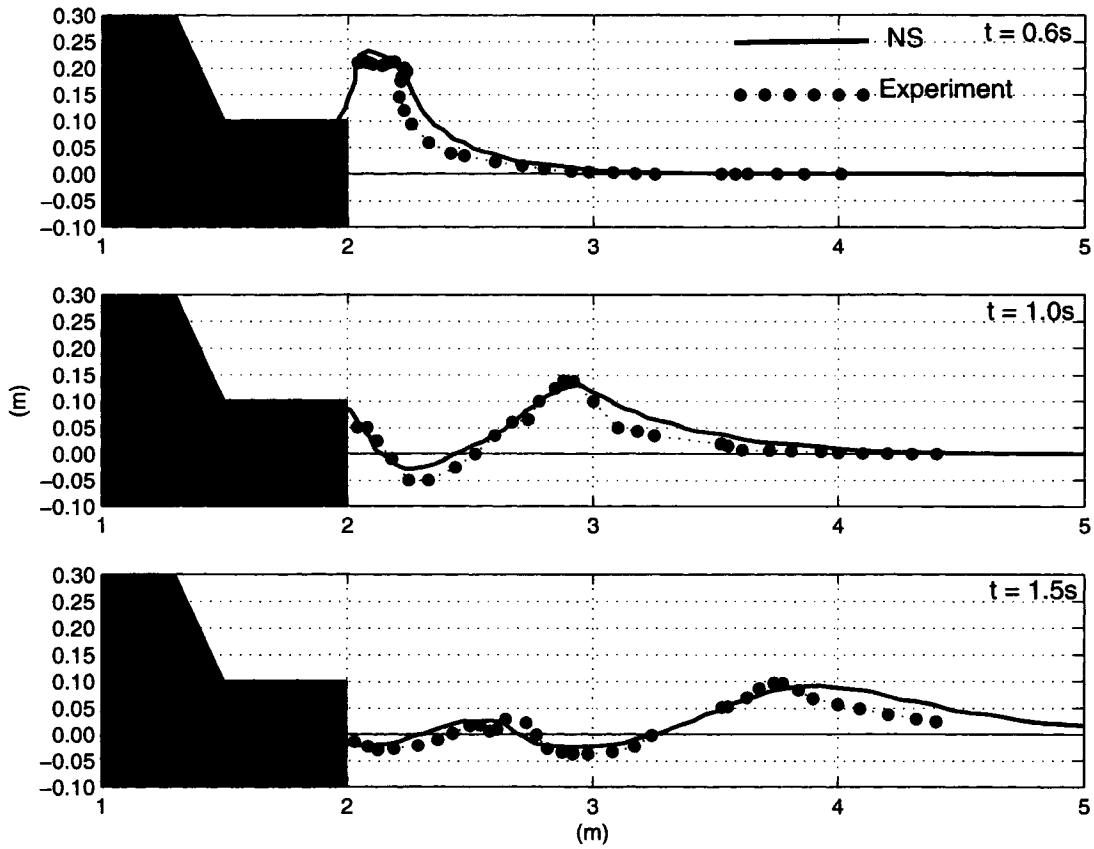

Figure 40: Sequence of free surface comparison (Navier-Stokes results versus laboratory experiment) after the triangular sliding box came to rest.

3.4.2 Discussion and conclusions

In this case study of waves generated by the TSB, the free surfaces computed by the NS approach agree well with laboratory experiment. In early stages after wave generation, some small differences are noticeable where turbulence near the free surface occurs i.e., $t = 0.6$ s. An advance in time of the first wave can be observed at $t = 1.5$ s, which might be attributed to initial turbulence phenomena and compressibility at the generation stage that the NS model does not take into account.

Caution has to be taken when the hydrostatic approach is used in wave generation regions. For instance, if a NLSW approach is used for the TSB problem, even though

Reproduced with permission of the copyright owner. Further reproduction prohibited without permission.

the initial impulsive wave would be reproduced fairly well, it will fail to predict the evolution of the wave at a later time. The wave will acquire a nearly triangular shape corresponding to the rate of volume displaced by the TSB. The initial NLSW impulsive wave will not collapse or produce a second wave. The wave will rearrange wrongly according to the shallow water phase velocity $C = \sqrt{g(\zeta + H)}$. Thus, the wave will move faster in general, and the parts of the wave having larger sea level will move faster than those wave parts having smaller sea level, causing an elongation of the wave. The generated NLSW wave will not be influenced by the gravitational collapse, either. Therefore, it would have larger amplitude than the experimental wave, and as a consequence, the NLSW wave will move faster than the wave generated experimentally.

3.5 Numerical simulation of wave propagation and dispersion. Indian Ocean tsunami, December 26, 2004.

3.5.1 Introduction

A numerical study which takes into account wave dispersion effects has been carried out in the Indian Ocean to reproduce the initial stage of wave propagation of the tsunami event that occured on December 26, 2004. Three different numerical models have been used: the nonlinear shallow water (NLSW) (nondispersive, see model description in Appendix A), the nonlinear Boussinesq (NLB) (Appendix C) and the Navier-Stokes aided by the volume of fluid method to track the free surface (NS-VOF). Numerical model results are compared against each other. General features of the wave propagation agreed very well in all numerical studies. However, some important differences are observed in the wave pattern when dispersion is not considered, i.e., the development in time of the wave front is shown to be strongly connected to the dispersion effects. Discussions and conclusions are made about the

Reproduced with permission of the copyright owner. Further reproduction prohibited without permission.

spatial and temporal distribution of the free surface, reaffirming that the dispersion mechanism is important for tsunami calculations.

Wave dispersion effects should be considered in tsunami calculations since the initial wave generated by the sea bottom uplift could have multiple amplitude and frequency components. As the initial wave propagates, separation of the wave into spectral components occurs. Thus, the leading wave reveals its amplitude as a train of waves are formed in its tail. In coastal regions close to the tsunami source but distant enough to allow this train of waves to develop, interaction of these waves with the leading wave's runup, drawdown and reflection from shelf or land is possible.

Often, populated areas along coasts are located in low-lying and flat regions that, together with natural and man made obstacles, make the retreat of the flood caused by the first tsunami wave very slow. Under these circumstances, subsequent waves as they shallow often ride over a region already flooded by the first wave, allowing these waves to impinge on structures, often with higher sea level and speed.

The multiple wave phenomenon was observed throughout the Sri Lanka coast, as described in John Headland's report at the American Society of Civil Engineering (ASCE), web page (http://www.asce.org/page/?id=53.). The first few rows of houses were destroyed by the tsunami wave, and acted to dissipate it. Interior houses, as a result, were not as extensively damaged. In another location along the coast; one witness said. "It wasn't one wave, it came in great surges, each one deeper than the last and pushing the water that had come in before in front of it". In fact, most witnesses talked of three main waves. The first knocked them off their feet, the second picked them up and carried them, often at up to 50 km/h, and the third and most powerful, bore them high, up to 15 m in some places or sucked them under. To explain these phenomena is not a simple task, since a train of waves approaching a particular coastal region, in addition to the transformation it may have experienced by dispersion

Reproduced with permission of the copyright owner. Further reproduction prohibited without permission.

effects, could be composed of a combination of waves coming from different parts of the source or it may be that these waves have been diverted by the ocean bathymetry or transformed by a submerged bar. Since this study intends to investigate the role of dispersion effects in tsunami calculations and its possible implication in propagation and runup, simplified model setups are used (one/two-dimensional) so that tsunami physics and behavior can be better explained.

Several studies have highlighted the importance of dispersion effects in tsunami propagation. Sato (1996), in the numerical calculation of the 1993 Okushiri Island tsunami, found that local tsunami enhancement can be explained by a series of dispersive waves which ride on the main tsunami front. Ortiz *et al.* (2001), suggested that the frequency dispersion mechanism, as prescribed by dispersive theory plays the main role in propagation of large and medium-size tsunamis. Heinrich *et al.* (1998), using the Boussinesq approach, found that the effect of dispersion can be significant. Imamura *et al.* (1990) and Liu *et al.* (1995) also considered the effect to be important.

In tsunami calculation, the dispersive effects are usually considered through the Boussinesq equations, Dunbar *et al.* (1991); Madsen & Schaffer (1999). Their numerical solutions require small space steps and often implicit schemes are used due to stringent numerical stability requirement (Shigihara, 2004). As the second order approximation to the numerical schemes leads to an error of approximation proportional to the third derivative, and since the dispersion terms in the Boussinesq equation also depend on the third derivatives, Imamura & Shuto (1989) constructed a numerical approach which uses numerical dispersion to simulate physical dispersion. This scheme was improved and applied to the propagation of tsunamis over slowly varying topography by Yoon (2002), thus opening the possibility of accounting for the dispersion of distant tsunamis. In the runup region, at the steep wave front where the tsunami wave starts to break, the dispersive effects tend to interact with the short

Reproduced with permission of the copyright owner. Further reproduction prohibited without permission.

wave generated by the nonlinear interactions due to limited spatial resolution, where oscillations tend to concentrate around the shortest space step. To suppress such oscillations, Goto & Shuto (1983) and Sato (1996) suggested introduction of the eddy diffusivity term. The NLSW, NLB and the NS-VOF methods are important tools for the tsunami investigations. Using these tools and hydraulic experiments Fujima (2001) examined the wave transformation on large bottom obstacles. He pointed out that the NLB approach, when compared with experiments and NS-VOF approach, reproduces the wave dispersion effects well.

This study aims to reproduce the Indian Ocean Tsunami (IOT) of Dec. 26, 2004 in its initial stage (two hours of tsunami wave propagation). With the help of the three different numerical tools for tsunami calculation mentioned above, the study demonstrates some of the effects of dispersion on tsunami propagation and runup.

3.5.2 Tsunami initial deformation

The generation mechanism for the Indian Ocean tsunami is mainly the static sea floor uplift caused by abrupt slip at the India/Burma plate interface. Permanent, vertical sea floor displacement is computed using the static dislocation formulae from Okada (1985). Inputs to these formulae are fault plane location, depth, strike, dip, slip, length and width as well as seismic moment and rigidity. The earthquake's total rupture extent can be estimated by several approaches. Finite fault seismic data inversion is one method which yields fault lengths on the order of 350 km to 650 km (e.g., Ji, 2004; Yagi, 2005). Another traditional method to delineate earthquake fault zones is plotting the aftershocks which occur in the first 24 hours following the main shock. The aftershocks are expected to cluster within the slip zone. This approach leads to an estimate of 1200 km for the fault length (NEIC -U.S. National Earthquake Information Center-, 2004). In this study, the fault extent is constrained by observed

Reproduced with permission of the copyright owner. Further reproduction prohibited without permission.

tsunami travel times to the northwest, east, and south of the slip zone. Fig. 41 displays the tsunami arrival time constraints on the fault zone. Tsunami arrival

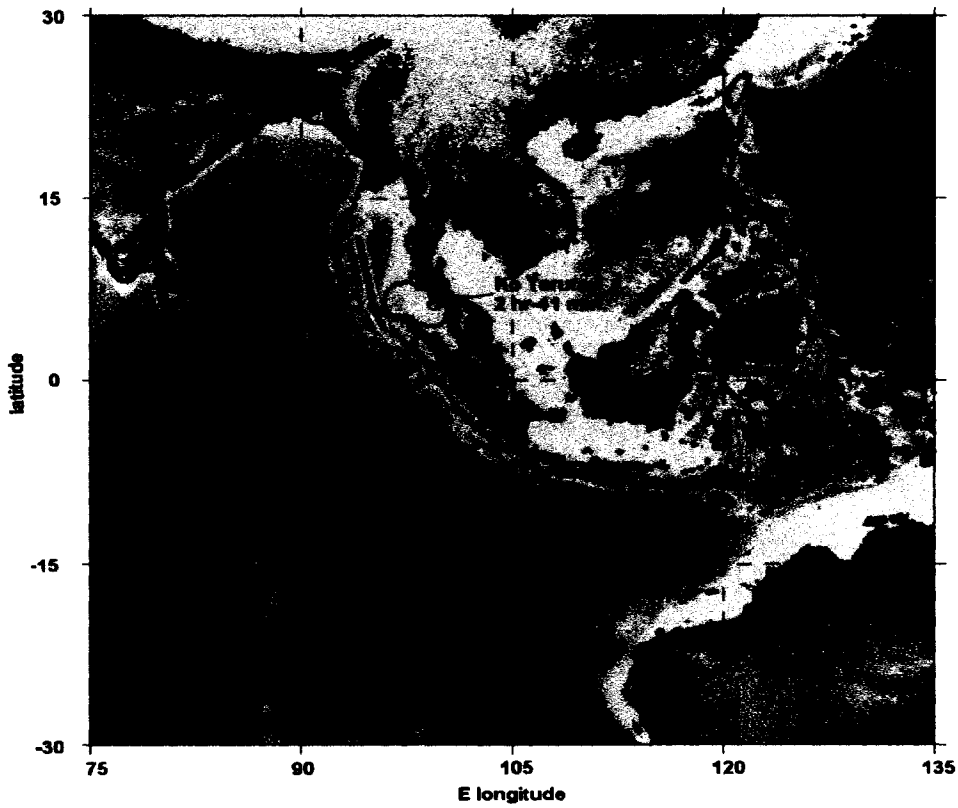

Figure 41: December 26, 2004 Sumatra earthquake uplift as constrained by tsunami travel times.

times at Paradip-India (SOI -Survey of India-, 2005), Ko Tarutao-Thailand (Iwasaki, 2005), and Cocos Island (Merrifield *et al.*, 2005) tide gauges are plotted in reverse. That is, the observed travel time contour is plotted with the tide gauge location as the origin point. This method indicates a fault zone approximately 1000 km by 200 km. The epicenter location lies on the southern end of the fault zone. To accommodate trench curvature, the fault plane is broken into two segments. Fault parameters for the two segments are listed in Table 1.

Reproduced with permission of the copyright owner. Further reproduction prohibited without permission.

Earthquake Parameters	Southern Fault Segment	Northern Fault Segment
Strike	335°	350°
Dip	8°	8°
Slip	110°	90°
Length	300 km	700 km
Depth (SW corner)	8 km	8 km
SW corner Latitude	3.0N	5.6N
SW corner Longitude	94.4E	93.3E
Moment	3.2×10^{29} dyne cm	7.6×10^{29} dyne cm
Rigidity	4.2×10^{11} dyne cm^{-2}	4.2×10^{11} dyne cm^{-2}

Table 1: Fault parameters used to generate vertical sea floor movement

Strike, dip and slip parameters are based on the definitions from Aki & Richards (1980). Strike is determined by the trench orientation. Dip is taken from the Harvard Centroid-Moment Tensor (CMT) solution (HRV -Harvard CMT Catalog-, 2005). The slip for the southern segment is based on the Harvard CMT solution while slip for the northern segment is set at 90° based on observed tsunami first motions on Indian tide gauges (NIO -India National Institute of Oceanography-, 2005). Depth is based on the finite fault inversion of Ji (2004). The total moment release (derived by assuming an average slip of 13 m and rigidity of 4.2×10^{11} dyne cm^{-2}) in the two segments equals 1.08×10^{30} dyne cm (Mw= 9.3) which is in good agreement with 1.3×10^{30} dyne cm proposed by Stein & Okal (2005), based on normal mode analysis. The total potential energy related to the bottom deformation is transferred to the sea level (Fig. 42) with a value of $\approx 5.39 \times 10^3$ terajoules.

3.5.3 Observations and discussions

First, the numerical models are applied to a simplified case for the IOT (one-dimensional channel case) along transect A-A, see Fig. 43.

Reproduced with permission of the copyright owner. Further reproduction prohibited without permission.

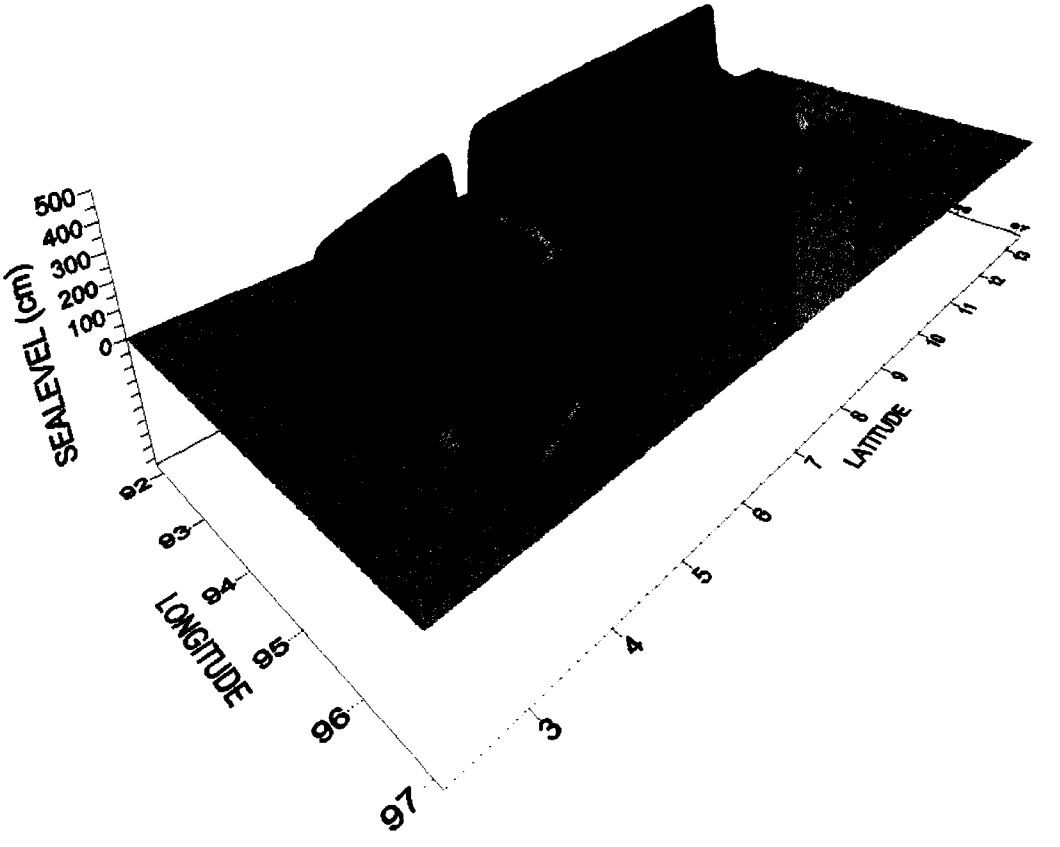

Figure 42: Tsunami initial deformation. Maximum uplift is 507 cm and maximum subsidence approximately 474 cm. Coordinates are given in degrees.

This numerical experiment is intended to visualize dispersive effects, test the NLSW (nondispersive) and NLB (dispersive) approaches and compare their results against the NS-VOF model. Transect A-A extends from 95.48° E, 4.93° N to 81.13° E, 1.8° S with a total length of $\sim$ 1745 Km. At both sides, the channel is bounded by walls so lateral wave radiation is restricted. Model parameters and CPU time for the numerical computation are given in Table 2. The chosen time step ensures that water particles travel the computational cell in at least three time steps. In all models, several spatial resolutions have been applied to verify model numerical convergence.

Reproduced with permission of the copyright owner. Further reproduction prohibited without permission.

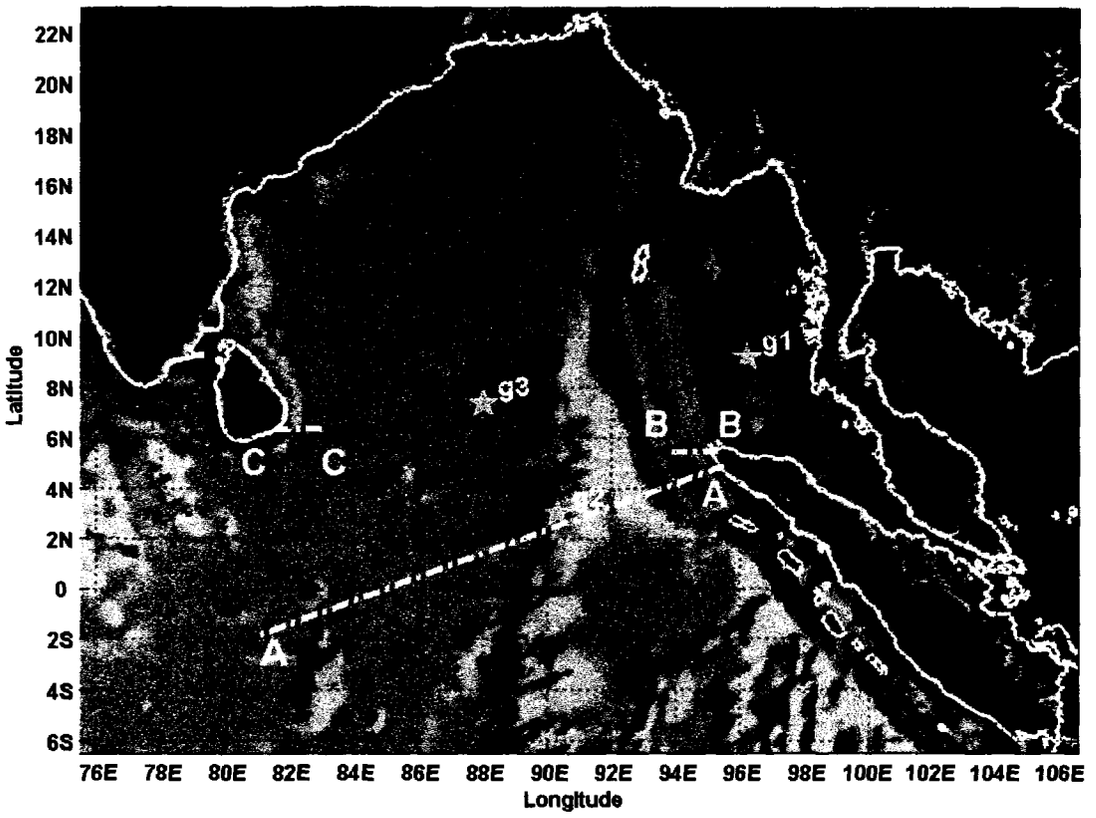

Figure 43: Indian Ocean relief. Initial free surface deformation. Location of numerical gauges and transects used in the numerical experiments.

Model	δx	δz	δt	Num. of cells	CPU time
NLSW	100 m	—	0.2 s	157059	30 min
NLB	100 m	—	0.2 s	157059	5 h
NS-VOF	(5-875) m	(0.2-40) m	(0.08-0.8) s	800000	72 h

Table 2: Parameters for the numerical computation along transect A-A (channel case)

Fig. 44 shows a series of free surface snapshots of the first two hours of the IOT propagation, based on the initial free surface deformation given by Kowalik *et al.* (2005), according to the surface deformation method described by Okada (1985). General features of the wave evolution agreed very well in all approaches. However,

Reproduced with permission of the copyright owner. Further reproduction prohibited without permission.

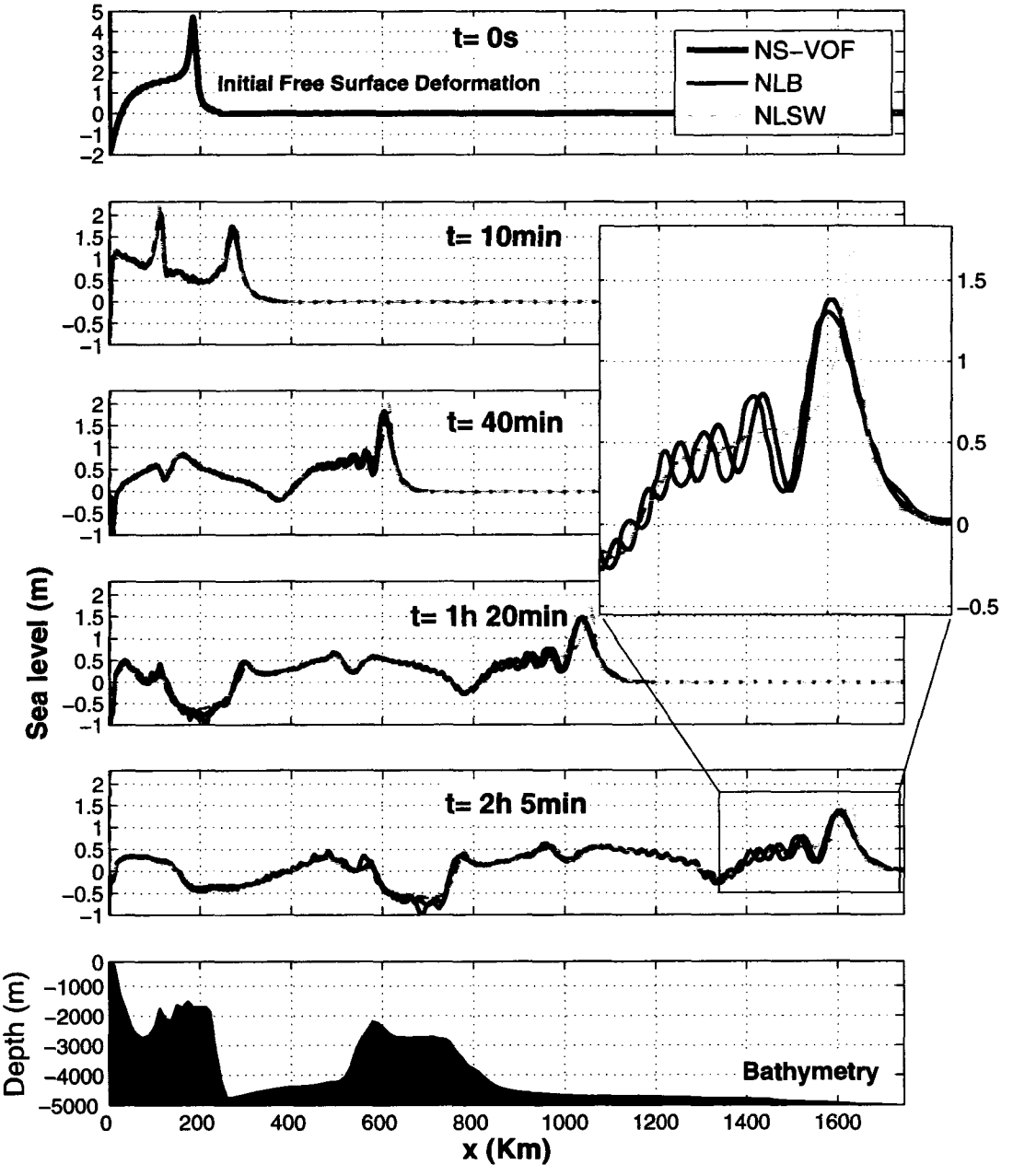

Figure 44: Tsunami along transect A-A as computed by three different methods.

some differences in reproducing the dispersion phenomena become more noticeable as time advances. For instance, at time $\geq$ 40 min, the wave dispersion is evident according to NLB and NS-VOF results. A train of waves is formed just behind the

Reproduced with permission of the copyright owner. Further reproduction prohibited without permission.

leading wave imparted by the wave signature, which comprises multiple amplitudes and frequency components. Major wave features are well reproduced by the NLSW method with the exception of the wave train. The leading NLSW wave is taller and shifted forward in space in relation to the dispersive approaches. The nondispersive NLSW approach overpredicts by $\sim$ 28% the wave height at time 2 h 5 min. A slight advance in time (2 min 15 s) of the NLSW leading wave crest is observed as well. However, the wave front tip of the NLSW leading wave matches its counterpart very well. This reaffirms the use of NLSW as an accurate candidate for determining the tsunami arrival time.

NLB and NS-VOF model results agreed better over general features. Good agreement is seen in the spatial and temporal distributions of the leading wave. However, the NLB wave train which follows the leading wave is shifted forward in time with respect to NS-VOF wave train. The shift increases in time as the wave diminishes in amplitude and length as shown in the zoomed window of Fig. 44. Values of $kh = (2\pi/L)h$ for the first, second and third wave at time 2 h 5 min according to NS-VOF results are 0.17, 0.46 and 0.56, respectively (h =4810 m is used for calculation). Their respective wavelengths are L =[179, 89 and 65] km measured from trough to trough. It is clear that the second and third waves fall into the category of intermediate water wave regime ($0.31 < kh < 3.14$). The approximation of the dispersive term in the NLB model is accurate in the estimation of wave speed for values of $kh < 1$, Kirby *et al.* (1998). In comparison to the linear dispersion relation, the error is less than 1%. Although the second, third and subsequent NLB waves shift slightly forward in relation to the NS-VOF, the NLB model does a good job in predicting the wave height, wave length and number of waves in the wave train.

The study is extended to visualize the wave dispersion effect in two-dimensions in the Bay of Bengal basin. Now, the computational domain is bounded by the window

Reproduced with permission of the copyright owner. Further reproduction prohibited without permission.

Model	δx	δy	δt	Num. of cells	CPU time
NLSW	1 min	1 min	3 s	1249600	16 min
NLB	1 min	1 min	3 s	1249600	1.5 h

Table 3: Numerical computation parameters for the two-dimensional case (Bay of Bengal case)

78° E, 1° N to 100° E, 14° N. In this experiment, just NLB and NLSW models are used. At all open boundaries, wave radiation condition is applied. Model parameters and CPU time for the numerical computations are given in Table 3. Fig. 45 shows sea level configuration at time 1 h 40 min using NLSW and NLB methods. Due to the dispersion effect, the NLB model result features a series of waves behind the leading wave, therefore the wave pattern is significantly different from that of NLSW model. From the NLB model result, it is seen that length of the wave train in the western region is longer than in the eastern region (close to Thailand and Indonesia). A simple explanation can be drawn from Eqs. (132), (133) and (134) in Appendix C, the magnitude of the dispersive term is proportional to the square of water depth; therefore, the dispersion effect in the western region (H =4–5 km) is much stronger than that in the eastern region (which is only several hundred meters deep). The obvious reason for the stronger dispersive effect in the western region is that the dispersion is enhanced by the longer distance of propagation.

Fig. 46 shows temporal variation of the free surface using NLSW and NLB models at specific locations or numerical gauges given in Fig. 43. Again, overall agreement between nondispersive and dispersive models is very good. The same behavior is observed as in the channel case along transect A-A. At gauge 1, agreement is excellent due to the proximity of the gauge to the tsunami source, since dispersive waves do not have time to develop. On the other hand, the sea level recorded at gauges 2 and 3,

Reproduced with permission of the copyright owner. Further reproduction prohibited without permission.

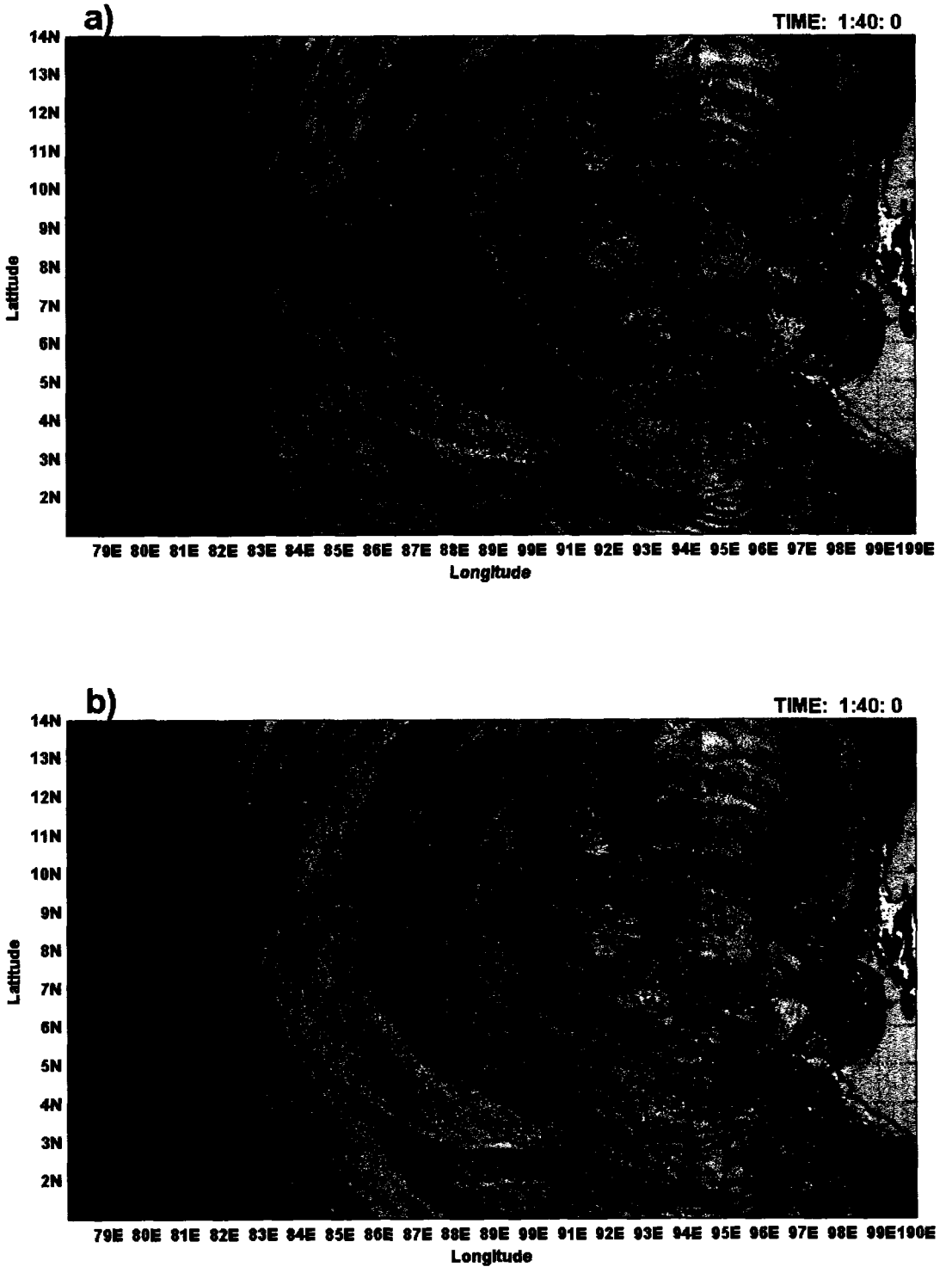

Figure 45: Comparison of water surfaces computed at 1h 40min from the onset of the earthquake: a) NLB model, b) NLSW model.

Reproduced with permission of the copyright owner. Further reproduction prohibited without permission.

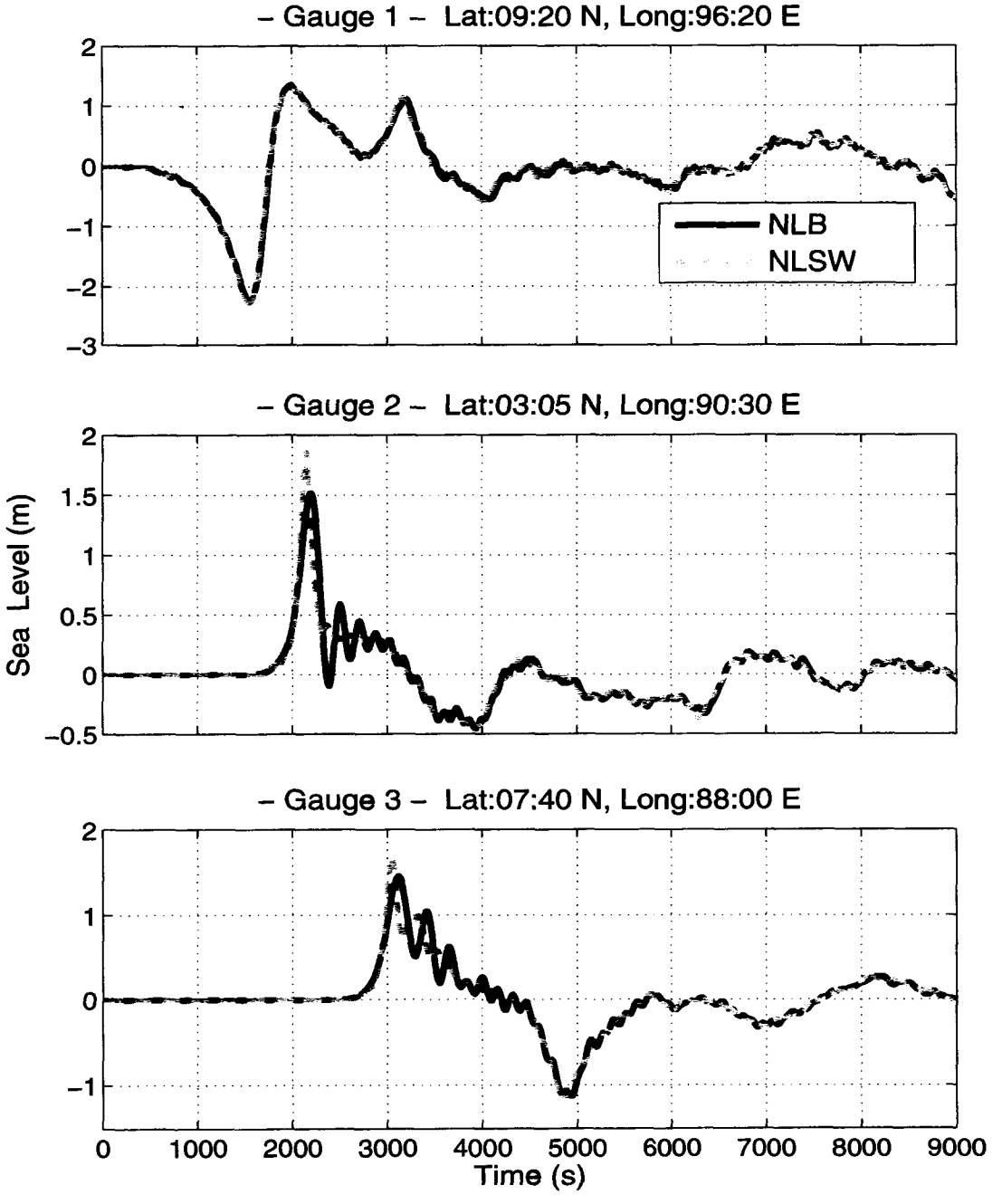

Figure 46: Comparison of water level at different locations obtained by two-dimensional NLB and NLSW models.

Reproduced with permission of the copyright owner. Further reproduction prohibited without permission.

features dispersive waves since the gauges are located farther away from the tsunami source. The leading wave height is overpredicted again by the NLSW approach by 22% at gauge 2 and by 14% at gauge 3. A shift in time of the wave crest can be noticed as well, 50 s at gauge 2, and 1 min 5 s at gauge 3. Note the good agreement of the NLSW and NLB leading wave front tip in all gauge records.

The last experiment is intended to visualize the implication of dispersive effects on the runup. Two places have been chosen, indicated by transects B-B and C-C in Fig. 43. One transect is located in the Northwest of Sumatra which was struck by a "near-field" tsunami, close to Banda Aceh. In contrast, the other one across the Bay of Bengal, Sri Lanka, experienced a "far-field" tsunami, close to Yala. The rapid arrival of the tsunami in near-field location, just 15 to 20 min, contrasts to the longer arrival in the far-field location, around 2 h. The numerical domains extend from 95.09° E, 5.47° N to 95.3° E, 5.47° N (transect B-B), and from 81.78° E, 6.35° N to 81.45° E, 6.35° N (transect C-C). At the offshore end of the channels the temporal variations of the free surface from the two-dimensional computation are established as boundary forcing. This experiment is intended to investigate the implication of dispersive effects on the runup; therefore, the two-dimensional contribution is avoided by constructing a channel to insulate the forced incident wave from other possible wave contributions coming from different routes. Unfortunately, the 1 min resolution is far too coarse to represent a runup. For the purpose of this experiment a fine grid size was used in the models by filling the gaps of bathymetry information by linear interpolation from the available data. A 10 m spatial resolution is applied in both experiments. Model parameters and CPU time for the numerical computation are given in Table 4.

Figs. 47, 48 and 49 illustrate tsunami propagation and runup in the coastal regions obtained by the NLSW and NLB models using one-dimensional channels described previously. In both experiments the computed maximum runup heights calculated

Reproduced with permission of the copyright owner. Further reproduction prohibited without permission.

Model	δx	δy	δt	Num. of cells	CPU time
NLSW (Trans.B-B)	10 m	10 m	0.2 s	22680	4 min
NLB "	10 m	10 m	0.2 s	22680	30 min
NLSW (Trans.C-C)	10 m	10 m	0.2 s	34020	5 min
NLB "	10 m	10 m	0.2 s	34020	40 min

Table 4: Parameters for the numerical computation for one-dimensional cases: Banda Aceh, Sumatra (transect B-B) and Yala, Sri Lanka (transect C-C).

by both methods are approximately 10 m. This result agrees with the observed maximum runup in Yala (http://www.drs.dpri.kyoto-u.ac.jp/sumatra/srilanka-ut/SriLankaU_Teng.html), but underestimates the observed one in Banda Aceh (http://www.eri.u-tokyo.ac.jp/namegaya/sumatera/surveylog/eindex.htm).

Fig. 47 shows snapshots of the runup at Banda Aceh at extreme stages. Regardless of the models, free surface profile, timing and runup heights match very well. On the other hand, in Yala (Fig. 49a), runup heights of the leading wave are almost the same in both models. However, Fig. 49c (3 h 7 min) shows that a higher runup is obtained by the NLB approach (37 min after leading wave runup), which is about 60% higher than the runup obtained by the NLSW approach. Thus, dispersion consideration in numerical models is necessary for accurate prediction, since it can produce significant differences in coastal runup and create oscillations according to continental shelf, bay or harbor natural frequency. Northern Sumatra is so close to the tsunami source that it is very sensitive to the tsunami source. In addition, the two-dimensional effects, a detailed topography/bathymetry, and wave refraction/reflection must be taken into consideration for a more accurate computation.

3.5.4 Conclusions

This case study compared three approaches to compute tsunami, i.e., the nonlinear shallow water (NLSW nondispersive), the nonlinear Boussinesq (NLB) and

Reproduced with permission of the copyright owner. Further reproduction prohibited without permission.

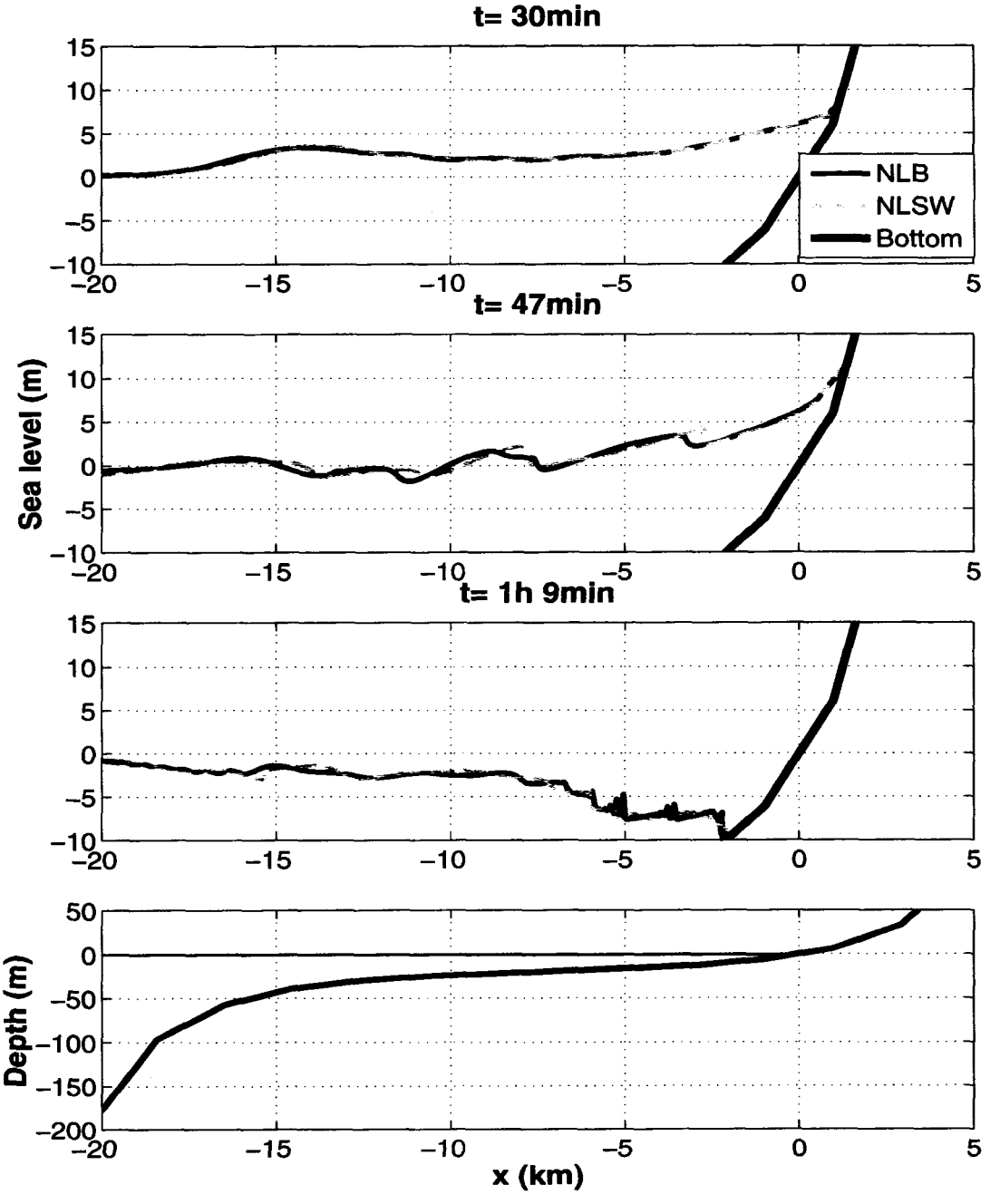

Figure 47: Comparison of tsunami runup/rundown at Banda Aceh, Sumatra (transect B-B), obtained by one-dimensional NLB and NLSW models.

Reproduced with permission of the copyright owner. Further reproduction prohibited without permission.

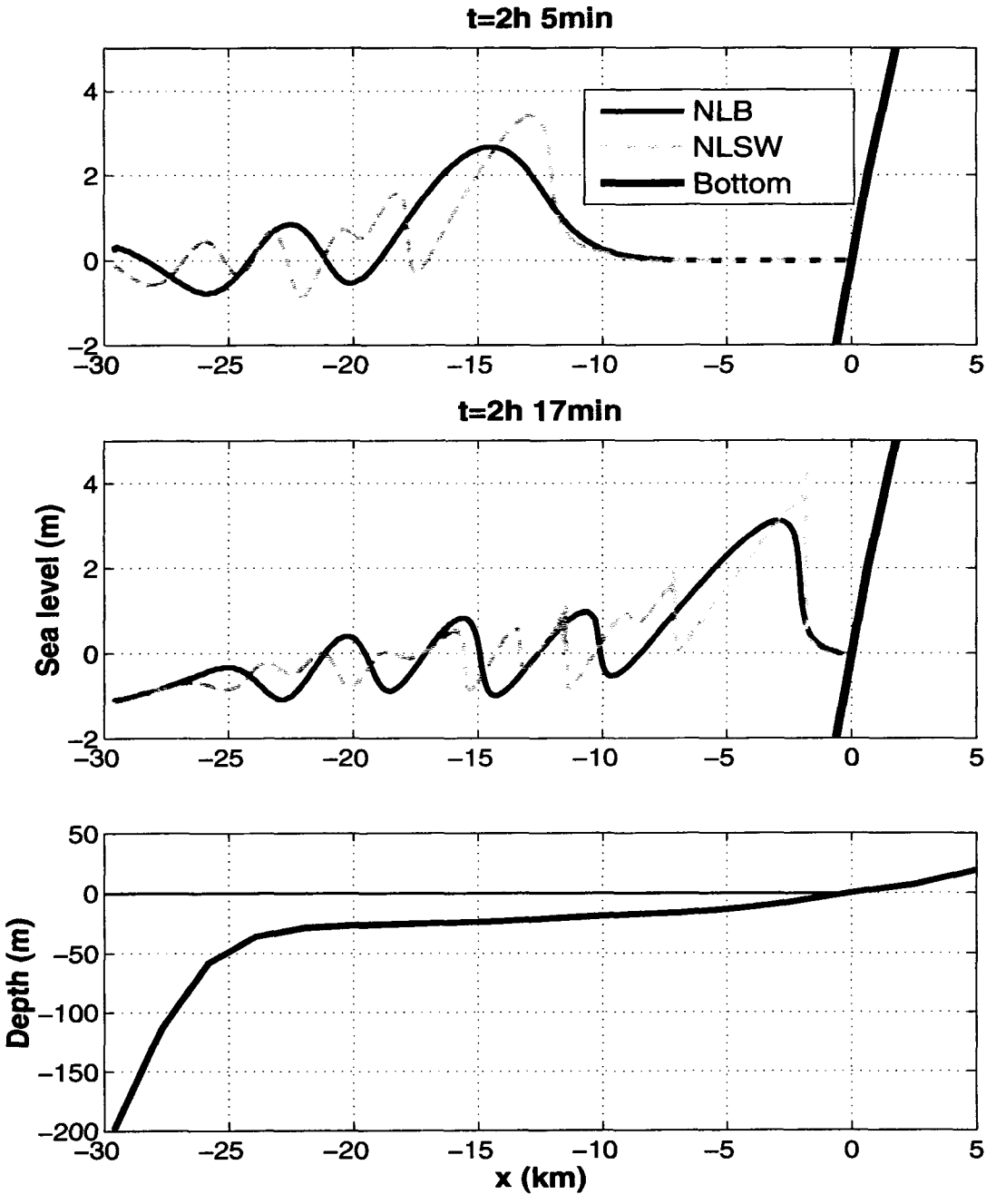

Figure 48: Comparison of tsunami propagation on the continental shelf at Yala, Sri Lanka (transect C-C), obtained by one-dimensional NLB and NLSW models.

Reproduced with permission of the copyright owner. Further reproduction prohibited without permission.

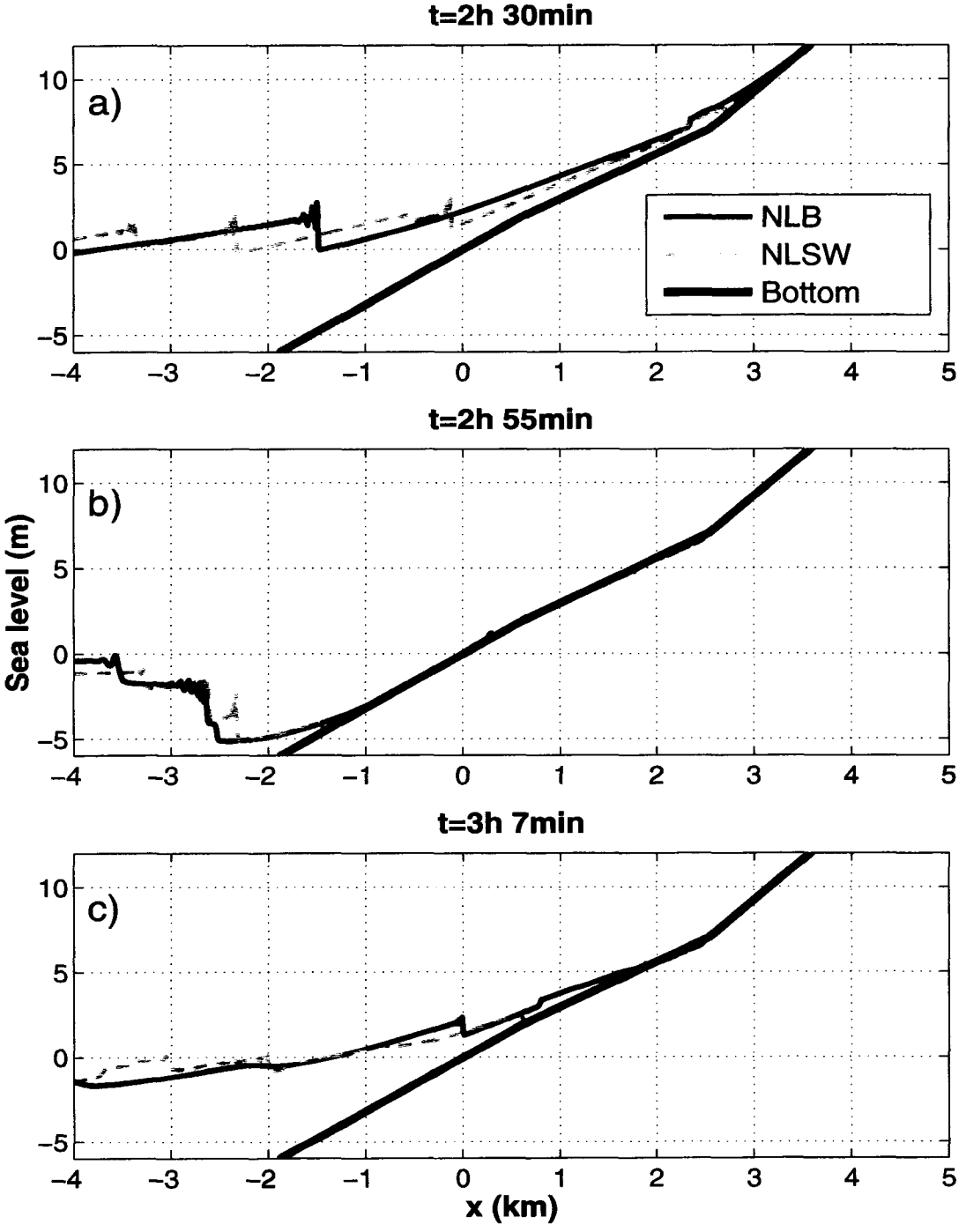

Figure 49: Comparison of tsunami runup/rundown at Yala, Sri Lanka (transect C-C), obtained by one-dimensional NLB and NLSW models.

Reproduced with permission of the copyright owner. Further reproduction prohibited without permission.

the Navier-Stokes aided by the volume of fluid method (NS-VOF). The NS-VOF method gives a frame of reference to validate the NLB and NLSW solutions. Since this approach introduces the vertical fluid velocity/acceleration and column-wise discretization, more accurate results are expected. However, this method still requires higher computational resources, often not available for practical three-dimensional tsunami computations.

Comparison of the three different methods shows that for practical purposes the NLSW model results are quite reliable, since this model gives consistent results with its counterparts. The NLSW approach is very attractive nowadays for tsunami calculation because this method has very low computational cost and maximum wave height and runup are often overpredicted, thus increasing the safety factor. The NLSW results are useful for preliminary hazard assessment, where a simple and quick estimation of maximum wave height, maximum run-up and location of maxima are required. Estimation of the wave front tip location for the IOT is excellent. This reaffirms its use as an accurate candidate for determining the tsunami arrival time.

Qualitatively and quantitatively the wave fronts reproduced by the nonlinear dispersive long-wave equations (NLB) and by NS-VOF share many features. For the longer integration time the similarity holds only for the main maximum, because the phase differences between secondary maxima increase with travel time (Fig. 44). Tsunami patterns away from the main front, including runup, have been reproduced by all three methods quite well and the sea level differences are quite small. The dispersion consideration in the numerical models is necessary for accurate prediction since it can produce significant differences in coastal runup when the wave front depicted in Fig. 48 will impinge on the coast, creating complicated patterns of oscillations as compared to the NLSW solution given in Fig. 49. Such oscillations arriving on the continental shelf, bays or harbors may enhance the tsunami oscillations through

Reproduced with permission of the copyright owner. Further reproduction prohibited without permission.

the resonance. As Ortiz *et al.* (2001) pointed out, the dispersion mechanism is not clearly established from the coastal observations, because such data are strongly influenced by the local bathymetry. Does IOT provide such validation? The general comparison between data and NLSW model results given for IOT by Kowalik *et al.* (2005), Lay *et al.* (2005) and Hirata *et al.* (2005) is quite good, even though these are nondispersive models. The computations in the nearshore regions will shed further information on the dispersive versus nondispersive processes; however, to undertake this direction fine resolution bathymetry is needed.

Although a very coarse grid size was adopted for the numerical simulations, numerical results based on the numerical models do fairly well along the coastlines of Sri Lanka. At the Indonesia coast, there are discrepancies for both arrival time and wave amplitude between numerical results and information recorded with tide gauges and tsunami field survey. The discrepancies could be caused by the lack of bathymetric information and uncertainties in the source mechanism as well.

Reproduced with permission of the copyright owner. Further reproduction prohibited without permission.

Chapter 4

Conclusions and Future Work

4.1 Conclusions

This study particularly emphasizes understanding tsunami physics that can lead to effective measures for damage mitigation. It was advanced by the development of a computer code for better formulating tsunami processes. The analysis of a set of laboratory experiments and actual tsunami events have guided the numerical and practical efforts by focusing the proposed investigations on the creation of practical and efficient tools for tsunami problems. The intended impact in the near future of this study is to mitigate the devastating consequences of tsunami events, including loss of human life, destruction of property and damage to the environment. The study achieved the following objectives:

- improved the predictive capability of the tsunami generation/runup model by including more accurately the effects of vertical velocity/acceleration, dispersion and wave breaking.
- increased the current understanding of the fundamental physics associated with tsunami generation, propagation, runup and effects by considering the vertical component of velocity/acceleration.
- described the complex runup flows within the context of their interactions with bottom topography or structures.
- prescribed complex wave generation mechanisms and wave propagation by means of curvilinear boundaries and moving objects.

Reproduced with permission of the copyright owner. Further reproduction prohibited without permission.

- validated the proposed model using appropriate laboratory experiments selected from the literature.

- determined the adequacy of the nonlinear shallow water approximation and other approximations (e.g., Boussinesq) for application to tsunami simulation.

The study involved three parallel efforts to develop:

1) a two-dimensional Navier-Stokes solver aided by the volume of fluid method to track the free surface to solve tsunami problems in a practical and efficient way.

2) a capability to represent complex curvilinear boundaries within a Cartesian grid system.

3) a capability to deal with arbitrarily transient-deformed moving boundaries.

The first goal was achieved through the development and validation of a two-dimensional Navier-Stokes solver and the volume of fluid method technique, which is capable of simulating incompressible fluid flow problems in Cartesian coordinates where the free surface can undergo severe deformations, including impact with solid boundaries and impact between converging fluid fronts. The method is also capable of handling the breakup of a fluid front from the main body of fluid as well as their eventual reconnection.

For the second goal, the geometric representation of curved object surfaces is implemented by using a technique that keeps the rectangular elements but supplements them with a function that defines the obstacle-cutting in the cell interior. This study has implemented a dynamic technique, based on the static technique reported in Nichols *et al.* (1980), Sicilian & Hirt (1984) and Gentry *et al.* (1966), allowing the geometry of a stationary or moving object to have any arbritrary shape in time. Object

Reproduced with permission of the copyright owner. Further reproduction prohibited without permission.

geometry is defined within the grid by computing the fractional face areas and fractional volume of each element that is blocked by the object. This method requires just two or three area fraction variables and one volume fraction variable for each element. This is relatively little information compared with other grid techniques used in computational fluid dynamics. Thus, this technique retains the simplicity of rectangular elements while representing complex and dynamic geometric shapes at a level consistent with the use of averaged flow quantities within each volume element. Another powerful advantage is that the grid and object geometry are free to be defined independently of one another, so grid and object geometries can be generated and modified with very little time or effort.

To fulfill the third goal, the numerical model was constructed to be practical and efficient for solving specific tsunami problems; therefore, an extension for the moving boundary problem was developed. The moving boundary algorithm has been conceived for wave generation triggered by landslides, seabottom uplift and rocks impacting the free surface. The model's accuracy in simulating flow motions and moving objects has been successfully validated in several cases where analytical solutions and/or laboratory experiment data were available.

4.1.1 Models results

The numerical solutions of the proposed Navier-Stokes aided by the volume of fluid method (NS-VOF) are compared with analytical results, shallow water models (linear (LSW), nonlinear (NLSW) and Boussinesq (NLB)) and laboratory experiments. Five numerical tests were conducted to evaluate model accuracy, performance and applicability of other theories. From the five case studies the following conclusions ensue:

Reproduced with permission of the copyright owner. Further reproduction prohibited without permission.

4.1.1.1 Initial stages of the dam-break wave problem

- To ensure a better and reliable prediction in runup regions, it is essential to use tsunami calculation tools that consider the vertical component of velocity/acceleration.

- The dam-break wave front during the initial stage cannot be modeled adequately by the hydrostatic NLSW approach because the vertical velocity component is significant and can not be neglected.

- The solutions based on the hydrostatic assumption overpredict the location of the wave tip, being more pronounced during the initial stage. The averaged wave tip speed is overpredicted by 25%.

- The water depth at the dam site does not reach a constant value instantaneously after the dam-gate breaks, as predicted by the hydrostatic assumption. It takes approximately 9 nondimensional time units to reach the depth constant value of $(4/9)D_o$ at the dam site.

- The free surfaces computed by the NS-VOF model agreed fairly well with the experiment. Some differences are noticeable where turbulence near the free surface occurs, which might be attributed to turbulence phenomena and compressibility that the NS model does not consider.

4.1.1.2 Runup onto a plane beach and deformable-subaerial landslide

- Because dispersion effects are important in the generation regions, a shallow water approach often is not appropriate to model a landslide and the wave it may generate.

- Agreements of LSW and NLSW models versus analytical solution are quite good when slide thickness is small, and no major differences exist between the LSW

Reproduced with permission of the copyright owner. Further reproduction prohibited without permission.

and NLSW results. For thick slides, the omission of the nonlinear term leads to differences in solutions, which become large with time.

- NLSW models and LSW analytical solution underestimate the runup and overestimate the rundown.
- Timing of maximum runup and rundown occurs slightly earlier in the NLSW solutions.
- Due to the inclusion of dispersion effects, the NS-VOF model predicts a wave a bit more elongated, skewed but with slightly smaller amplitude than the NLSW models.

4.1.1.3 Landslide (triangular-sliding-box)

- The simulation results of an impulsive wave interacting with moving objects are verified against the experimental data. This experiment demonstrates NS-VOF model's capability of simulating wave generation in the intermediate water depth regime.

4.1.1.4 Wave propagation and dispersion. Indian Ocean tsunami, Dec. 26, 2004

- General features of the wave propagation agree very well in all numerical models. However, some important differences are observed in the wave pattern when dispersion is not considered, i.e., the development in time of the wave front is shown to be strongly connected to the dispersion effects.
- Wave dispersion effects must be considered in tsunami hazard mitigation since the initial wave generated by the sea bottom uplift could have multiple amplitude and frequency components. As the initial wave propagates, separation of

Reproduced with permission of the copyright owner. Further reproduction prohibited without permission.

the wave occurs forming a train of waves. This train of waves interacts with the leading wave's runup, drawdown and reflection from shelf or land.

- Low-lying, flat regions make the retreat of the flood caused by the first wave very slow. Subsequent waves, as they shallow, often ride over a region already flooded by the first wave. The actual flooded region facilitates propagation of the following waves landward, allowing these waves to impinge on structures, sometimes with higher sea level and speed.

- Numerical calculation using NLSW approach has a very low computational cost, making it very attractive for quick estimation. In addition, maximum wave height, and often runup, are slightly overpredicted (on the safe-side). The NLSW approach is useful for simple and quick estimation of maximum wave height, maximum run-up and locations of maxima.

- Dispersion consideration in numerical models is necessary for accurate prediction since it can produce significant differences in coastal runup when the dispersive waves impinge on the coast and create complicated patterns of oscillations. Such oscillations arriving on the continental shelf, bays or harbors may enhance the tsunami oscillations through resonance.

4.2 Future Work

The two-dimensional numerical model presented in this study has proven to be an accurate hydrodynamic model, and can serve for studying more practical tsunami problems in the future. For practical simulations, one of the most important issues is the computational cost. A typical two-dimensional simulation for tsunami may have about one million cells and it could take 72 hours using one CPU on a X1 supercomputer. The present algorithm is vectorized and has been shown to be efficient

Reproduced with permission of the copyright owner. Further reproduction prohibited without permission.

with reasonable low computational cost. A parallel version is anticipated as the next advancement of this study is directed to solve three-dimensional tsunami problems. Practical tsunami simulation in three dimensions using an extended version of the present algorithm will require an enormous amount of computational resources since an implicit scheme imposes a system of linear equations or an iterative process for the solution of the pressure field. Most of the computational burden is attributed to the solver task; therefore, it is mandatory to work toward a simplified method of solution, e.g., explicit schemes or implementation of faster linear equation solvers like the general minimum residual method (GMRES), Ashby *et al.* (1990); Barrett *et al.* (1994), which has proven to be robust and easy to parallelize. Of course, parallelization on a high-performance machine is the obligatory next step toward the development of the three-dimensional model version.

The inclusion of the algorithm for moving and deformable objects greatly extended the model capability to simulate tsunami problems. One possible extension of the moving and deformable object algorithm is to solve the Bingham fluids. Many materials, such as volcanic lava and submarine sediments, behave approximately like a non-Newtonian fluid. These materials have a critical value or yield stress. Below this yield stress, they behave like a rigid body; above this yield stress, they behave like a viscous fluid. The Bingham plastic model is best-known for describing this viscoplastic behavior. Because a Bingham fluid changes from a solid-like material to a viscous fluid, a numerical algorithm should have the capability of dealing with the fluid motion, the solid motion and the phase change. Currently, the present model can satisfy separately the fluid motion and the rigid motion (in two-dimension) but not their interactions. Future work on tsunami wave generation by sub-aerial and submarine landslide using this model should also address the Bingham fluid problem.

Reproduced with permission of the copyright owner. Further reproduction prohibited without permission.

One significant advance in the grid generation that could be implemented in future studies and toward the completeness of tsunami calculation is the use of adaptive mesh refinement (AMR), Archer *et al.* (2004). AMR allows one to focus computations on regions of interest, instead of computing over a region using a uniform or nonuniform fixed mesh. For example, AMR allows one to track sharp interfaces as a wave front or any other sharp curved discontinuities with high resolution, while areas of lesser interest are kept at lower resolutions. Adaptive-mesh technique in some specific cases could be far more efficient than fixed grid, providing savings in both the computational time needed and data storage required. However, often there is overhead associated with AMR in terms of deciding when and how to adapt, and in keeping track of the evolving mesh. Adaptive cells are particularly better suited to high-performance machines, both serial and parallel.

The majority of flows in nature are turbulent. Because of this fact the model presented in this study should be advanced to consider this phenomena in three-dimension. In this study the laminar dissipation mechanisms inherent in the numerical method alone may be sufficient to produce reasonable results on turbulent processes. However, in other cases it may be necessary to supply additional dissipation with a simple turbulence model such as a constant eddy viscosity or a mixing length assumption. Unfortunately, there is no simple mechanism to answer this question and the modeler must exercise some engineering judgment. For instance, a large eddy simulation (LES) with a subgrid scale (SGS) model could be an option, Wu (2004).

Reproduced with permission of the copyright owner. Further reproduction prohibited without permission.

Bibliography

ADDESSIO, F. L., CARROLL, D. E., DUKOWICZ, J. K., HARLOW, F. H., JOHNSON, J. N., KASHIWA, B. A., MALTRUD, M. E. & RUPPEL, H. E. 1986 CAVEAT: A computer code for fluid dynamics problems with large distortion and internal slip. *Tech. Rep.* LA-10613-MS. Los Alamos National Laboratory.

AKI, K. & RICHARDS, P. G. 1980 *Quantitative Seismology Theory and Methods, Vol.2*. W. H. Freeman and Co., 557 pp.

AMSDEN, A. A. & HARLOW, F. H. 1970 The SMAC method: A numerical technique for calculating incompressible fluid flows. *Tech. Rep.* LA-4370. Los Alamos National Laboratory.

AMSDEN, A. A., O'ROURKE, P. J. & BUTLER, T. D. 1989 KIVA-II: A computer program for chemically reactive flows with sprays. *Tech. Rep.* LA-11560-MS. Los Alamos National Laboratory.

ARCHER, B., BETLACH, T., CLOVER, M., DENDY, E. & GITTINGS, M. 2004 SAGE User Manual. *Tech. Rep.* LA-UR-04-2959. Los Alamos National Laboratory.

ASHBY, S. F., MANTEUFFLE, T. A. & SAYLOR, P. E. 1990 A taxonomy for conjugated gradient methods. *SIAM J. Numer. Anal.* **27**, 1542–1568.

ASHGRIZ, N. & POO, J. Y. 1991 FLAIR: Flux line-segment model for advection and interface reconstruction. *J. Comp. Phys.* **93**, 449–468.

Reproduced with permission of the copyright owner. Further reproduction prohibited without permission.

BARRETT, R., BERRY, M., CHAN, T. F., DEMMEL, J., DONATO, J., DONGARRA, J., EIJKHOUT, V., POZO, R., ROMINE, C. & DER VORST, H. V. 1994 *Templates for the Solution of Linear Systems: Building Blocks for Iterative Methods, 2nd Edition*. Philadelphia, PA: SIAM.

BELL, J. B., COLLELA, P. & GLAZ, H. M. 1989 A second-order projection method for the incompressible Navier-Stokes equations. *J. Comp. Phys.* **85**, 275–283.

BELL, J. B. & MARCUS, D. L. 1992 A second-order projection method for variable-density flows. *J. Comp. Phys.* **110**, 334–348.

BRACKBILL, J. U. & RUPPEL, H. M. 1986 A method for adaptively zoned, particle-in-cell calculations in two dimensions. *J. Comp. Phys.* **65**, 314–343.

BRACKBILL, J. U. & SALTZMAN, J. S. 1982 Adaptive zoning for singular problems in two dimensions. *J. Comp. Phys.* **46**, 342–368.

CARRIER, G., WU, T. T. & YEH, H. 2003 Tsunami run-up and draw-down on a plane beach. *J. Fluid Mech.* **475**, 79–99.

CHAN, K.-C. 1970 SUMMAC: a numerical model for water waves. PhD thesis, Stanford University.

CHAN, K.-C. & STREET, R. L. 1968 A computer study of finite amplitude water wave. *J. Comp. Phys.* **6**, 68–69.

CHEN, S., JOHNSON, B. D. & RAAD, P. E. 1993 The surface marker method. In *Computational Modeling of Free and Moving Boundary Problems,1, Fluid Flow* (ed. L. C. Wrobel & C. A. Brebbia), , vol. 1, pp. 223–324. CM Publications, Boston.

CHORIN, A. J. 1968 Numerical solution of the Navier-Stokes equations. *Math. Comp.* **22**, 745–762.

Reproduced with permission of the copyright owner. Further reproduction prohibited without permission.

CHORIN, A. J. 1969 On the convergence of discrete approximations of the Navier-Stokes equations. *Math. Comp.* **23**, 341–357.

COLLELA, P. & WOODWARD, P. 1984 The piecewise parabolic method (PPM) for gas-dynamical simulation. *J. Comp. Phys.* **54**, 174.

DEAN, R. G. & DALRYMPLE, R. A. 1984 *Water wave mechanics for engineers and scientists*. World Scientific, pp. 353.

DEBAR, R. 1974 Fundamentals of KRAKEN code. *Tech. Rep.* Technical Rep. UCIR-760LA-5852. Lawrence Livermore National Laboratory (LLNL).

DRESSLER, R. F. 1952 Hydraulic resistance effect upon the dam-break functions. *J. of Research* **49(3)**, 217–225.

DRESSLER, R. F. 1954 Comparison of theories and experiments for hydraulic dam-break wave. *Int. Assoc. Sci. Pubs.* **3(38)**, 319–328.

DUNBAR, D., LEBLOND, P. & MURTY, T. S. 1991 Evaluation of tsunami amplitudes for the Pacific Coast of Canada. *Prog. Oceanog.* **26**, 115–177.

FEKKEN, G. 2004 Numerical simulation of free-surface flow with moving rigid bodies. PhD thesis, University of Groningen, 127 pp.

FOLEY, J., VAN DAM, A., FEINER, S. & HUGHES, J. 1995 *Computer Graphics: Principles and Practice*. Addison Wesley.

FUJIMA, K. 2001 Long wave propagation on large roughness. In *ITS Proceedings, Session. 7-22. Seattle, WA*, pp. 891–895.

GENTRY, R. A., MARTIN, R. E. & DALY, B. J. 1966 An Eulerian differencing method for unsteady compressible flow problems. *J. Comp. Phys.* **1**, 87–118.

Reproduced with permission of the copyright owner. Further reproduction prohibited without permission.

GERRITS, J. 2001 Dynamics of liquid-filled spacecraft. Numerical simulation of coupled solid-liquid. PhD thesis, University of Groningen, 112 pp.

GLOWINSKI, R. 1992 Finite element methods for Navier-Stokes equations. *Anne. Rev. Fluid Mech.* **24**, 167–204.

GOTO, C. & SHUTO, N. 1983 Numerical simulation of tsunami propagations and run-up. In *Tsunami-Their Science and Engineering* (ed. K. Iida & T. Iwasaki), pp. 439–451. Terra Scientific Publ. Comp., Tokyo.

GRESHO, P. M. 1990 On the theory of semi-implicit projection methods for viscous incompressible flow and its implementation via a finite element that also introduces a nearly consistent mass matrix. part 1: theory. *Int. J. for Num. Met. in Fluids* **11**, 587–620.

GRESHO, P. M. 1991 Incompressible fluid dynamic: some fundamental formulation issues. *Annu. Rev. Fluid Mech.* **23**, 413–453.

HARLOW, F. H. & WELCH, J. E. 1965 Numerical calculation of time-dependent viscous incompressible flow of fluid with a free surface. *The Physics of Fluids* **8**, 2182–2189.

HEDERSON, F. M. 1966 *Open Channel Flow.* The Macmillan Company, New York; Collier-Macmillan Limited, London.

HEINRICH, P. 1992 Nonlinear water waves generated by submarine and aerial landslides. *Journal of Waterway, Port, Coastal and Ocean Eng.* **118(3)**, 249–266.

HEINRICH, P., SCHINDELE, F. & GUIBORG, S. 1998 Modeling of the February 1996 Peruvian tsunami. *Geophys. Res. Lett.* **25(14)**, 2687–2690.

Reproduced with permission of the copyright owner. Further reproduction prohibited without permission.

HIRATA, K., SATAKE, K., TANIOKA, Y., KURAGANO, T., HASEGAWA, Y., HAYASHI, Y. & HAMADA, N. 2005 The Indian Ocean Tsunami: Tsunami source model from satellite altimetry. In *Proceedings of the International Tsunami Symposium* (ed. G. Papadopoulos & K. Satake), pp. 72–76. Chania Greece.

HIRT, C. W. & NICHOLS, B. D. 1981 Volume of fluid method for the dynamics of free boundaries. *J. Comp. Phys.* **39**, 201–225.

HIRT, C. W., NICHOLS, B. D. & ROMERO, N. C. 1975 SOLA-A: A numerical solution algorithm for transient fluid flows. *Tech. Rep.* LA-5852. Los Alamos National Laboratory.

HRV -HARVARD CMT CATALOG- 2005 Harvard Seismology: Centroid-Moment Tensor Project. http://www.seismology.harvard.edu/CMTsearch.html.

HUNT, B. 1982 Asymptotic solution for dam-break problem. *J. Hydr. Div., ASCE* **109(12)**, 1698–1706.

HUNT, B. 1987 A perturbation solution of the flood-routing problem. *J. Hydr. Res.* **25(2)**, 215–234.

IMAMURA, F. 1996 Simulation of wave-packet propagation along sloping beach by TUNAMI-CODE. In *Long Wave Runup Models* (ed. H. Yeh, P. Liu & C. Synolakis), pp. 231–241. World Scientific.

IMAMURA, F., GOTO, C., OGAWA, Y. & SHUTO, N. 1995 *Numerical Method of Tsunami Simulation with the Leap-Frog Scheme.* IUGG/IOC Time Project Manuals.

Reproduced with permission of the copyright owner. Further reproduction prohibited without permission.

IMAMURA, F. & SHUTO, N. 1989 Tsunami propagation simulation by use of numerical dispersion. *International Symposium on Computational Fluid Dynamics* pp. 390–395.

IMAMURA, F., SHUTO, N. & GOTO, C. 1990 Study on numerical simulation of the transoceanic propagation of tsunami. Part 2, characteristics of tsunami propagation over the Pacific Ocean. *Zisin. J, Seismol. Soc. Japan* **43**, 389–402.

IWASAKI, S. I. 2005 Posting of Thailand tide gauge data to Tsunami Bulletin Board. http://www.navy.mi.th/hydro/tsunami.htm.

JI, C. 2004 Preliminary result of the 04/12/26 (Mw 9.0), off W. coast of northern Sumatra earthquake. http://www.gps.caltech.edu/%7Ejichen/Earthquake/2004/aceh/aceh.html.

KERSHAW, D. S. 1976 The incomplete Cholesky conjugate gradient method for the iterative solution of systems of linear equations. *J. Comp. Phys.* **26**, 43–65.

KIM, J. & MOI, P. 1993 Application of a fractional-step method to incompressible Navier-Stokes equations. *J. Comp. Phys.* **50**, 308–323.

KIRBY, J. T., WEI, G., CHEN, Q., KENNEDY, A. B. & DALRYMPLE, R. A. 1998 FUNWAVE1.0: Fully nonlinear Boussinesq wave model documentation and user's manual. *Tech. Rep.* NO. CACR-98-06. University of Delaware.

KOSORIN, K. 1983 Hydraulic characteristics of some dam-break wave singularities. In *20th IAHR congress*, pp. 520–528. Int. Assoc. for Hydraulic Research, Delft, The Netherlands.

Reproduced with permission of the copyright owner. Further reproduction prohibited without permission.

KOTHE, D. B., MJOLSNESS, R. C. & TORREY, M. D. 1991 RIPPLE: A computer program for incompressible flows with free surfaces. *Tech. Rep.* LA-12007-MS. Los Alamos National Laboratory.

KOTHE, D. B. & RIDER, W. J. 1995 Practical considerations for interface tracking methods. In *6th Int. Symp. Comp. Fluid Dynamics*.

KOWALIK, Z. 2004 Tides distribution and tapping into tidal energy. *Oceanologia* **46(3)**, 291–331.

KOWALIK, Z., KNIGHT, W., LOGAN, T. & WHITMORE, P. 2005 Numerical modeling of the global tsunami: Indonesian tsunami of 26 December 2004. *Science of Tsunami Hazards* **23(1)**, 40–56.

KOWALIK, Z. & MURTY, T. S. 1993*a* *Numerical Modeling of Ocean Dynamics*. World Scientific, 481 pp.

KOWALIK, Z. & MURTY, T. S. 1993*b* Numerical simulation of two-dimensional tsunami runup. *Marine Geodesy* **16**, 87–100.

LAY, T., KANAMORI, H., AMMON, C. J., NETTLES, M., WARD, S. N., ASTER, R. C., BECK, S. L., BILEK, S. L., BRUDZINSKI, M. R., BUTLER, R., DESHON, H. R., EKSTROM, G., SATAKE, K. & SIPKIN, S. 2005 The great Sumatra-Andaman earthquake of 26 December 2004. *Science* **308**, 1127–1139.

LEMOS, C. M. 1996 Higher-order schemes for free surface flows with arbitrary configurations. *Int. J. for Num. Met. in Fluids* **23**, 545–566.

LIN, P. & LIU, P. L.-F. 1999 Free surface tracking methods and their applications to wave hydrodynamics. In *Advance in Coastal and Ocean Engineering* (ed. P. L.-F. Liu), , vol. 5, pp. 213–240. World Scientific.

Reproduced with permission of the copyright owner. Further reproduction prohibited without permission.

LIU, P. L.-F., CHO, Y. B., YOON, S. B. & SEO, S. N. 1995 Numerical simulation of the 1960 Chilean tsunami propagation and inundation at Hilo, Hawaii. In *Tsunami Progress in Prediction, Disaster Prevention and Warning* (ed. Y. Tsuchiya & N. Shuto). Kluwer Academic Publisher, Netherlands.

LIU, P. L.-F., LYNETT, P. & SYNOLAKIS, C. E. 2003 Analytical solution for force longwaves on a sloping beach. *J. Fluid Mech.* **478**, 101–109.

MADER, C. L. 2004 *Numerical Modeling of Water Waves*. Boca Raton: CRC Press.

MADSEN, P. A. & SCHAFFER, H. A. 1999 A review of Boussinesq-type equations for surface gravity waves. In *Advances in Coastal and Ocean Engineering* (ed. P. L.-F. Liu), , vol. 5, pp. 1–94. World Scientific, Singapore.

MARTIN, J. C. & MOYCE, W. J. 1952 A experimental study of the collapse of liquid columns on a rigid horizontal plane. *Phil. Trans. R. Soc. London A* **244**, 312–324.

MASAMURA, K. & FUJIMA, K. 1995 Three-dimensional analysis of long wave runup on a conical island by using MAC method. In *Long Wave Runup Models* (ed. H. Yeh, P. Liu & C. Synolakis), pp. 321–331. World Scientific.

MÉHAUTÉ, B. L. 1976 *An Introduction to Hydrodynamics & Water Waves*. Springer-Verlag, New York, Heidelberg Berlin.

MERRIFIELD, M. A., FIRING, Y. L., BRUNDRIT, G., FARRE, R., KILONSKY, B., KNIGHT, W., KONG, L., MAGORI, C., MANURUNG, P., MITCHELL, W., SHILLINGTON, F., WIJERATNE, E. M. S., JARDIN, J., NAKAHARA, S., PORTER, F.-Y. & TURESKY, N. 2005 Tide gauge observations of the Indian Ocean tsunami, December 26, 2004. *Geophys. Res. Lett., Jan.* **(32)**, L09603, doi:10.1029/2005GL022610.

Reproduced with permission of the copyright owner. Further reproduction prohibited without permission.

MIYATA, H. 1986 Finite-difference simulation of breaking waves. *J. Comp. Phys.* **65**, 179–214.

MIYATA, H. & NISHIMURA, S. 1985 Finite-difference simulation of nonlinear ship waves. *J. Fluid Mech.* **157**, 327–357.

MOHAPATRA, P. K., ESWARAN, V. & BHALLAMUDI, S. M. 1999 Two-dimension analysis of dam-break flow in vertical plane. *J. Hydr. Eng. ASCE* **125(2)**, 183–192.

MORSE, P. M. & FESHBACH, H. 1953 *Methods of Theoretical Physics, Part I.* New York: McGraw-Hill.

NAKAYAMA, T. & MORI, M. 1996 An eulerian finite element method for time dependent free surface problems in hydrodynamics. *Int. J. Num. Methods in Fluids* **22**, 175–194.

NEIC -U.S. NATIONAL EARTHQUAKE INFORMATION CENTER- 2004 Magnitude 9.0 off the west coast of northern Sumatra, Sunday, December 26, 2004 at 00:58:53 UTC. http://neic.usgs.gov/neis/bulletin/neic_slav_ts.html.

NICHOLS, B. D. & HIRT, C. W. 1971 Improved free surface boundary conditions for numerical incompressible-flow calculations. *J. Comp. Phys.* **8**, 434–448.

NICHOLS, B. D. & HIRT, C. W. 1975 Method for calculating multi-dimensional, transient free surface flow past bodies. In *Proc. of the 1st Int. Conf. Num. Ship Hydrodynamics*, pp. 253–277. Gaithersburg, Maryland, US.

NICHOLS, B. D., HIRT, C. W. & HOTCHKISS, R. S. 1980 SOLA-VOF: A solution algorithm for transient fluid flow with multiple free boundaries. *Tech. Rep.* LA-8355. Los Alamos National Laboratory.

Reproduced with permission of the copyright owner. Further reproduction prohibited without permission.

NIO -India National Institute of Oceanography- 2005 26 December 2004 Tsunami. http://www.nio.org/jsp/tsunami.jsp.

Noh, W. F. & Woodward, P. R. 1976 SLIC: Simple line interface method. In *Lecture Note in Physics, ed. A. I. van de Vooren and P. J. Zandbergen. 59:*, pp. 330–340.

Okada, Y. 1985 Surface deformation due to shear and tensile faults in a half-space. *Bulletin of the Seismological Society of America* **75**, 1135–1154.

Ortiz, M., Gómez-Reyes, E. & Vélez-Munoz, H. S. 2001 A fast preliminary estimation model for transoceanic tsunami propagation. In *ITS 2000 Proceedings*, pp. 723–739.

Phole, F. V. 1952 Motion of water due to breaking of a dam and related problems. *USNBS, Circ. 521* **8**, 47–53.

Raad, P. E. 1995 Modeling tsunami with marker and cell method. In *Long-Wave Runup Models* (ed. H. Yeh, P. Liu & C. Synolakis), pp. 181–203. World Scientific.

Raad, P. E. & Bidoae, R. 1998 Assessment and mitigation of large wave damage on three-dimensional shoreline structure. In *Abstract submitted to Okushiri Tsunami Workshop*. Saporo and Okushiri, Hokkaido, Japan.

Rider, J. & Kothe, D. B. 1995 Stretching and tearing interface tracking methods. In *12th AIAA Comp. Fluid Dynamics Conference*. Jun. 20, 1995, San Diego. Paper Number AIAA-95-1717 or LA-UR-95-1145.

Ritter, A. 1892 The propagation of water waves. *Ver Deutsch ingenieur zeitschr* **36, Pt. 3,33**, 954–974.

Reproduced with permission of the copyright owner. Further reproduction prohibited without permission.

SAKAKIYAMA, T. & KAJIMA, R. 1992 Numerical simulation of nonlinear wave interaction with permeable breakwaters. In *Proc. of 23th Int. Conf. Coastal Engng.*, pp. 1517–1530.

SATO, S. 1996 Numerical simulation of 1993 southwest Hokkaido earthquake tsunami around Okushiri Island. *Journal of Waterway, Port, Coastal and Ocean Eng.* **122(5)**, 209–215.

SHIGEMATSU, T., LIU, P. L.-F. & ODA., K. 2004 Numerical modeling of the initial stage of dam-break waves. *J. Hydraul. Res.* **42(2)**, 183–195.

SHIGIHARA, Y. 2004 A study on application of non-linear dispersive wave theory to the numerical simulation of tsunami. PhD thesis, Dept. of Engineering, Tohoku University (in Japanese).

SHIGIHARA, Y., FUJIMA, K., HOMMA, M. & SAITO, K. 2005 Numerical methods of linear dispersive wave equation for the practical problems. In *Asian and Pacific Coasts*, p. 14. Jeju, Korea.

SICILIAN, J. M. & HIRT, C. W. 1984 An efficient computational scheme for tracking contaminant concentrations in fluid flows. *J. Comp. Phys.* **56**, 428–447.

SOI -SURVEY OF INDIA- 2005 Preliminary report of tsunami observations. http://www.surveyofindia.gov.in/tsunami4.htm.

STANBY, P. K., CHEGINI, A. & BARNES, T. C. 1998 The initial stage of dam-break flow. *J. Fluid Mech.* **374**, 407–424.

STEIN, S. & OKAL, E. 2005 Ultra-long period seismic moment of the great December 26, 2004 Sumatra earthquake and implications for the slip process. http://www.earth.northwestern.edu/people/seth/research/sumatra2.html.

Reproduced with permission of the copyright owner. Further reproduction prohibited without permission.

STOKER, J. J. 1957 *Water Waves*. Intersciences Publishers.

STRELKOFF, T. 1986 Dam-break flow waves. In *Megatrends in Hydraulic Engineering* (ed. M. L. Albertson & C. N. Papadakis), pp. 257–266. California State University.

SUSSMAN, M. & FATEMI, E. 1999 An efficient, interface preserving level set re-distancing algorithm and its application to interfacial incompressible fluid flow. *SIAM J. Sci. Comput.* **20(4)**, 1165–1191.

SUSSMAN, M. & PUCKETT, E. G. 2000 A coupled level set and volume-of-fluid method for computing 3D and axisymmetric incompressible two-phase flows. *J. Comp. Phys.* **162**, 301–337.

SUSSMAN, M., SMEREKA, P. & OSHER, S. 1994 A level set approach for computing solutions to incompressible two-phase flow. *J. Comp. Phys.* **114**, 146–159.

TORREY, M. D., CLOUTMAN, L. D., MJOLSNESS, R. C. & HIRT, C. W. 1985 NASA-VOF2D: A computer program for incompressible flows with free surfaces. *Tech. Rep.* LA-10612-MS. Los Alamos National Laboratory.

UBBINK, O. & ISSA, R. 1999 A method for capturing sharp fluid interfaces on arbitrary meshes. *J. Comp. Phys.* **153**, 26–50.

UNVERDI, S. O. & TRYGGVASON, G. T. 1992 A front-tracking method for viscous, incompressible, multi-fluid flows. *J. Comp. Phys.* **100**, 25–37.

VAN KAN, J. 1986 A second-order accurate pressure-correction scheme for viscous incompressible flow. *SIAM, J. Sci. Stat. Comp.* **7**, 870–891.

VAN LEER, B. 1979 Towards the ultimate conservative difference schemes V. a second order equal to Godunov's method. *J. Comp. Phys.* **32**, 101–136.

Reproduced with permission of the copyright owner. Further reproduction prohibited without permission.

WATANABE, Y. & SAEKI, H. 1995 Numerical analysis of breaking waves. *Hydraulic Engineering Software* pp. 385–394.

WELCH, S., TRAPP, J. & MORTENSEN, G. 1994 Interface tracking in two-phase flow simulations using a simple subgrid counting procedure. *in Numerical Methods in Multiphase Flows, ASME, FED.* **185**, 293–299.

WHITHAM, G. B. 1955 The effect of hydraulic resistance in the dam-break problem. In *Proceedings Series A. Royal society of London*, pp. 226–227.

WU, T.-R. 2004 A numerical study of three-dimensional breaking waves and turbulence effects. PhD thesis, Cornell university.

YABE, T. & AOKI, T. 1991 A universal solver for hyperbolic equations by cubic-polynomial interpolation I. one-dimensional solver. *Computer Physics Communications* **66**, 219–232.

YABE, T., ISHIKAWA, T., WANG, P. Y., AOKI, T., KADOTA, Y. & IKEDA, F. 1991 A universal solver for hyperbolic equations by cubic-polynomial interpolation I. two and three-dimensional solver. *Computer Physics Communications* **66**, 233–242.

YAGI, Y. 2005 Preliminary results of rupture process for 2004 off coast of northern Sumatra giant earthquake (ver. 1). http://iisee.kenken.go.jp/staff/yagi/eq/Sumatra2004/Sumatra2004.html.

YOON, S. B. 2002 Propagation of distant tsunamis over slowly varying topography. *J. Geoph. Res.* **107 (c10, 4-1)**, 4–11.

Reproduced with permission of the copyright owner. Further reproduction prohibited without permission.

YOUNGS, D. L. 1982 Time dependent multi-material flow with large fluid distortion. In *Numerical Methods for fluid Dynamics* (ed. K. W. Morton & M. J. Baines). Academic press, New York.

Reproduced with permission of the copyright owner. Further reproduction prohibited without permission.

Appendix A

Nonlinear Shallow Water Model

The depth-average equations involve an assumption that vertical acceleration of water particles is small compared to the gravitational acceleration, and the vertical motion of water particles has no effect on the pressure distribution, so pressure can be assumed as hydrostatic. In addition, the horizontal velocity of water particles is uniform in the vertical direction. The nonlinear shallow water equations of motion and continuity in two-dimension system of coordinate are taken in the following form (Kowalik & Murty, 1993*a*)

$$\frac{\partial u}{\partial t} + u\frac{\partial u}{\partial x} + v\frac{\partial u}{\partial y} + g\frac{\partial \zeta}{\partial x} + \frac{1}{\rho D} r u \sqrt{u^2 + v^2} = 0, \tag{122}$$

$$\frac{\partial v}{\partial t} + u\frac{\partial v}{\partial x} + v\frac{\partial v}{\partial y} + g\frac{\partial \zeta}{\partial y} + \frac{1}{\rho D} r v \sqrt{u^2 + v^2} = 0, \tag{123}$$

$$\frac{\partial \zeta}{\partial t} + \frac{\partial uD}{\partial x} + \frac{\partial vD}{\partial y} = 0, \tag{124}$$

where ρ is the water density, u and v are vertically averaged velocity components along x and y directions respectively, H is the mean water depth, ζ is the sea level, $D = (\zeta + H)$ is the total depth, r is the friction coefficient, and g is the gravity acceleration.

The above equations are solved numerically by using a staggered grid (C grid) in space as shown in Fig. 50. Velocity components location for u and v are denoted by horizontal and vertical bars respectively. The u velocity grid points are offset from the v velocity grid points. Sea level locations are denoted by crosses. Velocity components and sea level (u, v and ζ) are organized into triplets as shown by the triangles. The depth is defined at the sea level location. To resolve the nonlinear

Reproduced with permission of the copyright owner. Further reproduction prohibited without permission.

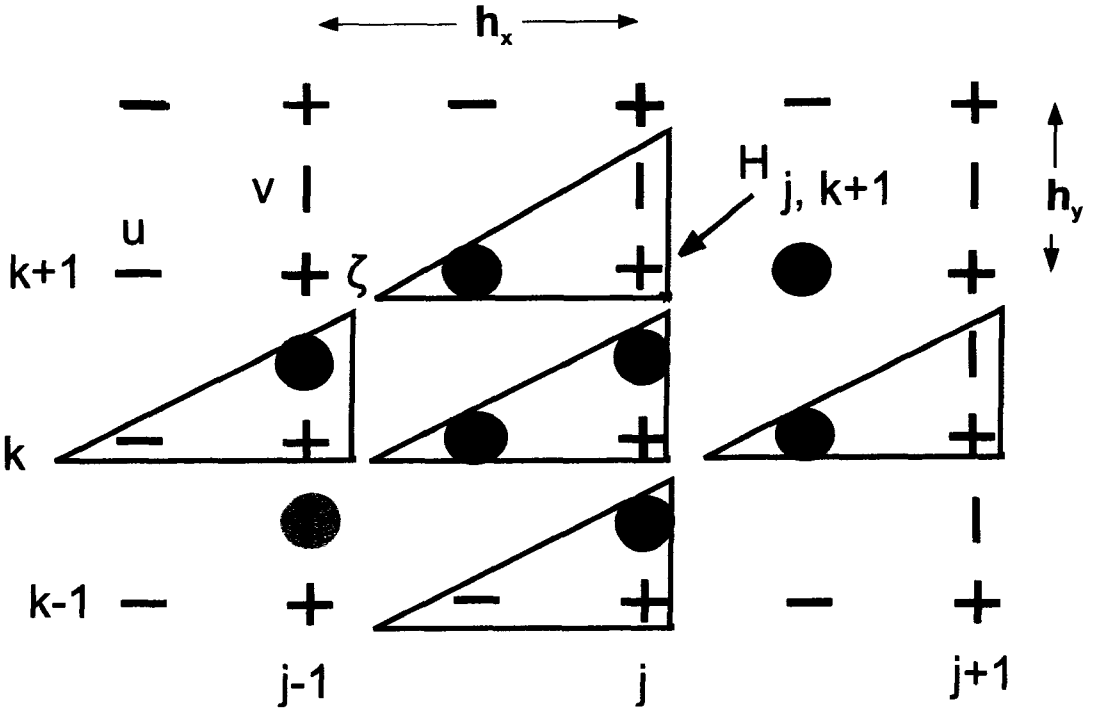

Figure 50: Nonlinear shallow water (NLSW) staggered grid.

terms in the equations of motion the v velocity is needed at the u locations and vice versa. To visualize how the averaged values are constructed, dark-gray and plain-gray circles are introduced at the velocity locations. The values of velocity marked by dark-gray circles, when they are averaged, will define the average of v velocity at the u location. The average of v velocity at this location is

$$\bar{v} = 0.25(v_{j,k-1} + v_{j,k} + v_{j-1,k} + v_{j-1,k-1}).$$

In a similar way the average of u velocities (plain-gray circles) at the v point is

$$\bar{u} = 0.25(u_{j+1,k} + u_{j+1,k+1} + u_{j,k+1} + u_{j,k}).$$

The grid size (space step) along the E-W direction is h_x, and the distance is jh_x, where index $j = 1, 2, 3....$ The space step along the N-S direction is h_y and the distance is kh_y, where index $k = 1, 2, 3, ...$

Reproduced with permission of the copyright owner. Further reproduction prohibited without permission.

The solution of Eqs. (122-124) is usually advanced in time by the two-time-level numerical scheme, Kowalik & Murty (1993*a*), Kowalik *et al.* (2005) and Imamura (1996). For the spatial derivatives the second order of approximation is constructed, thus

The numerical scheme is constructed as follows,

$$\begin{aligned} u_{j,k}^{m+1} &= u_{j,k}^{m} - \frac{gT}{h_x}(\zeta_{j,k}^{m} - \zeta_{j-1,k}^{m}) - \frac{2T}{\rho(D_{j-1,k}^{m} + D_{j,k}^{m})} r u_{j,k}^{m} \sqrt{(u_{j,k}^{m})^2 + (\bar{v}^{m})^2} \\ &\quad - \frac{u_p^m T}{h_x}(u_{j,k}^{m} - u_{j-1,k}^{m}) - \frac{u_n^m T}{h_x}(u_{j+1,k}^{m} - u_{j,k}^{m}) \\ &\quad - \frac{\bar{v}_p^m T}{h_y}(u_{j,k}^{m} - u_{j,k-1}^{m}) - \frac{\bar{v}_n^m T}{h_y}(u_{j,k+1}^{m} - u_{j,k}^{m}), \end{aligned} \tag{125}$$

$$\begin{aligned} v_{j,k}^{m+1} &= v_{j,k}^{m} - \frac{gT}{h_y}(\zeta_{j,k+1}^{m} - \zeta_{j,k}^{m}) - \frac{2T}{\rho(D_{j,k}^{m} + D_{j,k+1}^{m})} r v_{j,k}^{m} \sqrt{(\bar{u}^{m})^2 + (v_{j,k}^{m})^2} \\ &\quad - \frac{\bar{u}_p^m T}{h_x}(v_{j,k}^{m} - v_{j-1,k}^{m}) - \frac{\bar{u}_n^m T}{h_x}(v_{j+1,k}^{m} - v_{j,k}^{m}) \\ &\quad - \frac{v_p^m T}{h_y}(v_{j,k}^{m} - v_{j,k-1}^{m}) - \frac{v_n^m T}{h_y}(v_{j,k+1}^{m} - v_{j,k}^{m}), \end{aligned} \tag{126}$$

where index m stands for the time stepping, T is the time step,

$$u_p = 0.5(u_{j,k} + |u_{j,k}|),$$

$$u_n = 0.5(u_{j,k} - |u_{j,k}|),$$

$$v_p = 0.5(v_{j,k} + |v_{j,k}|),$$

and

$$v_n = 0.5(v_{j,k} - |v_{j,k}|)$$

are velocity switches used in the upwind/downwind method to turn on/off the upstream/downstream advective term derivatives, i.e., if $u_{j,k} > 0$ then $u_p = u_{i,j}$ and $u_n = 0$; conversely, if $u_{j,k} < 0$ then $u_p = 0$ and $u_n = u_{j,k}$.

Reproduced with permission of the copyright owner. Further reproduction prohibited without permission.

For the large scale computations the upwind/downwind method is essential as it displays strong stability. In order to get a higher order approximation in space for the continuity equation the upwind/downwind flux numerical original scheme proposed by Mader (2004) is expanded. The original numerical scheme has beem improved by an additional interpolation between the grid points based on the method of characteristic. Then, the continuity equation becomes

$$\begin{aligned} \zeta_{j,k}^{m+1} &= \zeta_{j,k}^{m} - \frac{T}{h_x}(flux_{x,j+1,k} - flux_{x,j,k}) \\ &\quad -\frac{T}{h_y}(flux_{y,j,k} - flux_{y,j,k-1}), \end{aligned} \tag{127}$$

where

$$flux_{x,j,k} = u_p^{m+1}\zeta_{p,x} + u_n^{m+1}\zeta_{n,x} + u_{j,k}^{m+1}\frac{(H_{j,k} + H_{j-1,k})}{2}, \tag{128}$$

$$\zeta_{p,x} = (0.5 + u_p^{m+1}\frac{T}{h_x})\zeta_{j-1,k}^{m} + (0.5 - u_p^{m+1}\frac{T}{h_x})\zeta_{j,k}^{m},$$

$$\zeta_{n,x} = (0.5 + u_n^{m+1}\frac{T}{h_x})\zeta_{j-1,k}^{m} + (0.5 - u_n^{m+1}\frac{T}{h_x})\zeta_{j,k}^{m},$$

$$flux_{y,j,k} = v_p^{m+1}\zeta_{p,y} + v_n^{m+1}\zeta_{n,y} + v_{j,k}^{m+1}\frac{(H_{j,k} + H_{j,k+1})}{2}, \tag{129}$$

$$\zeta_{p,y} = (0.5 + v_p^{m+1}\frac{T}{h_y})\zeta_{j,k}^{m} + (0.5 - v_p^{m+1}\frac{T}{h_y})\zeta_{j,k+1}^{m}$$

$$\zeta_{n,y} = (0.5 + v_n^{m+1}\frac{T}{h_y})\zeta_{j,k}^{m} + (0.5 - v_n^{m+1}\frac{T}{h_y})\zeta_{j,k+1}^{m}$$

The flux form of equation of continuity is important for successful computation in the domain which includes both dry and wet points. For instance, in one-dimesion, the $flux_j$ is located at the u_j point. As velocity is tested in this point to be positive or negative, the associated sea level is taken to form the flux. Usual form of the upstream/downstream flux

$$flux_j = u_p^{m+1}\zeta_{j-1}^{m} + u_n^{m+1}\zeta_j^{m} + u_j^{m+1}\frac{(H_j + H_{j-1})}{2}$$

Reproduced with permission of the copyright owner. Further reproduction prohibited without permission.

involves sea level ζ^m_{j-1} when velocity is positive and ζ^m_j when velocity is negative. A formulation given by Eqs. (127), (128) and (129) takes into account an additional fact, due to the new velocity, the sea level has been moved during one time step (T) from an original position to the new one. This distance depending on the velocity is equal to $\pm u_p^{m+1}T$ or to $\pm u_n^{m+1}T$. Notice that this technique adds a higher-order effect to the advective terms.

For the runup calculation a simple condition is used. The following steps are taken when the dry point ($j_{wet}+1$) is located to the right of the wet point j_{wet};

$$\text{if } (\zeta^m(j_{wet}) > -H(j_{wet}+1)), \text{ then } u^m_{j_{wet}+1} = u^m_{j_{wet}}.$$

Thus the velocity from the wet point is extrapolated to the nearest dry point, but the sea level is calculated through the equation of continuity. Wet and dry points are differentiated through the average (undisturbed) depth by setting negative values in the dry and positive values in the wet points. Additionally, the total depth in the dry grid points is taken as zero $D = H + \zeta = 0$. The total depth is usually taken as the parameter to be tested for the presence of the wet or dry points, Kowalik & Murty (1993*b*).

Reproduced with permission of the copyright owner. Further reproduction prohibited without permission.

Appendix B

Leap Frog Method

In one-dimension system of coordinate, equation of motion and continuity are expressed in flux form as

$$\frac{\partial M}{\partial t}+\frac{\partial M^2}{\partial x}+gD\frac{\partial \zeta}{\partial x}+\frac{gn^2}{D^{7/3}}M|M|=0 \quad \text{and} \quad \frac{\partial \zeta}{\partial t}+\frac{\partial M}{\partial x}=0, \tag{130}$$

where $M=uD$ is the water transport and n is the Manning's roughness coefficient. The numerical scheme is constructed on a space-time staggered grid having second order of approximation in space and time, Imamura *et al.* (1995)

The two-time-level numerical scheme reads

$$\zeta_j^m=\zeta_j^{m-1}-\frac{T}{h}(M_j^{m-1/2}-M_{j-1}^{m-1/2})$$

$$M_j^{m+1/2}=\frac{1}{(1+\mu_x)}[(1-\mu_x)M_j^{m-1/2}-\frac{gD_rT}{h}(\zeta_{j+1}^m-\zeta_j^m)$$
$$-\frac{T}{h}(\lambda_1\frac{(M_{j+1}^{m-1/2})^2}{D_{Mj+1}^{m-1/2}}+\lambda_2\frac{(M_j^{m-1/2})^2}{D_{Mj}^{m-1/2}}+\lambda_3\frac{(M_{j-1}^{m-1/2})^2}{D_{Mj-1}^{m-1/2}})] \tag{131}$$

where μ_x is a friction term factor, D_M is the total depth at M points, and D_r is the total depth which depends on the sea level and depth of the neighboring cells. Parameters λ_1, λ_2 and λ_3 are the up-down wind's switches used in the nonlinear term. They are defined as:

If $M_j^{m-1/2}<=0.0$ and $D_{Mj+1}^{m-1/2}<=0.0$ then $\lambda_1=0,\ \lambda_3=0$

If $M_j^{m-1/2}<=0.0$ and $D_{Mj+1}^{m-1/2}>0.0$ then $\lambda_1=0,\ \lambda_3=1$

If $M_j^{m-1/2}>0.0$ and $D_{Mj-1}^{m-1/2}<=0.0$ then $\lambda_1=0,\ \lambda_3=0$

If $M_j^{m-1/2}>0.0$ and $D_{Mj-1}^{m-1/2}>0.0$ then $\lambda_1=1,\ \lambda_3=0.$

Reproduced with permission of the copyright owner. Further reproduction prohibited without permission.

μ_x and D_M are defined as

$\mu_x = \frac{gn^2T}{2D_r^{7/3}}|M_j^{m-1/2}|$ and $D_{M_j}^{m-1/2} = \frac{1}{4}(D_j^{m-1} + D_{j+1}^{m-1} + D_j^m + D_{j+1}^m)$, respectively.

The runup condition depends on the value of D_r which is defined as:

If $D_j^m <= 0.0$ and $D_{j+1}^m <= 0.0$ then $D_r = 0.0$

If $D_j^m <= 0.0$ and $D_{j+1}^m > 0.0$ then $D_r = max(0.0, \zeta_{j+1}^m + H_j)$

If $D_j^m > 0.0$ and $D_{j+1}^m <= 0.0$ then $D_r = max(0.0, \zeta_j^m + H_{j+1})$

If $D_j^m > 0.0$ and $D_{j+1}^m > 0.0$ then $D_r = 0.5(D_j^m + D_{j+1}^m)$.

If $D_r = 0$ then $M_j^{m+1/2} = 0$, otherwise $M_j^{m+1/2}$ is calculated according to Eq. (131).

Reproduced with permission of the copyright owner. Further reproduction prohibited without permission.

Appendix C

Nonlinear Boussinesq Model

Equations of motion for the nonlinear Boussinesq model are taken from Shigihara (2004) and Shigihara *et al.* (2005). The equations are:

$$\frac{\partial u}{\partial t} + u\frac{\partial u}{\partial x} + v\frac{\partial u}{\partial y} + g\frac{\partial \zeta}{\partial x} + \frac{1}{\rho D} ru\sqrt{u^2+v^2} = \frac{\partial \psi}{\partial x}, \tag{132}$$

and

$$\frac{\partial v}{\partial t} + u\frac{\partial v}{\partial x} + v\frac{\partial v}{\partial y} + g\frac{\partial \zeta}{\partial y} + \frac{1}{\rho D} rv\sqrt{u^2+v^2} = \frac{\partial \psi}{\partial y}, \tag{133}$$

where the potential function ψ is defined as

$$\psi = \frac{H^2}{3}\left(\frac{\partial^2 u}{\partial x \partial t} + \frac{\partial^2 v}{\partial y \partial t}\right). \tag{134}$$

By substituting Eqs. (132) and (133) into Eq. (134) and neglecting both nonlinear and bottom friction terms from equations of motion yields the Poisson equation for the solution of ψ as

$$\frac{H^2}{3}\left(\frac{\partial^2 \psi}{\partial x^2} + \frac{\partial^2 \psi}{\partial y^2}\right) - \psi = \frac{gH^2}{3}\left(\frac{\partial^2 \zeta}{\partial x^2} + \frac{\partial^2 \zeta}{\partial y^2}\right). \tag{135}$$

Thus, the dispersive wave propagation results in an elliptical problem, where the potential function ψ plays the role of pressure corrector. Applying the same notation used in Appendix A, the finite difference forms for the equations of motion are

$$\begin{aligned} u_{j,k}^{m+1} = u_{j,k}^{m} - \frac{gT}{h_x}(\zeta_{j,k}^{m} - \zeta_{j-1,k}^{m}) - \frac{u_p^{m} T}{h_x}(u_{j,k}^{m} - u_{j-1,k}^{m}) - \frac{u_n^{m} T}{h_x}(u_{j+1,k}^{m} - u_{j,k}^{m}) \\ - \frac{\bar{v}_p^{u,m} T}{h_y}(u_{j,k}^{m} - u_{j,k-1}^{m}) - \frac{\bar{v}_n^{u,m} T}{h_y}(u_{j,k+1}^{m} - u_{j,k}^{m}) \\ - \frac{2T}{\rho(D_{j-1,k}^{m} + D_{j,k}^{m})} r u_{j,k}^{m}\sqrt{(u_{j,k}^{m})^2 + (\bar{v}^{m})^2} + \frac{T}{h_x}(\psi_{j,k}^{m} - \psi_{j-1,k}^{m}) \end{aligned} \tag{136}$$

Reproduced with permission of the copyright owner. Further reproduction prohibited without permission.

$$v_{j,k}^{m+1} = v_{j,k}^{m} - \frac{gT}{h_y}(\zeta_{j,k+1}^{m} - \zeta_{j,k}^{m}) - \frac{\bar{u}_p^{v,m}T}{h_x}(v_{j,k}^{m} - v_{j-1,k}^{m}) - \frac{\bar{u}_n^{v,m}T}{h_x}(v_{j+1,k}^{m} - v_{j,k}^{m})$$
$$- \frac{v_p^{m}T}{h_y}(v_{j,k}^{m} - v_{j,k-1}^{m}) - \frac{v_n^{m}T}{h_y}(v_{j,k+1}^{m} - v_{j,k}^{m}) \quad (137)$$
$$- \frac{2T}{\rho(D_{j,k}^{m} + D_{j,k+1}^{m})} r v_{j,k}^{m} \sqrt{(\bar{u}^{m})^2 + (v_{j,k}^{m})^2} + \frac{T}{h_y}(\psi_{j,k+1}^{m} - \psi_{j,k}^{m}).$$

Numerical form of continuity equation (Eq. 124 in Appendix A) is,

$$\zeta_{j,k}^{m+1} = \zeta_{j,k}^{m} - \frac{T}{h_x}(u_{j+1,k}^{m+1} D_{j+1,k}^{u,m} - u_{j,k}^{m+1} D_{j,k}^{u,m}) - \frac{T}{h_y}(v_{j,k}^{m+1} D_{j,k}^{v,m} - v_{j,k-1}^{m+1} D_{j,k-1}^{v,m}). \quad (138)$$

The above explicit numerical scheme uses Eqs. (136)–(138) to compute velocity and sea level, and Eq. (134) serves to compute the potential function. This computational process is unstable since a new stability condition arises due to dispersive terms. It requires that the space step of numerical computation h_x (assuming $h_x = h_y$), be $h_x > 1.5H$, Shigihara (2004). As the average depth of the Global Ocean is close to 4km the above condition introduces relatively large space steps which leads to poor spatial resolution and numerical instability. To circumvent stability requirements an implicit numerical scheme to derive the potential function has been constructed, Shigihara *et al.* (2005). It uses Poisson equation (Eq. 135) in the following implicit numerical form:

$$\Big[1 + \frac{2}{3}H_{j,k}^2\Big(\frac{1}{h_x^2} + \frac{1}{h_y^2}\Big)\Big]\psi_{j,k}^{m+1}$$
$$- \frac{H_{j,k}^2}{3}\Big(\frac{1}{h_x^2}\psi_{j+1,k}^{m+1} + \frac{1}{h_x^2}\psi_{j-1,k}^{m+1} + \frac{1}{h_y^2}\psi_{j,k+1}^{m+1} + \frac{1}{h_y^2}\psi_{j,k-1}^{m+1}\Big) =$$
$$\frac{gH_{j,k}^2}{3}\Big[2\Big(\frac{1}{h_x^2} + \frac{1}{h_y^2}\Big)\zeta_{j,k}^{m+1} \quad (139)$$
$$- \frac{1}{h_x^2}\zeta_{j+1,k}^{m+1} - \frac{1}{h_x^2}\zeta_{j-1,k}^{m+1} - \frac{1}{h_y^2}\zeta_{j,k+1}^{m+1} - \frac{1}{h_y^2}\zeta_{j,k-1}^{m+1}\Big].$$

Reproduced with permission of the copyright owner. Further reproduction prohibited without permission.

In order to solve the Poisson equation, the boundary condition for ψ is constructed from Eq. (134) in the following way:

$$\psi_{j,k}^{m+1} = \frac{H_{j,k}^2}{3T}\Big[\frac{1}{h_x}(u_{j+1,k}^{m+1} - u_{j,k}^{m+1} - u_{j+1,k}^{m} + u_{j,k}^{m}) + \frac{1}{h_y}(v_{j,k}^{m+1} - v_{j,k-1}^{m+1} - v_{j,k}^{m} + v_{j,k-1}^{m})\Big]. \tag{140}$$

Reproduced with permission of the copyright owner. Further reproduction prohibited without permission.